



U.S. Department of Transportation  
Federal Highway Administration

## Errata

**Date:** July 27, 2015

**Issuing Office:** Federal Highway Administration—Office of Research, Development, and Technology: LTPP

**Address:** Turner-Fairbank Highway Research Center, 6300 Georgetown Pike, McLean, VA 22101

**Name of Document:** LTPP Computed Parameter: Dynamic Modulus

**FHWA Publication No.:** FHWA-HRT-10-035

The following changes were made to the document after publication on the Federal Highway Administration Web site:

Location	Incorrect Values	Corrected Values
On Page 106, APPENDIX A. equation number (56), Change the equation to the corrected value	$\log \log(\eta) = \begin{cases} A + VTS \log(T_R) & T_R > T_{critical} \\ 2.7 \times 10^{12} & T_R \leq T_{critical} \end{cases}$	$\log \log(\eta) = \begin{cases} A + VTS \log(T_R) & T_R > T_{critical} \\ 1.095 & T_R \leq T_{critical} \end{cases}$

# LTPP Computed Parameter: Dynamic Modulus

PUBLICATION NO. FHWA-HRT-10-035

SEPTEMBER 2011



U.S. Department of Transportation  
**Federal Highway Administration**

Research, Development, and Technology  
Turner-Fairbank Highway Research Center  
6300 Georgetown Pike  
McLean, VA 22101-2296



## FOREWORD

The dynamic modulus,  $|E^*|$ , is a fundamental property that defines the strain response characteristics of asphalt concrete mixtures as a function of loading rate and temperature. The significance of this material property is threefold. First, it is one of the primary material property inputs in the *Mechanistic Empirical Pavement Design Guide* (MEPDG) and software developed by National Cooperative Highway Research Program Project 1-37A.<sup>(1,2)</sup> MEPDG uses a master curve and time-temperature shift factors in its internal modulus computation.<sup>(1)</sup> In MEPDG, the master curve is constructed using a hierarchical structure of inputs ranging from estimates based on mixture volumetrics and binder tests to full-scale mixture  $|E^*|$  testing.  $|E^*|$  is one of the primary properties measured in the Asphalt Mixture Performance Test protocol that complements the volumetric mix design.<sup>(3,4)</sup> Additionally, it is one of the fundamental linear viscoelastic material properties that can be used in advanced pavement response models based on viscoelasticity.

Given the significance of  $|E^*|$ , this study evaluated existing prediction models, developed new models, and populated the Long-Term Pavement Performance database to provide a valuable data source for the pavement community. Supplementing the full suite of material properties, performance history, traffic, and climate with  $|E^*|$  estimates will be advantageous in conducting MEPDG calibration, validation, and implementation.

Jorge E. Pagán-Ortiz  
Director, Office of Infrastructure  
Research and Development

### Notice

This document is disseminated under the sponsorship of the U.S. Department of Transportation in the interest of information exchange. The U.S. Government assumes no liability for the use of the information contained in this document. This report does not constitute a standard, specification, or regulation.

The U.S. Government does not endorse products or manufacturers. Trademarks or manufacturers' names appear in this report only because they are considered essential to the objective of the document.

### Quality Assurance Statement

The Federal Highway Administration (FHWA) provides high-quality information to serve Government, industry, and the public in a manner that promotes public understanding. Standards and policies are used to ensure and maximize the quality, objectivity, utility, and integrity of its information. FHWA periodically reviews quality issues and adjusts its programs and processes to ensure continuous quality improvement.

## TECHNICAL REPORT DOCUMENTATION PAGE

1. Report No. FHWA-HRT-10-035	2. Government Accession No.	3. Recipient's Catalog No.	
4. Title and Subtitle LTPP Computed Parameter: Dynamic Modulus		5. Report Date September 2011	
		6. Performing Organization Code:	
7. Author(s) Y. Richard Kim, B. Underwood, M. Sakhaei Far, N. Jackson, and J. Puccinelli		8. Performing Organization Report No. 1240.10	
9. Performing Organization Name and Address Nichols Consulting Engineers, Chtd. 1885 S. Arlington Avenue, Suite 111 Reno, NV 89509		10. Work Unit No.	
		11. Contract or Grant No. DTFH61-02-D-00139	
12. Sponsoring Agency Name and Address Turner-Fairbank Highway Research Center Federal Highway Administration 6300 Georgetown Pike McLean, VA 22101-2296		13. Type of Report and Period Covered Final Report	
		14. Sponsoring Agency Code	
15. Supplementary Notes Prepared in cooperation with the U.S. Department of Transportation, the Contracting Officer's Technical Representative (COTR) was Larry Wiser, Long-Term Pavement Performance Team.			
16. Abstract The dynamic modulus, $ E^*$ , is a fundamental property that defines the stiffness characteristics of hot mix asphalt (HMA) mixtures as a function of loading rate and temperature. In spite of the demonstrated significance of $ E^*$ , it is not included in the current Long-Term Pavement Performance (LTPP) materials tables because the database structure was established before $ E^*$ was identified as the main HMA property in the <i>Mechanistic Empirical Pavement Design Guide</i> (MEPDG). The objective of this study was to use readily available binder, volumetric, and resilient material properties in the LTPP database to develop $ E^*$ estimates. This report provides a thorough review of existing prediction models. In addition, several models have been developed using artificial neural networks for use in this project. This report includes assessments of each model, quality control checks applied to the data, and the final structure and format of the dynamic modulus data added to the LTPP database. A program was also developed to assist in populating the LTPP database, and the details of the program are provided in this report.			
17. Key Words Dynamic modulus, MEPDG, LTPP, Hot mix asphalt, Artificial neural network (ANN)		18. Distribution Statement Document is available to the U.S. public through the National Technical Information Service, Springfield, VA, 22161	
19. Security Classif. (of this report) Unclassified	20. Security Classif. (of this page) Unclassified	21. No. of Pages 263	22. Price

Form DOT F 1700.7 (8-72)

Reproduction of completed page authorized

SI* (MODERN METRIC) CONVERSION FACTORS				
APPROXIMATE CONVERSIONS TO SI UNITS				
Symbol	When You Know	Multiply By	To Find	Symbol
		<b>LENGTH</b>		
in	inches	25.4	millimeters	mm
ft	feet	0.305	meters	m
yd	yards	0.914	meters	m
mi	miles	1.61	kilometers	km
		<b>AREA</b>		
in <sup>2</sup>	square inches	645.2	square millimeters	mm <sup>2</sup>
ft <sup>2</sup>	square feet	0.093	square meters	m <sup>2</sup>
yd <sup>2</sup>	square yard	0.836	square meters	m <sup>2</sup>
ac	acres	0.405	hectares	ha
mi <sup>2</sup>	square miles	2.59	square kilometers	km <sup>2</sup>
		<b>VOLUME</b>		
fl oz	fluid ounces	29.57	milliliters	mL
gal	gallons	3.785	liters	L
ft <sup>3</sup>	cubic feet	0.028	cubic meters	m <sup>3</sup>
yd <sup>3</sup>	cubic yards	0.765	cubic meters	m <sup>3</sup>
NOTE: volumes greater than 1000 L shall be shown in m <sup>3</sup>				
		<b>MASS</b>		
oz	ounces	28.35	grams	g
lb	pounds	0.454	kilograms	kg
T	short tons (2000 lb)	0.907	megagrams (or "metric ton")	Mg (or "t")
		<b>TEMPERATURE (exact degrees)</b>		
°F	Fahrenheit	5 (F-32)/9 or (F-32)/1.8	Celsius	°C
		<b>ILLUMINATION</b>		
fc	foot-candles	10.76	lux	lx
fl	foot-Lamberts	3.426	candela/m <sup>2</sup>	cd/m <sup>2</sup>
		<b>FORCE and PRESSURE or STRESS</b>		
lbf	poundforce	4.45	newtons	N
lbf/in <sup>2</sup>	poundforce per square inch	6.89	kilopascals	kPa
APPROXIMATE CONVERSIONS FROM SI UNITS				
Symbol	When You Know	Multiply By	To Find	Symbol
		<b>LENGTH</b>		
mm	millimeters	0.039	inches	in
m	meters	3.28	feet	ft
m	meters	1.09	yards	yd
km	kilometers	0.621	miles	mi
		<b>AREA</b>		
mm <sup>2</sup>	square millimeters	0.0016	square inches	in <sup>2</sup>
m <sup>2</sup>	square meters	10.764	square feet	ft <sup>2</sup>
m <sup>2</sup>	square meters	1.195	square yards	yd <sup>2</sup>
ha	hectares	2.47	acres	ac
km <sup>2</sup>	square kilometers	0.386	square miles	mi <sup>2</sup>
		<b>VOLUME</b>		
mL	milliliters	0.034	fluid ounces	fl oz
L	liters	0.264	gallons	gal
m <sup>3</sup>	cubic meters	35.314	cubic feet	ft <sup>3</sup>
m <sup>3</sup>	cubic meters	1.307	cubic yards	yd <sup>3</sup>
		<b>MASS</b>		
g	grams	0.035	ounces	oz
kg	kilograms	2.202	pounds	lb
Mg (or "t")	megagrams (or "metric ton")	1.103	short tons (2000 lb)	T
		<b>TEMPERATURE (exact degrees)</b>		
°C	Celsius	1.8C+32	Fahrenheit	°F
		<b>ILLUMINATION</b>		
lx	lux	0.0929	foot-candles	fc
cd/m <sup>2</sup>	candela/m <sup>2</sup>	0.2919	foot-Lamberts	fl
		<b>FORCE and PRESSURE or STRESS</b>		
N	newtons	0.225	poundforce	lbf
kPa	kilopascals	0.145	poundforce per square inch	lbf/in <sup>2</sup>

\*SI is the symbol for the International System of Units. Appropriate rounding should be made to comply with Section 4 of ASTM E380.  
(Revised March 2003)

## TABLE OF CONTENTS

<b>EXECUTIVE SUMMARY .....</b>	<b>1</b>
<b>1.0 INTRODUCTION.....</b>	<b>5</b>
<b>2.0 PREDICTIVE MODELS .....</b>	<b>7</b>
<b>2.1 ORIGINAL WITCZAK EQUATION (NCHRP 1-37A) .....</b>	<b>7</b>
<b>2.2 MODIFIED WITCZAK EQUATION BASED ON <math> G^* </math> (NCHRP 1-40D) .....</b>	<b>8</b>
<b>2.3 HIRSCH MODEL.....</b>	<b>9</b>
<b>2.4 LAW OF MIXTURES PARALLEL MODEL (AL-KHATEEB MODEL) .....</b>	<b>10</b>
<b>2.5 ANN MODELS.....</b>	<b>10</b>
<b>2.6 SUMMARY OF INPUT VARIABLES .....</b>	<b>11</b>
<b>3.0 DATABASES.....</b>	<b>13</b>
<b>3.1 STATEMENT OF NEED.....</b>	<b>13</b>
3.1.1 Inconsistent Definition of Frequency.....	13
3.1.2 Use of Estimated $ G^* $ Values .....	14
3.1.3 Low-Temperature $ G^* $ Values .....	18
3.1.4 Aging Effects .....	18
<b>3.2 BINDER DATABASES .....</b>	<b>19</b>
3.2.1 Witczak Binder Database.....	19
3.2.2 FHWA Mobile Trailer Binder Database.....	20
3.2.3 FHWA TPF-5(019) Binder Database .....	21
3.2.4 NCDOT Binder Database .....	22
3.2.5 Citgo Binder Database .....	22
3.2.6 WRI Binder Database .....	22
<b>3.3 MIXTURE DATABASES .....</b>	<b>23</b>
3.3.1 Witczak Mixture Database.....	23
3.3.2 FHWA Mobile Trailer Mixture Database.....	23
3.3.3 FHWA TPF-5(019) Mixture Database .....	24
3.3.4 NCDOT Mixture Database .....	29
3.3.4 NCDOT Mixture Database .....	29
3.3.5 WRI Mixture Database .....	29
3.3.6 Citgo Mixture Database .....	30
3.3.7 FHWA $M_R$ Database .....	31
3.3.8 LTPP Data.....	32
3.3.9 Input Source Hierarchy .....	32
3.3.10 Data Structure and Detail.....	33
<b>4.0 EVALUATION OF <math> E^* </math>/PREDICTIVE MODELS .....</b>	<b>37</b>
<b>4.1 ANN STRUCTURE USED IN THIS STUDY .....</b>	<b>37</b>
<b>4.2 EVALUATION OF BINDER <math> G^* </math>-BASED MODELS.....</b>	<b>38</b>
<b>4.3 VISCOSITY-BASED ANN .....</b>	<b>52</b>
<b>5.0 ANN MODELS FOR POPULATING THE LTPP DATABASE.....</b>	<b>61</b>
<b>5.1 <math>M_R</math> ANN MODEL .....</b>	<b>63</b>
5.1.1 Forward Modeling .....	64
5.1.2 ANN Model $ E^* $ Backcalculation.....	72

<b>5.2 VV ANN MODEL.....</b>	<b>75</b>
<b>5.3 GV ANN MODEL.....</b>	<b>77</b>
<b>5.4 OTHER ANN MODELS .....</b>	<b>80</b>
<b>5.5 ERROR ASSESSMENT.....</b>	<b>80</b>
<b>6.0 PREDICTION OF <math>E^*</math>/ FOR LTPP LAYERS .....</b>	<b>83</b>
<b>6.1 MODEL PRIORITIZATION AND DECISION TREE DEVELOPMENT .....</b>	<b>83</b>
<b>6.2 DATA QC .....</b>	<b>84</b>
6.2.1 QC #1.....	84
6.2.2 QC #2.....	88
6.2.3 QC #3.....	89
6.2.4 QC #4.....	91
6.2.5 QC #5.....	93
6.2.6 QC #6.....	95
6.2.7 QC #7.....	95
<b>6.3 CONTRACTOR JUDGMENT .....</b>	<b>96</b>
<b>6.4 CONTRACTOR MASTERCURVE JUDGMENT .....</b>	<b>96</b>
<b>6.5 PREDICTION STATISTICS .....</b>	<b>96</b>
<b>6.6 LTPP DATABASE ADDITIONS .....</b>	<b>97</b>
<b>7.0 SUMMARY AND FUTURE WORK .....</b>	<b>103</b>
<b>APPENDIX A: PROCESSING ASPHALT BINDER VISCOSITY DATA.....</b>	<b>105</b>
<b>A.1 INTRODUCTION.....</b>	<b>105</b>
<b>A.2 TEMPERATURE SUSCEPTIBILITY RELATIONSHIP .....</b>	<b>105</b>
<b>A.3 R&amp;BT TEMPERATURE .....</b>	<b>106</b>
<b>A.4 PENETRATION .....</b>	<b>106</b>
<b>A.5 ABSOLUTE VISCOSITY .....</b>	<b>106</b>
<b>A.6 KINEMATIC VISCOSITY.....</b>	<b>107</b>
<b>A.7 EXAMPLE PROBLEM .....</b>	<b>107</b>
<b>A.8 TYPICAL VALUES FOR PURCHASE SPECIFICATION GRADE.....</b>	<b>107</b>
<b>APPENDIX B: PROCESSING ASPHALT BINDER SHEAR MODULUS DATA.....</b>	<b>109</b>
<b>B.1 INTRODUCTION.....</b>	<b>109</b>
<b>B.2 USE OF BBR DATA IN <math> G^* </math> MASTERCURVE GENERATION .....</b>	<b>109</b>
<b>B.3 ANALYSIS USING DSR MEASUREMENTS.....</b>	<b>109</b>
<b>B.4 ANALYSIS WITH BBR MEASUREMENTS .....</b>	<b>112</b>
<b>B.5 COMBINING DSR AND BBR ANALYSIS RESULTS .....</b>	<b>115</b>
<b>B.6 COMPARISON OF RESULTS WITH AND WITHOUT BBR</b> <b>MEASUREMENTS .....</b>	<b>117</b>
<b>B.7 EXTRACTING FULL BINDER <math> G^* </math> DATA FROM LIMITED</b> <b>ISOCHRONAL MEASUREMENTS .....</b>	<b>125</b>
<b>B.8 t-T SHIFT FACTOR SURROGATE MODEL DEVELOPMENT .....</b>	<b>127</b>
B.8.1 Phenomenological t-T Shift Factor Function Model.....	128
B.8.2 Use of Average t-T Shift Factor Function.....	130
<b>B.9 INCLUSION OF BBR DATA IN MASTERCURVE GENERATION.....</b>	<b>131</b>
<b>B.10 PAV- TO RTFO-AGING MODEL (PAR MODEL) .....</b>	<b>133</b>
<b>B.11 AGING EFFECT ON M-VALUE .....</b>	<b>141</b>
<b>B.12 VERIFICATION OF LIMITED DATA DEVELOPMENT .....</b>	<b>142</b>

B.12.1 Level 1a Verification.....	142
B.12.2 Level 1b Verification .....	146
B.12.3 Level 2 Verification .....	150
B.12.4 Level 3 Verification .....	153
<b>APPENDIX C: AMPT VERSUS TP-62.....</b>	<b>157</b>
<b>C.1 EXPERIMENTAL VERIFICATION OF AMPT AND TP-62 DIFFERENCES .....</b>	<b>157</b>
<b>C.2 COMPARISON OF AMPT AND TP-62 PROTOCOLS WITH THE AVAILABLE DATABASE .....</b>	<b>160</b>
<b>C.3 EVALUATION OF AMPT VERSUS TP-62 PROTOCOLS USING ANN MODEL .....</b>	<b>175</b>
<b>APPENDIX D: ANN MODEL FACTORS.....</b>	<b>201</b>
<b>D.1 INTRODUCTION.....</b>	<b>201</b>
<b>D.2 <math>M_R</math> ANN.....</b>	<b>203</b>
<b>D.3 VV ANN .....</b>	<b>208</b>
<b>D.4 <math> G^* </math>-BASED ANN (GV ANN) .....</b>	<b>212</b>
<b>APPENDIX E: ANNACAP SOFTWARE MANUAL .....</b>	<b>217</b>
<b>E.1 INTRODUCTION.....</b>	<b>217</b>
<b>E.2 DISCLAIMER.....</b>	<b>217</b>
<b>E.3 INSTALLATION INSTRUCTIONS.....</b>	<b>218</b>
<b>E.4 USING ANNACAP .....</b>	<b>218</b>
E.4.1 Program Main Screen .....	218
E.4.2 Input Data .....	219
E.4.3 Layer ID .....	220
E.4.4 $M_R$ -Based ANN .....	221
E.4.5 $ G^* $ -Based ANN .....	221
E.4.6 Viscosity-Based ANN .....	222
<b>E.5 BATCH MODE .....</b>	<b>223</b>
<b>E.6 OUTPUT DIRECTORY .....</b>	<b>228</b>
<b>E.7 RUN ANALYSIS .....</b>	<b>229</b>
<b>E.8 FORM OF SUPPLEMENTARY FUNCTIONS .....</b>	<b>233</b>
E.8.1 CAM Model Function .....	233
<b>E.9 TIME-TEMPERATURE SHIFT FACTOR FUNCTION FOR <math> G^* </math> .....</b>	<b>233</b>
E.9.1 Level 1 (WLF Function).....	233
E.9.2 Levels 2 and 3 .....	233
<b>E.10 SIGMOIDAL FUNCTION.....</b>	<b>234</b>
<b>E.11 TIME-TEMPERATURE SHIFT FACTOR FUNCTION FOR <math> E^* </math>.....</b>	<b>234</b>
<b>REFERENCES.....</b>	<b>235</b>

## LIST OF FIGURES

Figure 1. Illustration. Modulus prediction model decision tree .....	3
Figure 2. Graph. Comparison between the Witczak predictive model and measured $ G^* _b$ values in arithmetic scale .....	15
Figure 3. Graph. Comparison between the Witczak predictive model and measured $ G^* _b$ values in logarithmic scale.....	16
Figure 4. Graph. Comparison between the Witczak predictive model and measured $\delta_b$ to develop the $\delta_b$ model .....	16
Figure 5. Graph. Comparison between the Witczak predictive model and measured $ G^* _b$ values using Citgo binders in the North Carolina Department of Transportation (NCDOT) database in arithmetic scale .....	17
Figure 6. Graph. Comparison between the Witczak predictive model and measured $ G^* _b$ values using Citgo binders in the NCDOT database in logarithmic scale.....	17
Figure 7. Graph. Prediction of the processed Witczak, FHWA I, FHWA II, NCDOT I, NCDOT II, WRI, and Citgo databases using the modified Witczak in arithmetic scale.....	40
Figure 8. Graph. Prediction of the processed Witczak, FHWA I, FHWA II, NCDOT I, NCDOT II, WRI, and Citgo databases using the modified Witczak in logarithmic scale .....	40
Figure 9. Graph. Prediction of the processed Witczak, FHWA I, FHWA II, NCDOT I, NCDOT II, WRI, and Citgo databases using the Hirsch model in arithmetic scale.....	41
Figure 10. Graph. Prediction of the processed Witczak, FHWA I, FHWA II, NCDOT I, NCDOT II, WRI, and Citgo databases using the Hirsch model in logarithmic scale.....	41
Figure 11. Graph. Prediction of the processed Witczak, FHWA I, FHWA II, NCDOT I, NCDOT II, WRI, and Citgo databases using the Al-Khateeb model in arithmetic scale.....	42
Figure 12. Graph. Prediction of the processed Witczak, FHWA I, FHWA II, NCDOT I, NCDOT II, WRI, and Citgo databases using the Al-Khateeb model in logarithmic scale.....	42
Figure 13. Graph. Prediction of training data containing processed Witczak, FHWA I, NCDOT I, and WRI databases using $ G^* $ binder and gradation-based pilot ANN model (G-GR pANN) in arithmetic scale .....	43
Figure 14. Graph. Prediction of training data containing processed Witczak, FHWA I, NCDOT I, and WRI databases using G-GR pANN in logarithmic scale.....	43
Figure 15. Graph. Prediction of training data containing processed Witczak, FHWA I, NCDOT I, and WRI databases using preliminary $ G^* $ -based models used in phase I of the study (G-V) pANN in arithmetic scale .....	44
Figure 16. Graph. Prediction of training data containing processed Witczak, FHWA I, NCDOT I, and WRI databases using G-V pANN in logarithmic scale.....	44
Figure 17. Graph. Predicted moduli using G-GR pANN and modified Witczak models for the FHWA II database in arithmetic scale .....	45
Figure 18. Graph. Predicted moduli using G-GR pANN and modified Witczak models for the FHWA II database in logarithmic scale .....	45
Figure 19. Graph. Predicted moduli using G-V pANN and Hirsch models for the FHWA II database in arithmetic scale .....	46
Figure 20. Graph. Predicted moduli using G-V pANN and Hirsch models for the FHWA II database in logarithmic scale .....	46
Figure 21. Graph. Predicted moduli using G-GR pANN and modified Witczak models for the NCDOT II database in arithmetic scale .....	47

Figure 22. Graph. Predicted moduli using G-GR pANN and modified Witczak models for the NCDOT II database in logarithmic scale .....	47
Figure 23. Graph. Predicted moduli using G-V pANN and Hirsch models for the NCDOT II database in arithmetic scale .....	48
Figure 24. Graph. Predicted moduli using G-V pANN and Hirsch models for the NCDOT II database in logarithmic scale .....	48
Figure 25. Graph. Predicted moduli using G-GR pANN and modified Witczak models for the Citgo database in arithmetic scale .....	49
Figure 26. Graph. Predicted moduli using G-GR pANN and modified Witczak models for the Citgo database in logarithmic scale.....	49
Figure 27. Graph. Predicted moduli using G-V pANN and Hirsch models for the Citgo database in arithmetic scale .....	50
Figure 28. Graph. Predicted moduli using G-V pANN and Hirsch models for the Citgo database in logarithmic scale .....	50
Figure 29. Graph. Prediction of training data containing Witczak, FHWA I, and NCDOT I databases using Visc-GR pANN in arithmetic scale .....	53
Figure 30. Graph. Prediction of training data containing Witczak, FHWA I, and NCDOT I databases using Visc-GR pANN in logarithmic scale .....	54
Figure 31. Graph. Prediction of training data containing Witczak, FHWA I, and NCDOT I databases using Visc-V pANN in arithmetic scale .....	54
Figure 32. Graph. Prediction of training data containing Witczak, FHWA I, and NCDOT I databases using Visc-V pANN in logarithmic scale.....	55
Figure 33. Graph. Predicted moduli using Visc-GR pANN model for the FHWA II database in arithmetic scale .....	55
Figure 34. Graph. Predicted moduli using Visc-GR pANN model for the FHWA II database in logarithmic scale.....	56
Figure 35. Graph. Predicted moduli using Visc-V pANN model for the FHWA II database in arithmetic scale .....	56
Figure 36. Graph. Predicted moduli using Visc-V pANN model for the FHWA II database in logarithmic scale .....	57
Figure 37. Graph. Predicted moduli using Visc-GR pANN model for the NCDOT II database in arithmetic scale .....	57
Figure 38. Graph. Predicted moduli using Visc-GR pANN model for the NCDOT II database in logarithmic scale .....	58
Figure 39. Graph. Predicted moduli using Visc-V pANN model for the NCDOT II database in arithmetic scale .....	58
Figure 40. Graph. Predicted moduli using Visc-V pANN model for the NCDOT II database in logarithmic scale .....	59
Figure 41. Illustration. Network structure used for training the ANN models .....	63
Figure 42. Illustration. Stress distribution in the IDT specimen subjected to a strip load.....	65
Figure 43. Graph. Poisson's ratio versus reduced time for S12.5C .....	69
Figure 44. Graph. Comparison of predicted and measured $M_R$ values for S12.5C mixture .....	71
Figure 45. Graph. Comparison of predicted and measured $M_R$ values for S12.5CM mixture .....	71
Figure 46. Graph. Comparison of predicted and measured $M_R$ values for S12.5FE mixture .....	72
Figure 47. Graph. Comparison of predicted and measured $M_R$ values for B25.0C mixture.....	72

Figure 48. Graph. $M_R$ ANN model using 90 percent of randomly selected data as a training set in arithmetic scale.....	73
Figure 49. Graph. $M_R$ ANN model using 90 percent of randomly selected data as a training set in logarithmic scale.....	73
Figure 50. Graph. $M_R$ ANN model using 10 percent of randomly selected data as a verification set in arithmetic scale .....	74
Figure 51. Graph. $M_R$ ANN model using 10 percent of randomly selected data as a verification set in logarithmic scale .....	74
Figure 52. Graph. VV ANN model using 90 percent of randomly selected data as a training set in arithmetic scale.....	75
Figure 53. Graph. VV ANN model using 90 percent of randomly selected data as a training set in logarithmic scale.....	76
Figure 54. Graph. VV ANN model using 10 percent of randomly selected data as a verification set in arithmetic scale .....	76
Figure 55. Graph. VV ANN model using 10 percent of randomly selected data as a verification set in logarithmic scale .....	77
Figure 56. Graph. GV ANN model using 90 percent of randomly selected data as a training set in arithmetic scale.....	78
Figure 57. Graph. GV ANN model using 90 percent of randomly selected data as a training set in logarithmic scale.....	78
Figure 58. Graph. GV ANN model using 10 percent of randomly selected data as a verification set in arithmetic scale .....	79
Figure 59. Graph. GV ANN model using 10 percent of randomly selected data as a verification set in logarithmic scale .....	79
Figure 60. Illustration. Decision tree applied to population of LTPP database based on ranking of ANN models.....	83
Figure 61. Graph. Example of the effect of a violation of QC #1 for $M_R$ ANN model in semi-log scale.....	85
Figure 62. Graph. Example of the effect of a violation of QC #1 for $M_R$ ANN model in log-log scale .....	86
Figure 63. Graph. Example of the effect of a violation of QC #1 for VV ANN model in semi-log scale.....	86
Figure 64. Graph. Example of the effect of a violation of QC #1 for VV ANN model in log-log scale .....	87
Figure 65. Graph. Example of the effect of a violation of QC #1 for VV ANN model unshifted data .....	87
Figure 66. Graph. Example of the effect of a violation of QC #2 in semi-log scale .....	88
Figure 67. Graph. Example of the effect of a violation of QC #2 in log-log scale.....	89
Figure 68. Graph. Example of the effect of a violation of QC #2 unshifted data.....	89
Figure 69. Graph. Example of the effect of a violation of QC #3 in semi-log scale .....	90
Figure 70. Graph. Example of the effect of a violation of QC #3 in log-log scale.....	91
Figure 71. Graph. Example of the effect of a violation of QC #3 unshifted data.....	91
Figure 72. Graph. Example of the effect of a violation of QC #4 in semi-log scale .....	92
Figure 73. Graph. Example of the effect of a violation of QC #4 in log-log scale.....	92
Figure 74. Graph. Example of the effect of a violation of QC #4 unshifted data.....	93
Figure 75. Graph. Example of the effect of a violation of QC #5 in semi-log scale .....	94

Figure 76. Graph. Example of the effect of a violation of QC #5 in log-log scale.....	94
Figure 77. Graph. Example of the effect of a violation of QC #5 unshifted data.....	95
Figure 78. Illustration. ANN models and their appropriate input and output tables .....	102
Figure 79. Graph. A-VTS relationship .....	105
Figure 80. Graph. $ G^* $ versus frequency curves at different temperatures.....	110
Figure 81. Graph. $ G^* $ versus reduced frequency mastercurve at 59 °F (15 °C).....	111
Figure 82. Graph. t-T shift factor function at 59 °F (15 °C) .....	111
Figure 83. Graph. $D(t)$ at different temperatures for ALF AC5 binder .....	113
Figure 84. Graph. Comparison of optimization and regression GPL characterization results ...	114
Figure 85. Graph. $ G^* $ mastercurve for the WesTrack binder at 59 °F (15 °C).....	116
Figure 86. Graph. Optimized t-T shift function for WesTrack binder at 59 °F (15 °C) .....	116
Figure 87. Graph. Comparison of t-T shift factor functions calibrated with and without BBR data.....	118
Figure 88. Graph. $ G^* $ mastercurve using t-T shift factor function calibrated without BBR data.....	119
Figure 89. Graph. $ G^* $ mastercurves characterized with and without BBR data for ALF AC5 binder .....	121
Figure 90. Graph. $ G^* $ mastercurves characterized with and without BBR data for the MnRoad Pen 120-150 binder .....	122
Figure 91. Graph. $ G^* $ mastercurves characterized with and without BBR data for the WesTrack binder .....	122
Figure 92. Graph. t-T shift factor function characterized with and without BBR data for the ALF AC5 binder .....	123
Figure 93. Graph. t-T shift factor function characterized with and without BBR data for the MnRoad Pen 120-150 binder .....	123
Figure 94. Graph. t-T shift factor function characterized with and without BBR data for the WesTrack binder .....	124
Figure 95. Graph. Phenomenological t-T shift factor function.....	129
Figure 96. Graph. Effect of change in time from DSR to BBR on the t-T shift factor function model .....	129
Figure 97. Graph. t-T shift factor model verification with phenomenological model.....	130
Figure 98. Graph. Average t-T shift factor function .....	131
Figure 99. Graph. t-T shift factor model verification with average function model .....	131
Figure 100. Graph. Effect of temperature on aging ratio of asphalt binder.....	134
Figure 101. Graph. Effect of angular frequency on aging ratio of asphalt binder .....	135
Figure 102. Graph. Calibrated PAR model in arithmetic scale .....	135
Figure 103. Graph. Calibrated PAR model in logarithmic scale .....	136
Figure 104. Graph. Strength of PAR model in arithmetic scale .....	136
Figure 105. Graph. Strength of PAR model in logarithmic scale .....	137
Figure 106. Graph. PAR model verification in arithmetic logarithmic scale .....	137
Figure 107. Graph. PAR model verification in logarithmic scale .....	138
Figure 108. Graph. BBR-calibrated $\kappa_T$ relationship .....	139
Figure 109. Graph. Comparison of $ G^* $ mastercurve analysis under PAV and RTFO conditions for ALF AC10 binder .....	139
Figure 110. Graph. Calibrated PAR model for BBR conditions in arithmetic scale .....	140
Figure 111. Graph. Calibrated PAR model for BBR conditions in logarithmic scale .....	140

Figure 112. Graph. Verification of $m$ -value relationship.....	142
Figure 113. Graph. Comparison of typical $ G^* $ mastercurves characterized using full database and Superpave <sup>TM</sup> only database .....	143
Figure 114. Graph. Comparison of typical t-T shift factors characterized using full database and Superpave <sup>TM</sup> only database .....	144
Figure 115. Graph. Level 1a verification of limited data analysis procedure in arithmetic scale using phenomenological shift factor function model.....	144
Figure 116. Graph. Level 1a verification of limited data analysis procedure in logarithmic scale using phenomenological shift factor function model.....	145
Figure 117. Graph. Level 1a verification of limited data analysis procedure in arithmetic scale using average shift factor function model.....	145
Figure 118. Graph. Level 1a verification of limited data analysis procedure in logarithmic scale using average shift factor function model.....	146
Figure 119. Graph. Comparison of typical $ G^* $ mastercurve characterized using full database and Superpave <sup>TM</sup> only database plus PAR model.....	147
Figure 120. Graph. Comparison of typical t-T shift factors characterized using full database and Superpave <sup>TM</sup> only database plus PAR model.....	148
Figure 121. Graph. Level 1b verification of limited data analysis procedure in arithmetic scale using phenomenological shift factor function model.....	148
Figure 122. Graph. Level 1b verification of limited data analysis procedure in logarithmic scale using phenomenological shift factor function model.....	149
Figure 123. Graph. Level 1b verification of limited data analysis procedure in arithmetic scale using average shift factor function model.....	149
Figure 124. Graph. Level 1b verification of limited data analysis procedure in logarithmic scale using average shift factor function model.....	150
Figure 125. Graph. Level 2 verification of limited data analysis procedure in arithmetic scale using phenomenological shift factor function model.....	151
Figure 126. Graph. Level 2 verification of limited data analysis procedure in logarithmic scale using phenomenological shift factor function model.....	152
Figure 127. Graph. Level 2 verification of limited data analysis procedure in arithmetic scale using average shift factor function model.....	152
Figure 128. Graph. Level 2 verification of limited data analysis procedure in logarithmic scale using average shift factor function model.....	153
Figure 129. Graph. Level 3 verification of limited data analysis procedure in arithmetic scale using phenomenological shift factor function model.....	154
Figure 130. Graph. Level 3 verification of limited data analysis procedure in logarithmic scale using phenomenological shift factor function model.....	155
Figure 131. Graph. Level 3 verification of limited data analysis procedure in arithmetic scale using average shift factor function model.....	155
Figure 132. Graph. Level 3 verification of limited data analysis procedure in logarithmic scale using average shift factor function model.....	156
Figure 133. Graph. Test mixture gradation.....	158
Figure 134. Graph. Comparison of $/E^*/$ measured via AMPT and TP-62 protocols in arithmetic scale .....	159
Figure 135. Graph. Comparison of $ E^* $ measured via AMPT and TP-62 protocols in logarithmic scale .....	159

Figure 136. Graph. Frequency distribution of temperature in AMPT versus TP-62 databases .....	161
Figure 137. Graph. Range of temperature in AMPT versus TP-62 databases.....	162
Figure 138. Graph. Frequency distribution of frequency in AMPT versus TP-62 databases....	162
Figure 139. Graph. Range of loading frequency in AMPT versus TP-62 databases.....	163
Figure 140. Graph. Frequency distribution of percentage retained on $\frac{3}{4}$ -inch (19.05-mm) sieve ( $\rho_{34}$ ) in AMPT versus TP-62 databases .....	163
Figure 141. Graph. Range of percentage retained on $\frac{3}{4}$ -inch (19.05-mm) sieve ( $\rho_{34}$ ) in AMPT versus TP-62 databases .....	164
Figure 142. Graph. Frequency distribution of percentage retained on $\frac{3}{8}$ -inch (9.56-mm) sieve ( $\rho_{38}$ ) in AMPT versus TP-62 databases .....	164
Figure 143. Graph. Range of percentage retained on $\frac{3}{8}$ -inch (9.56-mm) sieve ( $\rho_{38}$ ) in AMPT versus TP-62 databases .....	165
Figure 144. Graph. Frequency distribution of percentage retained on #4 sieve ( $\rho_4$ ) in AMPT versus TP-62 databases .....	165
Figure 145. Graph. Range of percentage retained on #4 sieve ( $\rho_4$ ) in AMPT versus TP-62 databases .....	166
Figure 146. Graph. Frequency distribution of percentage passing #200 sieve ( $\rho_{200}$ ) in AMPT versus TP-62 databases .....	166
Figure 147. Graph. Range of percentage passing #200 sieve ( $\rho_{200}$ ) in AMPT versus TP-62 databases .....	167
Figure 148. Graph. Frequency distribution of specimen air voids in AMPT versus TP-62 databases .....	167
Figure 149. Graph. Range of specimen air voids in AMPT versus TP-62 databases .....	168
Figure 150. Graph. Frequency distribution of effective binder volume in AMPT versus TP-62 databases .....	168
Figure 151. Graph. Range of effective binder volume in AMPT versus TP-62 databases.....	169
Figure 152. Graph. Frequency distribution of VMA in AMPT versus TP-62 databases .....	169
Figure 153. Graph. Range of VMA in AMPT versus TP-62 databases .....	170
Figure 154. Graph. Frequency distribution of VFA in AMPT versus TP-62 databases.....	170
Figure 155. Graph. Range of VFA in AMPT versus TP-62 databases .....	171
Figure 156. Graph. Frequency distribution of $ G^* $ in AMPT versus TP-62 databases .....	171
Figure 157. Range of $ G^* $ in AMPT versus TP-62 databases .....	172
Figure 158. Graph. Percentage of difference between AMPT versus TP-62 databases based on similar ranges of different variables at 39.9 °F (4.4 °C) .....	172
Figure 159. Graph. Percentage of difference between AMPT versus TP-62 databases based on similar ranges of different variables at 69.9 °F (21.1 °C) .....	173
Figure 160. Graph. Percentage of difference between AMPT versus TP-62 databases based on similar ranges of different variables at 100 °F (37.8 °C) .....	173
Figure 161. Graph. Percentage of difference between AMPT versus TP-62 databases based on similar ranges of different variables at 129.2 °F (54.0 °C) .....	174
Figure 162. Graph. Percentage of difference between AMPT versus TP-62 databases based on similar ranges of different variables at 129.9 °F (54.4 °C) .....	174
Figure 163. Graph. Prediction of the combination of AMPT and TP-62 data using the modified Witczak and G-GR pANN models in arithmetic scale.....	179

Figure 164. Graph. Prediction of the combination of AMPT and TP-62 data using the modified Witczak and G-GR pANN models in logarithmic scale .....	179
Figure 165. Graph. Prediction of the combination of AMPT and TP-62 data using the Hirsch model in arithmetic scale.....	180
Figure 166. Graph. Prediction of the combination of AMPT and TP-62 data using the Hirsch model in logarithmic scale .....	180
Figure 167. Graph. Prediction of the combination of AMPT and TP-62 data using the Al-Khateeb model in arithmetic scale.....	181
Figure 168. Graph. Prediction of the combination of AMPT and TP-62 data using the Al-Khateeb model in logarithmic scale .....	181
Figure 169. Graph. Prediction of the AMPT data using the modified Witczak and AMPT pANN models in arithmetic scale .....	182
Figure 170. Graph. Prediction of the AMPT data using the modified Witczak and AMPT pANN models in logarithmic scale.....	182
Figure 171. Graph. Prediction of the AMPT data using the Hirsch model in arithmetic scale.....	183
Figure 172. Graph. Prediction of the AMPT data using the Hirsch model in logarithmic scale.....	183
Figure 173. Graph. Prediction of the AMPT data using the Al-Khateeb model in arithmetic scale.....	184
Figure 174. Graph. Prediction of the AMPT data using the Al-Khateeb model in logarithmic scale.....	184
Figure 175. Graph. Prediction of the TP-62 data using the modified Witczak and TP-62 pANN models in arithmetic scale .....	185
Figure 176. Graph. Prediction of the TP-62 data using the modified Witczak and TP-62 pANN models in logarithmic scale.....	185
Figure 177. Graph. Prediction of the TP-62 data using the Hirsch model in arithmetic scale ...	186
Figure 178. Graph. Prediction of the TP-62 data using the Hirsch model in logarithmic scale.....	186
Figure 179. Graph. Prediction of the TP-62 data using the Al-Khateeb model in arithmetic scale.....	187
Figure 180. Graph. Prediction of the TP-62 data using the Al-Khateeb model in logarithmic scale.....	187
Figure 181. Graph. Prediction of the FHWA II data using the modified Witczak and G-GR pANN models in arithmetic scale .....	188
Figure 182. Graph. Prediction of the FHWA II data using the modified Witczak and G-GR pANN models in logarithmic scale.....	188
Figure 183. Graph. Prediction of the FHWA II data using the AMPT pANN and TP-62 pANN models in arithmetic scale .....	189
Figure 184. Graph. Prediction of the FHWA II data using the AMPT pANN and TP-62 pANN models in logarithmic scale.....	189
Figure 185. Graph. Prediction of the FHWA II data using the Hirsch model in arithmetic scale.....	190
Figure 186. Graph. Prediction of the FHWA II data using the Hirsch model in logarithmic scale.....	190

Figure 187. Graph. Prediction of the FHWA II data using the Al-Khateeb model in arithmetic scale .....	191
Figure 188. Graph. Prediction of the FHWA II data using the Al-Khateeb model in logarithmic scale .....	191
Figure 189. Graph. Prediction of the NCDOT II data using the modified Witczak and G-GR pANN models in arithmetic scale .....	192
Figure 190. Graph. Prediction of the NCDOT II data using the modified Witczak and G-GR pANN models in logarithmic scale.....	192
Figure 191. Graph. Prediction of the NCDOT II data using the AMPT pANN and TP-62 pANN models in arithmetic scale .....	193
Figure 192. Graph. Prediction of the NCDOT II data using the AMPT pANN and TP-62 pANN models in logarithmic scale.....	193
Figure 193. Graph. Prediction of the NCDOT II data using the Hirsch model in arithmetic scale.....	194
Figure 194. Graph. Prediction of the NCDOT II data using the Hirsch model in logarithmic scale.....	194
Figure 195. Graph. Prediction of the NCDOT II data using the Al-Khateeb model in arithmetic scale .....	195
Figure 196. Graph. Prediction of the NCDOT II data using the Al-Khateeb model in logarithmic scale .....	195
Figure 197. Graph. Prediction of the Citgo data using the modified Witczak and G-GR pANN models in arithmetic scale .....	196
Figure 198. Graph. Prediction of the Citgo data using the modified Witczak and G-GR pANN models in logarithmic scale.....	196
Figure 199. Graph. Prediction of the Citgo data using the AMPT pANN and TP-62 pANN models in arithmetic scale.....	197
Figure 200. Graph. Prediction of the Citgo data using the AMPT pANN and TP-62 pANN models in logarithmic scale .....	197
Figure 201. Graph. Prediction of the Citgo data using the Hirsch model in arithmetic scale ...	198
Figure 202. Graph. Prediction of the Citgo data using the Hirsch model in logarithmic scale.....	198
Figure 203. Graph. Prediction of the Citgo data using the Al-Khateeb model in arithmetic scale.....	199
Figure 204. Graph. Prediction of the Citgo data using the Al-Khateeb model in logarithmic scale.....	199
Figure 205. Screenshot. ANNACAP main screen .....	219
Figure 206. Illustration. ANNACAP menu diagram .....	219
Figure 207. Screenshot. ANNACAP input screen.....	220
Figure 208. Screenshot. Output directory dialog.....	229
Figure 209. Screenshot. Choosing output directory.....	229

## LIST OF TABLES

Table 1. Predictive relationships for $ E^* $ .....	7
Table 2. Model variables.....	11
Table 3. Example of summarized mixture and binder properties in the original Witczak database.....	14
Table 4. Summary of $ G^* $ data available in the Witczak binder database.....	19
Table 5. Summary of $ G^* $ data available in the FHWA mobile trailer database.....	20
Table 6. Summary of $ G^* $ data available in the FHWA TPF-5(019) binder database .....	21
Table 7. Summary of $ G^* $ data available in the NCDOT binder database .....	22
Table 8. Summary of $ G^* $ data available in the Citgo binder database .....	22
Table 9. Summary of $ G^* $ data available in the WRI database .....	23
Table 10. Summary of $ E^* $ data available in the processed Witczak mixture database .....	25
Table 11. Summary of $ E^* $ data available in the FHWA I mobile trailer mixture database .....	26
Table 12. Summary of $ E^* $ data available in the FHWA II mobile trailer mixture database .....	27
Table 13. Summary of $ E^* $ data available in the FHWA TPF-5(019) mixture database.....	28
Table 14. Summary of $ E^* $ data available in the NCDOT mixture database .....	29
Table 15. Summary of $ E^* $ data available in the WRI database .....	30
Table 16. Summary of $ E^* $ data available in the Citgo mixture database .....	31
Table 17. Summary of $ E^* $ data available in the $M_R$ database.....	31
Table 18. Summary of extracted LTPP data.....	34
Table 19. Description of $ G^* $ -based ANN models .....	51
Table 20. Description of viscosity-based ANN models.....	53
Table 21. Parameters and number of nodes used in developed ANN models .....	62
Table 22. Geometry coefficients.....	65
Table 23. Probability distribution of error functions of each ANN model .....	81
Table 24. Input ranges of different ANN models .....	85
Table 25. Limiting $ E^* $ values used for QC #6.....	95
Table 26. Statistics of LTPP data populated with $ E^* $ .....	97
Table 27. Structure and format of the TST_ESTAR_MASTER table .....	99
Table 28. Structure and format of the TST_ESTAR_MODULUS table.....	99
Table 29. Structure and format of the TST_ESTAR_MODULUS_COEFF table .....	100
Table 30. Structure and format of the TST_ESTAR_GSTAR_INPUT table.....	100
Table 31. Structure and format of the TST_ESTAR_GSTAR_CAM_COEFF table .....	100
Table 32. Structure and format of the TST_ESTAR_VOLUM_INPUT table .....	101
Table 33. Structure and format of the TST_ESTAR_VISC_INPUT table.....	101
Table 34. Structure and format of the TST_ESTAR_VISC_MODEL_COEFF table.....	101
Table 35. Structure and format of the TST_ESTAR_MR_INPUT table.....	101
Table 36. Relationship between asphalt binder grade and viscosity parameters .....	108
Table 37. Calibrated CAM model and t-T shift factor function coefficients using BBR data.....	117
Table 38. Calibrated CAM model and t-T shift factor function coefficients omitting BBR data.....	118

Table 39. Percentage of difference between BBR-calibrated and non-BBR-calibrated $ G^* $ at TP-62 temperatures and frequencies .....	120
Table 40. Percentage of log difference between BBR-calibrated and non-BBR-calibrated $ G^* $ at TP-62 temperatures and frequencies .....	125
Table 41. PAR model coefficient summary for Superpave™ high temperature grades .....	134
Table 42. PAR model verification dataset summary .....	138
Table 43. TP summary .....	157
Table 44. Test mixture volumetric properties .....	158
Table 45. Statistical summary of AMPT and TP-62 test results .....	160
Table 46. Percentage of difference between AMPT versus TP-62 database based on similar ranges of different variables .....	175
Table 47. Summary of database used for training ANN models .....	175
Table 48. Summary of the database used for verification of ANN models .....	176
Table 49. Description of the developed ANN Models and their validation statistics .....	177
Table 50. $W_{ik}^1$ matrix elements for $M_R$ ANN (part 1) .....	204
Table 51. $W_{ik}^1$ matrix elements for $M_R$ ANN (part 2) .....	204
Table 52. $B_k^1$ vector elements for $M_R$ ANN (transposed for convenience) .....	205
Table 53. $W_{kj}^2$ matrix elements for $M_R$ ANN (part 1) .....	205
Table 54. $W_{kj}^2$ matrix elements for $M_R$ ANN (part 2) .....	206
Table 55. $W_{kj}^2$ matrix elements for $M_R$ ANN (part 3) .....	206
Table 56. $B_j^2$ vector elements for $M_R$ ANN (transposed for convenience) .....	207
Table 57. $W_{jl}^3$ vector elements for $M_R$ ANN (part 1) .....	207
Table 58. $W_{jl}^3$ vector elements for $M_R$ ANN (part 2) .....	207
Table 59. $W_{jl}^3$ vector elements for $M_R$ ANN (part 3) .....	207
Table 60. Normalization parameters for $M_R$ ANN .....	208
Table 61. $W_{ik}^1$ matrix elements for VV ANN .....	208
Table 62. $B_k^1$ vector elements for VV ANN (transposed for convenience) .....	209
Table 63. $W_{kj}^2$ matrix elements for VV ANN (part 1) .....	209
Table 64. $W_{kj}^2$ matrix elements for VV ANN (part 2) .....	210
Table 65. $W_{kj}^2$ matrix elements for VV ANN (part 3) .....	210
Table 66. $W_{kj}^2$ matrix elements for VV ANN (part 4) .....	211
Table 67. $B_j^2$ vector elements for VV ANN (transposed for convenience) .....	211
Table 68. $W_j^3$ vector elements for VV ANN .....	212
Table 69. Normalization parameters for VV ANN .....	212
Table 70. $W_{ik}^1$ matrix elements for GV ANN .....	213
Table 71. $B_k^1$ vector elements for GV ANN (transposed for convenience) .....	213
Table 72. $W_{kj}^2$ matrix elements for GV ANN (part 1) .....	214
Table 73. $W_{kj}^2$ matrix elements for GV ANN (part 2) .....	214
Table 74. $W_{kj}^2$ matrix elements for GV ANN (part 3) .....	215
Table 75. $B_j^2$ vector elements for GV ANN (transposed for convenience) .....	215
Table 76. $W_j^3$ vector elements for GV ANN .....	216
Table 77. Normalization parameters for GV ANN .....	216
Table 78. Relationship between binder purchase specification grade and A and VTS parameters .....	223
Table 79. File format for lab-aged files .....	225
Table 80. File format for field-aged files .....	227

Table 81. Output data format for single ANNACAP use .....	230
Table 82. Summary file format from batch mode in ANNACAP .....	231
Table 83. Output data format for batch mode ANNACAP use. ....	231

## LIST OF ABBREVIATIONS AND SYMBOLS

### Abbreviations

A	Regression intercept
AASHTO	American Association of State Highway and Transportation Officials
AC	Asphalt concrete
ALF	Accelerated loading facility
AMPT	Asphalt mixture performance tester
ANN	Artificial neural network
ANNACAP	Artificial Neural Networks for Asphalt Concrete Dynamic Modulus Prediction
ASTM	American Society for Testing and Materials
A-VTS	Regression intercept-regression slope of viscosity temperature susceptibility
BBR	Bending beam rheometer
CAM	Christensen Anderson Marasteanu
DSR	Dynamic shear rheometer
FHWA	Federal Highway Administration
G-GR	$ G^* $ binder and gradation-based
GPL	Generalized power law
GPS	General Pavement Study
GR	Gradation
G-V	Preliminary $ G^* $ -based model used in phase 1 of the study
GV	$ G^* $ -based model using consistent aged binder data
GV-PAR	$ G^* $ -based model using inconsistent aged binder data of pressure-aging vessel and rolling thin film oven aging conditions
HMA	Hot mix asphalt
IDT	Indirect tensile
LOE	Line of equality
LTOA	Long-term oven aging
LTPP	Long-Term Pavement Performance
LVE	Linear viscoelastic
MEPDG	<i>Mechanistic Empirical Pavement Design Guide</i>
NCDOT	North Carolina Department of Transportation

NCHRP	National Cooperative Highway Research Program
NCSU	North Carolina State University
NMSA	Nominal maximum-sized aggregate
pANN	Pilot artificial neural network
PAV	Pressure-aging vessel
PG	Performance grade
QC	Quality control
R&BT	Ring and ball temperature
RTFO	Rolling thin film oven
SHRP	Strategic Highway Research Program
SPS	Specific Pavement Study
STOA	Short-term oven aging
TFHRC	Turner-Fairbank Highway Research Center
TP	Test protocol
VFA	Percentage of voids filled with asphalt
Visc-GR	Viscosity-gradation model
Visc-V	Viscosity-volumetric model
VMA	Percentage of voids in mineral aggregate
VTS	Slope of temperature susceptibility relationship
VV	Viscosity-based model
VV-grade	Viscosity-based model using specification grade of the asphalt binder as recommended in the <i>Mechanistic Empirical Pavement Design Guide</i>
WLF	Williams-Landel-Ferry Model
WRI	Western Research Institute

## Symbols

$ E^* $	Dynamic modulus
$ G^* $	Dynamic shear modulus
$M_R$	Resilient modulus
t-T	Time-temperature shift factors
$\rho_{200}$	Percentage of aggregate passing #200 sieve
$\rho_4$	Percentage of aggregate retained #4 sieve
$\rho_{3/8}$	Percentage of aggregate retained $\frac{3}{8}$ -inch sieve

$\rho_{3/4}$	Percentage of aggregate retained $\frac{3}{4}$ -inch sieve
$V_a$	Percentage of air void
$V_{beff}$	Percentage of effective asphalt content (by volume of mix)
$f$	Loading frequency
$\eta$	Binder viscosity
$ G^* _b$	Dynamic shear modulus of asphalt binder
$\delta_b$	Binder phase angle associated with $ G^* _b$
$f_s$	Dynamic shear frequency
$T$	Temperature
$T_R$	Temperature in Rankine scale
$ E^* _m$	Dynamic modulus of hot mix asphalt (pounds per square inch)
$Pc$	Aggregate contact volume
$\phi$	Phase angle of hot mix asphalt
$ G^* _g$	Dynamic shear modulus of asphalt binder at the glassy state
$V_{mix}$	Air voids by volume of the mix
$\omega$	Angular frequency in radians per second
$t$	Time
$f_R$	Reduced frequency
$m_e$	Fitting coefficient
$k$	Fitting coefficient
$\delta$	Binder phase angle (degree)
$G_{mb}$	Bulk specific gravity
$G_{mm}$	Maximum specific gravity
$SSE$	Sum of squared error
$Sy$	Standard deviation
$Se$	Standard error
$\sigma_a$	Applied stress
$\varepsilon_r$	Recoverable strain
$\nu$	Poisson's ratio

$P$	Applied load
$U$	Recoverable horizontal displacement
$V$	Recoverable vertical displacement
$k_1$	Constant value in NCHRP 1-28 elastic solution for Poisson's ratio
$k_2$	Constant value in NCHRP 1-28 elastic solution for Poisson's ratio
$k_3$	Constant value in NCHRP 1-28 elastic solution for Poisson's ratio
$k_4$	Constant value in NCHRP 1-28 elastic solution for Poisson's ratio
$E$	Young's modulus
$D$	Compliance
$R$	Radius of specimen
$x$	Horizontal distance from center of specimen
$E'$	Storage modulus
$E''$	Loss modulus
$E_\infty$	Equilibrium modulus
$\omega_r$	Angular reduced frequency
$E_i$	Modulus of the $i$ th Maxwell element
$\rho_i$	Relaxation time of the $i$ th Maxwell element
$A_{kj}$	Matrix element in the $k$ th row and $j$ th column of matrix A
$B_k$	Vector element in the $k$ th row of vector B
$\tau_j$	Retardation time of the $j$ th Voigt element determined a priori
$t_k$	Time of interest
$\alpha_1$	Shift factor coefficient 1
$\alpha_2$	Shift factor coefficient 2
$\alpha_3$	Shift factor coefficient 3
$(\log E^*/_{ANN})_i$	Logarithm of the modulus determined from the ANN models at a particular temperature frequency combination
$(\log E^*_{fit})_i$	Logarithm of the modulus determined from the optimized sigmoidal fit
$(\log E^*_{avg})_i$	Logarithm of the average modulus determined from the ANN models for a given layer
$A$	Intercept of temperature susceptibility relationship

$T_{critical}$	Temperature in Rankine at which the viscosity is exactly equal to $2.7 \times 10^{12}$ cP ( $0.0027 \times 10^{12}$ Pas)
$PEN$	Penetration number at given test temperature
$\nu$	Kinematic viscosity (cSt)
$\rho$	Density (oz/in <sup>3</sup> (g/cm <sup>3</sup> ))
$a_T$	Time-temperature shift factor
$\omega_T$	Frequency at the physical temperature
$\omega_{TR}$	Reduced frequency of $\omega_T$ at the reference temperature
$\omega_c$	Fitting coefficient
$C_1$	Fitting coefficient
$C_2$	Fitting coefficient
$C_3$	Fitting coefficient
$S(t)$	Beam stiffness
$D_0$	Regression coefficient
$D_1$	Regression coefficient
$ D^* $	Dynamic axial creep compliance
$\partial/G^*/\partial T$	Derivative $ G^* $ with respect to time
$E(t)$	Uniaxial relaxation modulus
$E'(\omega)$	Storage modulus
$D(t)$	Creep compliance
$\kappa_T$	Temperature factors
$\kappa_\omega$	Frequency factors
$\beta_1$	Second order polynomial coefficient
$\beta_2$	Second order polynomial coefficient
$\beta_3$	Second order polynomial coefficient
$f(T)$	Transfer function
$H_k^1$	Value of the nodes at the first hidden layer
$\hat{H}_k^1$	Transferred value of the nodes at the first hidden layer

$H_j^2$	Value of the nodes at the second hidden layer
$\hat{H}_j^2$	Transferred value of the nodes at the second hidden layer
$H_l^3$	Value of output node $l$ ( $M_R$ ANN)
$H^3$	Value of the output node (GV ANN and VV ANN)
$\hat{H}_l^3$	Transferred value of the output node $l$ , normalized output ( $M_R$ ANN)
$\hat{H}^3$	Transferred value of the output node, normalized output (GV ANN and VV ANN)
$P_i$	Input variables
$W_{ik}^1$	Weight factors for the first hidden layer
$W_{kj}^2$	Weight factors for the second hidden layer
$B_k^1$	Bias factors for the first layer
$B_j^2$	Bias factors for the second layer
$B_l^0$	Bias factors for the outer layer ( $M_R$ ANN)
$B^0$	Bias factor for the outer layer (GV ANN and VV ANN)
$(Sig_l)_{\max}$	Maximum value for sigmoidal coefficient $l$ in the trained data ( $M_R$ ANN)
$(Sig_l)_{\min}$	Minimum value for sigmoidal coefficient $l$ in the trained data ( $M_R$ ANN)
$\log  E^* _{\max}$	Maximum $\log  E^* $ of the trained data (GV ANN and VV ANN)
$\log  E^* _{\min}$	Minimum $\log  E^* $ of the trained data (GV ANN and VV ANN)
$\hat{P}_i$	Normalized value for given input variable, $i$
$MIN_i$	Minimum value of variable, $i$ , in calibration dataset
$MAX_i$	Maximum value of variable, $i$ , in calibration dataset
$Sig_1$	First sigmoidal function coefficient
$Sig_2$	Second sigmoidal function coefficient
$Sig_3$	Third sigmoidal function coefficient
$Sig_4$	Fourth sigmoidal function coefficient
$M_R^5$	Resilient modulus at 41° F (5 °C), MPa

$M_R^{25}$	Resilient modulus at 77° F (25 °C), MPa
$M_R^{40}$	Resilient modulus at 104° F (40 °C), MPa
$R$	Coefficient in WLF function
$E_a$	Coefficient in WLF function
$t_R$	Inverse of reduced frequency of loading (Hz)
$\delta$	Sigmoidal function fitting coefficient
$\beta$	Sigmoidal function fitting coefficient
$D'$	First vector component of $ D^* $
$D''$	Second vector component of $ D^* $
$V_{be}$	The effective volume of the binder



## EXECUTIVE SUMMARY

The dynamic modulus,  $|E^*|$ , is a fundamental property that defines the stiffness characteristics of hot mix asphalt (HMA) mixtures as a function of loading rate and temperature. Given the significance of  $|E^*|$  in pavement engineering, this project was undertaken to provide the Long-Term Pavement Performance (LTPP) database with  $|E^*|$  estimates using material properties currently available for LTPP test sections. In this report, existing models used to estimate  $|E^*|$  values and additional models that have been developed based on the use of artificial neural networks (ANNs) were evaluated. Using the results of the model evaluation, the research team developed a model selection hierarchy and populated the LTPP database with  $|E^*|$  estimates at five temperatures and six frequencies. It also developed shift factors and sigmoidal functions that can be used to construct mastercurves.

The seven models identified at the outset of this project as potentially suitable for the task at hand include the following:

1. Original Witczak equation (National Cooperative Highway Research Program (NCHRP) 1-37A).<sup>(2)</sup>
2. Modified Witczack dynamic shear ( $|G^*|$ ) equation (NCHRP 1-40D).<sup>(5)</sup>
3. Hirsch model.<sup>(6)</sup>
4. Law of mixtures parallel model.<sup>(7)</sup>
5. Resilient modulus ( $M_R$ )-based ANN model.
6. Viscosity-based ANN model.
7. Binding shear modulus ( $/G^*/$ )-based ANN model.

The existing predictive models (1–4 above) are collectively referred to in this report as “closed-form models.” Specific comparisons are drawn regarding their forms and required input parameters.

An extensive independent database was required to develop the ANN models and to fairly assess the predictive capabilities of each model in the list of possible models. At the outset of the project, the most comprehensive material database available was compiled through the efforts of Dr. Matthew Witczak at Arizona State University. Witczak’s database consists of 7,400 data points from 346 mixtures, all of which were used in the calibration of the NCHRP 1-40D predictive models.<sup>(5)</sup> A smaller subset of the data (2,750 data points from 205 mixtures) was also used in developing the NCHRP 1-37A predictive model.<sup>(2)</sup> In addition, the database contains  $|G^*|$  data obtained from different materials and aging conditions. Through this research project, the Witczak database was combined with mixtures from other national projects and efforts undertaken at North Carolina State University (NCSU). The expanded mixture database currently includes 22,505 data points.

In addition to a mixture database, binder properties were compiled into a similarly expansive database. Substantial efforts have been expended to develop the appropriate binder data processing techniques. The required processing varied depending on the type of data available (i.e.,  $|G^*|$ , viscosity, or binder grade). Only the critical points are presented in this report, and the details are provided in the appendices.

Closed-form models were compared using datasets that were not used in the calibration of the respective models. It was found that the law of mixtures parallel model shows a significant bias, but the Hirsch model shows reasonable predictions, except for insensitivity under extreme conditions.<sup>(7,6)</sup> For the verification database, the Hirsch model shows slightly better statistical predictions than either of the Witczak models.<sup>(6)</sup> This finding, along with other statistical analyses, led the research team to adopt the Hirsch model input parameters into the viscosity-based (VV) and  $|G^*|$ -based ANN models.

Comparisons between the ANN models and the closed-form models were made. Overall, the ANN models provide better predictability than any of the closed-form solutions. Additionally, the ANN models are more sensitive to the input parameters. Based on these findings, the ANN models were chosen to populate the LTPP database moduli values. The primary advantage of using ANN modeling over statistical regression techniques is that the functional form of the relationship is not needed a priori. Considering that many variables affect  $|E^*|$  values and their interactions, the ANN technique may capture complicated nonlinear relationships between  $|E^*|$  and other mixture variables better than regression analysis.

Early in the project, concerns arose because the database combined moduli that had been measured using two different methods, the American Association of State Highway and Transportation Officials (AASHTO) test protocol (TP)-62 and the asphalt mixture performance tester (AMPT) protocol.<sup>(8,9,4)</sup> A study of the available databases revealed that the mixtures that are tested according to the AASHTO TP-62 protocol tend to yield higher moduli values than similar mixtures tested using the AMPT protocol. Statistical analysis to assess the significance of the difference was not performed, but the two data ranges tend to overlap, suggesting a lack of statistical significance in their differences. A limited experimental study wherein the modulus of a single mixture was measured using the two protocols is also discussed. The study shows a statistically significant difference of about 12 percent in the measured moduli across all studied temperatures and frequencies. However, in light of the fact that both protocols are readily available and that neither of the available protocols can be discounted without a more comprehensive and controlled experimental program, the decision was made to include all available data from both the AMPT protocol and AASHTO TP-62 in the calibration process.

Details of the three ANN models, including the required input parameters, model structure, and input range, are presented in this report. The models are prioritized based on engineering judgment and statistical analysis. From this prioritization, a decision tree was developed for populating  $|E^*|$  of the LTPP layers (see figure 1). A user may follow this decision structure and determine the best model to use for the available input parameters.

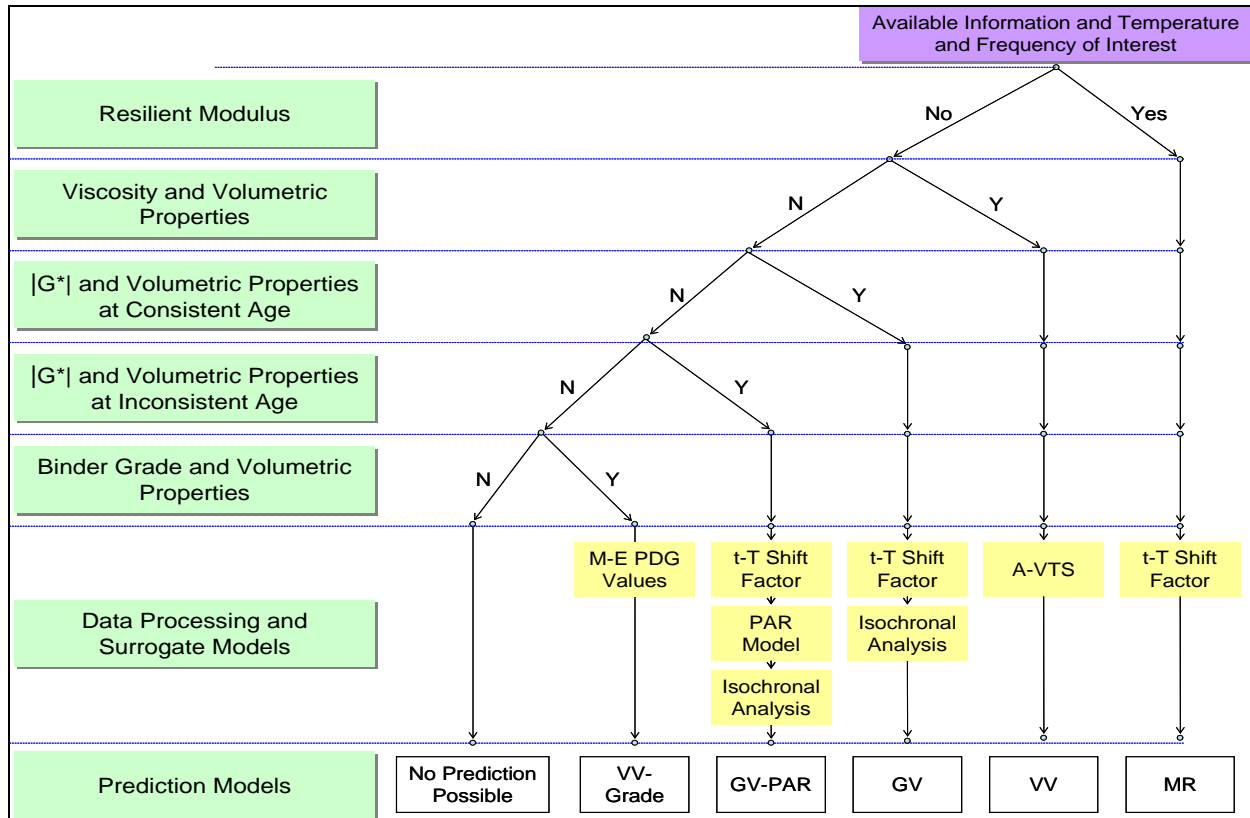


**Figure 1. Illustration. Modulus prediction model decision tree.**

At the end of phase I of this study, it was discovered that some State agencies report effective binder content by mass instead of by volume (i.e., gravimetric instead of volumetric). As a result, there were concerns about the use of a predictive model based on the volumetric properties of the asphalt mixtures. After reviewing the database and carrying out some volumetric computations, volumetric-based properties could still be calculated when gravimetric quantities were reported. Details of how these volumetric-based quantities were computed are provided in this report.

A key component to the prediction of moduli values is ensuring that the predicted values are rational and acceptable. To meet this criterion for the finalized ANN predictions, a set of quality control (QC) checks on both the input parameters and model predictions were performed. In total, seven QC checks were developed, one for the inputs and six for the modulus predictions, and are described in detail in section 6.2 of this report. Executable software, Artificial Neural Networks for Asphalt Concrete Dynamic Modulus Prediction (ANNACAP), was developed as part of this project for this purpose. The software can be run for individual layers (manual mode) or all layers simultaneously (batch mode). An unpublished manual for the software is provided in appendix E of this report.

Statistics for the population effort are also presented in this report. The LTPP database contains information for 1,806 layers that meet the criteria established for this project. These layers have binder data available at a combination of different aging conditions, including unaged or original-aged, rolling thin film oven (RTFO)-aged, pressure-aging vessel (PAV)-aged, and field-aged. For the field-aged data, 2,223 records are available because some layer properties have

been measured at different dates. The total resulting number of records is 7,641. Using the combined ANN models and requisite internal QC checks, modulus values are predicted for 363 records/layers in the original-aged level, 469 records/layers in the RTFO-aged level, 1 record/layer in the PAV-aged level, and 503 records in the field-aged level. Combined, these numbers translate to predictions for 17.5 percent of the total number of records available. However, these records are distributed in such a way that a higher percentage of the layers has some sort of valid prediction. Of the 1,806 layers in the database, 1,010 layers, or 56 percent, have a modulus prediction for some aging condition. Of these 1,010 layers, 615 layers, or 34 percent of the total 1,806 layers, have reasonable predictions (i.e., an “A” grade), and 89 layers, or 4.9 percent of the total 1,806 layers, have unreasonable predictions (i.e., an “F” grade). The remaining 306 layers, representing 17 percent of the 1,806 layers, have questionable predictions (i.e., a “C” grade). Thus, the total percentage of layers with a completely valid or questionable prediction is 51 percent. The quality grading system referenced is different from the standard record status definition used in the LTPP database.<sup>(10)</sup> The research team established strict QC checks to ensure that only the highest quality data were assigned an “A” grade. The data that did not achieve an “A” grade were not considered unusable data. All predictions are included in the database so that users can determine the data that are suitable for their needs. In addition, the Federal Highway Administration (FHWA) can revise the criteria used for the quality checks as deemed appropriate based on the opinions of its experts.

## 1.0 INTRODUCTION

$|E^*|$  is a fundamental property that defines the stiffness characteristics of HMA mixtures as a function of loading rate and temperature. The significance of this material property is threefold. First, it is one of the primary material property inputs in the *Mechanistic Empirical Pavement Design Guide* (MEPDG) and software developed by NCHRP Project 1-37A.<sup>(2)</sup> MEPDG uses a mastercurve and time-temperature (t-T) shift factors in its internal computations. The mastercurve is constructed using a hierarchical structure of inputs ranging from laboratory tests on HMA mixtures and binders to estimates based on properties of the HMA mixtures. Second,  $|E^*|$  is one of the primary HMA properties measured in the Superior PERforming Asphalt PAVEment (Superpave<sup>TM</sup>) simple performance TP that complements the volumetric mix design. Third,  $|E^*|$  is one of the fundamental linear viscoelastic (LVE) material properties that can be used in advanced HMA and pavement models that are based on viscoelasticity.

Despite the demonstrated significance of  $|E^*|$ , it is not included in the current LTPP materials tables because the database structure was established long before  $|E^*|$  was identified as the main HMA property in the MEPDG. It is not practical to perform MEPDG level 1 laboratory  $|E^*|$  tests on material samples from LTPP test sections at this time due to a lack of materials, budget limitations, and the absence of a suitable test method that is applicable to field samples obtained from relatively thin pavement structures. However, the LTPP database does contain other data that can be used to estimate the  $|E^*|$  mastercurve and associated shift factors, estimate  $|E^*|$  at specific load durations and temperatures, or develop inputs to the models contained in the MEPDG.

The primary objective of this project, as stated in the task order proposal request, was to “...develop estimates of the dynamic modulus of HMA layers on LTPP test sections following the models used in the MEPDG....” The team evaluated existing models used to estimate  $|E^*|$  values and additional models that are developed based on the use of ANNs.



## 2.0 PREDICTIVE MODELS

Several alternative predictive relationships have been developed to estimate  $|E^*|$  from simpler material properties and volumetrics. These predictive relationships can be used to populate the LTPP database with estimated  $|E^*|$  values. Table 1 lists the predictive relationships identified by the research team. These relationships are described briefly in the following subsections.

**Table 1. Predictive relationships for  $|E^*|$ .**

Model Number	Model
1	Original Witczak equation (NCHRP 1-37A) <sup>(2,11)</sup>
2	Modified Witczak $ G^* $ equation (NCHRP 1-40D) <sup>(5)</sup>
3	Hirsch model <sup>(6)</sup>
4	Law of mixtures parallel model <sup>(7)</sup>
5	ANN model
6	$M_R$ - $ E^* $ model

### 2.1 ORIGINAL WITCZAK EQUATION (NCHRP 1-37A)

Andrei et al. revised the original Witczak  $|E^*|$  predictive equation based on data from 205 mixtures with 2,750 data points.<sup>(11)</sup> The revised equation is as follows:

$$\log_{10} |E^*| = -1.249937 + 0.02923 p_{200} - 0.001767(p_{200})^2 - 0.002841 p_4 - 0.05809 V_a \\ - 0.082208 \frac{V_{beff}}{V_{beff} + V_a} + \frac{3.871977 - 0.0021 p_4 + 0.003958 p_{3/8} - 0.000017(p_{3/8})^2 + 0.00547 p_{3/4}}{1 + \exp(-0.603313 - 0.313351 \log f - 0.393532 \log \eta)} \quad (1)$$

Where:

- $p_{200}$  = Percentage of aggregate passing #200 sieve.
- $p_4$  = Percentage of aggregate retained in #4 sieve.
- $p_{3/8}$  = Percentage of aggregate retained in  $\frac{3}{8}$ -inch (9.56-mm) sieve.
- $p_{3/4}$  = Percentage of aggregate retained in  $\frac{3}{4}$ -inch (19.01-mm) sieve.
- $V_a$  = Percentage of air voids (by volume of mix).
- $V_{beff}$  = Percentage of effective asphalt content (by volume of mix).
- $f$  = Loading frequency (hertz).
- $\eta$  = Binder viscosity at temperature of interest ( $10^6$  P ( $10^5$  Pas)).

Witczak's equation is based on a nonlinear regression analysis using the generalized reduced gradient optimization approach in Microsoft® Excel's Solver. This model incorporates mixture volumetrics and aggregate gradation and is currently one of two options for level 3 analysis using the NCHRP 1-37A MEPDG program.<sup>(2)</sup> For the viscosity term in equation 1, the program converts all level 2 and 3 inputs into regression intercept-regression slope of viscosity temperature susceptibility (A-VTS) values for the formulation of the  $|E^*|$  mastercurve. Furthermore, Witczak's model has an equation (not listed) to convert A-VTS coefficients from virgin or tank binders to RTFO- and PAV-aged binder values.

The limitations of Witczak's equation, acknowledged by Bari, include relying on other models to translate the currently used  $|G^*|$  measurement into binder viscosity.<sup>(5)</sup> Because the original Witczak predictive equation is based on regression analysis, extrapolation beyond the calibration database should be restricted. Bari also mentions that there is limited volumetric influence (precision) when the model is compared to the Shell Oil model.<sup>(5)</sup> Other researchers have also noted the need for improved sensitivity to volumetrics, such as the percentage of voids in mineral aggregate (VMA), the percentage of voids filled with asphalt (VFA), asphalt concrete percentage (AC), and  $V_a$ .<sup>(12)</sup>

## 2.2 MODIFIED WITCZAK EQUATION BASED ON $|G^*|$ (NCHRP 1-40D)<sup>(5)</sup>

To include binder  $|G^*|$  in the predictive model, Witczak reformulated the model to include the binder variable directly. The updated model is as follows:

$$\log_{10} |E^*| = -0.349 + 0.754 \left( |G^*|_b^{-0.0052} \right) \left( \begin{array}{l} 6.65 - 0.032 p_{200} + 0.0027(p_{200})^2 + 0.011 p_4 - 0.0001(p_4)^2 \\ + 0.006 p_{3/8} - 0.00014(p_{3/8})^2 - 0.08 V_a - 1.06 \left( \frac{V_{b\text{eff}}}{V_{b\text{eff}} + V_a} \right) \end{array} \right) + \frac{2.558 + 0.032 V_a + 0.713 \left( \frac{V_{b\text{eff}}}{V_{b\text{eff}} + V_a} \right) + 0.0124 p_{3/8} - 0.0001(p_{3/8})^2 - 0.0098 p_{3/4}}{1 + \exp(-0.7814 - 0.5785 \log |G^*|_b + 0.8834 \log \delta_b)} \quad (2)$$

Where:

- $|G^*|_b$  = Dynamic shear modulus of asphalt binder (pounds per square inch).
- $\delta_b$  = Binder phase angle associated with  $|G^*|_b$  (degrees).

As with the NCHRP 1-37A model, equation 2 is based on a nonlinear regression analysis using 346 mixtures with 7,400 data points. The measured results of the unmodified binders have a better correlation with the model ( $R^2 = 0.87$ ) compared to those of the modified binders ( $R^2 = 0.79$ ) in arithmetic scale. In logarithmic scale, both binder types have  $R^2 = 0.99$ . The binder phase angle is predicted using an empirical equation ( $R^2 = 0.83$ ). This equation is one of two options for level 3 analysis in the most current MEPDG program.

Because some of the mixtures in this database do not contain  $|G^*|_b$  data, the Cox-Mertz rule, using correction factors for the non-Newtonian behaviors (see equations 3–5), is used to calculate  $|G^*|_b$  from A-VTS values as follows:

$$|G^*|_b = 0.0051 f_s \eta_{f_s, T} (\sin \delta_b)^{7.1542 - 0.4929 f_s + 0.0211 f_s^2} \quad (3)$$

$$\begin{aligned} \delta_b = 90 &+ (-7.3146 - 2.6162 * VTS') * \log(f_s * \eta_{f_s, T}) \\ &+ (0.1124 + 0.2029 * VTS') * \log(f_s * \eta_{f_s, T})^2 \end{aligned} \quad (4)$$

$$\log \log \eta_{f_s, T} = 0.9699 f_s^{-0.0527} * A + 0.9668 f_s^{-0.0575} * VTS \log T_R \quad (5)$$

Where:

- $f_s$  = Dynamic shear frequency.
- $\delta_b$  = Binder phase angle predicted from equation 4 (degrees).
- $\eta_{fs,T}$  = Viscosity of asphalt binder at a particular loading frequency ( $f_s$ ) and temperature ( $T$ ) determined from equation 5 (centipoise).
- $T_R$  = Temperature in Rankine scale.

## 2.3 HIRSCH MODEL

Christensen et al. examined four different models based on the law of mixtures parallel model and chose the model that incorporates the binder modulus, VMA, and VFA because it provides accurate results in the simplest form.<sup>(6,7)</sup> The other more complicated forms attempt to incorporate the modulus of the mastic or the film thickness, which are difficult parameters to measure. The suggested model for  $|E^*|$  estimation is provided in equations 6–8 as follows:

$$|E^*|_m = P_c \left[ 4,200,000 \left( 1 - \frac{VMA}{100} \right) + 3 |G^*|_b \left( \frac{VFA * VMA}{10,000} \right) \right] + \frac{(1 - P_c)}{\left( 1 - \frac{VMA}{100} \right) + \frac{VMA}{4,200,000}} \quad (6)$$

$$\phi = -21(\log P_c)^2 - 55 \log P_c \quad (7)$$

$$P_c = \frac{\left( 20 + 3 |G^*|_b (VFA)/(VMA) \right)^{0.58}}{650 + \left( 3 |G^*|_b (VFA)/(VMA) \right)^{0.58}} \quad (8)$$

Where:

- $|E^*|_m$  = Dynamic modulus of HMA (pounds per square inch).
- $P_c$  = Aggregate contact volume.
- $\phi$  = Phase angle of HMA.

A strength of this model is the empirical phase angle equation, which is important for the interconversion of  $|E^*|$  to the relaxation modulus or creep compliance. Weaknesses of the model include a lack of a strong dependence on volumetric parameters, particularly at low  $V_a$  and VFA conditions. Also, questions arise regarding the ability of the  $|G^*|_b$  parameter to account for the possible beneficial effects of modifiers.<sup>(7)</sup> It must be noted that only 206 data points were used to determine the coefficients in the Hirsch model compared to 2,750 data points for the original Witczak model and 7,400 data points for the modified Witczak model.

## 2.4 LAW OF MIXTURES PARALLEL MODEL (AL-KHATEEB MODEL)

Based on their findings from the Hirsch model, Al-Khateeb et al. suggest the following model:<sup>(7)</sup>

$$|E^*|_m = 3 \left( \frac{100 - VMA}{100} \right) \left( \frac{\left( \frac{90 + 10,000 \left( |G^*|_b / VMA \right)}{1,100 + \left( 900 \left( |G^*|_b / VMA \right) \right)^{0.66}} \right)^{0.66}}{|G^*|_g} \right) \quad (9)$$

Where:

$|G^*|_g$  = Dynamic shear modulus of asphalt binder at the glassy state (assumed to be 145,000 psi (999,050 kPa)).

Like the Hirsch model, this formulation is based on the law of mixtures for composite materials. In this model, the different material phases (aggregate, asphalt binder, and air) are considered to exist in parallel. Therefore, this model is a simpler interpretation of the Hirsch model. The researchers note that their model addresses one of the primary shortcomings of the Hirsch model (i.e., the Hirsch model's inability to accurately predict  $|E^*|$  of the mixture at low frequencies and high temperatures).

Strengths of this model include the improved prediction of high-temperature and low-frequency  $|E^*|$  data for mixtures used in the FHWA accelerated loading facility (ALF) test strips. Weaknesses include a lack of model verification and the fact that the researchers who developed this model did so based on  $|E^*|$  values obtained from tests at higher than recommended strain amplitudes (200  $\mu\epsilon$  versus the recommended maximum of 75–150  $\mu\epsilon$ ).

## 2.5 ANN MODELS

The NCSU research team employed the ANN technique to develop new  $|E^*|$  predictive models. The primary advantage of this approach over statistical regression is that the functional form of the relationship is not needed a priori. Considering that so many variables affect  $|E^*|$  values and their interactions, the ANN technique captures complicated nonlinear relationships between  $|E^*|$  and other mixture variables better than regression analysis.

The ANN technique was used in this research to develop several different models. The first model is the ANN model that predicts  $|E^*|$  values using the input variables employed in the modified Witczak equation (i.e., binder dynamic modulus and phase angle, aggregate gradation, and volumetrics of the HMA mixture). The effort to develop this ANN model is described later in this report. The ANN technique was also applied to backcalculate  $|E^*|$  values from  $M_R$ . During the FHWA DTFH61-05-RA-00108 project, the NCSU research team developed a mechanistic approach to compute  $M_R$  from  $|E^*|$  of HMA.<sup>(13,14)</sup> This approach was verified successfully using measured data from mixtures with varying gradations and binder characteristics. The verified solutions were then applied to an available  $|E^*|$  database to estimate the  $M_R$  values corresponding to the  $|E^*|$  values. This database was used to develop an inverse algorithm based on the ANN technique that can predict  $|E^*|$  from  $M_R$ . The development and verification of  $M_R$ - $|E^*|$  ANN are

presented later in this report. Finally, the ANN technique was used to develop an  $|E^*|$  predictive model based on binder viscosity information. This ANN model is also described in this report.

## 2.6 SUMMARY OF INPUT VARIABLES

Table 2 presents the necessary input variables for each predictive relationship discussed previously. For models that utilize  $|G^*_b$ , predictions are only possible at the temperatures and frequencies where  $|G^*_b$  values are available. Having  $|G^*_b$  only at the conditions used in Superpave™ testing is not sufficient for generating  $|E^*$  values over the range of conditions typically needed for mechanistic analysis (14–129.2 °F (-10–54 °C)). For example, if the user has  $|G^*_b$  at only 147.2 °F (64 °C) and 10 radians per second (rad/s), then it is possible to predict the  $|E^*$  value only at 147.2 °F (64 °C) and 10 rad/s. To predict  $|E^*$  at 77 °F (25 °C) and 25 rad/s, the user must measure  $|G^*_b$  at 77 °F (25 °C) and 25 rad/s.

**Table 2. Model variables.**

Variable Description	Model Number						LTPP Data Availability	
	1	2	3	4	5	6	Specific Pavement Study (SPS) <sup>1</sup>	General Pavement Study (GPS) <sup>1</sup>
Mixture $M_R$						X	Yes	Yes
$ G^*_b$		X	X	X	X		Yes <sup>2</sup>	No
$\delta_b$	X			X			Yes	No
VMA (percent)			X	X			Yes	Yes <sup>4</sup>
VFA (percent)				X			Yes	Yes <sup>4</sup>
Aggregate passing #200 sieve (percent)	X	X			X		Yes	Yes
Aggregate passing #4 sieve (percent)	X	X			X		Yes	Yes
Aggregate passing $^{3/8}$ -inch sieve (percent)	X	X			X		Yes	Yes
Aggregate passing $^{3/4}$ -inch sieve (percent)	X	X			X		Yes	Yes
$V_a$ (by volume of the mix ( $V_{mix}$ )) (percent)	X	X			X		Yes	Yes
Effective asphalt content (by total volume of the mixture) (percent)	X	X			X		Yes	Yes <sup>4</sup>
Loading frequency (Hz)	X						Yes	No
A-VTS	X						Yes <sup>3</sup>	Yes <sup>5</sup>

1 inch = 25.4 mm

<sup>1</sup>The in-service pavement sections are classified in the LTPP program as GPS and SPS.

<sup>2</sup> $|G^*_b$  was tested for SPS-9 sections only.

<sup>3</sup>Data for penetration at 77 and 115 °F (25 and 46 °C), cone and plate viscometer at 77 °F (25 °C), absolute viscosity at 140 °F (46 °C), and kinematic viscosity at 275 °F (135 °C) are available.

<sup>4</sup>Indicates information was reported by an agency.

<sup>5</sup>Data for ring and ball softening point, penetration at 39.2 and 77 °F (4 and 25 °C), absolute viscosity at 140 °F (46 °C), and kinematic viscosity at 275 °F (135 °C) are available (reported by agency).

Note: Blank cells indicate that the input parameter is not required in the model.

A preliminary review of available information in the LTPP materials database revealed that measured  $|G^*/_b$  data are only available for most of the SPS-9 projects and only at 10 rad/s at multiple temperatures. Even the available  $|G^*/_b$  data are measured from binders aged at different levels (i.e., RTFO-aged versus PAV-aged binders). The lack of complete  $|G^*/_b$  data at multiple temperatures and multiple frequencies is a serious problem because all of the models except the original Witczak equation require this information. (Note that the  $M_R$ - $|E^*$  ANN model needs the binder t-T shift factor as well.) During the course of this project, the NCSU research team developed empirical models that allow the estimation of the RTFO-aged  $|G^*/_b$  values at multiple temperatures and frequencies from the  $|G^*/_b$  values obtained at a single frequency and multiple temperatures and aging levels.

## 3.0 DATABASES

To accomplish the goals of the project, modulus values from multiple mixtures and binders were necessary. These databases were assembled from existing national efforts and from data obtained at NCSU. In the following sections, the databases are summarized by material type (i.e., binder or mixture). First, the specific reasons for such databases are given.

### 3.1 STATEMENT OF NEED

The most comprehensive database for both binder moduli and viscosity and mixture moduli that is currently available is the one used to develop the Witczak and modified Witczak models. This database is extensive and covers a range of material characteristics. At the outset of this project, such a database was sufficient to meet the project goals. However, an indepth evaluation of the database identified the following three problems in using it for model development:

1. Different definitions of frequency for the binder  $|G^*|$  and mixture  $|E^*|$  data are used.
2. Estimated rather than measured  $|G^*|$  and  $\delta_b$  data are used to populate the database.
3. The estimated  $|G^*|$  data at temperatures lower than or equal to 39.9 °F (4.4 °C) are estimated in a manner that is inconsistent with other temperatures, and the method of estimation is not satisfactorily explained.

#### 3.1.1 Inconsistent Definition of Frequency

In developing the Witczak database, researchers used two definitions for frequency. The decision to use two definitions was motivated by widespread confusion between frequency and time for LVE materials and the differences in the binder and mixture fields. Researchers studying asphalt binders have been influenced by rheology and often cite the relationship between time and frequency as follows:

$$t = \frac{1}{\omega} = \frac{1}{2\pi f_s} \quad (10)$$

Where:

$\omega$  = Angular frequency in radians per second.

$t$  = Time.

$f_s$  = Shear frequency.

Conversely, researchers who focus on AC tend to use the argument that time and frequency are related as follows:

$$t = \frac{1}{f} = \frac{1}{f_c} \quad (11)$$

Where:

$f$  = Frequency (hertz).

$f_c$  = Frequency under axial compression.

This latter interpretation is more accurate if the time under consideration is the pulse time (i.e., it equates the modulus at a given frequency to the appropriate modulus when the material is subjected to a load pulse of a given duration). The former definition is more accurate when it is necessary to equate the modulus determined at a given frequency to the material modulus under a fixed load after a given duration.

The use of different definitions for frequency appears to be an effort to appease both mixture and binder branches and their techniques for data interpretation. To coordinate these two datasets, the Witczak data match time from equations 10 and 11. Such an approach allows the prediction of the modulus of AC at 10 Hz and 77 °F (25 °C). As a result, the appropriate binder modulus that can substitute into equation 2 is the one at 10 rad/s (1.59 Hz) and 77 °F (25 °C). This is referred to as the inconsistent definition of frequency in this report because the frequency at which  $|E^*|$  and  $|G^*|$  are measured is not consistent. A small sample of the database that clearly shows this inconsistent definition is shown in table 3.

**Table 3. Example of summarized mixture and binder properties in the original Witczak database.**

Mix Number	Temperature (°C)	Mixture $ E^* $ Test Data		Binder Stiffness Data		
		$f_c$ (Hz)	$ E^* $ (psi)	$f_s$ (Hz)	$ G^* $ (psi)	$\delta_b$ (degrees)
1	4.4	1	1.35E+06	0.16	9.81E+02	54.7

$$^{\circ}\text{C} = (\text{°F}-32)/1.8$$

$$1 \text{ psi} = 6.89 \text{ kPa}$$

A more logical approach, which was used in all of the other  $|G^*|$ -based models and is presented in table 2, is to use a consistent definition for frequency. To predict the mixture modulus at 10 Hz and 77 °F (25 °C), the logical binder modulus that should be used is the one at 10 Hz and 77 °F (25 °C). Such an effort required the complete repopulation of the Witczak database, which was part of the effort in this project.

Because part of this research effort was to assess the sensitivity of existing models, independent databases were needed. These databases are summarized in the following sections; however, it should be noted that for fairness, care was taken to ensure that the inconsistent definition was used to make predictions using the modified Witczak model. The consistent definition was used for development of the ANN-based model.

### 3.1.2 Use of Estimated $|G^*|$ Values

The  $|G^*|$  data in the Witczak database are not measured values and were estimated using the predictive equations given in equations 3–5. Such an approach was deemed necessary for consistency purposes. Even though the  $|G^*|$  binders were measured for several of the mixtures, no such data were available for approximately half of the mixtures in the database. By using  $|G^*|$  from the predictive equations, the entire database could be used to develop the modified Witczak model. Therefore, the effects of the errors in the binder modulus model were integrated into the

predictive capabilities of the model. To evaluate the predictive power of these models and to assess the need to return to the measured data, the measured and predicted  $|G^*|$  and  $\delta_b$  values for the 8,940 data points from 41 binders (including 9 modified binders) used in developing equations 3–5 were compared. Figure 3 illustrates that the model shows little bias, but the errors in the predictive models are significant. In some cases, the errors exceeded 100 percent, which could translate directly to errors in the predicted mixture moduli. The predicted  $\delta_b$  is shown in figure 4, and the errors were even more significant than they were for the predicted  $|G^*|$ . Again, such errors can have a significant effect on the predictive model's capabilities. An independent dataset was also used to assess the errors, and the results are shown in figure 5 (arithmetic scale) and figure 6 (logarithmic scale). This analysis shows that any given binder may have significant bias, the effects of which will directly translate to  $|E^*|$  predictions.

To correct this problem, the binder data in the Witczak database were completely ignored, and only mixtures that had independently measured  $|G^*$  values available were used. This approach reduced the number of usable mixtures to approximately half the number that was initially thought to be available.

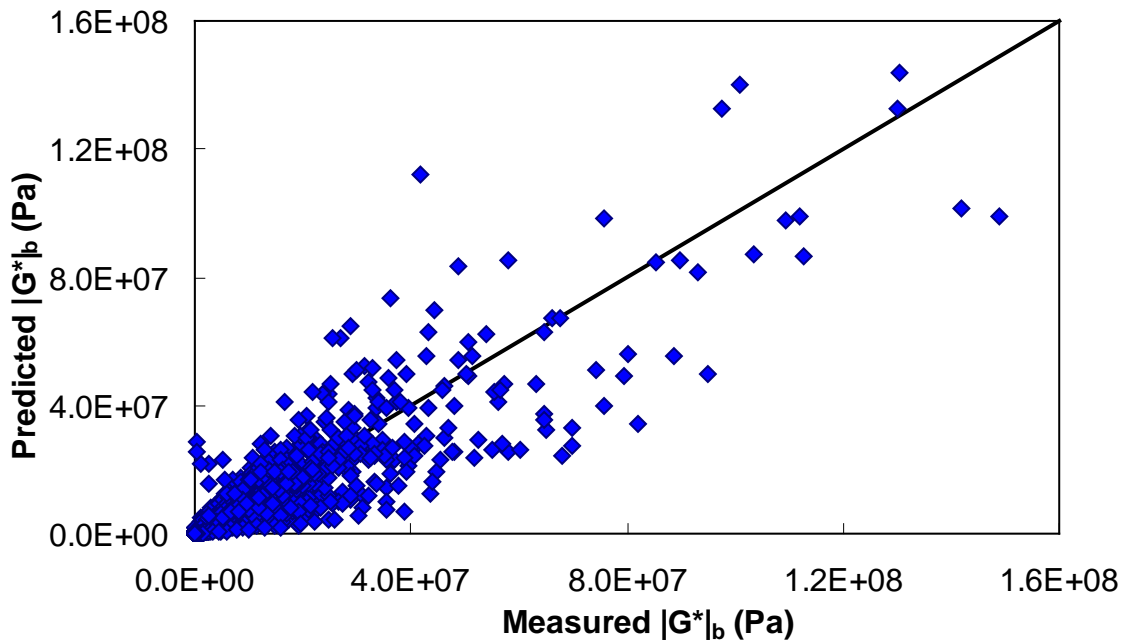


**Figure 2. Graph. Comparison between the Witczak predictive model and measured  $|G^*|_b$  values in arithmetic scale.**

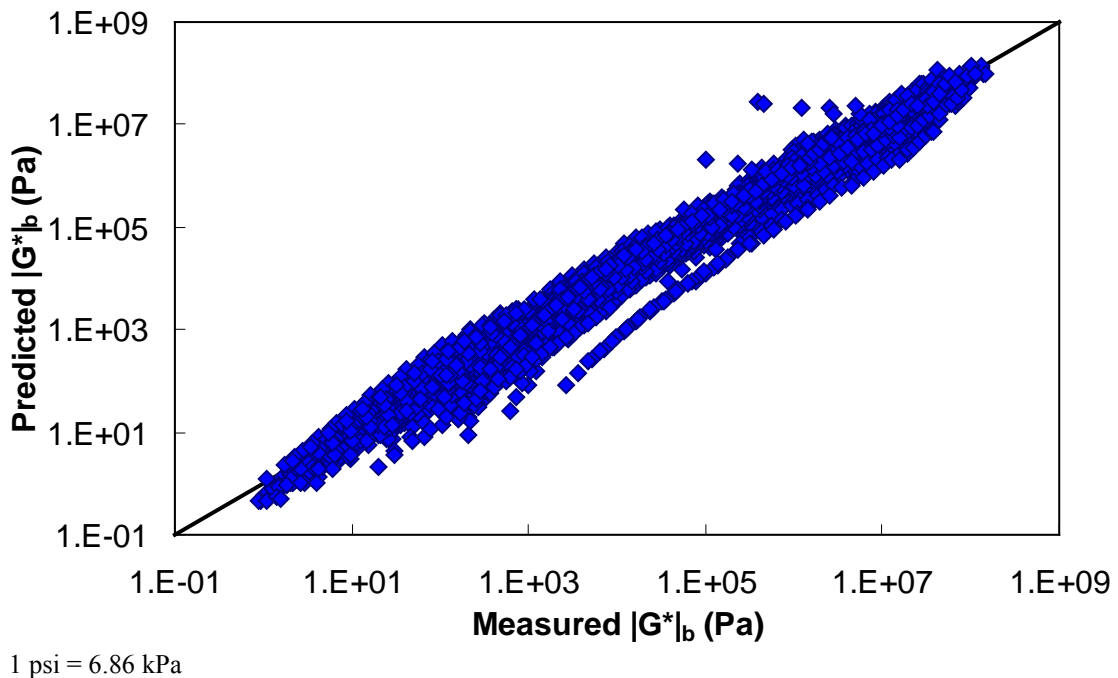


**Figure 3. Graph.** Comparison between the Witczak predictive model and measured  $|G^*|_b$  values in logarithmic scale.

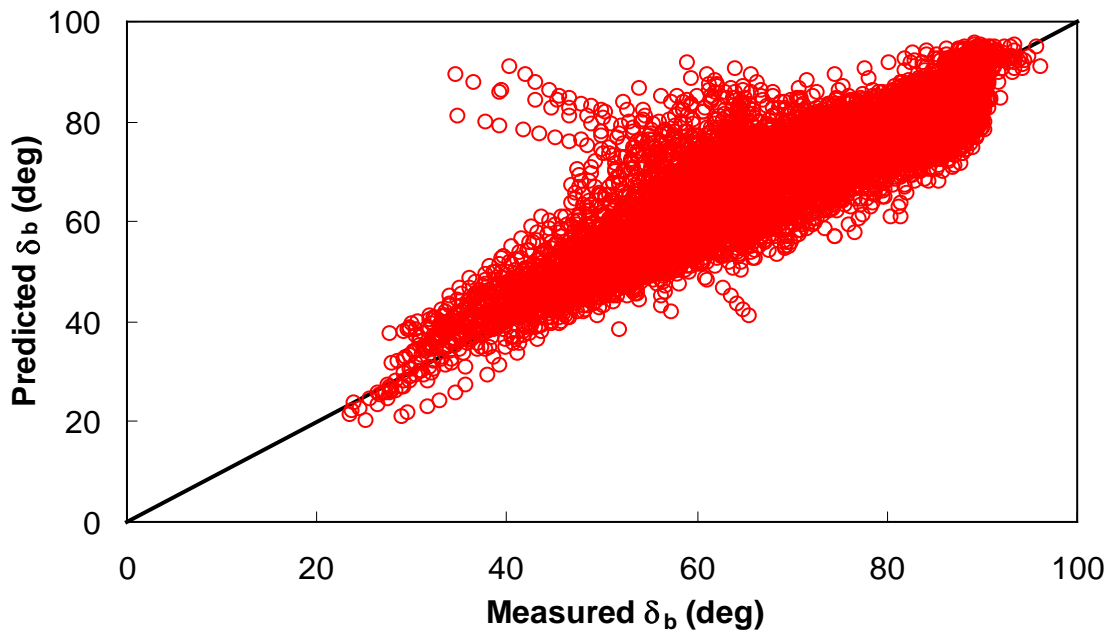
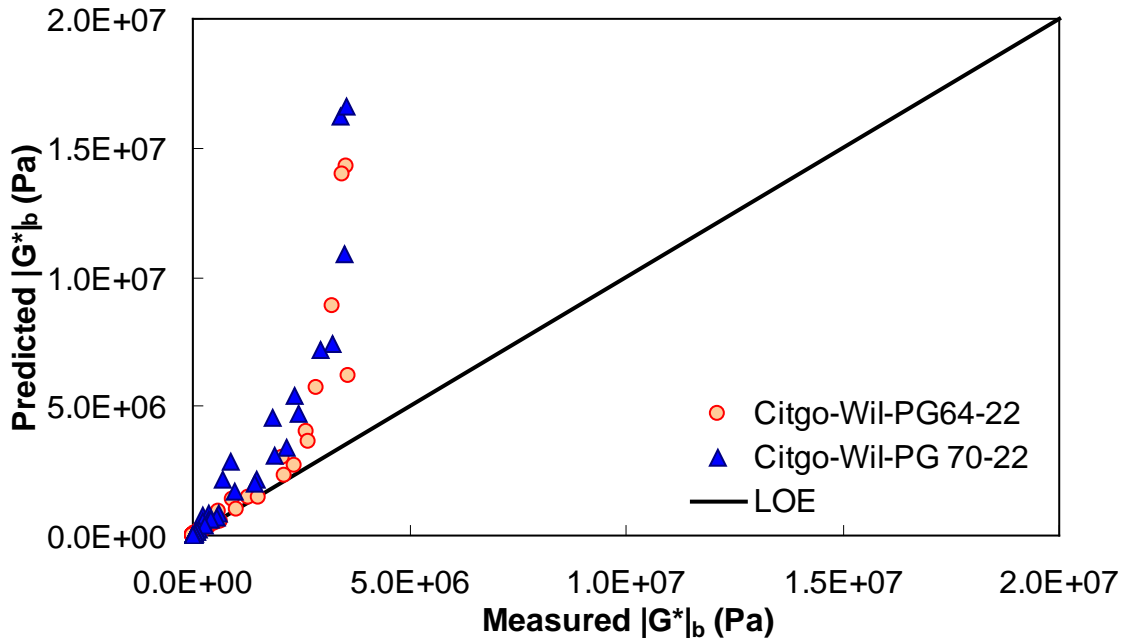
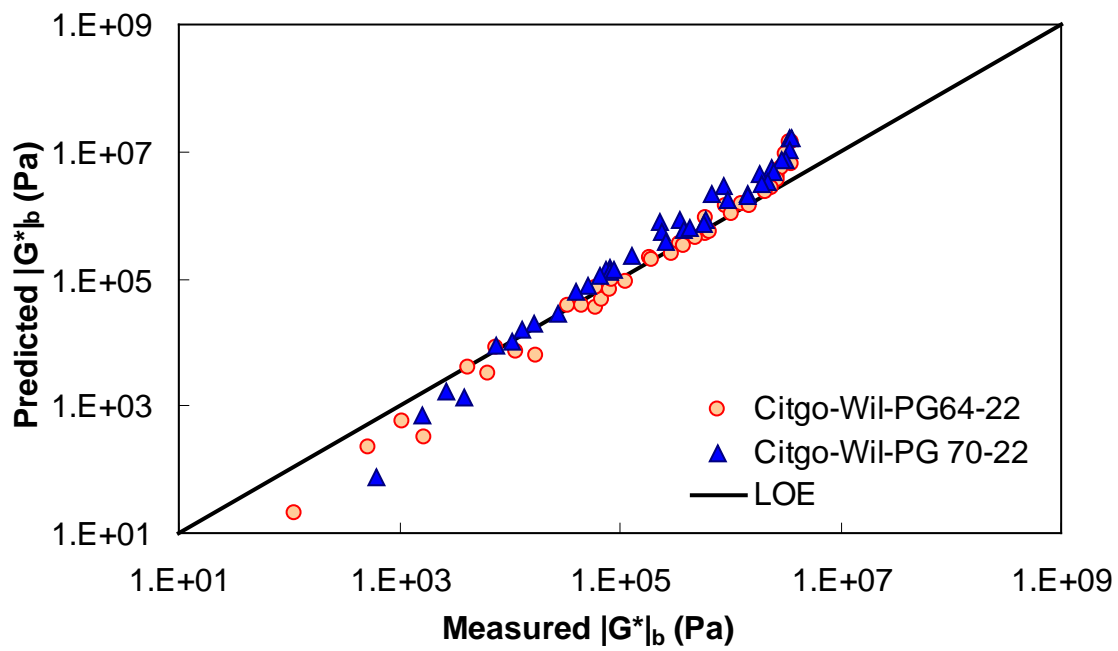


**Figure 4. Graph.** Comparison between the Witczak predictive model and measured  $\delta_b$  to develop the  $\delta_b$  model.



1 psi = 6.86 kPa

**Figure 5. Graph. Comparison between the Witczak predictive model and measured  $|G^*|_b$  values using Citgo binders in the North Carolina Department of Transportation (NCDOT) database in arithmetic scale.**



1 psi = 6.86 kPa

**Figure 6. Graph. Comparison between the Witczak predictive model and measured  $|G^*|_b$  values using Citgo binders in the NCDOT database in logarithmic scale.**

### 3.1.3 Low-Temperature $|G^*|$ Values

Through the process of determining that the binder data in the Witczak database consist of predicted values, it was also found that the low-temperature binder moduli were not determined in the same way as the intermediate and high temperatures. It was not possible to discern how these values were determined for the database because they do not agree with the predictions made from a surrogate model. Additionally, they are approximately two orders of magnitude smaller than typical values for these temperatures. Measured moduli for the available binders were provided only for temperatures as low as 59 °F (15 °C).

To address this problem, the measured binder data that were available had to be processed in a way that would allow extrapolation. According to the Christensen Anderson Marasteanu (CAM) model, shown in equations 12 and 13, the following is assumed for all binders in the database:

$$|G^*| = \frac{G_g}{\left(1 + \left(\frac{f_c}{f_R}\right)^k\right)^{\frac{m_e}{k}}} \quad (12)$$

$$\delta = \frac{90m_e}{1 + (f_R/f_c)^k} \quad (13)$$

Where:

- $G_g$  = Maximum shear modulus or glassy modulus (pascal).  
 $\delta$  = Binder phase angle (degree).  
 $f_R$  = Reduced frequency (hertz).  
 $f_c, m_e$ , and  $k$  = Fitting coefficients.

Equation 12 has been characterized for each of the binders using least square optimization techniques. The fit was verified, and the low-temperature binder stiffness was determined. Note that for consistency, this functional form was also used to populate the binder data at the same temperatures as the  $|E^*|$  measurements. Unfortunately, the Witczak binders do not provide available data to assess potential errors using this extrapolation methodology. To fully assess the errors, additional binder data, which include bending beam rheometer (BBR) measurements or shear modulus measurements taken at extremely low temperatures, and dynamic shear rheometer (DSR) measurements at intermediate and high temperatures are required.

### 3.1.4 Aging Effects

After accounting for these binder data issues, it was found that the lack of binder data at different aging levels is a serious limitation of the Witczak database. This limitation is important because the LTPP database contains binder modulus values at original-, RTFO-, PAV-aged, and even recovered conditions. Accounting for these inconsistencies in the analysis process required an understanding of their effects on the binder shear modulus. Because the data in the Witczak database are insufficient for this purpose, additional binder databases were necessary.

### 3.2 BINDER DATABASES

There are six binder datasets: (1) Witczak, (2) FHWA mobile trailer, (3) FHWA TPF-5(019), (4) NCDOT, (5) Western Research Institute (WRI), and (6) Citgo.<sup>(15)</sup> The following sections describe these binder datasets.

#### 3.2.1 Witczak Binder Database

Table 4 summarizes the binders that make up the Witczak binder database. Each of these binders corresponds to a particular mixture or mixtures in the Witczak  $|E^*|$  database. The binders in this database have measured  $|G^*|$  values available at a range of temperatures and frequency combinations as well as various aging conditions (original, RTFO, and PAV). Additionally, in table 4, a subset of these binders has measured BBR results. Note that the Citgo and WRI binders are the only ones with BBR data. Each binder has BBR stiffness and slope values at -11.2, -0.4, and 10.4 °F (-24, -18, and -12 °C) (WesTrack) or -22, -11.2, and -0.4 °F (-30, -24, and -18 °C) (all others) and times of 8, 15, 30, 60, 120, and 240 s, respectively. All binders in this database have viscosity data in the form of temperature susceptibility function parameters A and VTS.

**Table 4. Summary of  $|G^*|$  data available in the Witczak binder database.**

Binder Code	Temperature (°C)	Frequency (rad/s)	Performance Grade (PG)	Original	RTFO	PAV	BBR Available	
ALF AC-5	15, 25, 35, 45, 60, 70, 80, 95, 105, and 115	1, 1.59, 2.51, 3.98, 6.31, 10, 15.9, 25.1, 39.8, 63.1, and 100	58	✓	✓	✓	✓	
ALF AC-10				✓	✓	✓	✓	
Paramount PG 58-22				✓	✓	✓		
ALF AC-20	15, 25, 35, 45, 60, 70, 80, 95, 105, and 115		64	✓	✓	✓	✓	
WesTrack				✓	✓	✓	✓	
Chevron PG 64-22				✓	✓	✓		
Paramount PG 64-16	15, 25, 35, 45, 60, 70, 80, 95, 105, and 115		70	✓	✓	✓		
Navajo PG 70-10				✓	✓	✓		
ALF-Novophalt				✓	✓	✓	✓	
Chevron PG 76-16	15, 25, 35, 45, 60, 70, 80, 95, 105, and 115	76	✓	✓	✓	✓		
Navajo PG 76-16			✓	✓	✓			
ALF-Styrelf			✓	✓	✓	✓		
MNRD120P	15, 25, 35, 45, 60, 70, 80, 95, and 105		58	✓	✓	✓	✓	
MNRD120P			64	✓	✓	✓	✓	
MPA Citgo 70-22	25, 35, 45, 60, 70, 80, 95, 105, and 115		70	✓	✓	✓		
MPA-Elvaloy			76	✓	✓	✓		
MPA-TA			✓	✓	✓	✓		
MPA-Novophalt			82	✓	✓	✓		
MPA-Stylink			82	✓	✓	✓		

°C = (°F-32)/1.8

Note: Blank cells indicate data are unavailable in the database.

### 3.2.2 FHWA Mobile Trailer Binder Database

The FHWA mobile trailer database contains original-, RTFO-, and PAV-aged  $|G^*|$  values for a range of binders throughout the United States (see table 5). Note that the temperature and frequency combinations are not as consistent or as broad as those in the Witczak database. All of the asphalt binders in this database have viscosity data available.

**Table 5. Summary of  $|G^*|$  data available in the FHWA mobile trailer database.**

Binder Code	Temperature (°C)	Frequency (rad/s)	PG	Original	RTFO	PAV	BBR Available
IA_0358	5, 17, 23, 25, 40, and 45	0.1, 0.63, 1, 3.14, 6.3, 10, 31.45, 62.9, 100, 157.199	58	✓	✓	✓	
WI_0357	5, 15.6, 19.6, 22, 23.6, 25, 31.2, 45			✓	✓	✓	
ME_0359	5, 17.9, 23.9, 25, 37.5, and 45			✓	✓	✓	
LA_0462	5, 25, 45, and 54			✓	✓	✓	
WA_0463	5, 15, 25, 38, and 45			✓	✓	✓	
KS_0464	5, 31, and 45			✓	✓	✓	
NY_0466	4.4, 5, 13, 21.1, 25, 37.8, 45, and 54.4			✓	✓	✓	
MA_0467	4.4, 5, 13, 15, 22, 25, 37.8, 45, and 54.4			✓	✓	✓	
NC_0360	5, 20.8, 25, and 45		70	✓	✓	✓	
MN_0465	5, 13, 25, 45, and 54.4			✓	✓	✓	
AZ_0356	5, 22, 25, and 45	-10, 4.4, 21.1, 37.8, and 54.5	76	✓	✓	✓	
CO_0777-BA					✓		
CO_0777-BA+ADVERA				✓			
CO_0777-BA+SASOBIT			58		✓		
OK_0673					✓		
SD_0674					✓		
MO_0672			70		✓		
AL_0675					✓		
NJ_0671			76		✓		
ME_0570			64		✓		
NE_0569		4.4, 21.1, 37.8, and 54.10			✓		
KS_0568					✓		
KS_0568 (2)			70		✓		

$$^{\circ}\text{C} = (^{\circ}\text{F}-32)/1.8$$

Note: Blank cells indicate data are unavailable in the database.

### 3.2.3 FHWA TPF-5(019) Binder Database

A portion of the current FHWA ALF binder data is available to the research team and is summarized in table 6. For these materials, DSR values are available at a wider range of frequencies than in the other databases. At the time this report was written, BBR results were not available; however, the possibility of obtaining such values along with data from other binders in the TPF-5(019) study is under investigation. Also, these binders have  $|G^*|$  values measured under original-, RTFO-, and PAV-aged conditions. Viscosity values are not available for these materials.

**Table 6. Summary of  $|G^*|$  data available in the FHWA TPF-5(019) binder database.**

Binder Code	Temperature (°C)	Frequency (rad/s)	PG	Original	RTFO	PAV	BBR Available
Binder (AB)-B-6261		0.100, 0.126, 0.158, 0.200,	52		✓		
SBS LG base-B-6275		0.251, 0.316, 0.398, 0.501,	58		✓		
PG 70-22 1-B-6267		0.631, 0.794, 1.000, 1.259,			✓		
PG 70-22 2-B-6272	7, 19, 25, 31, 40, 46, 58, 64, 70, and 82	1.585, 1.995, 2.512, 3.162, 3.981, 5.012, 6.309, 7.942,			✓		
PG 70-22 3-B-6298		10.000, 12.589, 15.849, 19.952, 2.118, 31.622,	70		✓		
SBS LG-B-6295		39.809, 50.115, 62.091, 79.426, and 100.000			✓		
Terpoly-B-6289			76		✓		
CRTB-B-6286					✓		

°C = (°F-32)/1.8

Note: Blank cells indicate data are unavailable in the database.

### 3.2.4 NCDOT Binder Database

The binders corresponding to NCDOT mixture data are available in the NCDOT binder database, which is summarized in table 7. Data for these binders, both  $|G^*|$  and viscosity, are available only for the RTFO-aged condition.

**Table 7. Summary of  $|G^*|$  data available in the NCDOT binder database.**

Binder Code	Temperature (°C)	Frequency (rad/s)	PG	Original	RTFO	PAV	BBR Available
AA-Inman	16, 22, 28, and 40	0.06, 0.31, 0.63, 3.14, 6.28, 31.42, 62.83, and 94.25	64		✓		
El Paso-Apex					✓		
El Paso-Charlotte					✓		
Citgo-Wil-64					✓		
AA-Sali-70			70		✓		
Citgo-Wil-70					✓		
AA-Sali-76			76		✓		

°C = (°F-32)/1.8

Note: Blank cells indicate data are unavailable in the database.

### 3.2.5 Citgo Binder Database

Table 8 summarizes the binders that are used in the Citgo database. This database contains original-, RTFO-, and PAV-aged  $|G^*|$  and BBR results for two different binders used in NCHRP 9-25 and 9-31.<sup>(16,17)</sup> No viscosity measures are available for these binders.

**Table 8. Summary of  $|G^*|$  data available in the Citgo binder database.**

Binder Code	Temperature (°C)	Frequency (rad/s)	PG	Original	RTFO	PAV	BBR Available
Citgo_A	15, 25, 35, 45, 60, and 75	0.1, 0.159, 0.251, 0.398, 0.631, 1, 1.59, 2.51, 3.98, 6.31, 10, 15.9, 25.1, 39.8, 63.1, and 100	70	✓	✓	✓	✓
Citgo_B				✓	✓	✓	✓

°C = (°F-32)/1.8

Note: Blank cells indicate data are unavailable in the database.

### 3.2.6 WRI Binder Database

The WRI binder database consists of two sets of binders from the Kansas and Nevada test sites. The four binders used at the Kansas site are from different crude sources, but all are PG 64-22. Additionally, the four binders used at the Nevada site are from different crude sources, each of which meets the AC-30 requirements of AASHTO M226-80, “Standard Specification for Viscosity Graded Asphalt Cement.”<sup>(18)</sup> Table 9 summarizes the relevant information for the binders in this database. Viscosity values for these binders are not available.

**Table 9. Summary of  $|G^*|$  data available in the WRI database.**

<b>Binder Code</b>	<b>Temperature (°C)</b>	<b>Frequency (rad/s)</b>	<b>PG</b>	<b>Original</b>	<b>RTFO</b>	<b>PAV</b>	<b>BBR Available</b>
KS-1-Sinclair Tulsa	0.0, 10.0, 20.0, 30.0, 40.0, 50.0, 60.0, 70.0, and 80.0	0.10, 0.13, 0.16, 0.20, 0.25, 0.32, 0.40, 0.50, 0.63, 0.79, 1.0, 1.26, 1.58, 2.0, 2.51, 3.16, 3.9, 5.0, 6.3, 7.9, 10.0, 12.59, 15.6, 19.9, 25.11, 31.6, 39.8, 50.1, 63.1, 79.4, and 100.0	64	✓	✓	✓	✓
KS-2-Coastal Eldorado				✓	✓	✓	✓
KS-3-Koch Muskogee				✓	✓	✓	✓
KS-4-Royal Trading				✓	✓	✓	✓
NV-1-Sinclair WY				✓	✓	✓	✓
NV-2-Crown Nevada	0.0, 10.0, 20.0, 30.0, 40.0, 50.0, 60.0, and 70.0	5.0, 6.3, 7.9, 10.0, 12.59, 15.6, 19.9, 25.11, 31.6, 39.8, 50.1, 63.1, 79.4, and 100.0	AC-30	✓	✓	✓	✓
NV-3-Crown Venezuela				✓	✓	✓	✓
NV-4-Crown Canadian				✓	✓	✓	✓

°C = (°F-32)/1.8

Note: Blank cells indicate data are unavailable in the database.

### 3.3 MIXTURE DATABASES

The mixture databases for this project are similar in content to the binder databases; however, the temperatures and frequencies are different. These mixture databases contain the volumetric information listed in table 2. There are seven mixture datasets: (1) Witczak, (2) FHWA mobile trailer I, (3) FHWA mobile trailer II, (4) FHWA TPF-5(019), (5) NCDOT, (6) WRI, and (7) Citgo. The following sections describe the mixture databases.

#### 3.3.1 Witczak Mixture Database

Over the years, differences in TPs used to develop the database have led to limitations of the use of some mixtures in the Witczak database. The complete database contains 7,400 data points; however, the database used for this project has been limited to 3,180 data points for 106 mixtures. To avoid confusion, this limited database is referred to as the “processed Witczak database.” These mixtures are summarized in table 10 along with the spread of volumetric properties. Note that for all of the mixtures in this database, the true measured  $|G^*|$  data are available (see table 4).

#### 3.3.2 FHWA Mobile Trailer Mixture Database

A primary difference between the FHWA mobile trailer database and the processed Witczak database is TP. The mobile trailer database is populated with  $|E^*|$  data obtained from the procedure and equipment suggested for AMPTs, whereas the processed Witczak database is populated using data obtained from the AASHTO TP-62 protocol.<sup>(8)</sup> For modeling purposes, the mobile trailer mixture database is separated into two groups: FHWA I and FHWA II, which are summarized in table 11 and table 12, respectively. Note that a comparison of table 10 with table 11 and table 12 shows that the processed Witczak database covers an overall broader range

of conditions than the mobile trailer mixture database. However, the latter database has smaller values of some parameters, particularly those related to the mixture gradation (i.e.,  $\rho_{3/4}$ ,  $\rho_{3/8}$ , and  $\rho_4$ ). This indicates that smaller nominal maximum-sized aggregate (NMSA) mixtures are represented more strongly in the mobile trailer database than they are in the processed Witczak database.

### **3.3.3 FHWA TPF-5(019) Mixture Database**

The FHWA ALF study mixtures are available for the TP-62 test conditions. These mixtures consist of the same aggregate type and gradation, air void content, and asphalt content. The only differences between these mixtures are the asphalt type and a slight difference in the effective asphalt content. Table 13 presents a summary of the FHWA TPF-5(019) mixtures.<sup>(15)</sup>

**Table 10. Summary of  $|E^*|$  data available in the processed Witczak mixture database.**

Binder Code	Number of Mix Variations	Total Number of Tests	Temperature (°C)	Frequency (Hz)	Aging Condition			
					Plant or Unaged	Short-Term Oven Aging (STOA)	Long-Term Oven Aging (LTOA) or Field	
MPA Citgo 70-22	4	4	-17.8, 4.4, 21.1, 37.8, and 54.4	25, 10, 5, 1, 0.5, and 0.1	4			
MPA-Elvaloy	4	4			4			
MPA-Novophalt	4	4			4			
MPA-Stylink	4	4			4			
MPA-TA	4	4			4			
ALF AC-5	6	6				4	2	
ALF AC-10	2	2				1	1	
ALF AC-20	6	6				4	2	
WesTrack	34	34			22	12		
Chevron 64-22	17	17				17		
Paramount 64-16	1	1			1			
Navajo 70-10	2	2				2		
ALF-Novophalt	2	2				1	1	
Chevron 76-16	2	2					2	
ALF-Styrelf	2	2				1	1	
MNRD120P	8	8			6	2		
MNRDACP20	4	4			1	3		
$\rho_{3/4}$		Maximum	26.1					
$\rho_{3/4}$		Minimum	0					
$\rho_{3/8}$		Maximum	41					
$\rho_{3/8}$		Minimum	15					
$\rho_4$		Maximum	73					
$\rho_4$		Minimum	30					
$\rho_{200}$		Maximum	6.6					
$\rho_{200}$		Minimum	2.6					
$V_a$		Maximum	12.5					
$V_a$		Minimum	0.7					
$V_{beff}$		Maximum	13.5					
$V_{beff}$		Minimum	6.1					
VMA		Maximum	22.2					
VMA		Minimum	11.2					
VFA		Maximum	95.1					
VFA		Minimum	32.8					

$^{\circ}\text{C} = (\text{ }^{\circ}\text{F}-32)/1.8$

Note: Blank cells indicate data are unavailable in the database.

**Table 11. Summary of  $|E^*|$  data available in the FHWA I mobile trailer mixture database.**

Binder Code	Number of Mix Variations	Total Number of Tests	Temperature (°C)	Frequency (Hz)	Aging Condition			
					Plant or Unaged	STOA	LTOA or Field	
WI_0357	9	36	15.6, 19.6, 23.6, and 31.3	25, 10, 5, 1, 0.5, and 0.1	24	12		
ME_0359	9	36	17.9, 23.9, and 37.5		24	12		
LA_0462	9	28	25, 45, and 54		15	13		
NY_0466	12	32	13, 25, and 45		20	12		
MA_0467	5	16	15, 25, and 45		16			
NC_0360	13	52	21, 25, and 45		40	12		
MN_0465	11	39	13, 25, and 45		27	12		
AZ_0356	9	26	22 and 44		14	12		
CO_0777	1	4	4.4, 21.1, 37.8, and 54.4		4			
CO_0777+ ADV	1	4			4			
CO_0777+ SAS	1	4			4			
OK_0673	13	34			22	12		
SD_0674 <sup>1</sup>	6	24			12	12		
MO_0672 <sup>2</sup>	6	24				24		
AL_0675 <sup>3</sup>	24	96			72	24		
NJ_0671 <sup>1</sup>	6	24			12	12		
ME_0570	11	44	21.1, 37.8, and 54.4		32	12		
NE_0569	16	54			46	8		
KS_0568 <sup>1</sup>	6	30						
KS_0568(2) <sup>1</sup>	4	20						
$\rho_{3/4}$		Maximum			11.6			
$\rho_{3/4}$		Minimum			0			
$\rho_{3/8}$		Maximum			45.1			
$\rho_{3/8}$		Minimum			2.3			
$\rho_4$		Maximum			67.4			
$\rho_4$		Minimum			22.3			
$\rho_{200}$		Maximum			6.6			
$\rho_{200}$		Minimum			2.7			
$V_a$		Maximum			8.7			
$V_a$		Minimum			4.5			
$V_{beff}$		Maximum			12.7			
$V_{beff}$		Minimum			4.8			
VMA		Maximum			20			
VMA		Minimum			9.5			
VFA		Maximum			70.3			
VFA		Minimum			43			

$^{\circ}\text{C} = (\text{ }^{\circ}\text{F}-32)/1.8$

<sup>1</sup> $V_{beff}$  is not given, <sup>2</sup>inconsistent ID numbers for correlating volumetric and  $|E^*|$  data, and <sup>3</sup>measured  $|E^*|$  under confining pressure.

Note: Blank cells indicate data are unavailable in the database.

**Table 12. Summary of  $|E^*|$  data available in the FHWA II mobile trailer mixture database.**

Binder Code	Number of Mix Variations	Total Number of Tests	Temperature (°C)	Frequency (Hz)	Aging Condition		
					Plant or Unaged	STOA	LTOA or Field
IA_0358	7	28	17, 23, and 40	25, 10, 5, 1, 0.5, and 0.1	16	12	
WA_0463	6	24	15, 25, 38, and 45		12	12	
KS_0464	8	32	25, 31, and 45		20	12	
$\rho_{3/4}$		Maximum			2.1		
$\rho_{3/4}$		Minimum			0		
$\rho_{3/8}$		Maximum			17		
$\rho_{3/8}$		Minimum			14.7		
$\rho_4$		Maximum			45.9		
$\rho_4$		Minimum			34.1		
$\rho_{200}$		Maximum			6.5		
$\rho_{200}$		Minimum			3.8		
$V_a$		Maximum			8.5		
$V_a$		Minimum			5.7		
$V_{beff}$		Maximum			11.5		
$V_{beff}$		Minimum			8.2		
VMA		Maximum			19.9		
VMA		Minimum			15.1		
VFA		Maximum			65.5		
VFA		Minimum			52.1		

$^{\circ}\text{C} = (\text{°F}-32)/1.8$

Note: Blank cells indicate data are unavailable in the database.

**Table 13. Summary of  $|E^*|$  data available in the FHWA TPF-5(019) mixture database.**

Binder Code	Number of Mix Variations	Total Number of Tests	Temperature (°C)	Frequency (Hz)	Aging Condition		
					Plant or Unaged	STOA	LTOA or Field
PG 70-22 3-B-6298	1	3	-10, 5, 20, 40, and 54	25, 10, 5, 1, 0.5, and 0.1		3	
SBS LG-B-6295	1	3				3	
Terpoly-B-6289	1	3				3	
CRTB-B-6286	1	3				3	
$\rho_{3/4}$					0.0		
$\rho_{3/8}$					14.8		
$\rho_4$					44		
$\rho_{200}$					6.7		
$V_a$					4		
$V_{beff}$	Maximum				12.4		
	Minimum				12.3		
VMA	Maximum				16.4		
	Minimum				16.3		
VFA	Maximum				75.6		
	Minimum				75.5		

°C = (°F-32)/1.8

Note: Blank cells indicate data are unavailable in the database.

### 3.3.4 NCDOT Mixture Database

The NCDOT mixture database consists of 36 AC mixtures covering a range of materials. All of the mixtures were tested at NCSU. The test conditions for the mixtures in this database are most similar to the TP-62 protocol. The database is summarized in table 14.

**Table 14. Summary of  $|E^*|$  data available in the NCDOT mixture database.**

Binder Code	No. of Mix Variations	Total No. of Tests	Temperature (°C)	Frequency (Hz)	Aging Condition		
					Plant or Unaged	STOA	LTOA or Field
El Paso-Charlotte-64	2	2	-10, 10, 35, and 54	25, 10, 5, 1, 0.5, 0.1, 0.05, and 0.01		2	
Citgo-Wil-64	24	24				24	
AA-Sali-70	1	1				1	
Citgo-Wil-70	8	8				8	
AA-Sali-76	1	1				1	
$\rho_{3/4}$	Maximum				31		
	Minimum				0		
$\rho_{3/8}$	Maximum				55		
	Minimum				1		
$\rho_4$	Maximum				67		
	Minimum				14		
$\rho_{200}$	Maximum				6.6		
	Minimum				3		
$V_a$	Maximum				4.9		
	Minimum				3		
$V_{beff}$	maximum				14.2		
	Minimum				7.3		
VMA	Maximum				18.4		
	Minimum				10.8		
VFA	Maximum				79.1		
	Minimum				67.7		

°C = (°F-32)/1.8

Note: Blank cells indicate data are unavailable in the database.

### 3.3.5 WRI Mixture Database

The results of laboratory testing and analysis of plant-produced AC mixtures from two sets of four test sections constructed for the WRI on US-77 in Kansas and on I-15 in Clark County, NV, are documented in this database. In each of these two sites, the four test sections were constructed using the same asphalt mixture and four binders from different crude sources. The laboratory testing was conducted on plant-produced samples that were compacted to a target air void of 7 percent using a gyratory compactor. The tests were conducted for the as-received plant-aged condition and after LTOA in accordance with AASHTO R30-02, “Standard Specification for Mixture Conditioning of Hot Mix Asphalt (HMA).”<sup>(19)</sup> A summary of the relevant information in this database is shown in table 15.

**Table 15. Summary of  $E^*$ / data available in the WRI database.**

<b>Binder Code</b>	<b>No. of Mix Variations</b>	<b>Total No. of Tests</b>	<b>Temperature (°C)</b>	<b>Frequency (Hz)</b>	<b>Aging Condition</b>		
					<b>Plant or Unaged</b>	<b>STOA</b>	<b>LTOA or Field</b>
KS-1-Sinclair	4	4	4.4, 21.1, and 40	10, 1, 0.1, and 0.01	2		2
KS-2-Coastal	4	4			2		2
KS-3-Koch	4	4			2		2
KS-4-Royal	4	4			2		2
NV-1-Sinclair WY	2	2	4, 20, and 40	10, 5, 1, 0.5, 0.1, 0.05, and 0.01	1		1
NV-2-Crown	2	2			1		1
NV-3-Crown	2	2			1		1
NV-4-Crown	2	2			1		1
$\rho_{3/4}$		Maximum			9		
$\rho_{3/4}$		Minimum			1		
$\rho_{3/8}$		Maximum			40		
$\rho_{3/8}$		Minimum			14		
$\rho_4$		Maximum			50		
$\rho_4$		Minimum			32		
$\rho_{200}$		Maximum			6.6		
$\rho_{200}$		Minimum			4.2		
$V_a$		Maximum			7.4		
$V_a$		Minimum			6.6		
$V_{beff}$		Maximum			9.8		
$V_{beff}$		Minimum			6.4		
VMA		Maximum			17.2		
VMA		Minimum			13.4		
VFA		Maximum			57.4		
VFA		Minimum			47.1		

°C = (°F-32)/1.8

Note: Blank cells indicate data are unavailable in the database.

### 3.3.6 Citgo Mixture Database

The Citgo database consists of two mixtures fabricated with the same aggregate structure (0.4-inch (9.5-mm) Superpave™ mixture) but with different asphalt binders. Both STOA and LTOA were conducted on these mixtures. A summary of the mixture properties is presented in table 16. These two mixtures are included in NCHRP projects 9-25 and 9-31.<sup>(16,17)</sup> For this database, the modulus values were measured in accordance with the AASHTO TP-62 protocol, and the aging was conducted in accordance with AASHTO R30-02.<sup>(8,19)</sup>

**Table 16. Summary of  $|E^*|$  data available in the Citgo mixture database.**

Binder Code	No. of Mix Variations	Total No. of Tests	Temperature (°C)	Frequency (Hz)	Aging Condition		
					Plant or Unaged	STOA	LTOA or Field
Citgo-A	2	4	4, 20, and 40	10, 5, 1, 0.5, 0.1, 0.05, and 0.01		2	2
Citgo-B						2	2
$\rho_{3/4}$				0			
$\rho_{3/8}$				6			
$\rho_4$				50			
$\rho_{200}$				5.1			
$V_a$				4.3			
$V_{beff}$				11.5			
VMA				15.8			
VFA				72.6			

 $^{\circ}\text{C} = (\text{°F}-32)/1.8$ 

Note: Blank cells indicate data are unavailable in the database.

### 3.3.7 FHWA $M_R$ Database

Under the FHWA DTFH61-05-RA-00108 project, NCSU researchers tested a set of mixtures for both  $|E^*|$  and  $M_R$ .<sup>(14)</sup> The importance of this database is that it can be used to verify the predictive capabilities of the  $M_R$  ANN model. In total, seven different mixtures are included with two different asphalt binder types. The asphalt binders used for these mixtures are not part of the binder database. Because these mixtures are only used for the  $M_R$  ANN verification, the relevant information is different (see table 17). The designation for these mixes follows the NCDOT convention where the first letter represents either a surface mix (S) or a base mix (B). The second number represents the NMSA, and the final letter represents the gradation of fine (F), coarse (C), or flat and elongated (FE). The “M” on the last mix denotes that the binder was modified. Two of the study mixtures are derivations of the S12.5C mix in that only the asphalt content was changed by either  $\pm 1$  percent.

**Table 17. Summary of  $|E^*|$  data available in the  $M_R$  database.**

Mix	Percent $V_a$	Percent AC	Asphalt Grade
S12.5C	4	5.5	PG 64-22
S12.5C-AC+1	4	6.5	
S12.5C-AC-1	4	4.5	
S12.5FE	4	5.7	
S12.5F	4	4.8	
B25.0C	4	4.9	
S12.5CM	4	5.5	

### **3.3.8 LTPP Data**

Mixture and binder properties of AC layers on LTPP test sections at different aging conditions (i.e., original-, TFO/RTFO-, PAV-aged, and field-aged) were extracted from the LTPP database for use as inputs for the models developed as part of this study. The following list provides the criteria for selecting the layers to be considered in dynamic modulus estimates:<sup>(20)</sup>

- Layer thickness of 1 inch (25.4 mm) or greater as reported in the TST\_L05B table.
- Virgin or recycled hot mix, hot laid, and dense graded AC (i.e., MATL\_CODE 1 or 13 in the TST\_L05B table).
- Placed as an original layer, overlay layer, or AC layer below the surface (i.e., DESCRIPTION 1, 3, or 4 in the TST\_L05B table).

### **3.3.9 Input Source Hierarchy**

Many properties of interest for this project are available in multiple locations within the LTPP database. Because of this, the team established a hierarchy of data sources to extract information from the LTPP database. The following lists provide the priority used in extracting data (lower numbers denote higher priority) for each of the aging conditions. Included are the LTPP module and the specific table name for each data source.

Binder shear modulus and phase angle are as follows:<sup>(20)</sup>

#### **Original properties:**

1. TST module (TST\_AE07).
2. SPS module (SPS9\_SP\_PMA\_AC\_PROPERTIES).

#### **TFO/RTFO- and PAV-aged properties:**

1. TST module (TST\_AE07).
2. SPS module (SPS9\_SP\_PMA\_AC\_PROPERTIES).

#### **Field-aged properties:**

1. TST module (TST\_AE07).

Viscosity ring/ball, penetration, absolute viscosity, and kinematic viscosity are as follows:<sup>(20)</sup>

#### **Original properties:**

1. TST module (TST\_AE02/AE04/AE05).
2. SPS module (SPS?\_PMA\_AC\_PROPERTIES).

3. RHB module (RHB\_ACO\_PROP/HMRAP\_COMBINE\_AC).
4. INV module (INV\_PMA ASPHALT).

**TFO/RTFO and PAV-aged properties:**

1. RHB module (RHB\_ACO\_LABAGED\_AC/HMRAP\_LABAGED\_AC).
2. INV module (INV\_PMA ASPHALT).

**Field-aged properties:**

1. TST module (TST\_AE02/AE04/AE05).

Volumetrics-VMA, VFA,  $V_a$ , theoretical maximum specific gravity ( $G_{mb}$ ), and bulk specific gravity ( $G_{mm}$ ) are as follows:<sup>(20)</sup>

**Original-, TFO/RTFO-, and PAV-aged properties:**

1. SPS module (SPS\_PMA\_MIXTURE\_PROP) (as-placed).
2. RHB module (RHB\_ACO\_MIX\_PROP/HMRAP\_MIX\_PROP) (as-placed).
3. INV module (INV\_PMA\_ORG\_MIX).

**Field-aged properties:**

1. TST module (TST\_AC02/AC03).

$M_R$  is as follows:<sup>(20)</sup>

**Field-aged:**

1. TST module (TST\_AC07).

### **3.3.10 Data Structure and Detail**

Table 18 provides the location within the LTPP database where the information was extracted and a summary of the data utilized in this project.

**Table 18. Summary of extracted LTPP data.**

<b>Field Name</b>	<b>Description</b>
STATE_CODE	Code representing State or province
PROJECT_ID	SHRP_ID for GPS sections and PROJECT_ID for SPS sections
PROJECT_LAYER	Project layer code as established in TST_LO5B for SPS sections; layer code as established in TST_LO5B for GPS sections <sup>(20)</sup>
CONSTRUCTION_DATE	Date layer was constructed
SAMPLE_TYPE	1—original binder, 2—lab-aged (TFO/RTFO), 3—lab-aged (PAV), and 4—field-aged
GSTAR_SAMPLE_DATE	Date of  G*  sampling (if field-aged sample)
GSTAR_1	Binder complex modulus at temperature 1
PHASE_ANGLE_1	Phase angle at temperature 1
GSTAR_TEMP_1	Binder complex modulus at temperature 1
GSTAR_2	Binder complex modulus at temperature 2
PHASE_ANGLE_2	Phase angle at temperature 2
GSTAR_TEMP_2	Binder complex modulus at temperature 2
GSTAR_3	Binder complex modulus at temperature 3
PHASE_ANGLE_3	Phase angle at temperature 3
GSTAR_TEMP_3	Binder complex modulus at temperature 3
GSTAR_4	Binder complex modulus at temperature 4
PHASE_ANGLE_4	Phase angle at temperature 4
GSTAR_TEMP_4	Binder complex modulus at temperature 4
GSTAR_5	Binder complex modulus at temperature 5
PHASE_ANGLE_5	Phase angle at temperature 5
GSTAR_TEMP_5	Binder complex modulus at temperature 5
GSTAR_6	Binder complex modulus at temperature 6
PHASE_ANGLE_6	Phase angle at temperature 6
GSTAR_TEMP_6	Binder complex modulus at temperature 6
GSTAR_SOURCE	LTPP module from which binder complex modulus was extracted (i.e., TST = testing, RHB = rehabilitation, SPS = SPS construction, INV = inventory, and CALC = calculated)
BINDER_SAMPLE_DATE	Date of binder sampling (if field-aged sample)
RING BALL	Ring/ball (°F) results
RING BALL_SOURCE	LTPP module from which ring and ball was extracted (i.e., TST = testing, RHB = rehabilitation, SPS = SPS construction, INV = inventory, and CALC = calculated)
PENETRATION_39.2F	Penetration at 39.2 °F
PENETRATION_39.2F_SOURCE	LTPP module from which penetration at 39.2 °F was extracted (i.e., TST = testing, RHB = rehabilitation, SPS = SPS construction, INV = inventory, and CALC = calculated)
PENETRATION_77F	Penetration at 77 °F
PENETRATION_77F_SOURCE	LTPP module from which penetration at 77 °F was extracted (i.e., TST = testing, RHB = rehabilitation, SPS = SPS construction, INV = inventory, and CALC = calculated)
PENETRATION_115F	Penetration at 115 °F

PENETRATION_115F_SOURCE	LTPP module from which penetration at 115 °F was extracted (i.e., TST = testing, RHB = rehabilitation, SPS = SPS construction, INV = inventory, and CALC = calculated)
ABSOLUTE_VISCOSITY	Absolute viscosity at 140 °F (poises)
ABSOLUTE_VISCOSITY_SOURCE	LTPP module from which absolute viscosity was extracted (i.e., TST = testing, RHB = rehabilitation, SPS = SPS construction, INV = inventory, and CALC = calculated)
KINEMATIC_VISCOSITY	Kinematic viscosity at 275 °F (centistokes)
KINEMATIC_VISCOSITY_SOURCE	LTPP module from which kinematic viscosity was extracted (i.e., TST = testing, RHB = rehabilitation, SPS = SPS construction, INV = inventory, and CALC = calculated)
VMA	Voids in mineral aggregate
VMA_SOURCE	LTPP module from which VMA was extracted (i.e., TST = testing, RHB = rehabilitation, SPS = SPS construction, INV = inventory, and CALC = calculated)
VFA	Voids filled with asphalt
VFA_SOURCE	LTPP module from which VFA was extracted (i.e., TST = testing, RHB = rehabilitation, SPS = SPS construction, INV = inventory, and CALC = calculated)
AIR_VOID_SAMPLE_DATE	Date of air void sampling (if field-aged sample)
AIR_voids	Percent air voids
AIR_voids_SOURCE	LTPP module from which air voids was extracted (i.e., TST = testing, RHB = rehabilitation, SPS = SPS construction, INV = inventory, and CALC = calculated)
GMB	Bulk specific gravity of the mix
GMB_SOURCE	LTPP module from which bulk specific gravity was extracted ((i.e., TST = testing, RHB = rehabilitation, SPS = SPS construction, INV = inventory, and CALC = calculated))
GMM	Maximum specific gravity
GMM_SOURCE	LTPP module from which maximum specific gravity was extracted (i.e., TST = testing, RHB = rehabilitation, SPS = SPS construction, INV = inventory, and CALC = calculated)
MR_SAMPLE_DATE	Date of resilient modulus sampling (if field-aged sample)
MR_5	Resilient modulus at 5 °C
MR_25	Resilient modulus at 25 °C
MR_40	Resilient modulus at 40 °C
MR_SOURCE	LTPP module from which resilient modulus was extracted (i.e., TST = testing, RHB = rehabilitation, SPS = SPS construction, INV = inventory, and CALC = calculated)
BINDER_GRADE	Binder grade information (only populated for RTFO data)

°C = (°F-32)/1.8

For GPS projects, each layer is specific to one test section. As such, the data utilized from the LTPP database are section-specific. However, for SPS projects, the same materials were used in the construction of many test sections on one SPS project. Inputs for these SPS projects were computed as the average of the layer over the entire SPS project. Therefore,  $|E^*|$  estimates were developed for each PROJECT\_LAYER\_CODE (as reported in the TST\_LO5B table) and reported as project-level data.<sup>(20)</sup> For SPS projects that were linked to GPS test sections, priority was given to data from the SPS project. If those data were not available, the SPS records were populated with data from the corresponding GPS test section.

In some cases, the AC layers were sampled and tested multiple times and at varying ages. If test results were available from multiple sample dates,  $|E^*|$  was computed for each sample date. The corresponding age was calculated and included with the data.

$V_a$  for field-aged samples are not directly available in the LTPP database; therefore, the following equation was used to calculate air voids from bulk- and maximum-specific gravities measured from field samples:

$$V_a = \left(1 - \frac{G_{mb}}{G_{mm}}\right) * 100\% \quad (14)$$

Where:

$V_a$  = Air voids (percent).

$G_{mb}$  = Bulk specific gravity.

$G_{mm}$  = Maximum specific gravity.

In addition, because VFA information is not available directly in the LTPP database, the following equation was used to compute VFA:

$$VFA = \left(1 - \frac{V_a}{VMA}\right) * 100\% \quad (15)$$

## 4.0 EVALUATION OF $|E^*|$ /PREDICTIVE MODELS

ANNs are used to solve problems in the asphalt pavement field with the primary application being the backcalculation of pavement layer moduli from falling weight deflectometer measurements.<sup>(21-23)</sup> This method has also been applied successfully to assess the roughness progression in flexible pavements and to analyze the surface wave data obtained from the nondestructive testing of asphalt pavements.<sup>(24,25)</sup> An often cited drawback of these approaches is their inability to extrapolate when a situation arises that is beyond that used to train the ANNs. To overcome this shortcoming, it is important that the dataset used to train the ANNs covers the entire range of conditions expected to be encountered during use. The objective of this study is to show that ANN modeling techniques can be applied to predict  $|E^*|$  values of AC to a higher degree of accuracy than currently available models using the same input parameters.

### 4.1 ANN STRUCTURE USED IN THIS STUDY

A preliminary study was conducted to determine the feasibility and predictability of the ANN modeling technique relative to the existing models. This feasibility study was first conducted based on  $|G^*|$  because more closed-form models exist that use this parameter as their primary input parameter. The ANN models used in this preliminary study are not the final models suggested by the research team, but they are similar in form and validation. To ensure full coverage of the expected conditions, the most recent Witczak database with available measured  $|G^*|$  data and a portion of the dataset obtained at NCSU with support from the NCDOT were utilized as the TP-62 training database. Also, appropriate portions of the FHWA mobile trailer database and the WRI database (from the Kansas and Nevada sites) were considered the AMPT training database. A combination of the AMPT and TP-62 databases has been used to train the network after investigations, which are summarized in appendix C of this report.

The ANN model developed herein contains a mapping ANN architecture and is based on supervised learning. In the developed network, the learning method is a feed forward back propagation, which is one of the best known types of ANN. The sigmoidal function was chosen as the transfer function. The three-layer network was selected as the best network configuration. The first two layers consist of 12–14 nodes based on the different cases studied for the development of the models.

To evaluate the goodness of fit in arithmetic scale,  $|E^*|$  is considered to be the dependent variable, and the error is given as follows:

$$\text{Sum of Squared Error, } SSE_{\text{normal}} = \sum \left[ |E^*|_{\text{predicted}} - |E^*|_{\text{measured}} \right]^2 \quad (16)$$

$Sy$  is defined as the standard deviation of the measured  $|E^*|$  values. To evaluate the goodness of fit in logarithmic scale, the dependent variable is the log ( $|E^*|$ ), and the error is as follows:

$$\text{Sum of Squared Error, } SSE_{\log} = \sum \left[ \log(|E^*|_{\text{predicted}}) - \log(|E^*|_{\text{measured}}) \right]^2 \quad (17)$$

$Sy$  is defined as the standard deviation of the measured  $\log(|E^*|)$  values. The standard error is defined as follows:

$$\text{Standard Error, } Se = \sqrt{\frac{SSE}{n-1}} \quad (18)$$

Where:

$n$  = Number of observations.

## 4.2 EVALUATION OF BINDER $|G^*|$ -BASED MODELS

A literature review of current versions of the modified Witczak and Hirsch models showed that these two models have high goodness-of-fit statistics for their original training databases of 7,400 and 206 data points, respectively. (See references 11, 5, 12, 6, 7, and 13.) The literature purports high correlation coefficients and small errors of  $R^2 = 0.80$  and  $Se/Sy = 0.45$  in arithmetic scale,  $R^2 = 0.90$  and  $Se/Sy = 0.32$  in logarithmic scale for the modified Witczak model, and  $R^2 = 0.98$  in logarithmic scale for the Hirsch model. The developers of the Hirsch model report only the logarithmic-based  $R^2$  value.

These results demonstrate that the goodness-of-fit for each model is dependent on the number of observations or the width of the range of the different variables considered in the development of each model. The deterioration of the statistical parameters when these models are applied to some expanded and independent databases is not entirely unexpected given the nature of regression models. Additional insight is gained by examining line-of-equality (LOE) plots for each of the models in both arithmetic and logarithmic scales.

In this section, the existing models (including the modified Witczak, Hirsch, and Al-Khateeb models) are evaluated along with the two ANNs using the verification databases shown in figure 7 through figure 16. Also, figure 17 through figure 28 show predictions of the  $|E^*|$  values from the verification databases using the different models. The first observation is that the Al-Khateeb model exhibits a significant bias (i.e., a power trend between the predicted  $|E^*$  and the measured  $|E^*$  values) in all the predictions. This finding is not entirely unexpected given the limited database used in calibrating the model. However, due to the bias relative to the other two existing models, it was decided that this model would be eliminated from consideration in any future analysis. It should be noted that the scales in figure 7 through figure 28 vary to provide the greatest clarity in the data.

The Hirsch model behaves in a reasonable fashion, although it exhibits undesirable behavior at low  $|E^*|$  values in the LOE graphs shown in figure 9 and figure 10. When the prediction is good, the expectation is that a group of data points following the LOE with an oval shape in the LOE graph would be seen. However, the Hirsch predictions shown in figure 9 and figure 10 exhibit a horizontal pattern amplified in the bottom left side of the log-log LOE graph. This undesirable pattern in the Hirsch model predictions is related to the insensitivity of the model and its inability to distinguish the performance differences among different mixtures for a given set of environmental and other conditions.<sup>(26)</sup> This issue is discussed later in this section.

The developers of the Hirsch model note that during initial development, substantial errors occurred when predictions were made at extremely high and low modulus values. The authors of the model attempted to correct this issue in subsequent efforts by expanding the calibration database to include 15.8 and 129.2 °F (-9 and 54 °C) data.<sup>(6)</sup> However, it is unclear if such efforts succeeded in reducing potential prediction errors because the authors did not have access to and/or show a large enough verification database. Regardless of this potential model shortcoming, predictions were made for the complete range of temperatures that a typical user is likely to apply to the model (i.e., 14 to 129.2 °F (-10 to 54 °C)). For an independent and expanded database, it appears that the Hirsch model developers, with their available dataset, were not able to completely address the original shortcomings of their model because plateau areas appear at the high and low modulus values, as shown in figure 9, figure 10, figure 19, figure 20, figure 23, figure 24, figure 27, and figure 28. The undesirable pattern in the Hirsch model predictions at low modulus values (high temperatures) is related to the insensitivity of the model to the changes in volumetric parameters. Errors at the low temperature of 14 °F (-10 °C) (high modulus values) are caused by the model having a limited modulus of approximately 3,500,000 psi (24,115,000 kPa) even though values higher than this are often measured in the laboratory at 14 °F (-10 °C). These drawbacks raise concerns over the use of the Hirsch model for the prediction of modulus values over the complete range needed for the MEPDG input. However, it will be shown later that the parameters on which this model is based seem to be promising and adequate for consideration in predicting the  $|E^*|$  values using the ANN model.

The modified Witczak model shows a larger scatter than the ANN models. The performance of the modified Witczak model in all the databases presented in figure 7 and figure 8 indicates that this model tends to overestimate the measured  $|E^*|$  values over the entire range, particularly at the extreme modulus values. It is believed that this effect is due to the aforementioned use of inappropriate  $|G^*|$  values at temperatures less than or equal to 39.9 °F (4.4 °C) (overestimation at high modulus values) and the use of  $|E^*|$  values at higher than recommended strain levels (overestimation at low modulus values). The modified Witczak predictions also tend to have a bias at high temperatures relating to insensitivity to volumetric changes and the inability of this model to clearly capture these differences.<sup>(26)</sup>

The prediction of the Citgo  $|E^*|$  data is presented in figure 25 through figure 28. It should be noted that the binder data at 39.2 °F (4 °C) are extrapolated from the CAM model more so than other binders in the database. For predictions of both aging conditions, the model inputs are the same, which causes the slight horizontal pattern. For this dataset, figure 25 through figure 28 show that the ANN-based  $|E^*|$  predictions are more erratic compared to the modified Witczak and Hirsch models. It is believed that this dataset was used in the calibration of the Hirsch model. As a result, it is somewhat unfair to compare the predictions using this model. After a careful exploration of the training dataset, it was found that mixtures that have similar  $|G^*|$  values at 39.2 °F (4 °C) and have similar volumetric properties also have higher measured  $|E^*|$  values than the Citgo mixtures. It was also found that these similar mixtures are coarse gradations, whereas the Citgo mixtures are finely graded. For this reason, the ANN models are capable of finding differences between these mixtures. However, including only the modified Witczak volumetric parameters causes model confusion at the low modulus values and, hence, the observed variability. The reason this variability shows so clearly with the Citgo mixture is likely due to the close similarity of it with mixtures in the training database. To address this issue thoroughly, new parameters that better represent the relative effects of the gradation and

volumetric properties may need to be identified. This effort is beyond the scope of this current project.

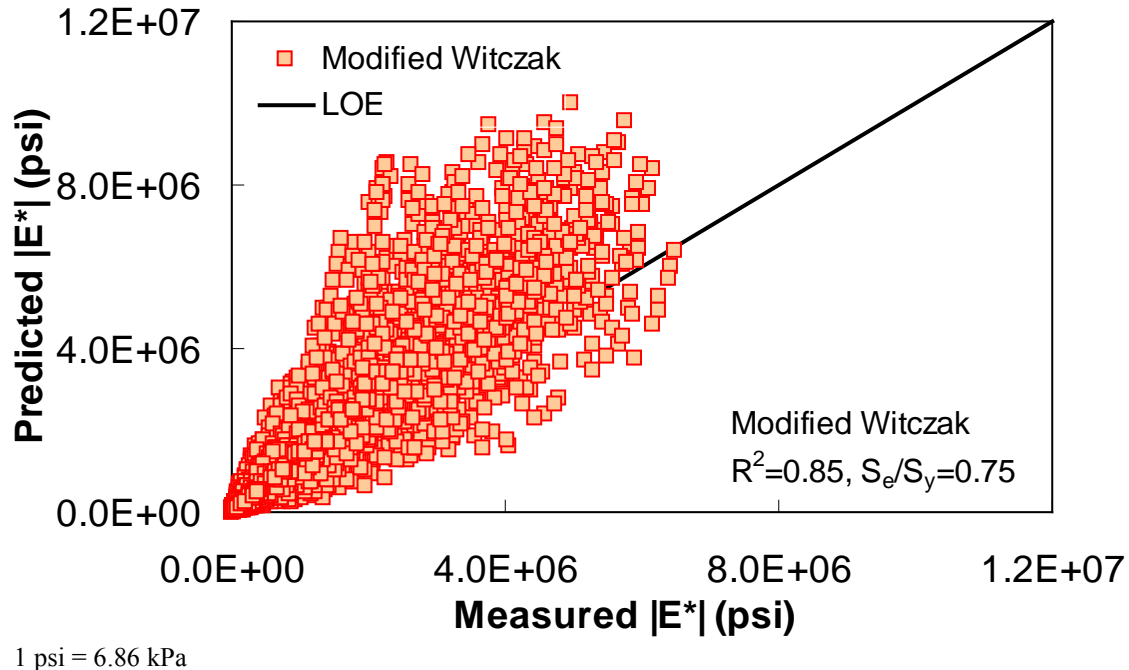


**Figure 7. Graph. Prediction of the processed Witczak, FHWA I, FHWA II, NCDOT I, NCDOT II, WRI, and Citgo databases using the modified Witczak in arithmetic scale.**

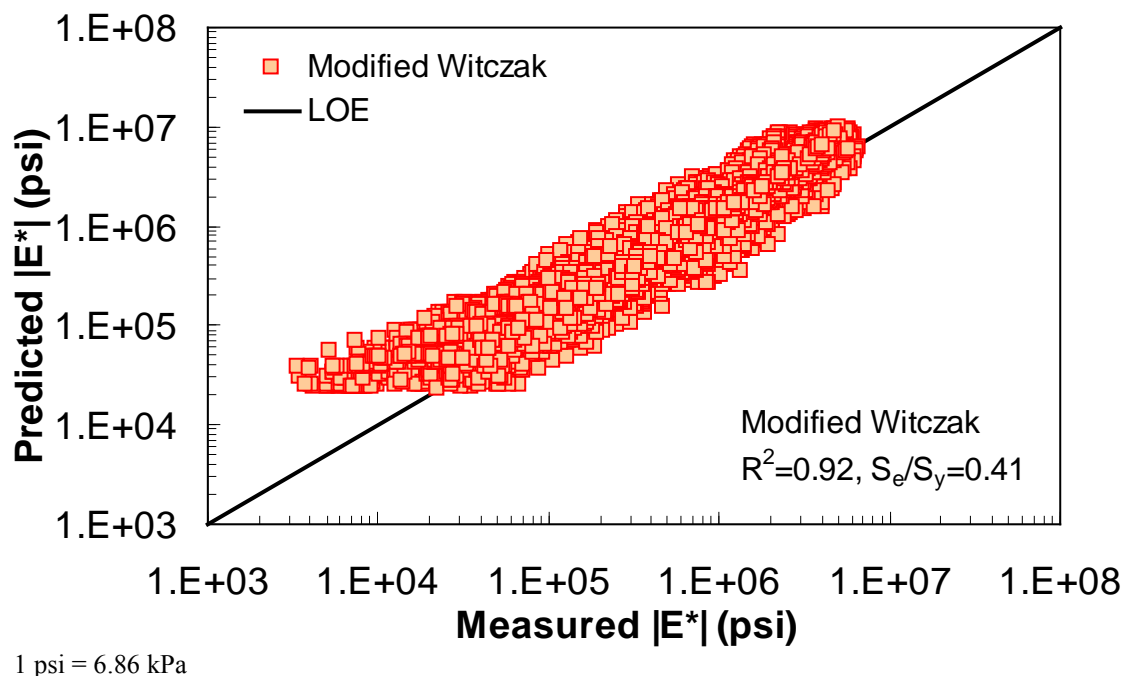


**Figure 8. Graph. Prediction of the processed Witczak, FHWA I, FHWA II, NCDOT I, NCDOT II, WRI, and Citgo databases using the modified Witczak in logarithmic scale.**

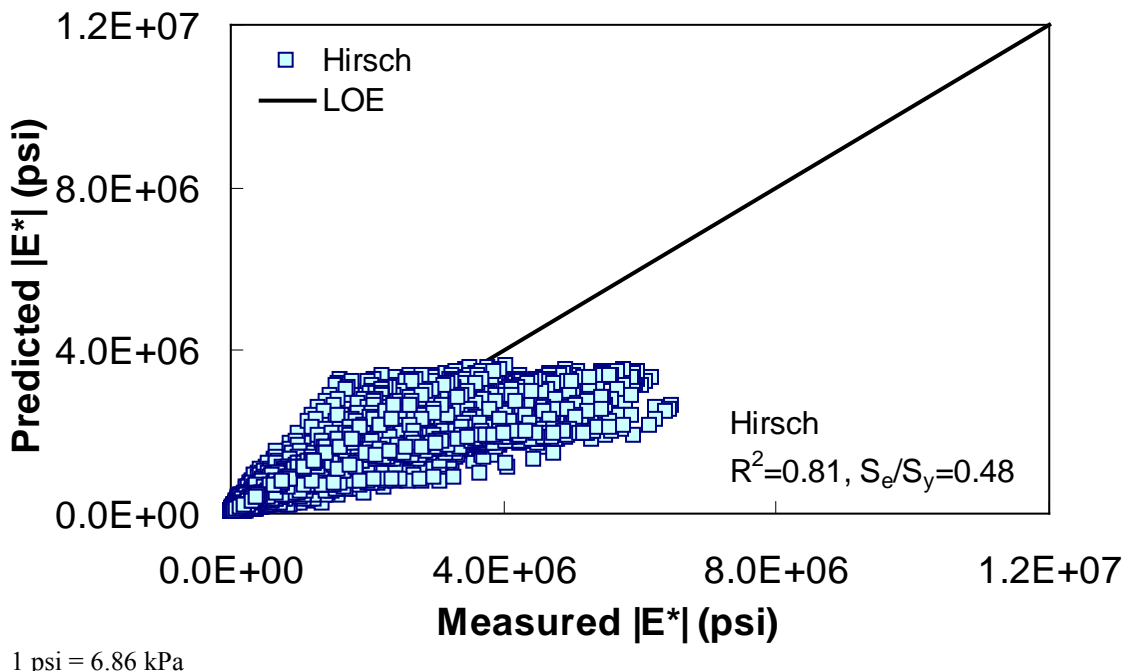


**Figure 9. Graph. Prediction of the processed Witczak, FHWA I, FHWA II, NCDOT I, NCDOT II, WRI, and Citgo databases using the Hirsch model in arithmetic scale.**

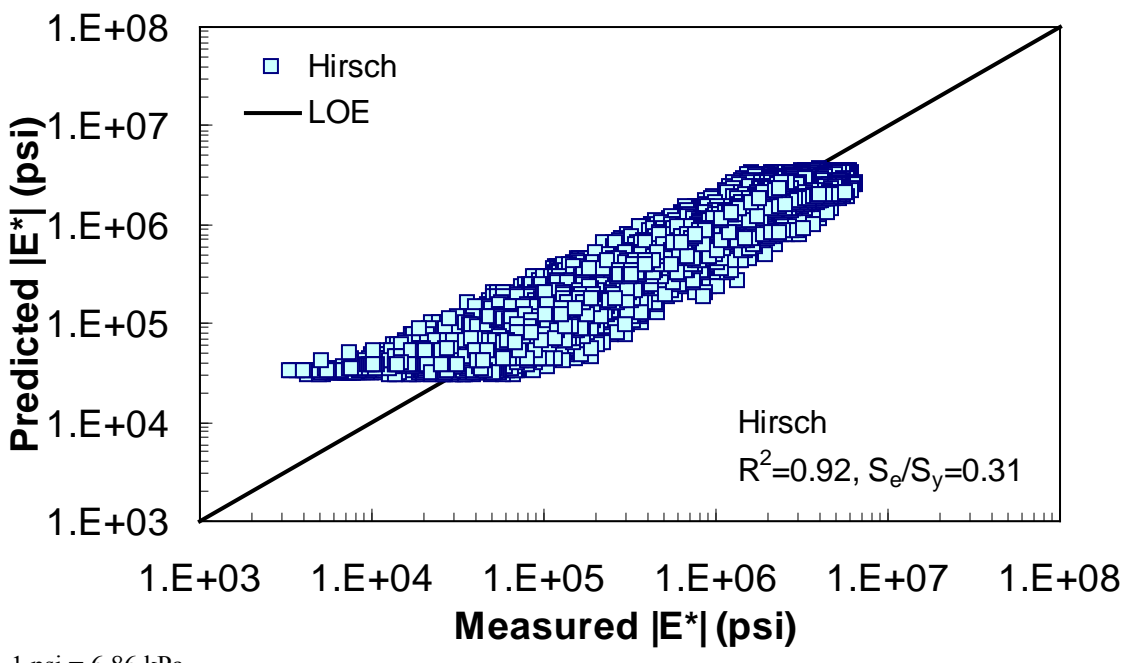


**Figure 10. Graph. Prediction of the processed Witczak, FHWA I, FHWA II, NCDOT I, NCDOT II, WRI, and Citgo databases using the Hirsch model in logarithmic scale.**

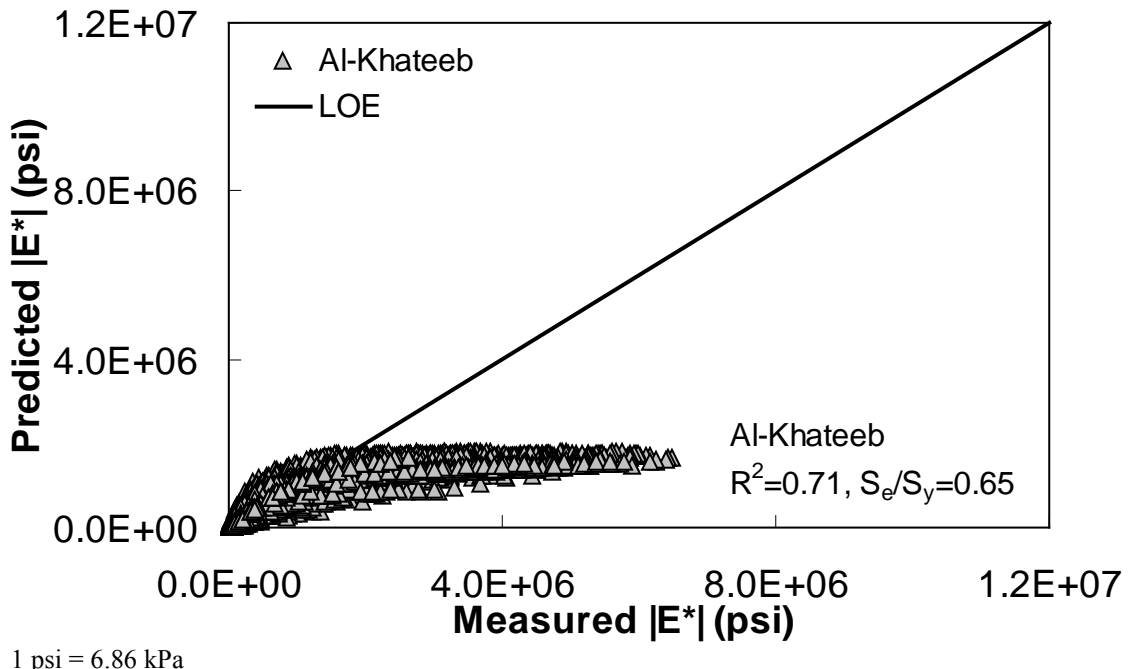


**Figure 11.** Graph. Prediction of the processed Witczak, FHWA I, FHWA II, NCDOT I, NCDOT II, WRI, and Citgo databases using the Al-Khateeb model in arithmetic scale.

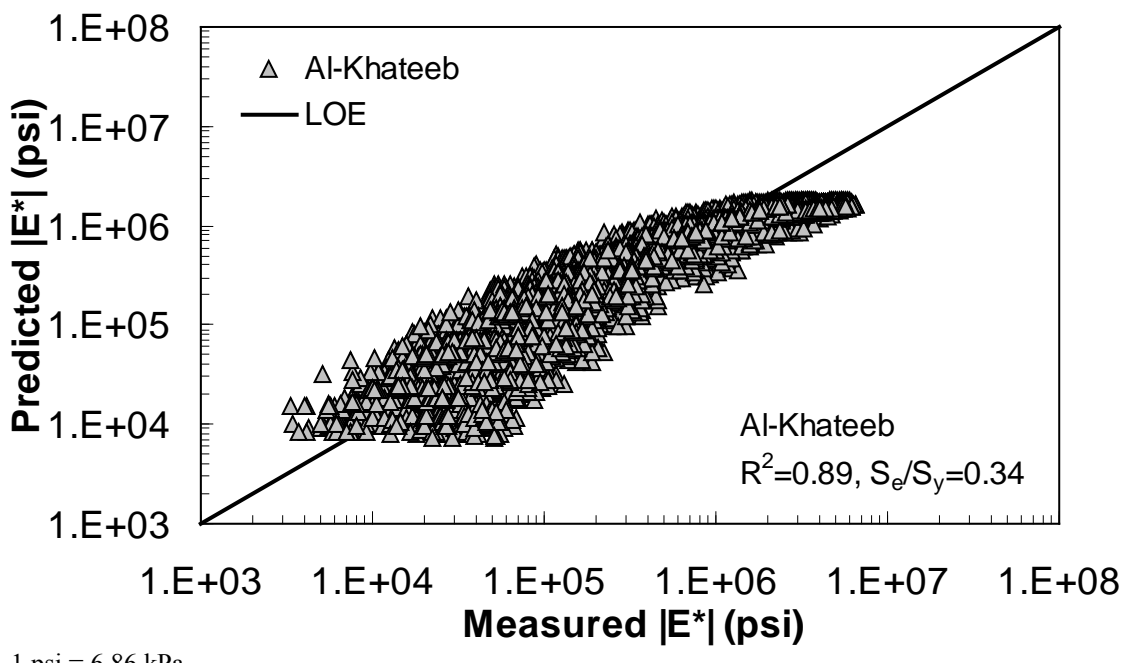


**Figure 12.** Graph. Prediction of the processed Witczak, FHWA I, FHWA II, NCDOT I, NCDOT II, WRI, and Citgo databases using the Al-Khateeb model in logarithmic scale.

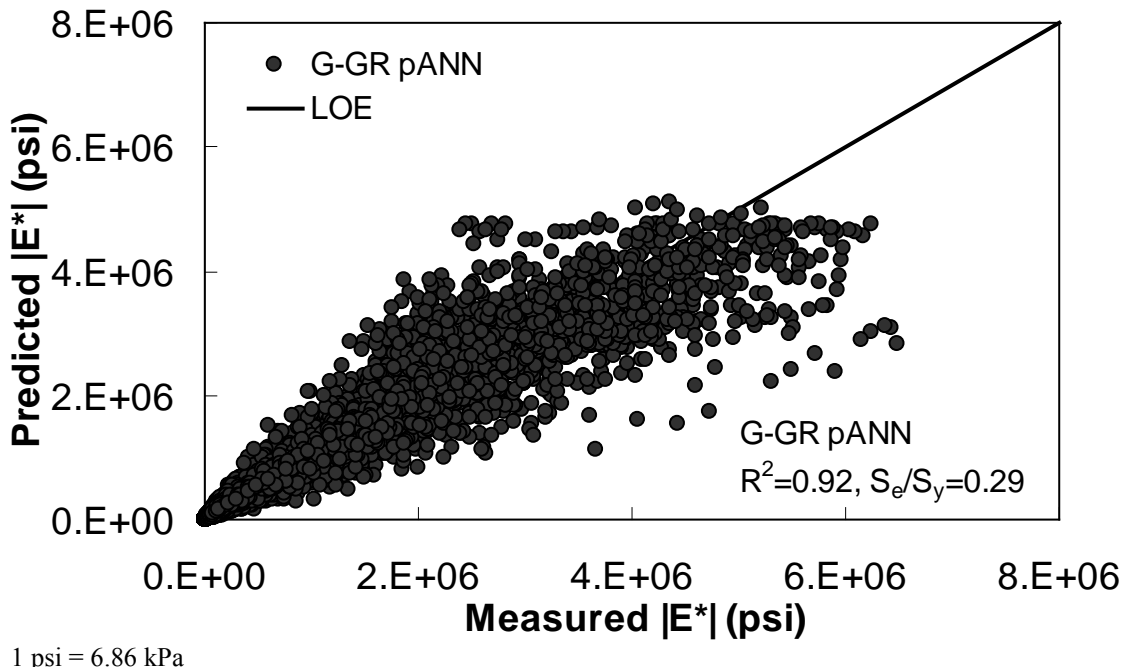


**Figure 13.** Graph. Prediction of training data containing processed Witczak, FHWA I, NCDOT I, and WRI databases using  $|G^*|$  binder and gradation-based pilot ANN model (G-GR pANN) in arithmetic scale.

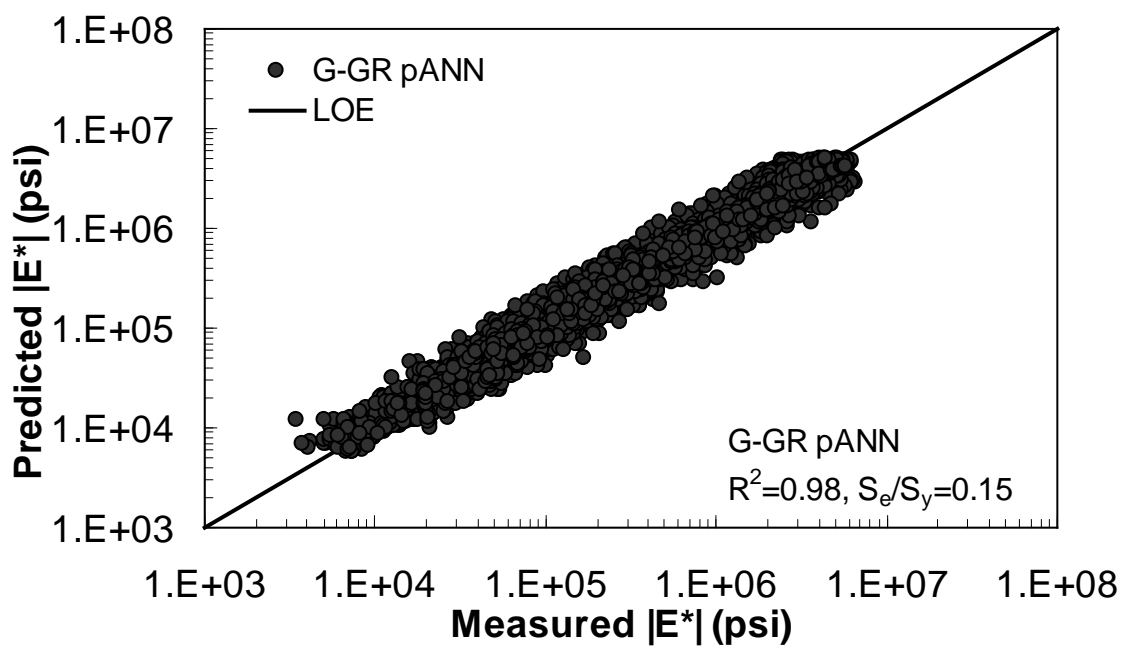
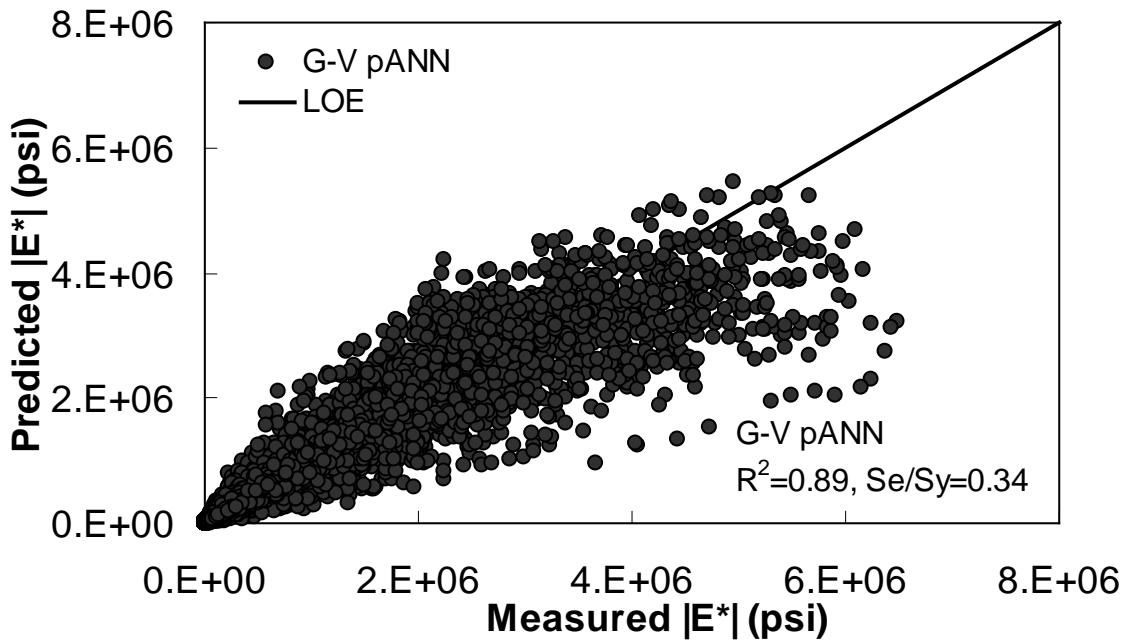
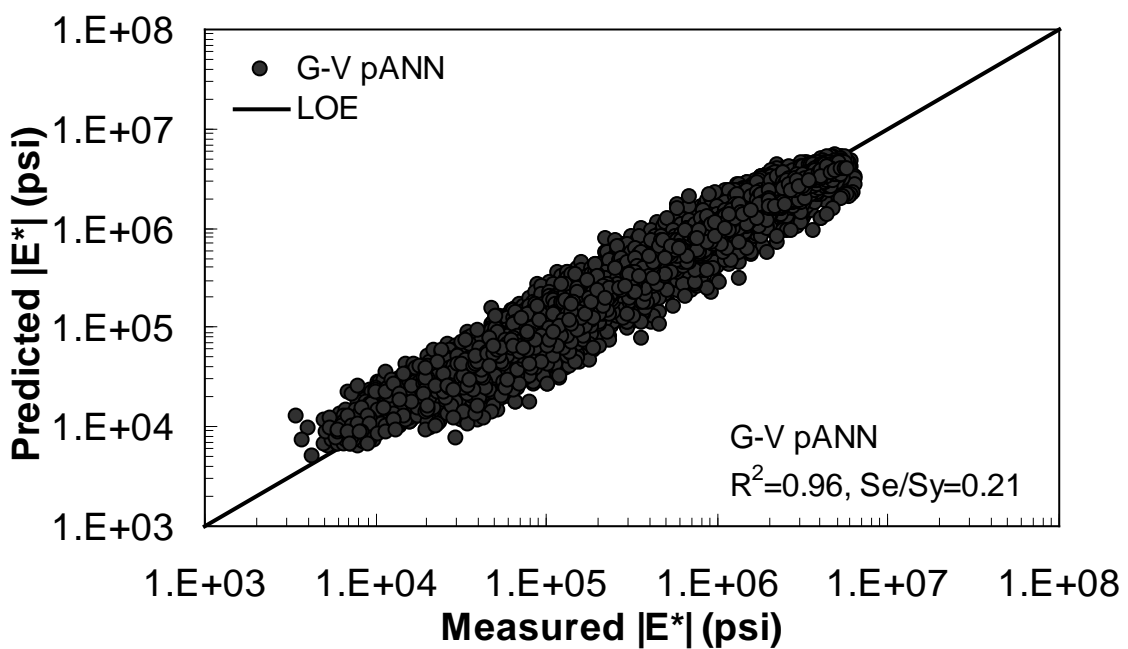


**Figure 14.** Graph. Prediction of training data containing processed Witczak, FHWA I, NCDOT I, and WRI databases using G-GR pANN in logarithmic scale.



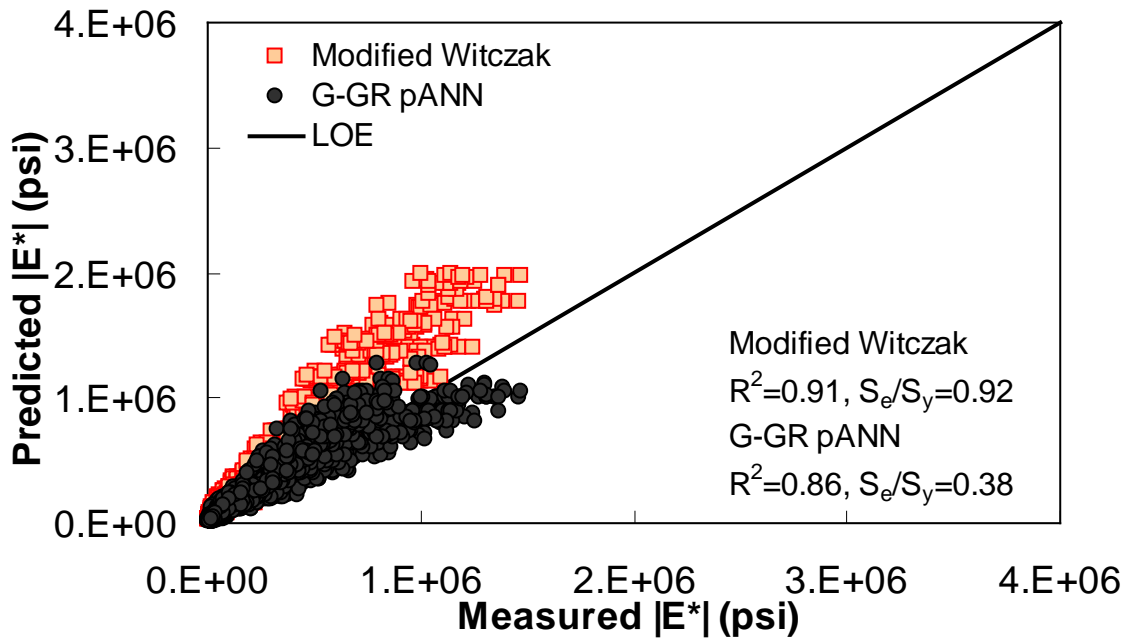
1 psi = 6.86 kPa

**Figure 15.** Graph. Prediction of training data containing processed Witczak, FHWA I, NCDOT I, and WRI databases using preliminary  $|E^*|$ -based models used in phase I of the study (G-V) pANN in arithmetic scale.



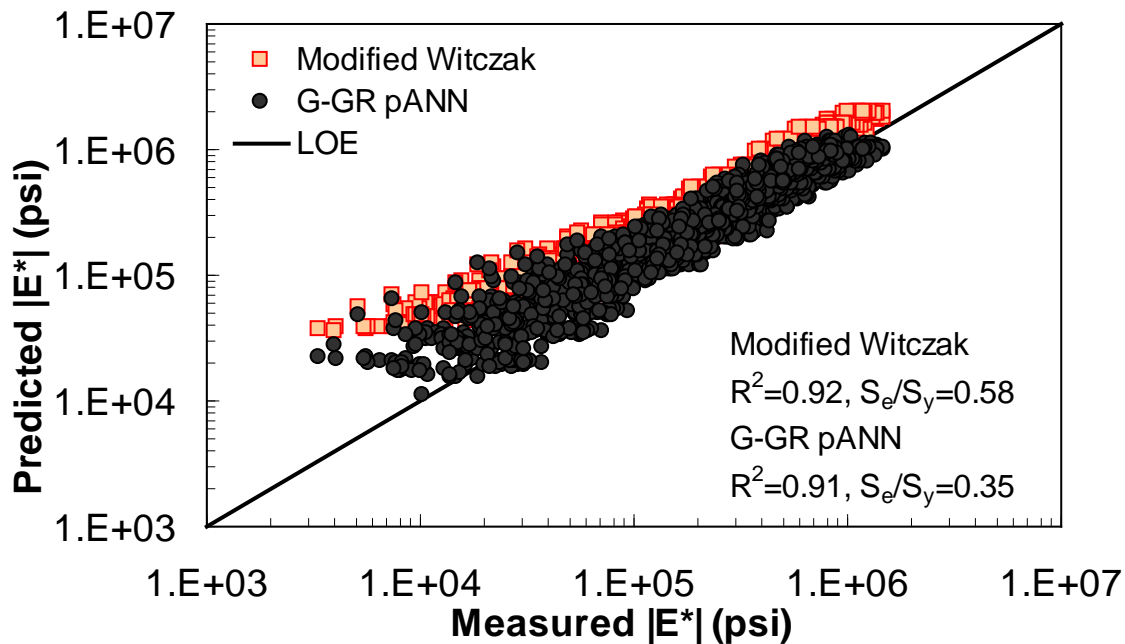
1 psi = 6.86 kPa

**Figure 16.** Graph. Prediction of training data containing processed Witczak, FHWA I, NCDOT I, and WRI databases using G-V pANN in logarithmic scale.



1 psi = 6.86 kPa

**Figure 17. Graph.** Predicted moduli using G-GR pANN and modified Witczak models for the FHWA II database in arithmetic scale.



1 psi = 6.86 kPa

**Figure 18. Graph.** Predicted moduli using G-GR pANN and modified Witczak models for the FHWA II database in logarithmic scale.

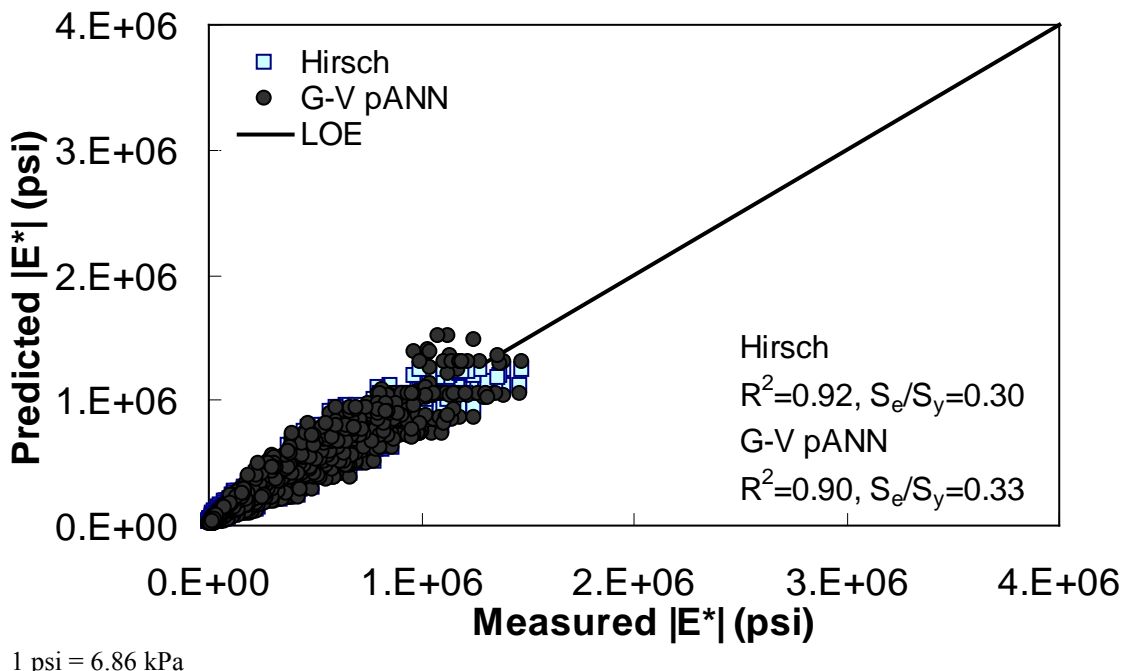


**Figure 19. Graph. Predicted moduli using G-V pANN and Hirsch models for the FHWA II database in arithmetic scale.**

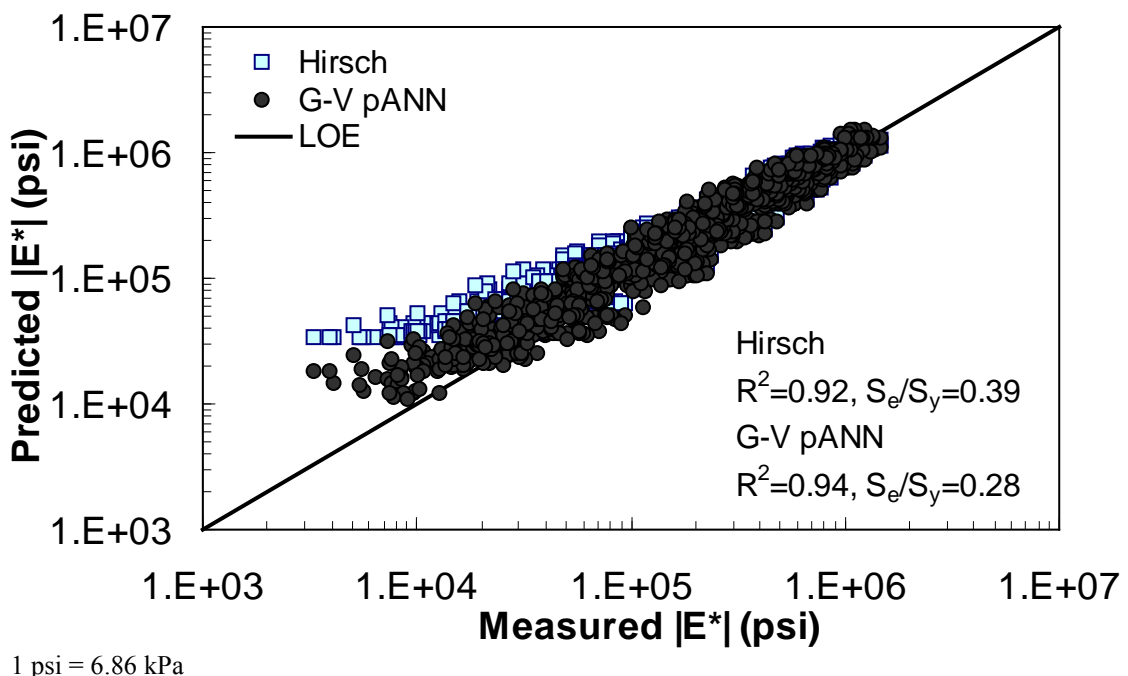


**Figure 20. Graph. Predicted moduli using G-V pANN and Hirsch models for the FHWA II database in logarithmic scale.**

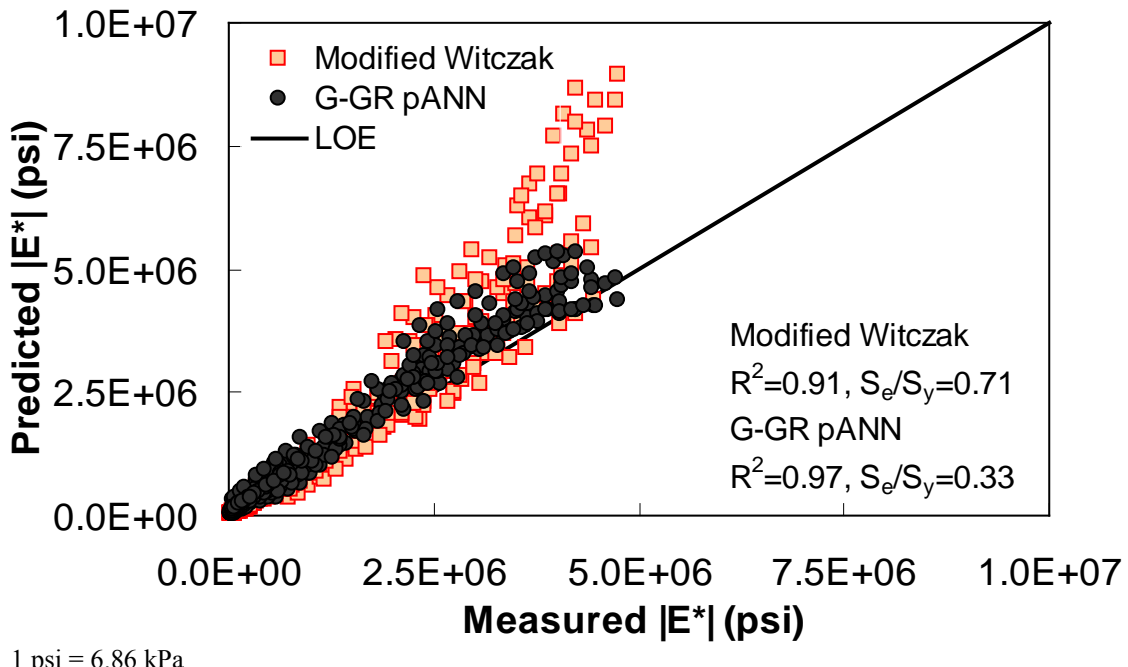


**Figure 21. Graph. Predicted moduli using G-GR pANN and modified Witczak models for the NCDOT II database in arithmetic scale.**

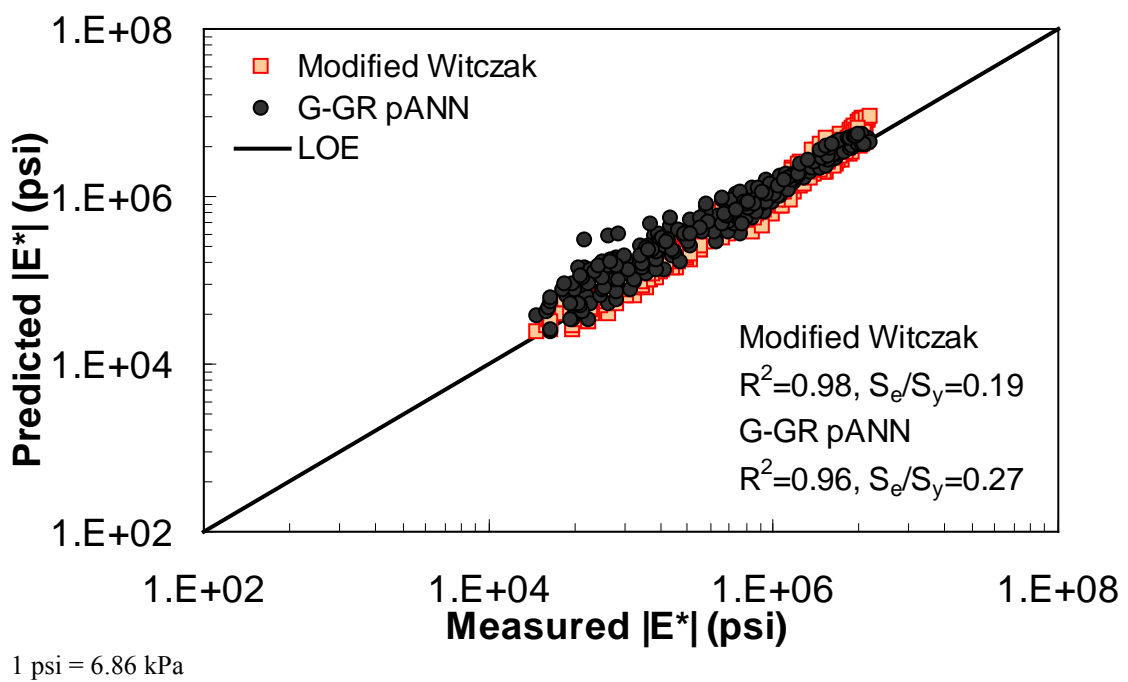


**Figure 22. Graph. Predicted moduli using G-GR pANN and modified Witczak models for the NCDOT II database in logarithmic scale.**

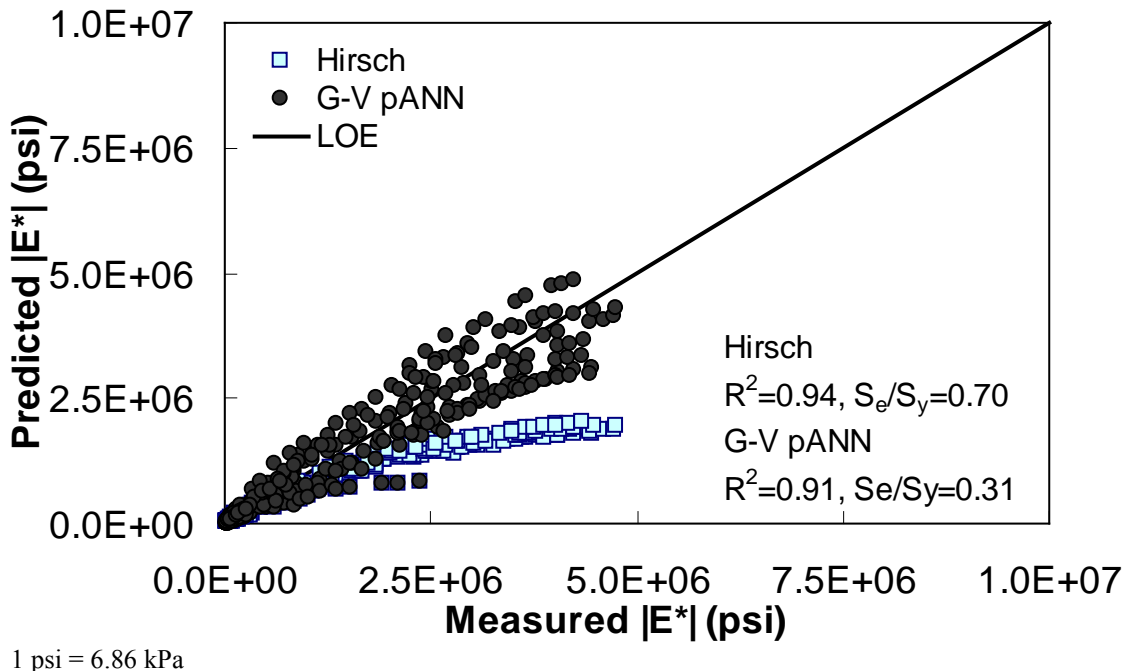


**Figure 23. Graph. Predicted moduli using G-V pANN and Hirsch models for the NCDOT II database in arithmetic scale.**

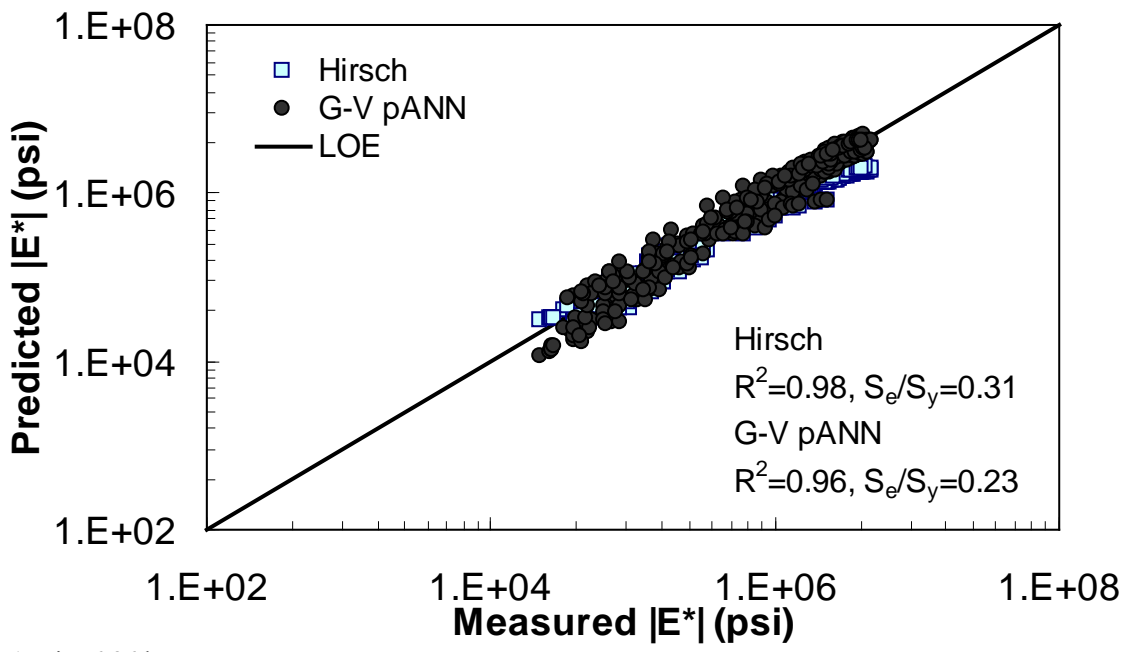
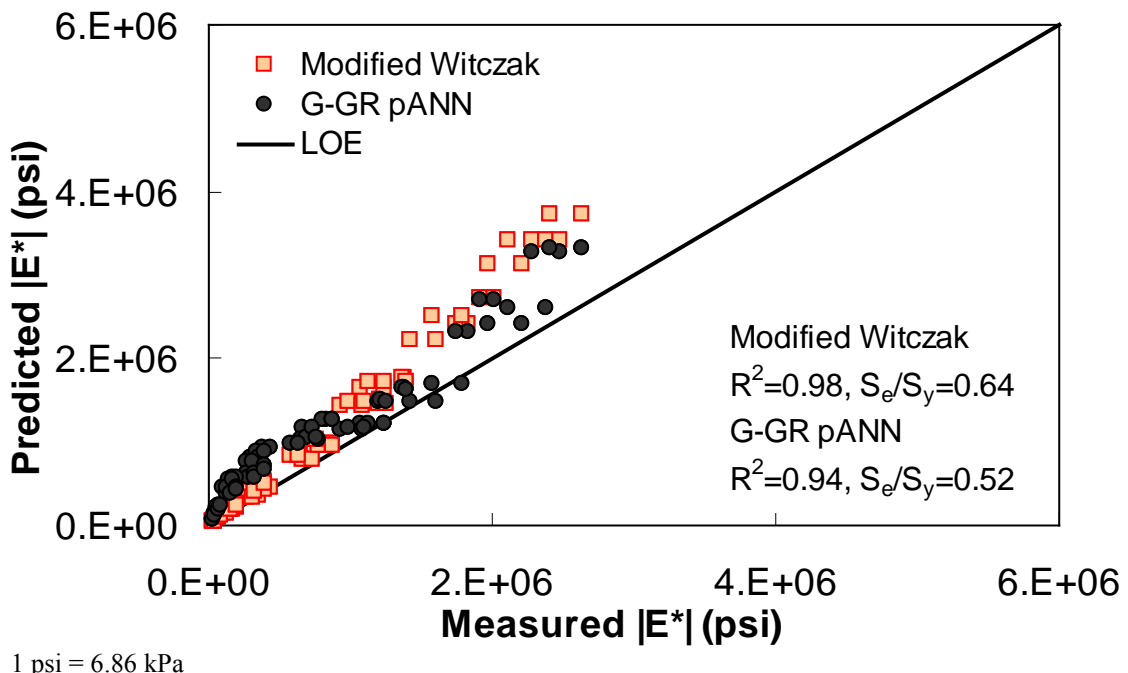
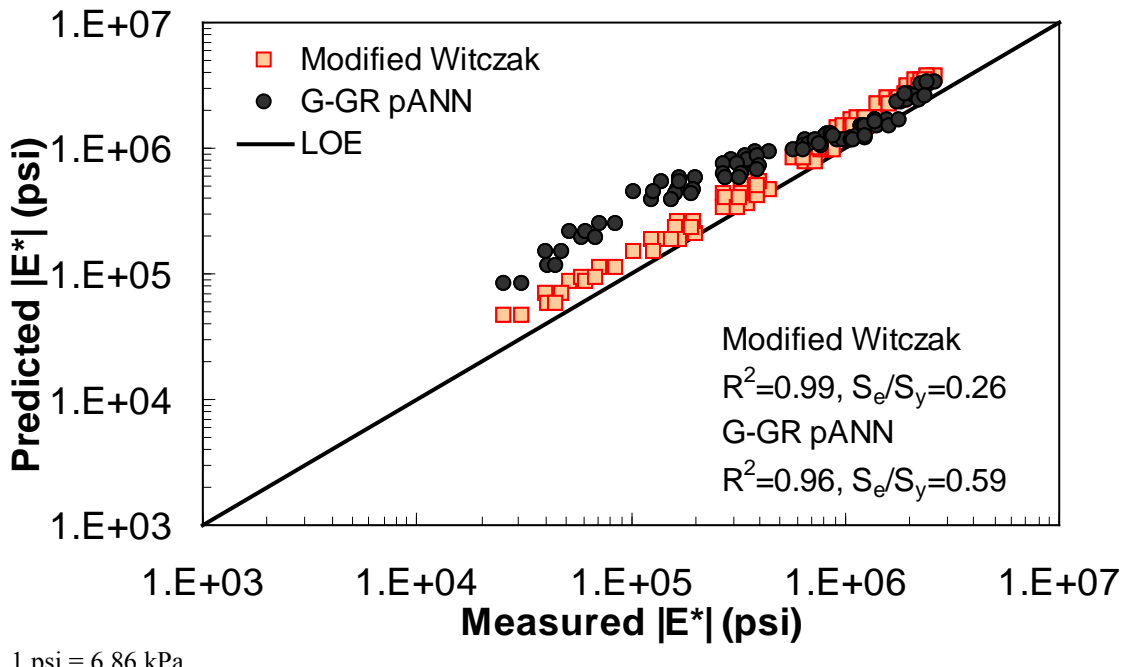


**Figure 24. Graph. Predicted moduli using G-V pANN and Hirsch models for the NCDOT II database in logarithmic scale.**



1 psi = 6.86 kPa

**Figure 25. Graph. Predicted moduli using G-GR pANN and modified Witczak models for the Citgo database in arithmetic scale.**



1 psi = 6.86 kPa

**Figure 26. Graph. Predicted moduli using G-GR pANN and modified Witczak models for the Citgo database in logarithmic scale.**

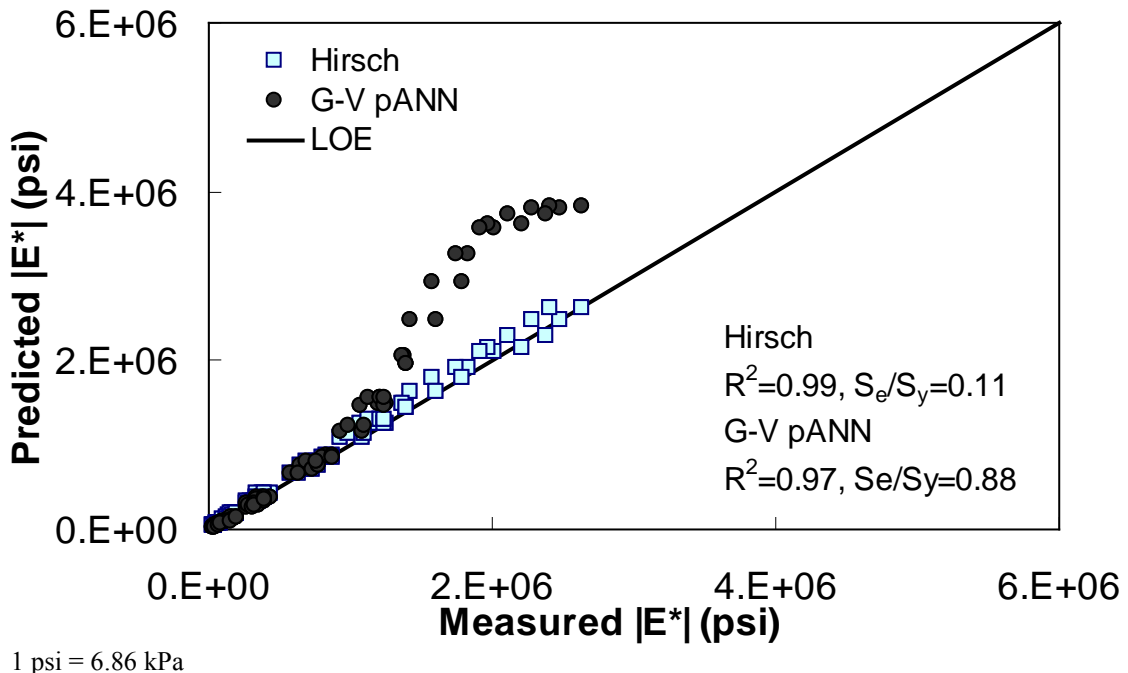


**Figure 27. Graph. Predicted moduli using G-V pANN and Hirsch models for the Citgo database in arithmetic scale.**

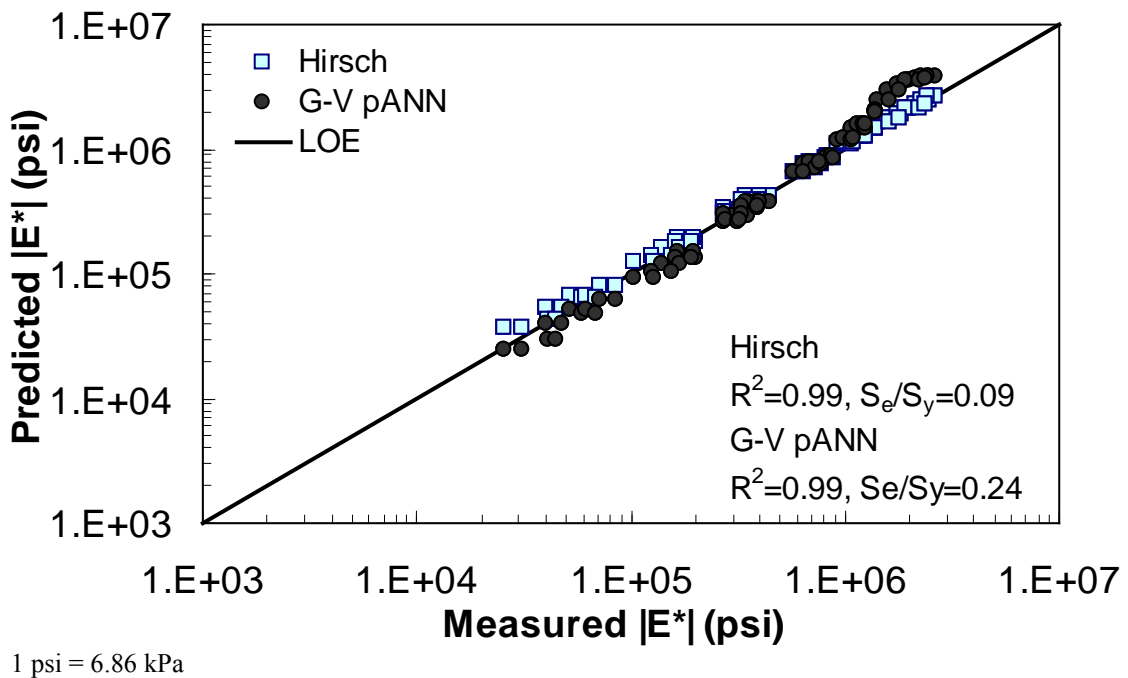


**Figure 28. Graph. Predicted moduli using G-V pANN and Hirsch models for the Citgo database in logarithmic scale.**

The feasibility of calibrating an ANN using the Hirsch parameters and the modified Witczak model parameters has been investigated. Table 19 shows that the key difference in input requirements for these two models is the lack of gradation parameters for the Hirsch model. Note the naming convention for the ANN models followed in this portion of the report. The first letter group represents the major binder property used (“G” for  $|G^*|$  and “Visc” for viscosity). The second letter group signifies whether gradation parameters were used (“GR” when they are included and “V” when only volumetric properties are used). Finally, the designation pANN denotes that the model is an ANN model but that it is used only for the pilot studies. The finalized ANN models developed in this project have no prefix before ANN. Due to the issues discussed in appendix C regarding AMPT and TP-62 measured moduli, both types of data were used in the calibration of the ANN model. The calibration results for this model are shown in figure 13 to figure 16, and the verification data are shown in figure 17 to figure 28.

**Table 19. Description of  $|G^*|$ -based ANN models.**

ANN Model	Parameters Used to Train	Training Database	Verification Database
G-GR pANN	$ G^* $	FHWA I Processed Witczak <sup>1</sup> NCDOT I	FHWA II NCDOT II
	$V_a$		
	$V_{beff}$		
	$\rho_{34}$		
	$\rho_{38}$		
	$\rho_4$		
	$\rho_{200}$		
G-V pANN	$ G^* $		
	VMA (percent)		
	VFA (percent)		

<sup>1</sup>Portions of the Witczak database (mixtures 1–135) and also some mixtures from the remaining portion that do not have reliable measurements (very high  $|E^*|$  measurements) were omitted. The portions of the Witczak database used for developing  $|G^*|$ -based models are the ones that have measured  $|G^*|$  values.

For the FHWA II dataset shown in figure 17 and figure 18, the G-GR pANN model shows more scatter than the predictions made from the G-V pANN model and the Hirsch model. Because none of the FHWA II mixtures contain data at 14 °F (-10 °C) ( $|E^*|$  measurement based on AMPT protocol), there is no observed bias in the Hirsch model shown in figure 19 and figure 20. For the NCDOT II database that contains low temperature data (figure 21 through figure 24), the bias in the Hirsch model is clear. Also, the G-GR pANN and G-V pANN models are similar, with the G-GR pANN model showing a slight improvement both visually and from the statistical measurements.

With the exception of the Citgo dataset, which was discussed previously with regard to the Witczak-based ANNs, the  $|G^*|$ -based ANN model appears to yield better predictions than the Hirsch and modified Witczak models. The overall performance of this  $|G^*|$ -based ANN model shows that considering the VMA and VFA parameters together with the t-T dependent binder rheological parameter provides more promising predictions for both the training and verification databases than the parameters used in the modified Witczak model.

The findings from figure 7 to figure 28 are as follows:

- The Al-Khateeb model displays a significant bias and, therefore, is removed from future analysis.
- The Hirsch model performs reasonably well, although the horizontal pattern shown in the LOE graph indicates problems associated with the insensitivity of the model to the input variables.
- The pANN models show the least scatter with the least bias overall.
- The pANN models trained with the Hirsch model parameters should yield predictions as good as if not better than the models trained with the modified Witczak parameters. The reason for this was not explored in detail.
- The primary advantage of ANN modeling over statistical regression techniques is that the functional form of the relationship is not needed a priori. Considering that many variables affect  $|E^*|$  values and their interaction, the ANN technique may capture complicated nonlinear relationships between  $|E^*|$  and other mixture variables better than regression analysis.

### 4.3 VISCOSITY-BASED ANN

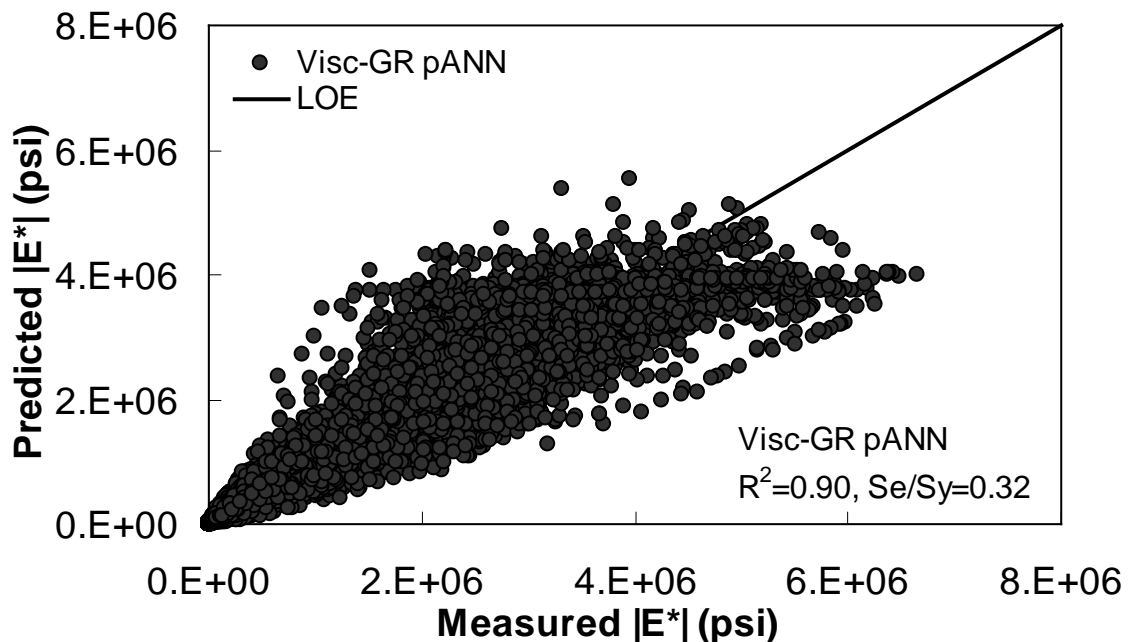
Two viscosity-based ANN models with two different sets of parameters were developed (see table 20). The performance of each model is shown in figure 29 through figure 40 for both training and verification databases. Like the  $|G^*|$ -based ANN models, the difference in these two viscosity-based ANN models are related to the input parameters used for training. In the first ANN, viscosity-gradation (Visc-GR) pANN, the parameters suggested by the original Witczak model are adopted, whereas in the second ANN (viscosity-volumetric (Visc-V) pANN), the Hirsch model parameters are chosen, with the exception that frequency and viscosity are chosen instead of  $|G^*|$ . Results of the training for the two models are shown in figure 29 to figure 32. Figure 33 to figure 40 show the verification dataset. Note that some of the points used in the training data have also been used in calibrating the original Witczak model. These points represent only a very small portion of the total data shown in figure 29 to figure 32. Results of the independent model verification process are shown for different databases in figure 33 to figure 40. Through these figures, it appears that the ANN models perform better than the original Witczak model. It is also evident that although the Visc-GR pANN model performs better in training, the Visc-V pANN model is better for model verification. Based on these findings, it appears that, like the  $|G^*|$ -based models, removing gradation parameters from the necessary inputs yielded improved and more stable modulus predictions.

**Table 20. Description of viscosity-based ANN models.**

ANN Model	Parameters Used to Train	Training Database	Verification Database
Visc-GR pANN	$f$ (hertz)	FHWA I Witczak <sup>1</sup> NCDOT I	FHWA II NCDOT II
	$\eta (10^9 \text{ P})$		
	$V_a$		
	$V_{beff}$		
	$\rho_{34}$		
	$\rho_{38}$		
	$\rho_4$		
	$\rho_{200}$		
Visc-V pANN	$f$ (hertz)	FHWA I Witczak <sup>1</sup> NCDOT I	FHWA II NCDOT II
	$\eta (10^9 \text{ P})$		
	VMA (percent)		
	VFA (percent)		

1 Pas = 10 P

<sup>1</sup>Portions of the Witczak database that do not have reliable measurements (high  $|E^*|$  measurements) were neglected.



1 psi = 6.86 kPa

**Figure 29. Graph. Prediction of training data containing Witczak, FHWA I, and NCDOT I databases using Visc-GR pANN in arithmetic scale.**

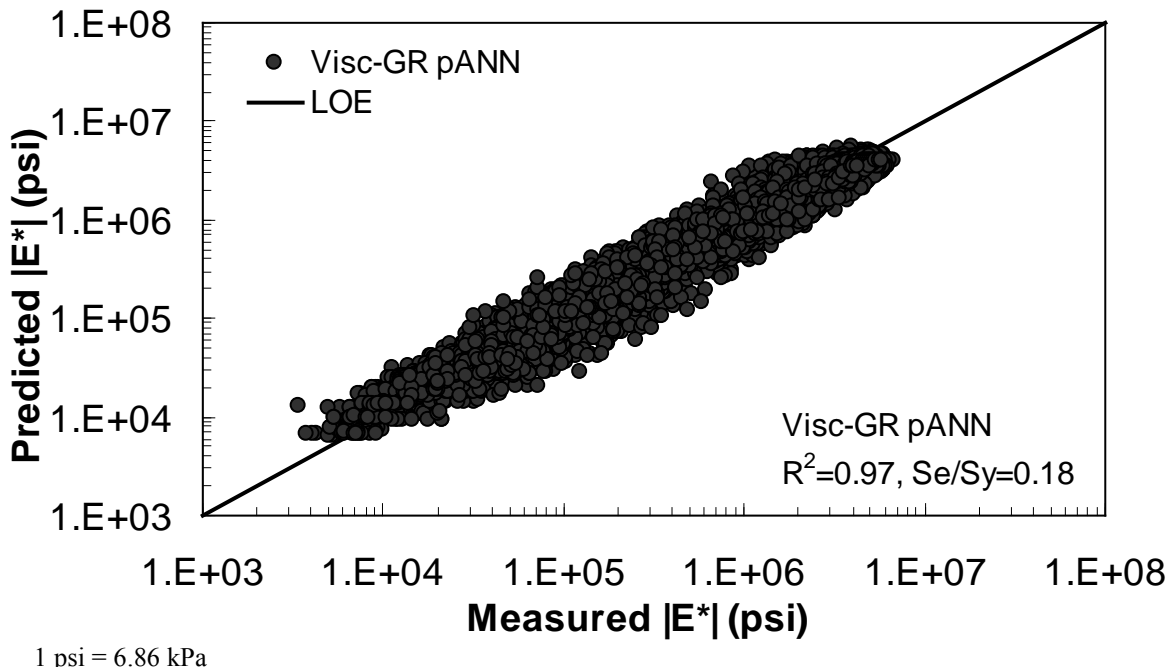


**Figure 30. Graph.** Prediction of training data containing Witczak, FHWA I, and NCDOT I databases using Visc-GR pANN in logarithmic scale.

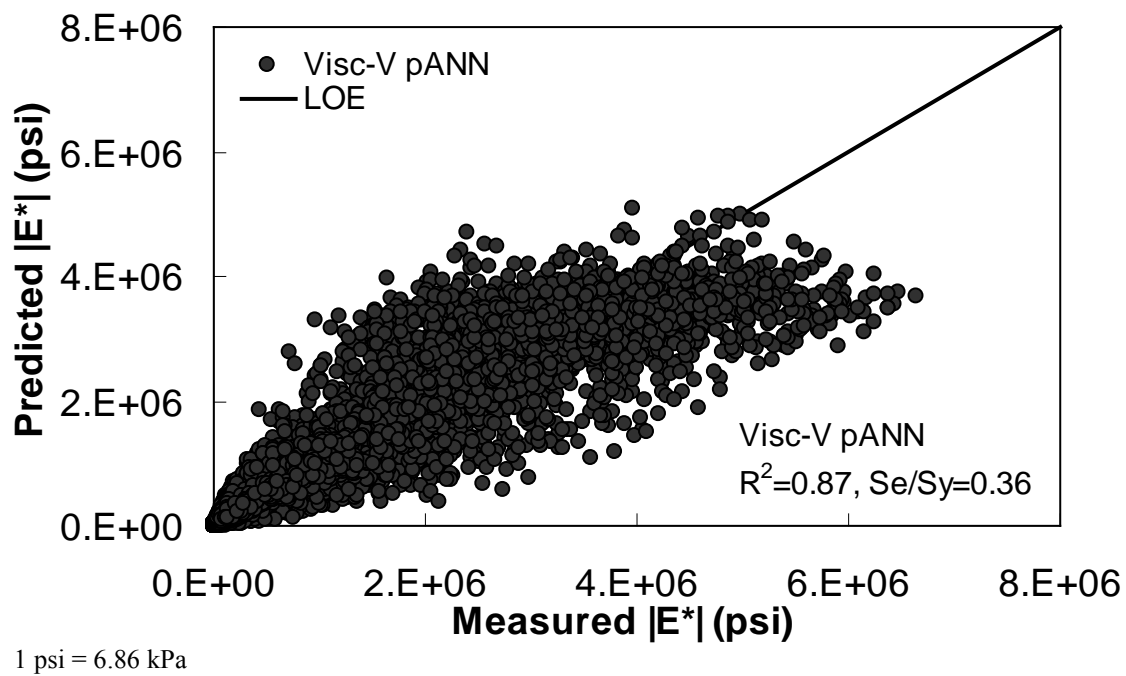


**Figure 31. Graph.** Prediction of training data containing Witczak, FHWA I, and NCDOT I databases using Visc-V pANN in arithmetic scale.

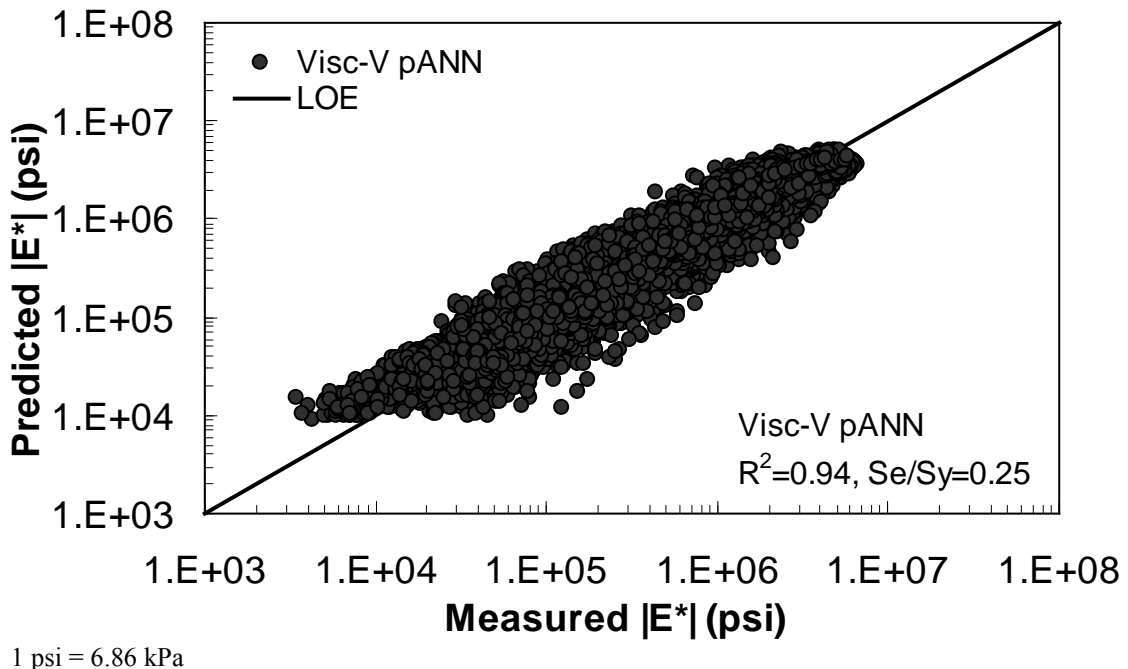


**Figure 32. Graph.** Prediction of training data containing Witczak, FHWA I, and NCDOT I databases using Visc-V pANN in logarithmic scale.

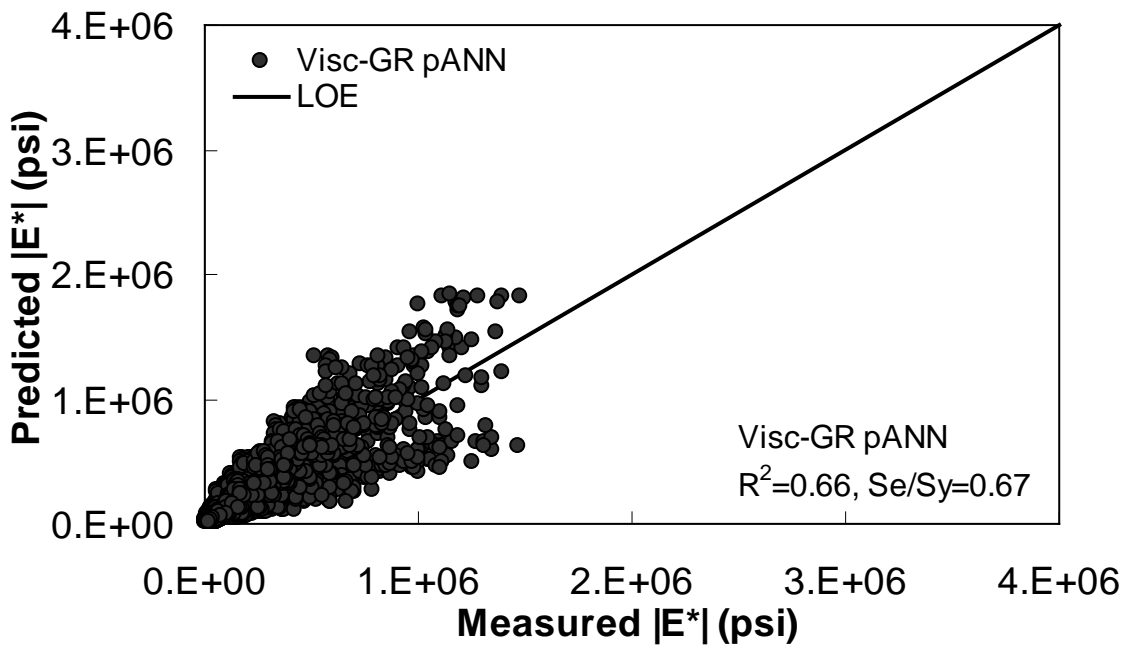


**Figure 33. Graph.** Predicted moduli using Visc-GR pANN model for the FHWA II database in arithmetic scale.

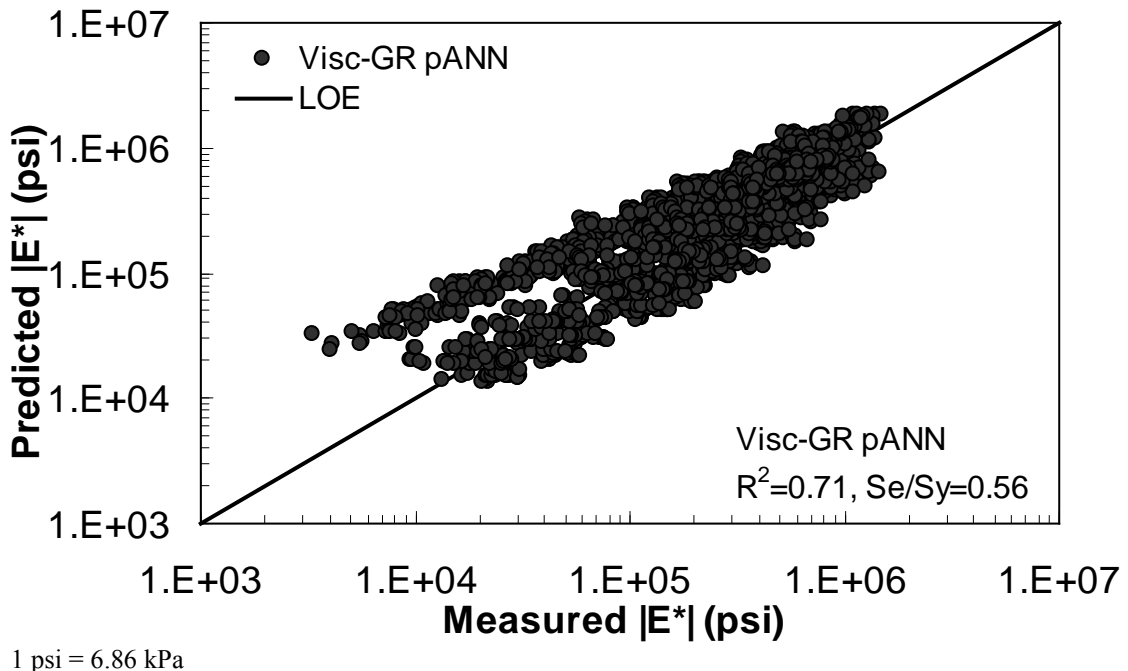


**Figure 34. Graph. Predicted moduli using Visc-GR pANN model for the FHWA II database in logarithmic scale.**

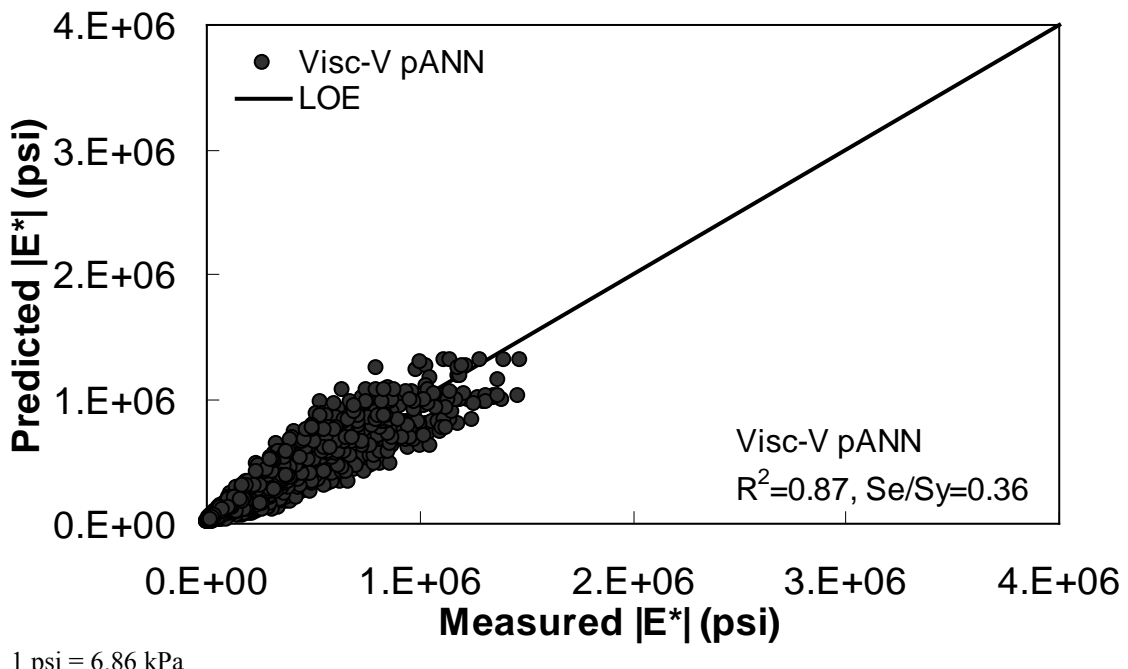


**Figure 35. Graph. Predicted moduli using Visc-V pANN model for the FHWA II database in arithmetic scale.**

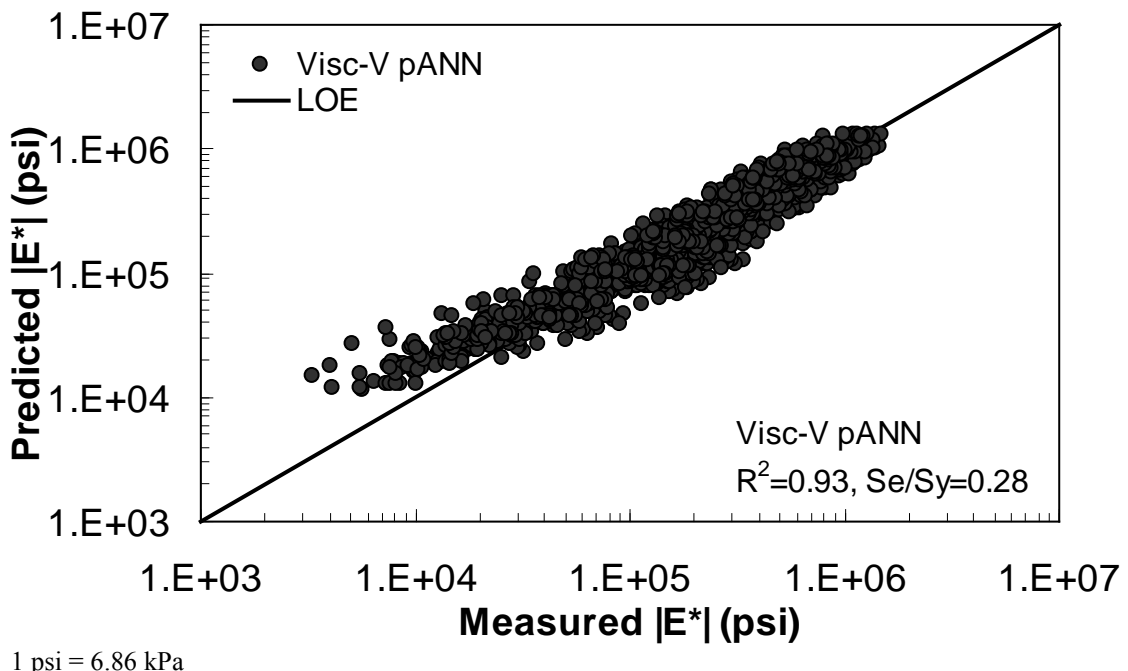


**Figure 36. Graph. Predicted moduli using Visc-V pANN model for the FHWA II database in logarithmic scale.**

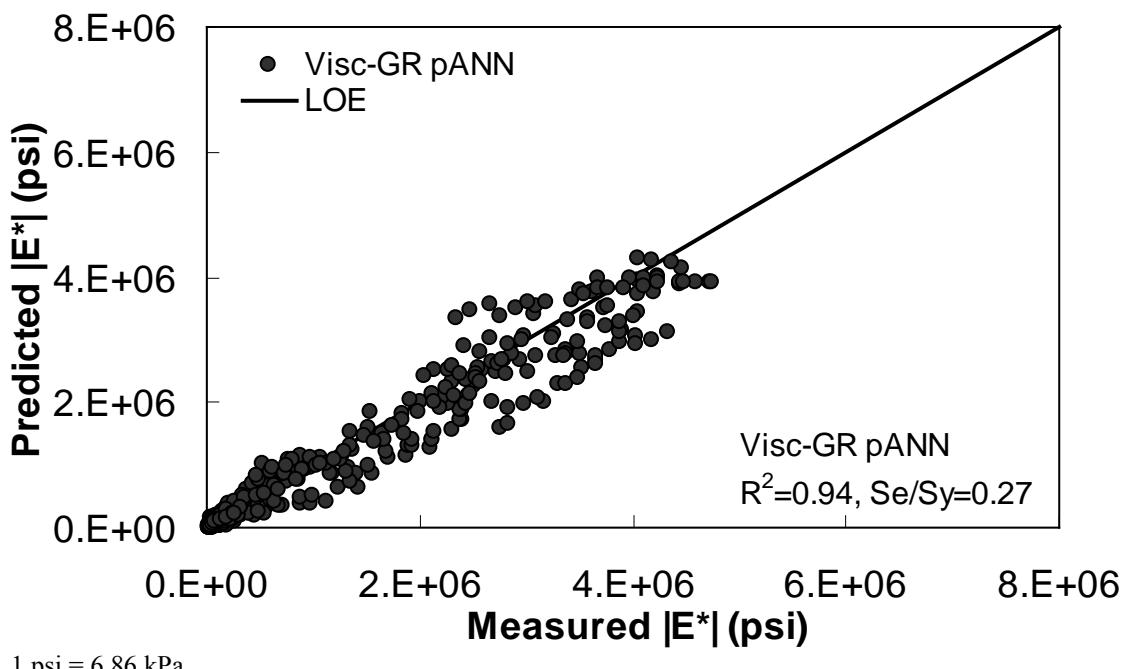


**Figure 37. Graph. Predicted moduli using Visc-GR pANN model for the NCDOT II database in arithmetic scale.**

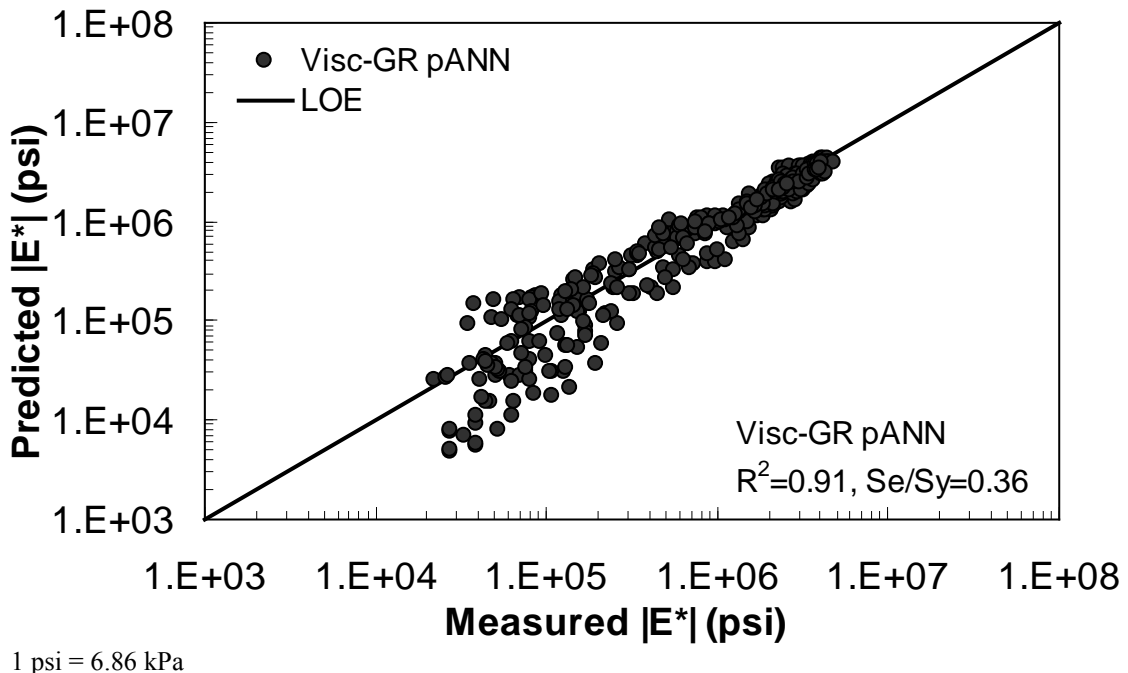


**Figure 38. Graph. Predicted moduli using Visc-GR pANN model for the NCDOT II database in logarithmic scale.**

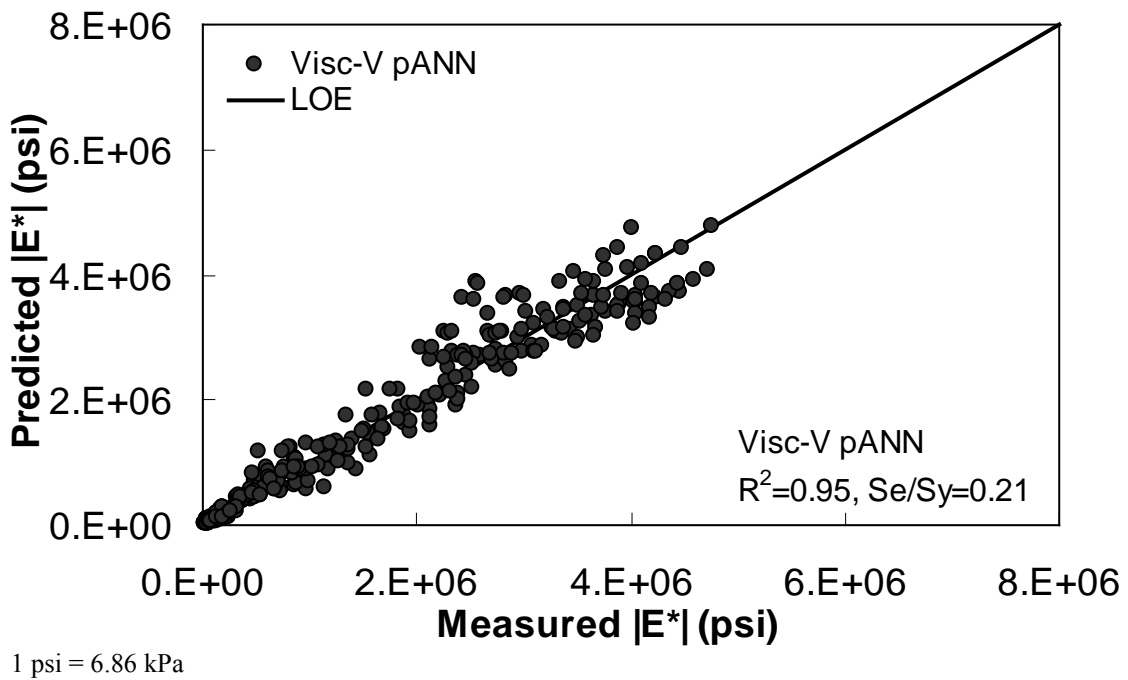


**Figure 39. Graph. Predicted moduli using Visc-V pANN model for the NCDOT II database in arithmetic scale.**

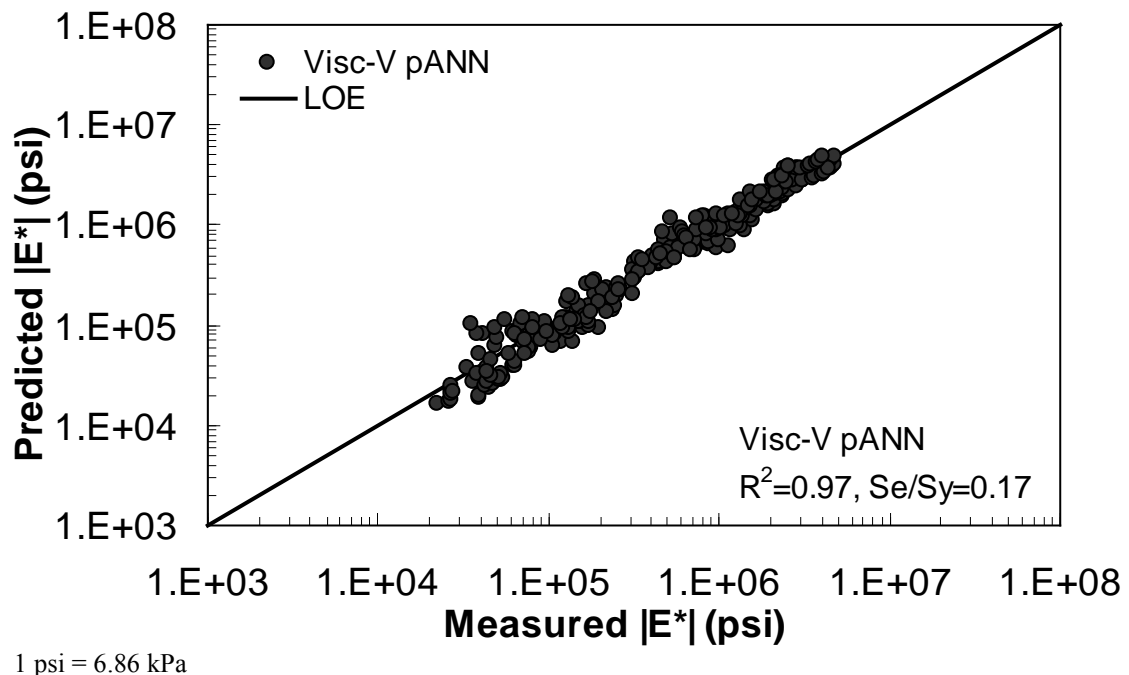


**Figure 40. Graph.** Predicted moduli using Visc-V pANN model for the NCDOT II database in logarithmic scale.



## 5.0 ANN MODELS FOR POPULATING THE LTPP DATABASE

Three ANN models have been developed for populating the LTPP database sections. These models are differentiated by the following primary input parameters: (1) the  $M_R$  model uses the resilient modulus, (2) the VV model uses the binder viscosity, and (3) the  $|G^*|$ -based (GV) model uses the binder shear modulus. The subsequent sections provide a description of each model along with the final verification plots and statistics. The models in this chapter use normalized inputs, whereas those discussed in the previous section use nonnormalized inputs.

The term *normalizing a vector* often refers to changing the magnitude of an element by dividing it by a norm of the vector. For neural networks, this definition often means changing the scale of a vector by the minimum value and the range of the vector so that all the components are between 0 and 1 or 1 and -1. Linear and uniform normalizations are the common methods used for this purpose. In some cases, such as lab- and field-measured data used to develop the ANN models in this study, linear normalization seems to be more meaningful when no specific distributions of the data are known or present. In addition to normal distribution, a Gaussian normalization (based on the mean and standard deviation of the data for each parameter) could be performed. In some cases, these statistics could be used to get rid of outliers (e.g., data points outside of the three standard deviations). Although such types of nonlinear normalization and related procedures may be useful in some applications (e.g., when the measurement range is meant to be normally distributed or distributed with some statistical uniformity), for the type of engineering applications where the data represent different conditions, it is not possible to find a statistical distribution of those input values. For example, if temperature is an input and different datasets represent different discrete values/ranges, then it is not useful to find a mean temperature value and its standard deviation to normalize the data. In this study, the linear model was adopted because of its simplicity. After applying this normalization (scaling) scheme to the data and developing the ANN models, it was found that the predictions were acceptable, and there was no further investigation into the need of nonlinear normalization. This issue is one that possibly warrants future study.

The decision to utilize normalized input-based ANN models was not finalized at the time of the study presented in the previous chapter. After deciding to use normalized input-based ANN models, the pilot analysis was not redone because the normalization only improved the predictability and thus did not change the final conclusions of the pilot study. Based on these fitting statistics and on engineering judgment, the models were ranked to develop a decision tree so that a user can determine which ANN model is best suited to a specific set of input parameters.

Due to differences in the required inputs for each model, different subsets of the entire database were used in training and verification. The total number of points used for each model, along with a summary of the required input parameters, is provided in table 21. Of the total available points for each model, 90 percent were randomly selected for the purpose of training the networks, and 10 percent were used for verification. The Witczak database was used for calibrating the VV ANN model, except that the data at the temperatures equal to or less than 32 ° F (0 °C) were not used because of unacceptably high  $|E^*|$  values. It should be mentioned that the GV and  $|G^*|$ -based model using inconsistent aged binder data of PAV- and RTFO-aging

conditions (GV-PAR) models, like the VV and viscosity-based model using specification grade of the asphalt binder (VV-grade) models, represent the same trained network, but they are identified by different terms due to the binder values used in each case. In the GV-PAR model, the binder values are based on two aging conditions, PAV and RTFO. In the VV-grade model, the values of A and VTS are chosen, as recommended in MEPDG, based on the specification grade of the asphalt binder. Sections using this model have less than two viscosity measurements, but the VMA, VFA, and binder grade values are available. Descriptions of the binder analysis necessary for using these models are given in appendices A and B.

All of the ANN models developed herein contain a mapping ANN architecture and are based on supervised learning. In the developed network, the learning method used is a feed forward back propagation, and the sigmoidal function is the transfer function. The three-layer network with two hidden layers was selected as the best configuration. The number of nodes in each layer differs according to the selected model (see table 21). These node numbers were determined after a systematic study of each model. In each case, the network follows the same basic structure that is schematically illustrated in figure 41. A more formal mathematical representation for each of these models is given in appendix D.

**Table 21. Parameters and number of nodes used in developed ANN models.**

ANN Model	Parameters Used to Train ANN Models							Number of Data Points	Number of Nodes
	$M_R$ at 5, 25, and 40 °C (MPa)	Shift Factor ( $\alpha_1, \alpha_2, \alpha_3$ )	$f_R$ (Hz)	Viscosity ( $10^9$ P)	VMA (Percent)	VFA (Percent)	$ G^* $ (psi)		
$M_R$	✓	✓						11,730	12
VV			✓	✓	✓	✓		14,682	14
GV					✓	✓	✓	12,907	12
GV-PAR					✓	✓	✓	12,907	12
VV-grade			✓	✓	✓	✓		14,682	14

°C = (°F-32)/1.8

1 Pas = 10 P

1 psi = 6.86 kPa

Note: Blank cells indicate that the parameter was not used to train the model.

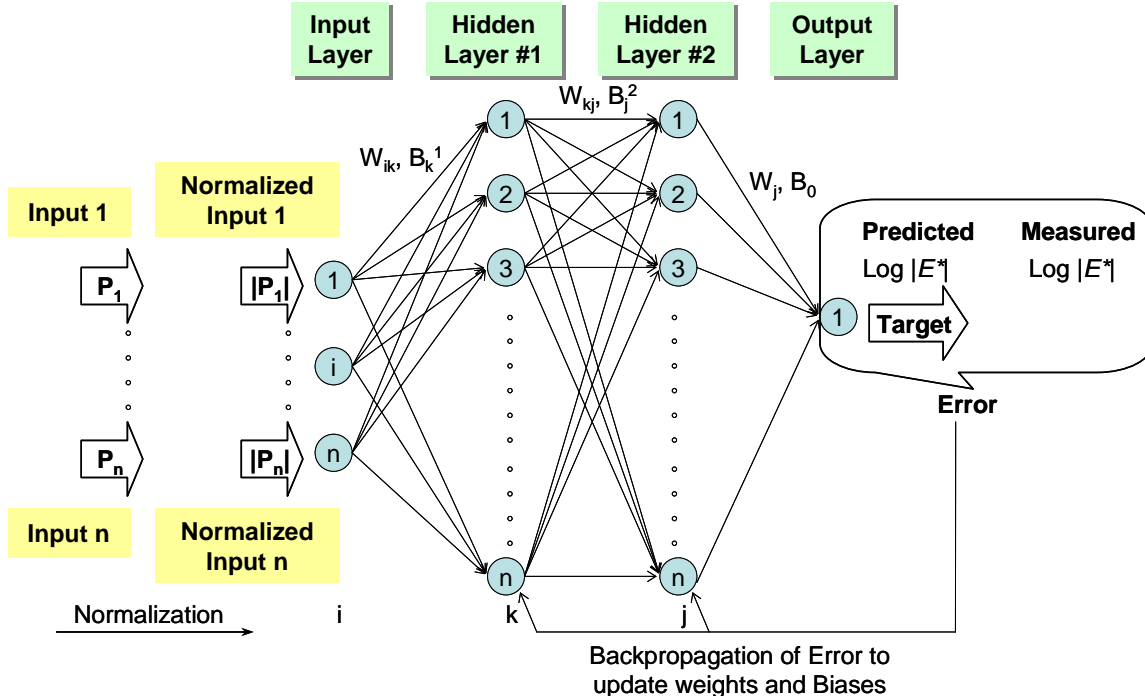


**Figure 41. Illustration. Network structure used for training the ANN models.**

### 5.1 $M_R$ ANN MODEL

The 1993 AASHTO *Guide for Design of Pavement Structures* employs  $M_R$  as the material property representing the stiffness characteristics of layer materials.<sup>(27)</sup>  $M_R$  is defined as the ratio between applied stress ( $\sigma_a$ ) and recoverable strain ( $\varepsilon_r$ ) as follows:

$$M_R = \frac{\sigma_a}{\varepsilon_r} \quad (19)$$

Several testing standards have been developed for the determination of  $M_R$  of AC using the indirect tensile (IDT) test method (American Society for Testing and Materials (ASTM) D4123-82, NCHRP 1-28, State Highway Research Program (SHRP) P-07, and NCHRP 1-28A).

(See references 28–31.) In light of these facts, the LTPP database has stored  $M_R$  as the primary measured mixture stiffness term for many of the layers. Due to the industry's transition from  $M_R$  to  $|E^*|$ , a significant amount of  $M_R$  data that have been collected in State highway agencies may become obsolete unless the  $M_R$  values can be converted to  $|E^*|$  values. The NCSU research team successfully developed a method to make this conversion using an ANN-based methodology to predict the  $|E^*|$  values at multiple temperatures and frequencies when only the  $M_R$  values at three temperatures are available.

The difficulty in performing this conversion stems from the fact that  $M_R$  provides a snapshot of the material behavior under one loading history (i.e., 0.1-s haversine loading followed by a 0.9-s rest period) at different testing temperatures (normally three temperatures at 41, 77, and 104 °F (5, 25, and 40 °C)). Zhang explored the possibility of characterizing the viscoelastic properties obtained from  $M_R$  tests using Fourier analysis.<sup>(32)</sup> It was concluded that this type of analysis is impractical due to the difficulty in solving a large number of variables and the limited range of

results, which provided little information other than  $M_R$  data. Another challenge is that Fourier analysis requires a loading and deformation history in order to fit, which most databases do not contain. Because an analytical method is not feasible, any attempt to predict  $|E^*|$  from  $M_R$  is, at best, empirical in nature.

One difficulty in any empirical model is acquiring a database large enough to represent the range of possible inputs. Because a large database containing both  $M_R$  and  $|E^*|$  does not exist, a theoretical approach has been developed based on LVE principles. The resulting forward model is used along with the mixtures in the Witczak database to develop the ANN model training database.

### 5.1.1 Forward Modeling

Developing a database with  $|E^*|$  and  $M_R$  values can be a time-consuming task if the properties are measured in the laboratory, especially for a database comprehensive enough to encompass a large range of mixture variables such as binders, gradations, NMSA, VMA, VFA, air voids, etc. The proposed method was to use a comprehensive  $|E^*|$  database and populate the database with  $M_R$  values by using LVE principles.

$M_R$  can be calculated by several different methods, including ASTM D4123-82, NCHRP 1-28 method, the SHRP P07 protocol, AASHTO TP31-96 standard, or the Roque and Buttlar equation 17, which accounts for the bulging effects of the specimen. (See references 28, 29, 30, 33, and 34.) The NCHRP 1-28 elastic solutions are used in this report.<sup>(29)</sup> The equations for calculating  $M_R$  and Poisson's ratio are as follows:

$$M_R = \frac{P}{Ud} (k_1 - k_2 \nu) \quad (20)$$

$$\nu = \frac{k_3 + k_1(V/U)}{k_4 + k_2(V/U)} \quad (21)$$

Where:

$M_R$	=	Resilient modulus (MPa).
$\nu$	=	Poisson's ratio.
$P$	=	Applied load (N).
$U$	=	Recoverable horizontal displacement (m).
$V$	=	Recoverable vertical displacement (m).
$k_1, k_2, k_3, k_4$	=	Constants.

Equations 20 and 21 can be combined to yield the following relationship:

$$M_R = \frac{P}{Ud} \left[ k_1 - k_2 \frac{k_3 + k_1(V/U)}{k_4 + k_2(V/U)} \right] \quad (22)$$

These equations are based on the linear elastic solutions developed by Hondros after accounting for the nonuniform stress and strain distributions in the IDT specimen (see figure 42).<sup>(35)</sup> The constants in equations 20 and 21 are listed in table 22. Note that these constants are different

from the constants for  $|E^*|$  because the coefficients for  $M_R$  are derived using linear elastic theory, whereas those for  $|E^*|$  are derived using LVE theory.

**Table 1. Geometry coefficients.**

IDT $ E^* $	$\beta_1$	$\beta_2$	$\gamma_1$	$\gamma_2$
	-0.0134	-0.0042	0.0037	0.0116
$M_R$	$k_3$	$k_4$	$k_1$	$k_2$
	-0.00067	0.000209	-0.00018	0.000578

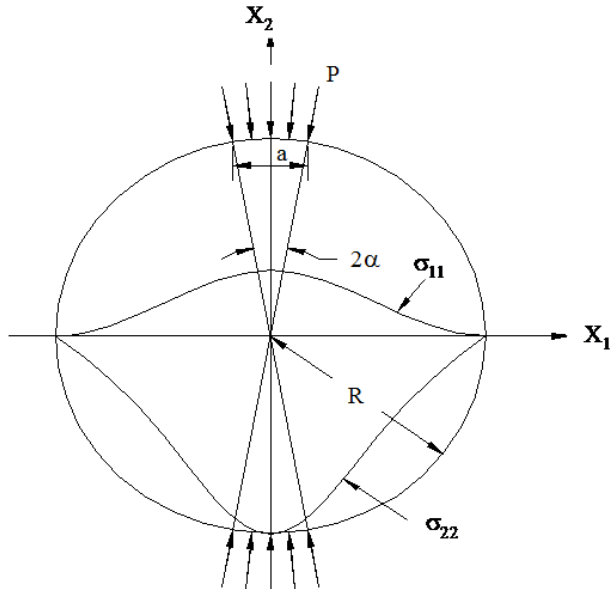


**Figure 1. Illustration. Stress distribution in the IDT specimen subjected to a strip load.**

For linear elastic materials, the stress-strain relationship is represented by the generalized Hooke's law. It is assumed that the rectangular coordinate of  $x_1$  is in the horizontal direction,  $x_2$  is in the vertical direction, and  $x_3$  is in the depth direction of the IDT specimen. Two strains that are of interest are  $\varepsilon_{11}$  and  $\varepsilon_{22}$ . According to the generalized Hooke's law, these two strains are related to stresses as follows:

$$\varepsilon_{11} = \frac{1}{E}(\sigma_{11} - \nu\sigma_{22}) = D(\sigma_{11} - \nu\sigma_{22}) \quad (23)$$

$$\varepsilon_{22} = \frac{1}{E}(\sigma_{22} - \nu\sigma_{11}) = D(\sigma_{22} - \nu\sigma_{11}) \quad (24)$$

Where:

$E$  = Young's modulus.

$D$  = Compliance.

Application of the elastic-viscoelastic correspondence principle to these linear elastic solutions results in the following LVE stress-strain relationships:

$$\varepsilon_{11} = \int_0^t D(t-\tau) \frac{\partial}{\partial \tau} [\sigma_{11} - \nu(t-\tau)\sigma_{22}] d\tau \quad (25)$$

$$\varepsilon_{22} = \int_0^t D(t-\tau) \frac{\partial}{\partial \tau} [\sigma_{22} - \nu(t-\tau)\sigma_{11}] d\tau \quad (26)$$

The Hondros equations used to calculate the resulting stresses in the horizontal and vertical directions are as follows:

$$\sigma_{11} = \frac{2P}{\pi ad} [f(x) - g(x)] \quad (27)$$

$$\sigma_{22} = -\frac{2P}{\pi ad} [f(x) + g(x)] \quad (28)$$

$$f(x) = \frac{(1-x^2/R^2)\sin 2\alpha}{1+(2x^2/R^2)\cos 2\alpha + x^4/R^4} \quad (29)$$

$$g(x) = \tan^{-1} \left[ \frac{1-x^2/R^2}{1+x^2/R^2} \tan \alpha \right] \quad (30)$$

Where:

$R$  = Radius of specimen (m).

$x$  = Horizontal distance from center of specimen (m).

$\alpha$  = Radial angle (radians).

Combining equation 27 through equation 30 results in the following expressions for the horizontal and vertical strains:

$$\varepsilon_{11}(x_1, t) = \frac{2}{\pi ad} \int_0^t D(t-\tau) \frac{\partial P}{\partial \tau} \{ [f(x) - g(x)] + \nu(t-\tau)[f(x) + g(x)] \} d\tau \quad (31)$$

$$\varepsilon_{22}(x_2, t) = -\frac{2}{\pi ad} \int_0^t D(t-\tau) \frac{\partial P}{\partial \tau} \{ [f(x) + g(x)] + \nu(t-\tau)[f(x) - g(x)] \} d\tau \quad (32)$$

The displacements at the gauge length can be calculated by integrating the nonuniform strains in equations 31 and 32 along the gauge length (i.e.,  $-l$  to  $+l$ ) as follows:

$$U = \int_{-l}^l \varepsilon_{11}(x_1, t) dx \quad (33)$$

$$V = \int_{-l}^l \varepsilon_{22}(x_2, t) dx \quad (34)$$

or

$$U = \frac{2}{\pi ad} \int_0^t D(t-\tau) \frac{\partial P}{\partial \tau} \left( \int_{-l}^l [f(x) - g(x)] dx + \nu(t-\tau) \int_{-l}^l [f(x) + g(x)] dx \right) d\tau \quad (35)$$

$$V = \frac{2}{\pi ad} \int_0^t D(t-\tau) \frac{\partial P}{\partial \tau} \left( - \int_{-l}^l [f(x) + g(x)] dx + \nu(t-\tau) \int_{-l}^l [g(x) - f(x)] dx \right) d\tau \quad (36)$$

For the gauge length of 2.0 inches (50.8 mm), equations 35 and 36 reduce to the following:

$$U = \frac{2}{\pi ad} \int_0^t D(t-\tau) \frac{\partial P}{\partial \tau} \{ \gamma_1 + \nu(t-\tau) \gamma_2 \} d\tau \quad (37)$$

$$V = \frac{2}{\pi ad} \int_0^t D(t-\tau) \frac{\partial P}{\partial \tau} \{ \beta_1 + \nu(t-\tau) \beta_2 \} d\tau \quad (38)$$

Where the values of  $\beta_1$ ,  $\beta_2$ ,  $\gamma_1$ , and  $\gamma_2$  are shown in table 22. Equations 37 and 38 require two time-dependent material properties (i.e., creep compliance and Poisson's ratio). It has been proven that the creep compliance of AC can be predicted from  $|E^*$  using theoretical relationships.<sup>(36)</sup> In this study, the following approach is used to convert the  $|E^*$  mastercurve to the creep compliance.

The complex modulus,  $E^*$ , is represented in equation 39 as follows:

$$E^* = E' + iE'' \quad (39)$$

Where:

$E'$  = Storage modulus =  $|E^*|$  cosine  $\phi$ .

$E''$  = Loss modulus =  $|E^*|$  sine  $\phi$ .

$\phi$  = Phase angle.

The storage modulus,  $E'$ , can be represented in terms of a Prony series in equation 40 as follows:

$$E'(\omega_r) = E_\infty + \sum_{i=1}^n \frac{\omega_r^2 \rho_i^2 E_i}{\omega_r^2 \rho_i^2 + 1} \quad (40)$$

Where:

$E_\infty$  = Elastic modulus (MPa).

$\omega_r$  = Angular reduced frequency.

$E_i$  = Modulus of the  $i$ th Maxwell element.

$\rho_i$  = Relaxation time of the  $i$ th Maxwell element.

An exact conversion to  $D(t)$  can be obtained by solving the following equations:

$$[A]\{D\} = \{B\}, \text{ or } A_{kj}D_j = B_k \quad (41)$$

$$A_{kj} = E_\infty \left(1 - e^{-(t_k/\tau_j)}\right) + \sum_{i=1}^m \frac{\rho_i E_i}{\rho_i - \tau_j} \left(e^{-(t_k/\rho_i)} - e^{-(t_k/\rho_i)}\right) \quad \rho_i \neq \tau_j \quad (42)$$

$$B_k = 1 - \left(E_\infty + \sum_{i=1}^m E_i e^{-(t_k/\rho_i)}\right) / \left(E_\infty + \sum_{i=1}^m E_i\right) \quad (43)$$

Where:

$A_{kj}$  = Matrix element in the  $k$ th row and  $j$ th column of matrix  $A$ .

$B_k$  = Vector element in the  $k$ th row of vector  $B$ .

$E_\infty$  = Equilibrium modulus (MPa).

$E_i$  = Modulus of the  $i$ th Maxwell element.

$\rho_i$  = Relaxation time of the  $i$ th Maxwell element determined a priori.

$\tau_j$  = Retardation time of the  $j$ th Voigt element determined a priori.

$t_k$  = Time of interest.

$m$  = Number of Prony coefficients.

By solving for compliance of column  $j$  of matrix  $A$  ( $D_j$ ), the Prony series representation for  $D(t)$  can be determined. Equation 42 does not show a solution for  $\rho_i = \tau_j$  because the error increases when such a case exists.<sup>(36,37)</sup>

The second time-dependent material property in equation 37 is Poisson's ratio. The time-dependent nature of Poisson's ratio has been reported.<sup>(37)</sup> Poisson's ratio values for the S12.5C mixture are shown in figure 43 against the reduced time to show a typical trend.

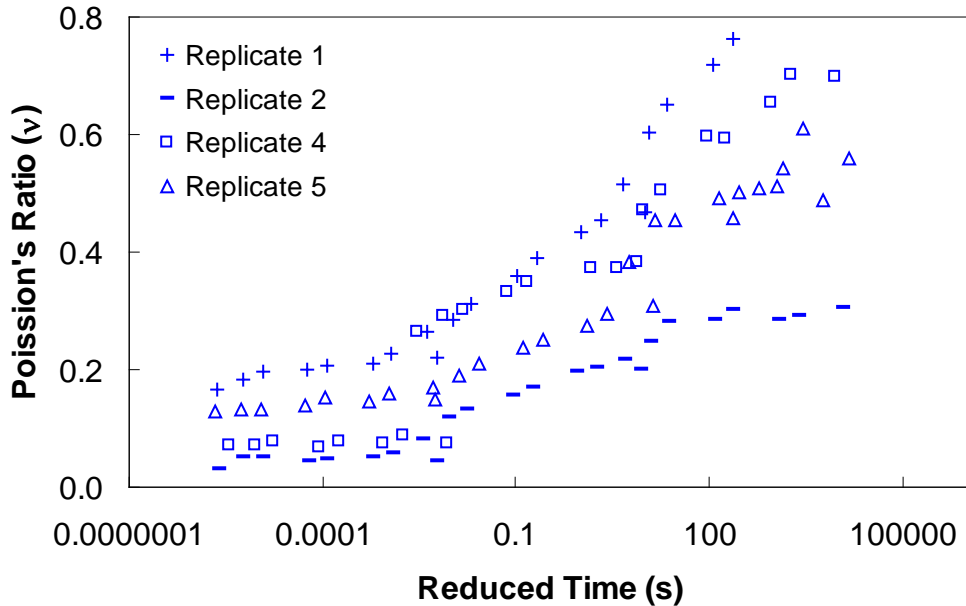


**Figure 43. Graph. Poisson's ratio versus reduced time for S12.5C.**

The Poisson's ratio values are calculated from equation 21 using the data from the IDT  $|E^*|$  test. As can be seen in figure 43, a large sample-to-sample variability is evident in Poisson's ratio values. Another problem with Poisson's ratio is that equation 25 is difficult to solve because two time-dependent properties are inherent in the equation. If Poisson's ratio in equations 25 and 26 is assumed to be constant, the two equations reduce to the following:

$$U = \frac{2(\gamma_1 + \nu\gamma_2)}{\pi ad} \int_0^t D(t-\tau) \frac{\partial P}{\partial \tau} d\tau \quad (44)$$

$$V = \frac{2(\beta_1 + \nu\beta_2)}{\pi ad} \int_0^t D(t-\tau) \frac{\partial P}{\partial \tau} d\tau \quad (45)$$

In figure 43, the measured Poisson's ratio exceeds the theoretical limits of zero to 0.5. A high Poisson's ratio occurs at large reduced times when the temperature is high and/or the loading time is long. Some Poisson's ratios are higher than 0.5, indicating that damage has occurred in the specimen.<sup>(28,38)</sup> The biggest challenge in determining Poisson's ratio in the IDT test is to induce a large enough horizontal displacement to overcome the electronic noise in the testing system without causing damage in the specimen. Mirza et al. provide a method to evaluate the quality of the data using a deflection ratio.<sup>(39)</sup>

The effect on  $M_R$  when a constant Poisson's ratio is assumed is evaluated by using three Poisson's ratios at each temperature of each mixture and calculating the percentage of difference in the predicted  $M_R$  values. The Poisson's ratio values used in this comparison are 0.15, 0.2, and 0.25 for 41 °F (5 °C); 0.25, 0.3, and 0.35 for 77 °F (25 °C); and 0.4, 0.45, and 0.5 for 104 °F (40 °C). It was found that the difference in  $M_R$  values is negligible when Poisson's ratio, which is used to predict the displacements, is used to calculate  $M_R$ . A more indepth analysis of equations 20 and 37 along with the geometry coefficients in these equations, which are shown in

table 22 (i.e.,  $k_1$ ,  $k_2$ ,  $\gamma_1$ , and  $\gamma_2$ ), reveals that the effect of change in Poisson's ratio on the term  $(k_1-k_2\nu)$  in the numerator of equation 20 is about the same as that on the horizontal displacement calculated from equation 37, which appears in the denominator of equation 20. Therefore, it is concluded that the effect of Poisson's ratio on  $M_R$  calculation is minimal. Vinson draws a similar conclusion that a Poisson's ratio of 0.15 to 0.45 does not affect  $M_R$  much based on a theoretical finite-element analysis.<sup>(40,28)</sup> For the remainder of this report, equation 44 is used, with constant Poisson's ratios of 0.2, 0.35, and 0.45 for 41 °F (5 °C), 77 °F (25 °C), and 104 °F (40 °C), respectively.

Because the numerical integration of equation 44 requires calculating all the previous time steps to arrive at the current time step, calculation times can grow exponentially.<sup>(41)</sup> To reduce the calculation time, the state variable approach described in equation 46 through equation 48 is used in this study.

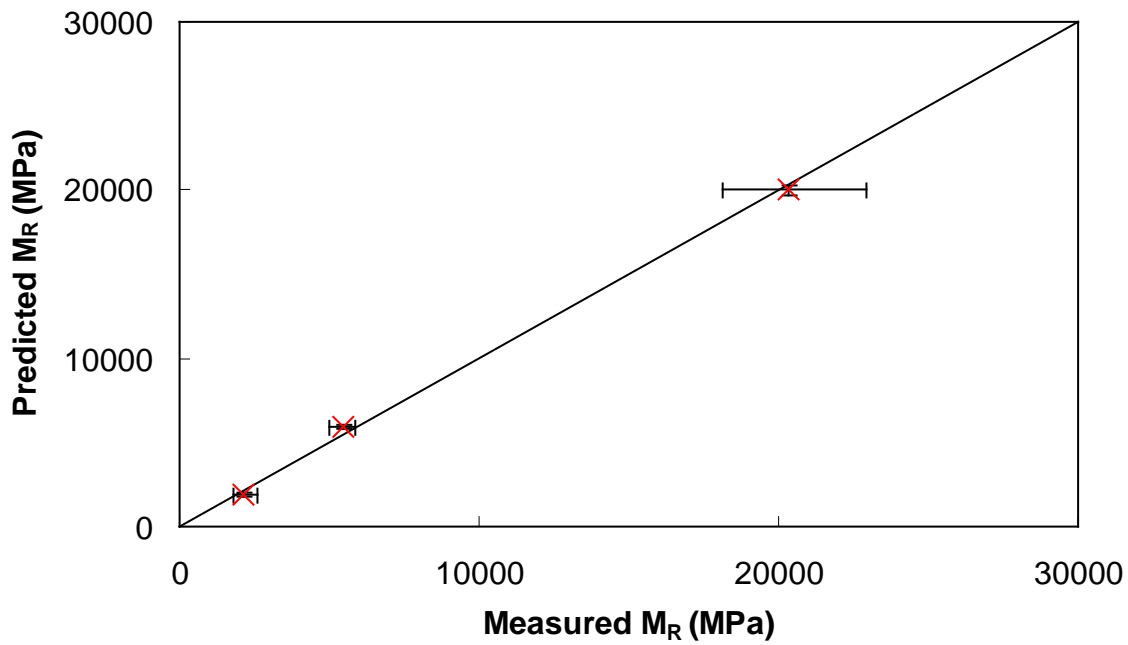
$$\varepsilon^{n+1} = \int_0^{t^{n+1}} D(t^{n+1} - \tau) \frac{d\sigma}{dt} d\tau = \eta_o^{n+1} - \sum_{i=1}^n \eta_i^{n+1} \quad (46)$$

Where:

$$\eta_o^{n+1} = (D_o + \sum_{i=1}^m D_i)(\sigma^{t^{n+1}} - \sigma^{t^o}) \quad (47)$$

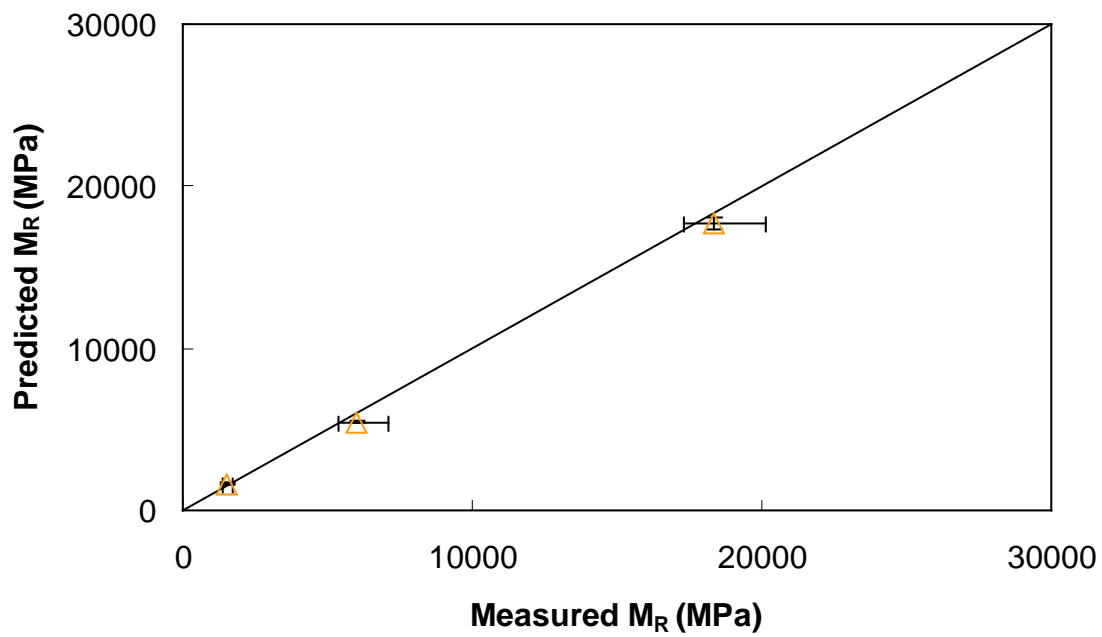
$$\eta_i^{n+1} = e^{-\frac{\Delta t}{\tau_o}} \eta_i^n + e^{-\frac{\Delta t}{2\tau_o}} [\sigma^{t^{n+1}} - \sigma^{t^n}] D_i \quad (48)$$

Figure 44 through figure 47 show the results of predicted versus measured values using a LOE graph. For both mixtures, the predicted and measured  $M_R$  values are in good agreement, suggesting that the proposed approach based on the theory of linear viscoelasticity using the IDT  $|E^*/|$  can provide a reasonable estimate of  $M_R$  of AC.



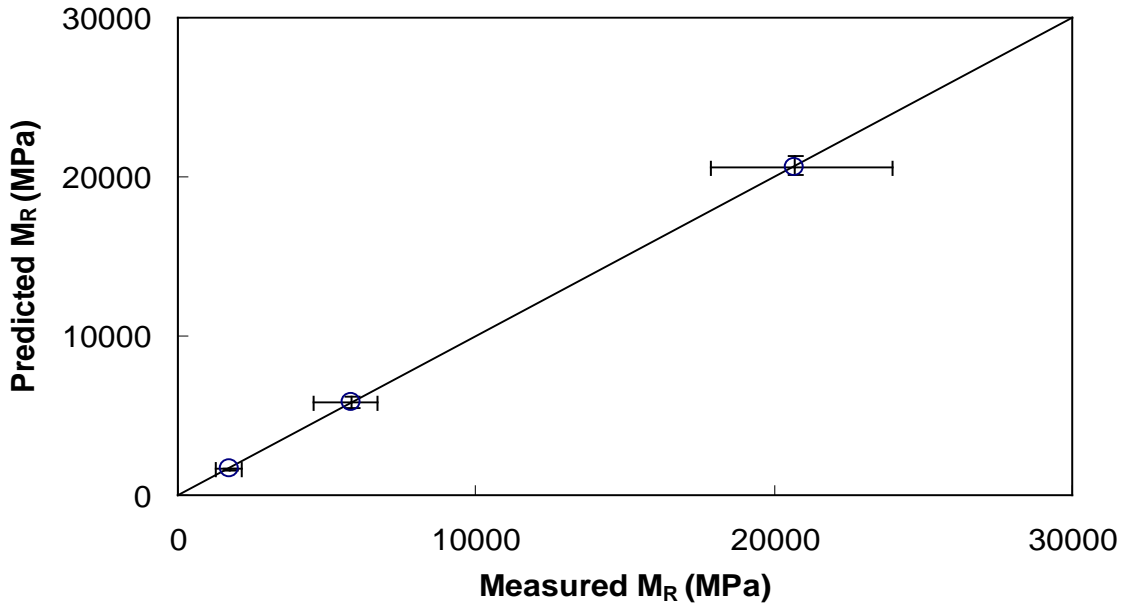
1 psi = 6.86 kPa

**Figure 44.** Graph. Comparison of predicted and measured  $M_R$  values for S12.5C mixture.



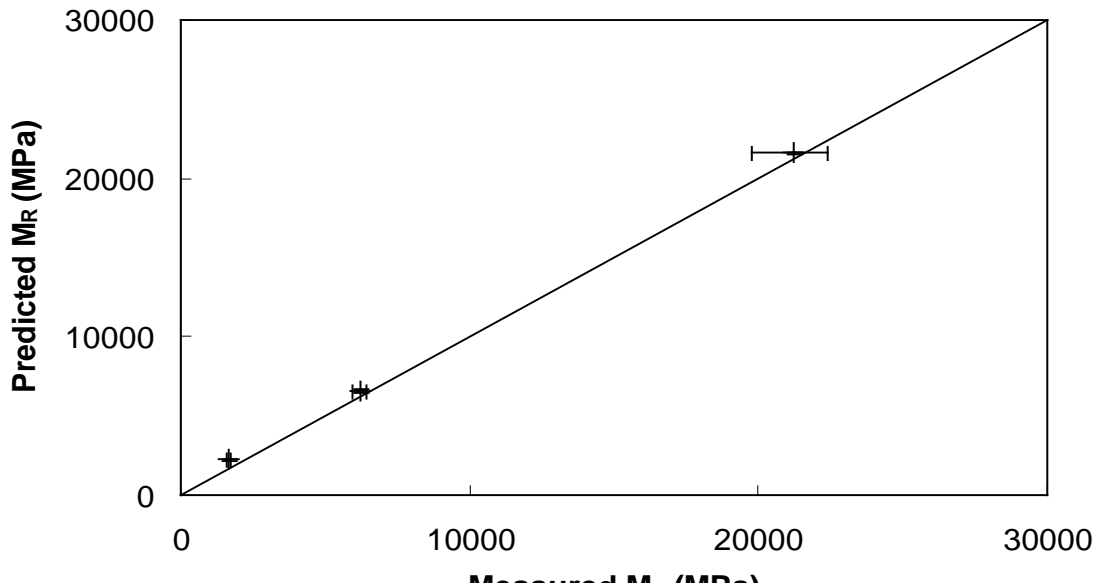
1 psi = 6.86 kPa

**Figure 45.** Graph. Comparison of predicted and measured  $M_R$  values for S12.5CM mixture.



1 psi = 6.86 kPa

**Figure 46. Graph. Comparison of predicted and measured  $M_R$  values for S12.5FE mixture.**



1 psi = 6.86 kPa

**Figure 47. Graph. Comparison of predicted and measured  $M_R$  values for B25.0C mixture.**

### 5.1.2 ANN Model $|E^*|$ Backcalculation

The characterization and verification results of the  $M_R$  ANN model are shown in figure 48 through figure 51. In figure 49, the results of characterization are shown in logarithmic space, and the model displays excellent fitting statistics with a high  $R^2 = 0.98$  (0.90 in arithmetic space) and a low  $Se/Sy = 0.15$  (0.32 in arithmetic space). The verification plots are shown in figure 50

and figure 51, and the model is found to predict the moduli values with statistics similar to those from the calibration dataset.

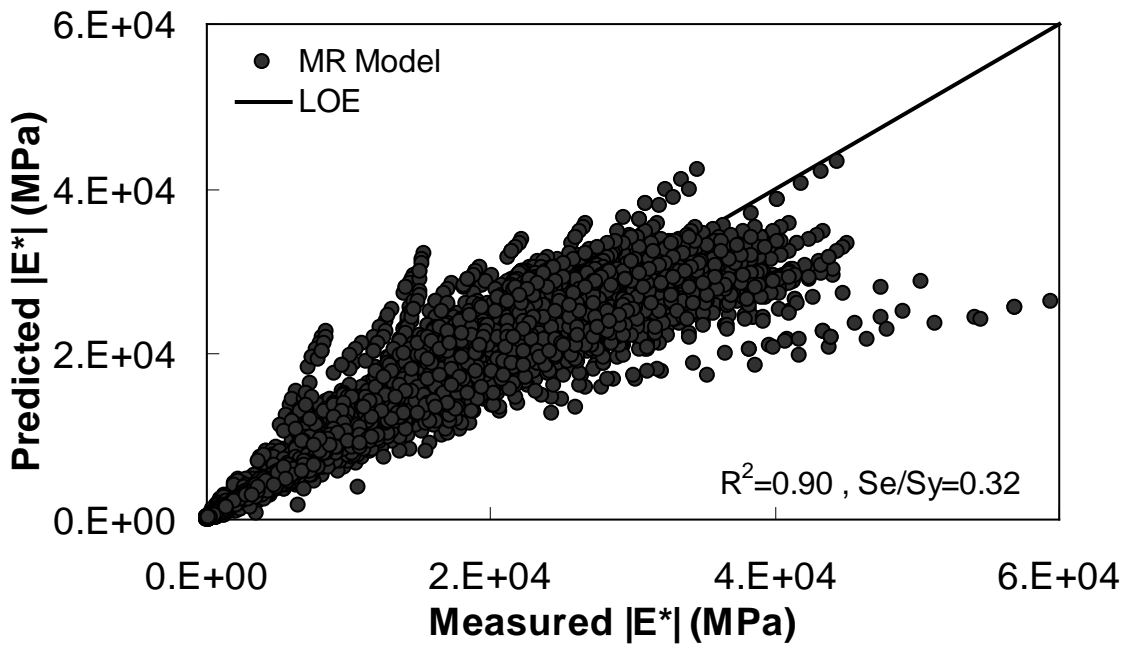


**Figure 48.** Graph.  $M_R$  ANN model using 90 percent of randomly selected data as a training set in arithmetic scale.

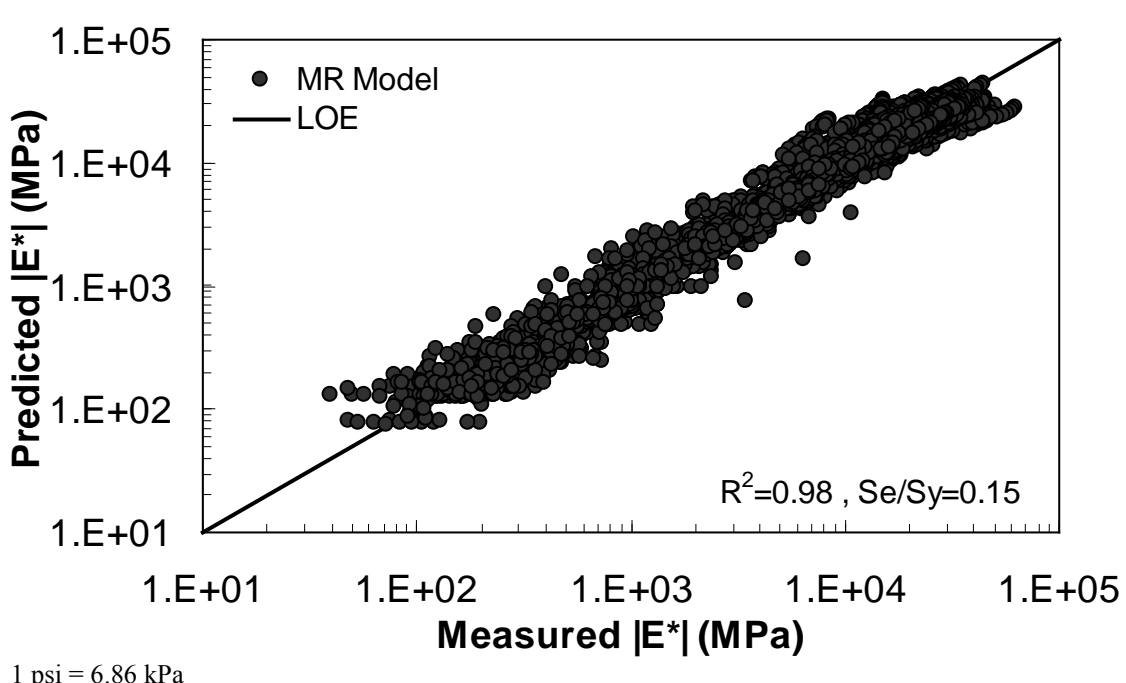


**Figure 49.** Graph.  $M_R$  ANN model using 90 percent of randomly selected data as a training set in logarithmic scale.

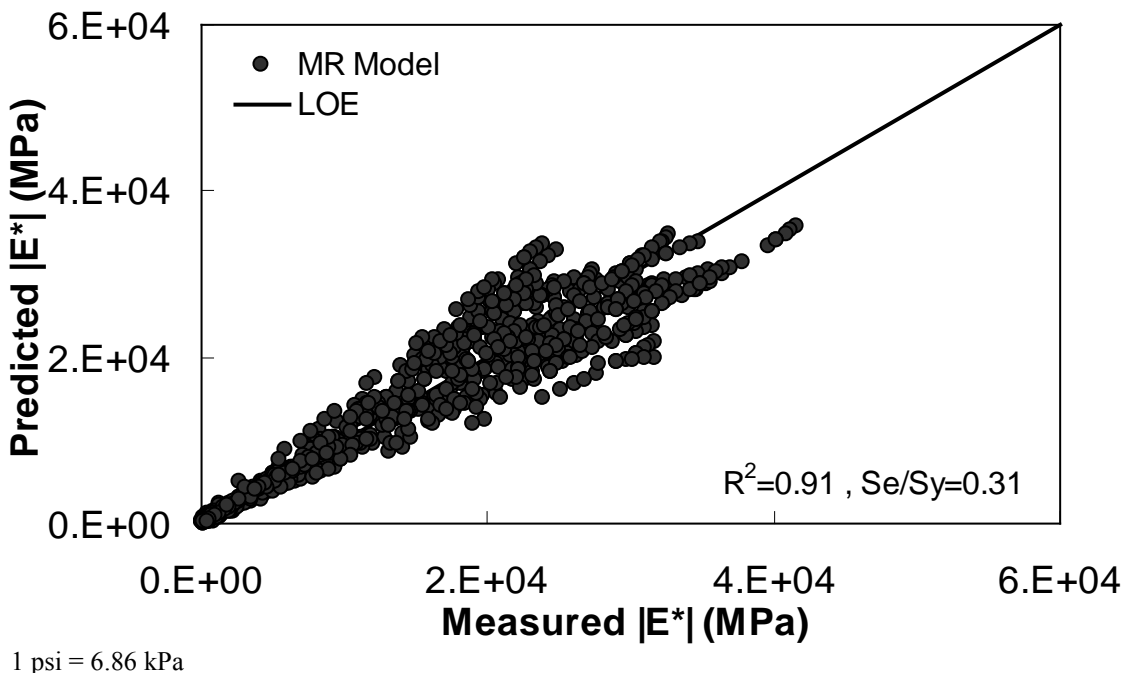


**Figure 50.** Graph.  $M_R$  ANN model using 10 percent of randomly selected data as a verification set in arithmetic scale.

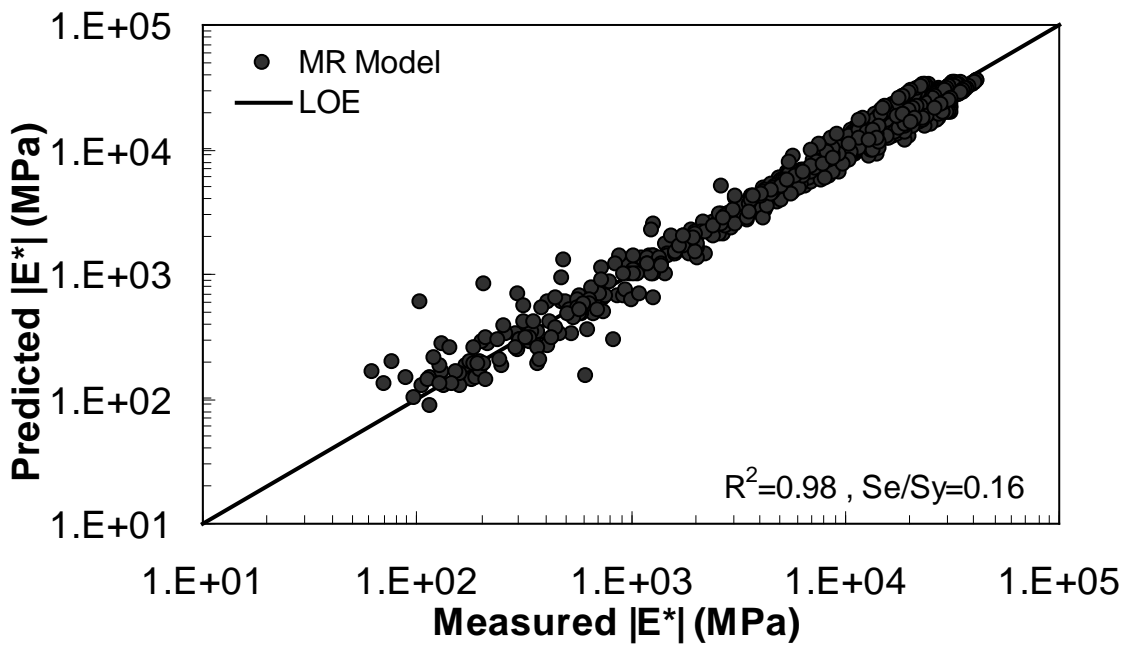


**Figure 51.** Graph.  $M_R$  ANN model using 10 percent of randomly selected data as a verification set in logarithmic scale.

## 5.2 VV ANN MODEL

The characterization and verification results of the VV ANN model are shown in figure 52 through figure 55 in a manner similar to that shown for the  $M_R$  ANN model. Like the  $M_R$  ANN model, the VV model shows good fitting statistics with a high  $R^2 = 0.95$  (0.93 in arithmetic space) and a low  $Se/Sy = 0.23$  (0.26 in arithmetic space). The verification plots are shown in figure 54 and figure 55. Although the verification statistics are not as favorable as those found for the  $M_R$  ANN model, they are still better overall than those of the existing closed-form solutions.

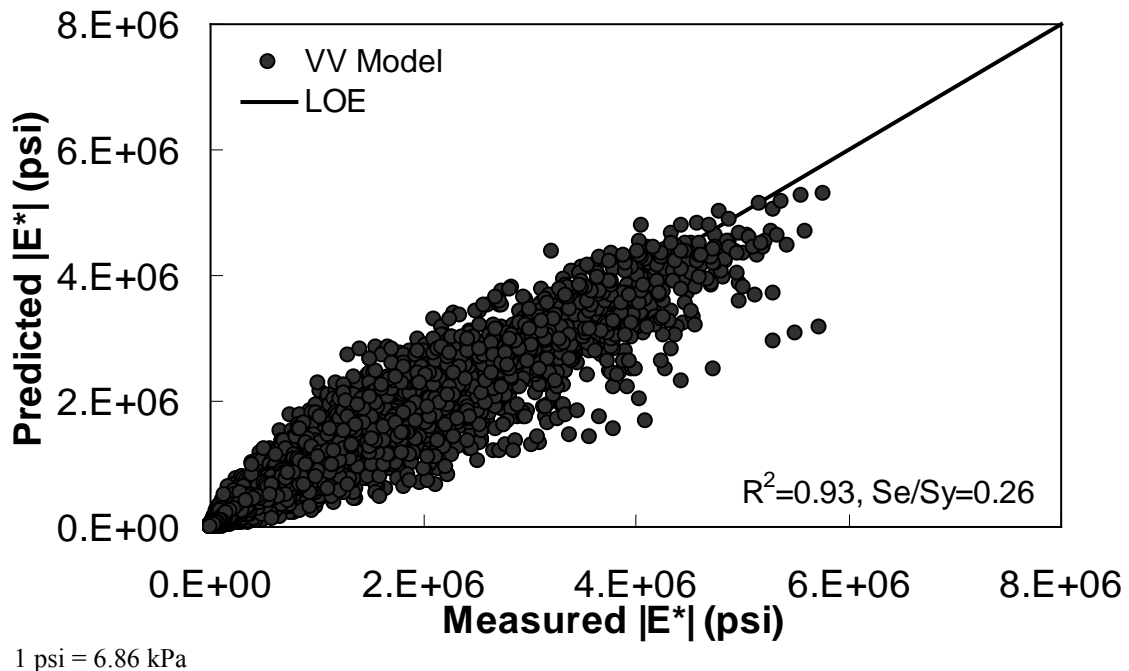
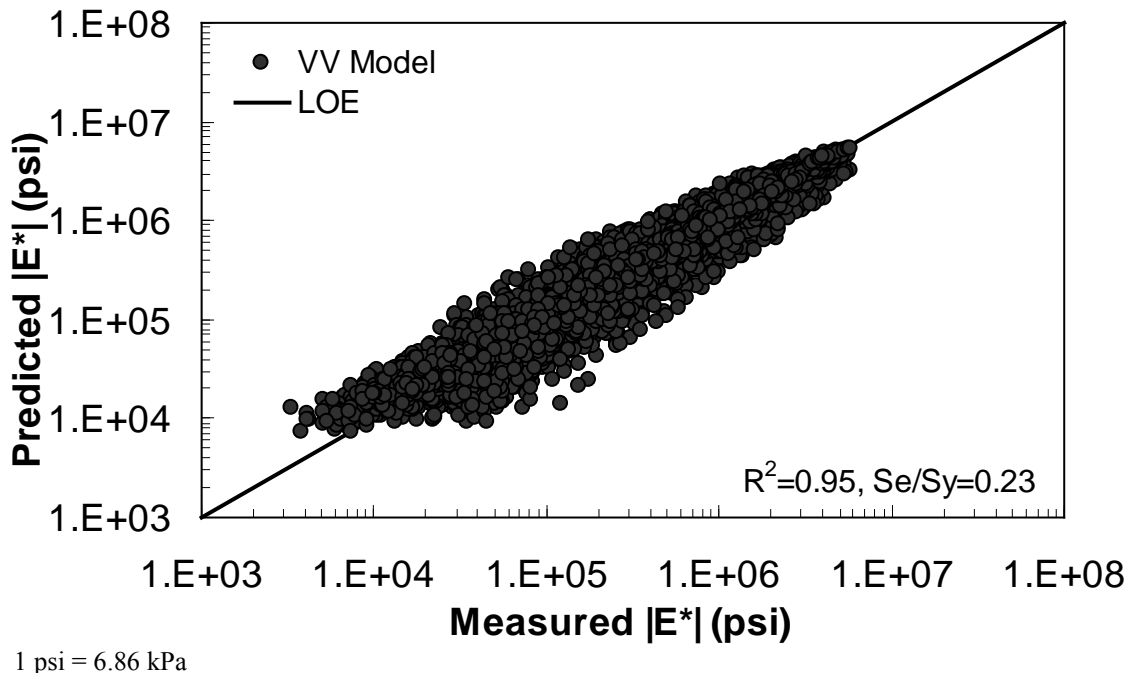
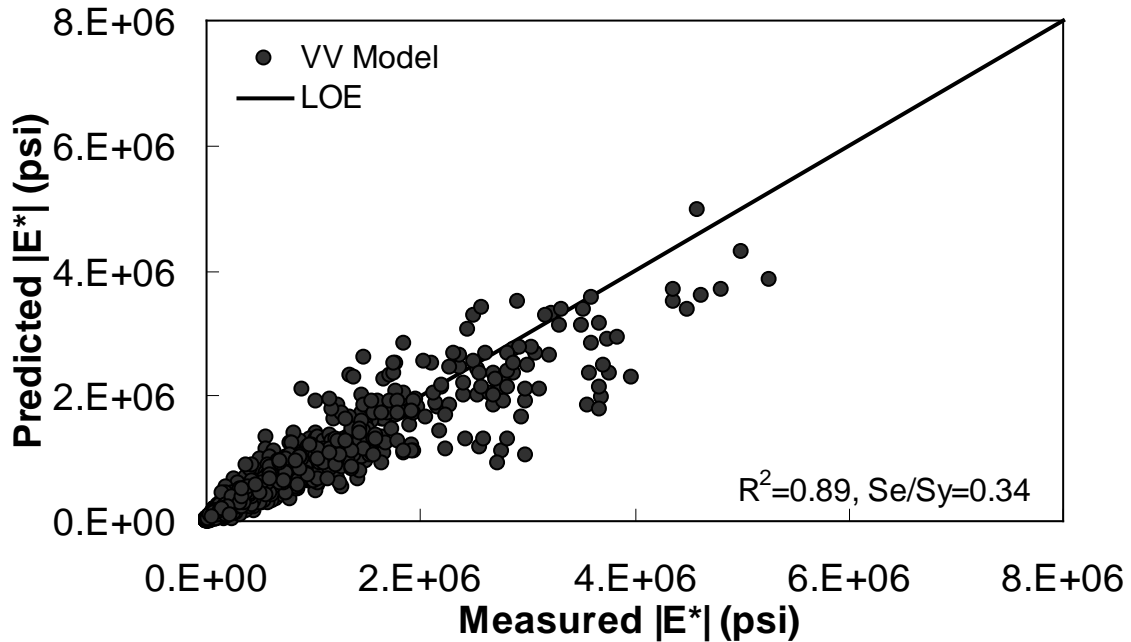


**Figure 52. Graph. VV ANN model using 90 percent of randomly selected data as a training set in arithmetic scale.**



1 psi = 6.86 kPa

**Figure 53. Graph. VV ANN model using 90 percent of randomly selected data as a training set in logarithmic scale.**



1 psi = 6.86 kPa

**Figure 54. Graph. VV ANN model using 10 percent of randomly selected data as a verification set in arithmetic scale.**

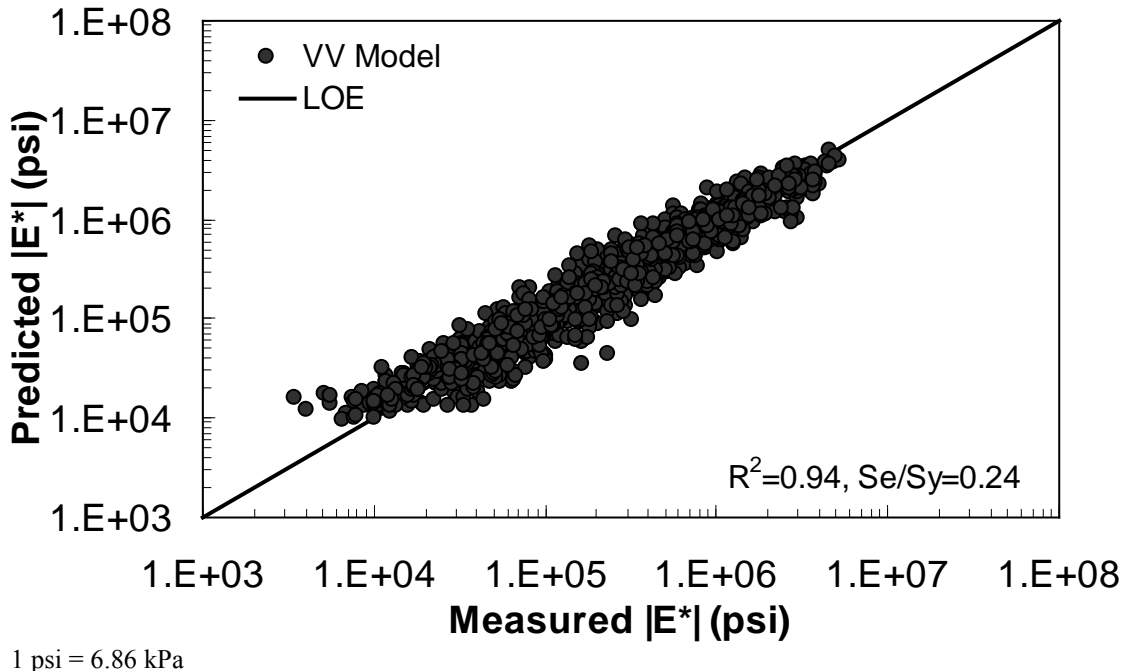


**Figure 55. Graph. VV ANN model using 10 percent of randomly selected data as a verification set in logarithmic scale.**

### 5.3 GV ANN MODEL

The characterization and verification results of the GV ANN model are shown in figure 56 through figure 59. The calibration dataset for this model shows similar or slightly better fitting statistics than the VV ANN model, with an  $R^2 = 0.96$  (0.90 in arithmetic space) and a  $Se/Sy = 0.19$  (0.32 in arithmetic space). The verification plots are shown in figure 58 and figure 59, and the model predictions agree favorably with the measured moduli. Care must be taken when visually comparing the predictability of the VV ANN and GV ANN models because each uses a different number of datapoints for calibration and verification (see table 21).

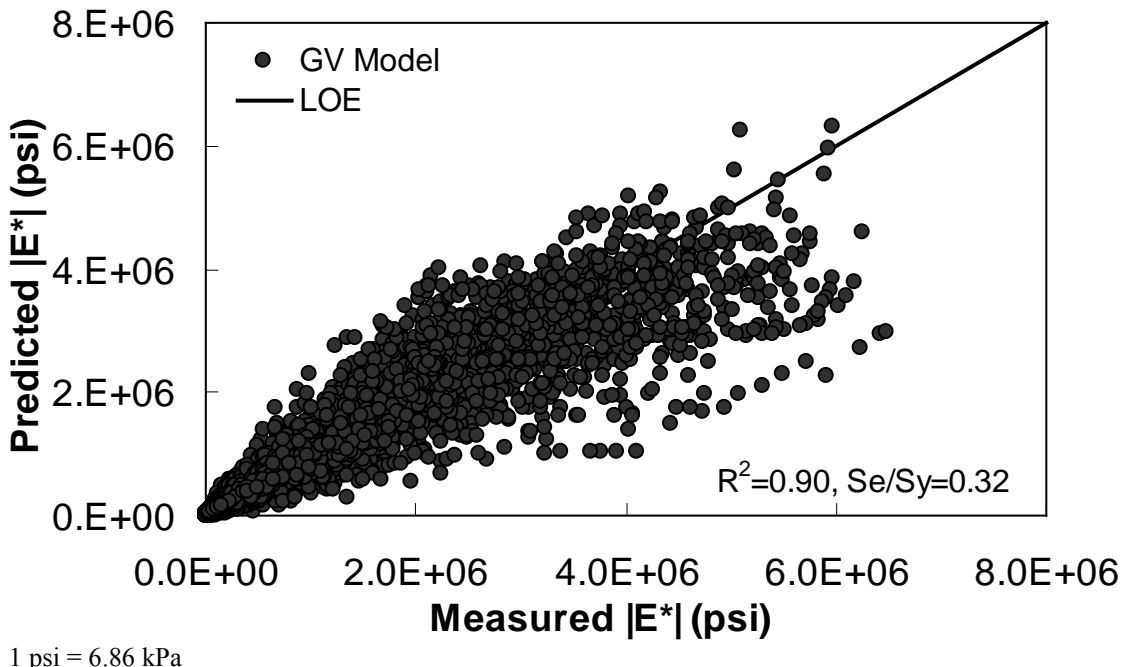


**Figure 56. Graph. GV ANN model using 90 percent of randomly selected data as a training set in arithmetic scale.**

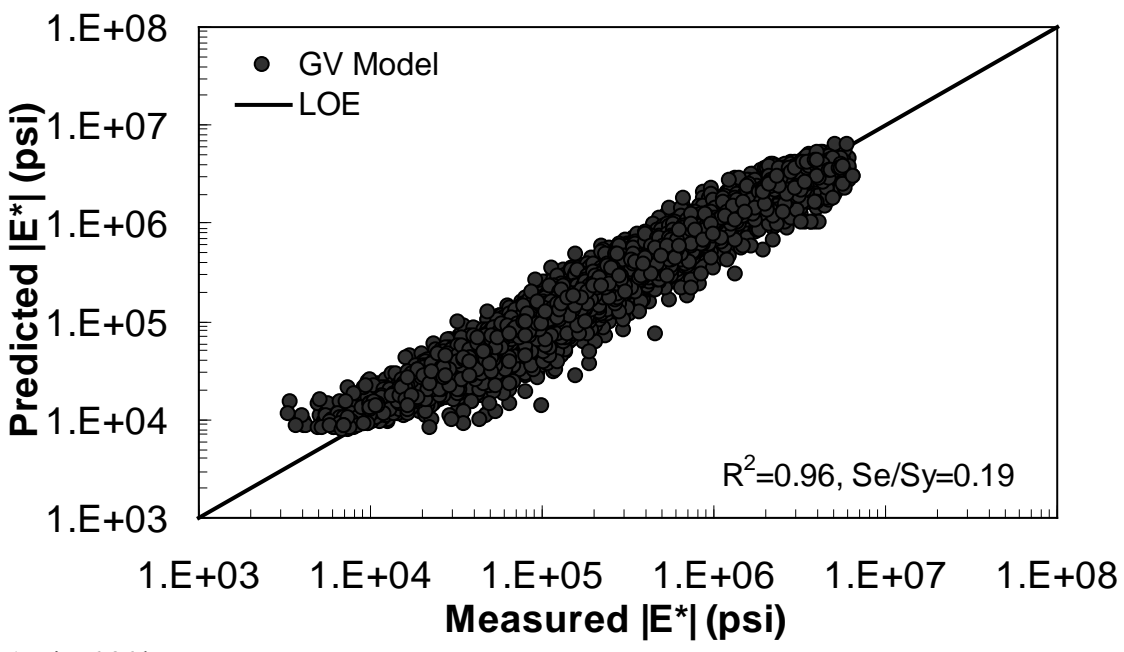


**Figure 57. Graph. GV ANN model using 90 percent of randomly selected data as a training set in logarithmic scale.**

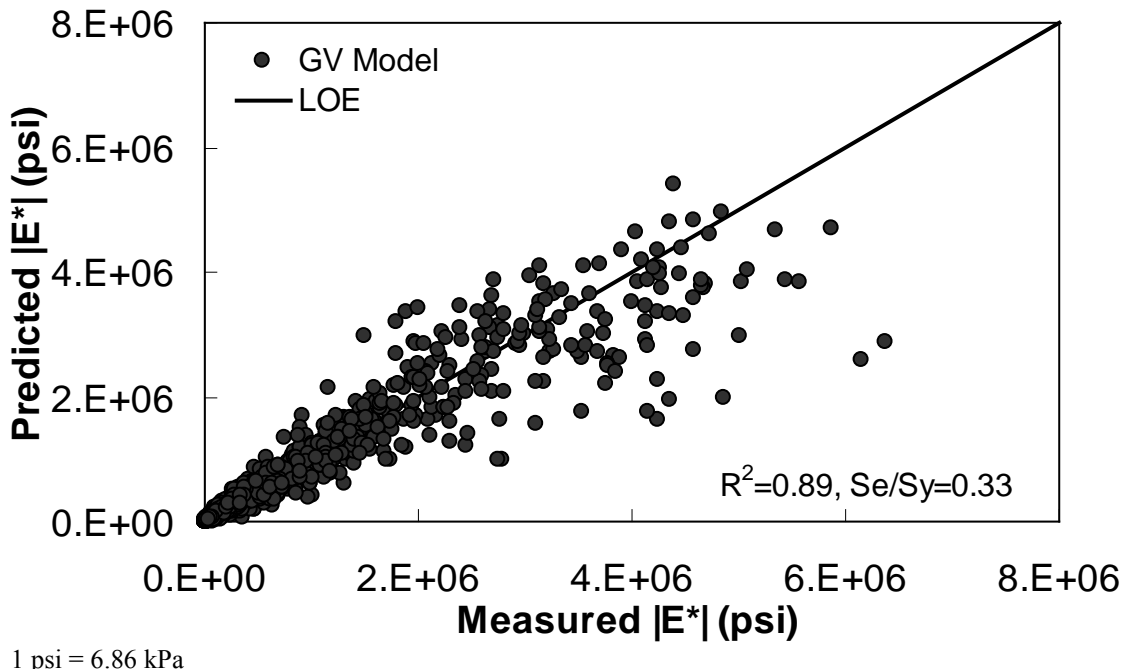


**Figure 58. Graph.** GV ANN model using 10 percent of randomly selected data as a verification set in arithmetic scale.

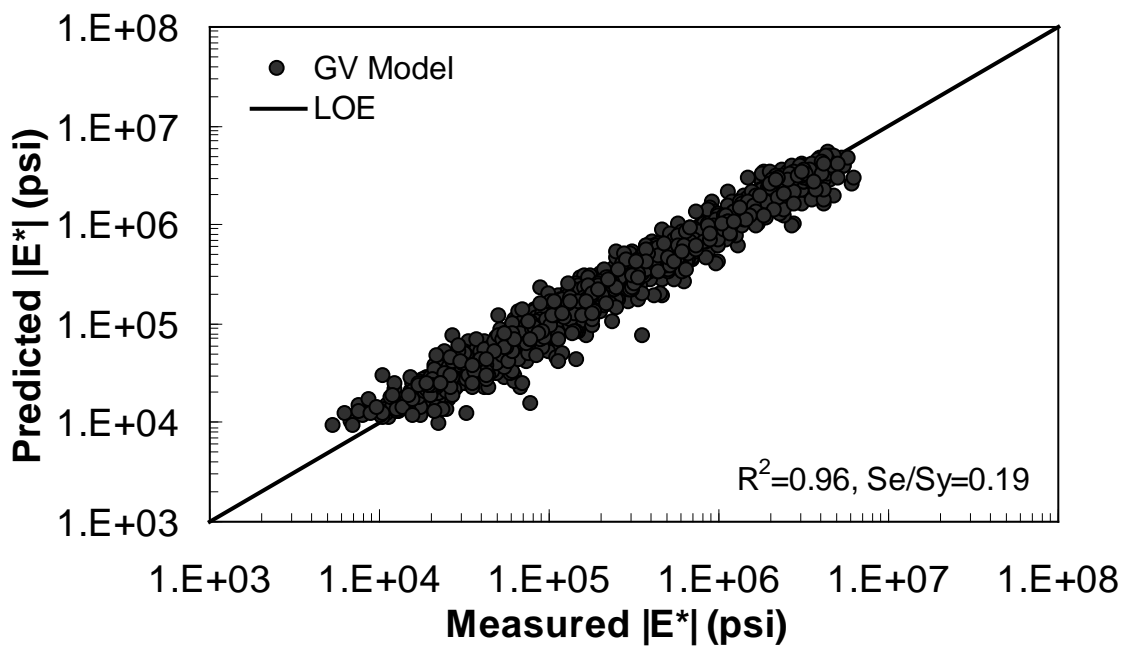


**Figure 59. Graph.** GV ANN model using 10 percent of randomly selected data as a verification set in logarithmic scale.

## 5.4 OTHER ANN MODELS

Through the course of this study, some effort was made to develop ANN models with gravimetric (as opposed to volumetric) input variables. Ultimately, these models were not fully developed nor were they used in the modeling efforts because, after a preliminary review, it was determined that such models would not be useful. Although it is true that some layers contained gravimetric-based effective asphalt contents, these sections also contained enough information to allow the volumetric properties VMA and VFA to be computed. The most common relationship for the three key volumetric properties is shown in equation 49 as follows:

$$V_a = VMA \left( 1 - \frac{VFA}{100} \right) \quad (49)$$

## 5.5 ERROR ASSESSMENT

For statistical validity, the expected error for each of the three main ANN models has been assessed using the following error function:

$$\%Error = \frac{|E^*|_{Measured} - |E^*|_{Predicted}}{|E^*|_{Measured}} * 100 \quad (50)$$

A probability distribution function for the error was computed for each model by using the verification dataset for the respective model. These datasets are shown in figure 50 and figure 51 for  $M_R$  ANN, figure 54 and figure 55 for VV ANN, and figure 58 and figure 59 for GV ANN. The distribution function is shown for each model, including the previously discussed closed-form models presented in table 23. The distribution of each error function is approximately normal and, as such, the error values that encompass a 95 percent reliability interval for the percentage of error in each model can be readily computed.

Because the number of data points used to verify each model is so large (see the last row in table 23), the distribution is assumed normal, and a  $z$ -score of 1.96 is used to compute the reliability ranges.  $Sy$  is computed after compiling the percent error values for each prediction of the respective model. After rounding slightly for convenience, the suggested reliability range for each ANN model is as follows:

- $M_R$  ANN:  $\pm 55$  percent.
- VV ANN:  $\pm 75$  percent.
- GV ANN:  $\pm 60$  percent.

It is also found from table 23 that when the closed-form solutions are applied to a completely independent dataset, each solution yields a substantial number of predictions with errors exceeding -105 percent. The dataset used to compute these statistics is completely independent of the data used in calibrating any of these closed-form solutions. It also includes a mixture of AMPT and TP-62 measured moduli.<sup>(8)</sup> The high number of large negative error observations

suggests a bias towards over-prediction of the  $|E^*|$  values with each model. The bias in predictions can be clearly observed by examining figure 8 for the modified Witczak model and figure 10 for the Hirsch model. A comparison of figure 7 and figure 9 shows a tendency of the Hirsch model to underpredict  $|E^*|$  at higher modulus values more so than the modified Witczak model. This trend is also captured in table 23, where the error distribution for the Hirsch model is skewed towards positive values. As a result of the existence of these prediction errors, the reliability ranges for the closed-form solutions are much larger than the ranges observed for the ANN models as follows:

- Original Witczak:  $\pm 200$  percent.
- Modified Witczak:  $\pm 175$  percent.
- Hirsch:  $\pm 125$  percent.

**Table 23. Probability distribution of error functions of each ANN model.**

Percentage Error Range	ANN Model (Percentage Within Range)					
	$M_R$	VV	GV	Original Witczak	Modified Witczak	Hirsch
< -105	0.75	2.31	0.49	22.04	31.12	10.25
-105 to -90	0.32	0.86	0.77	2.86	5.11	2.65
-90 to -75	0.43	1.91	1.05	3.15	8.43	3.14
-75 to -60	0.21	2.44	2.02	3.72	8.97	4.46
-60 to -45	0.53	4.75	3.42	7.06	10.49	5.86
-45 to -30	5.98	7.59	8.02	8.30	11.39	8.58
-30 to -15	15.06	14.32	16.11	9.83	9.24	12.34
-15 to 0	24.89	17.56	21.34	10.11	7.89	14.57
0 to 15	28.53	19.14	21.48	12.02	4.48	13.81
15 to 30	19.02	15.12	15.69	13.65	2.06	10.11
30 to 45	3.74	8.65	6.28	6.20	0.54	7.67
45 to 60	0.32	4.16	2.58	1.05	0.27	4.81
60 to 75	0.21	1.06	0.63	0.00	0.00	1.39
75 to 90	0.00	0.13	0.14	0.00	0.00	0.35
> 105	0.00	0.00	0.00	0.00	0.00	0.00
Number of data points used	936	1,515	1,434	1,048	1,115	1,434



## 6.0 PREDICTION OF $E^*$ FOR LTPP LAYERS

### 6.1 MODEL PRIORITIZATION AND DECISION TREE DEVELOPMENT

The developed ANN models were ranked based on the performance of each model for an independent dataset that contains all of the required input parameters to be used in the different models. The decision tree in figure 60 is the result of this prioritization and was used to populate the LTPP database. As suspected at the outset of this project, the  $M_R$  ANN model yields the best prediction possible and is the preferred model. This finding is not surprising given that the  $M_R$  ANN model takes actual mixture measured quantities as input. The intuition is also supported in the fitting statistics shown in the figures presented in section 5.0. If  $M_R$  data are not available, the next preferred model is the VV ANN model. Although the VV ANN shows poorer fitting statistics than the GV ANN model in terms of logarithmic space, it shows better statistics in terms of arithmetic space. The arithmetic statistics were used to rank these models because the moduli values are expressed and utilized in terms of their arithmetic value. Of the three ANN models, GV ANN received the lowest ranking. However, GV-PAR outranked the VV-grade because the model GV-PAR uses measurements taken directly from the material of interest. The VV-grade model uses viscosity values representative of the binder grade.

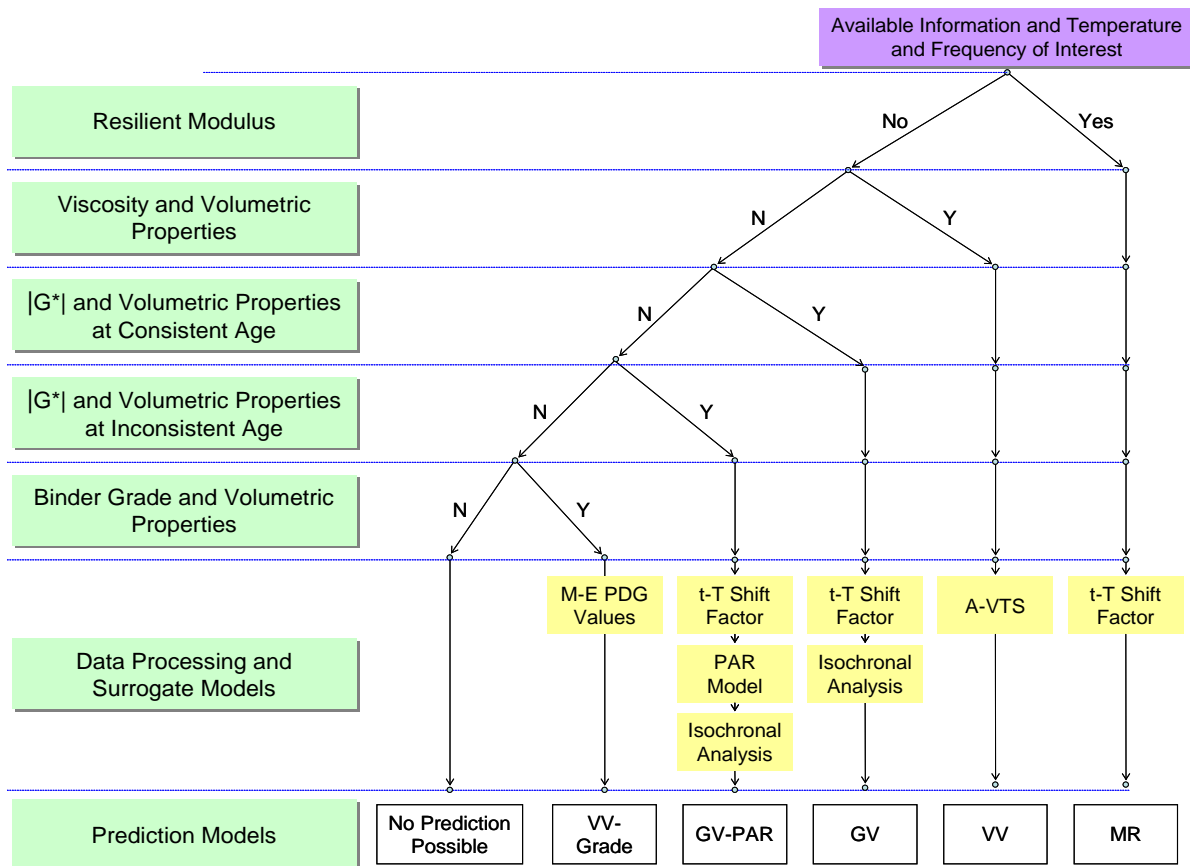


**Figure 60. Illustration. Decision tree applied to population of LTPP database based on ranking of ANN models.**

The input sets available for each section are different. Consequently, the models that can be utilized for a given section may differ. All the models that can be used for a specific section have been identified. If any of the inputs are outside the range of the calibration data, then the model for that section is considered to be a violated model, and predictions with it may or may not be reasonable. Any available model that does not violate the input range criteria is used as the predictive model for that section. In cases where only two violated models are available, the model for that section must be decided manually by the user.

## 6.2 DATA QC

Two sets of internal QC checks were applied to the  $|E^*|$  data produced for submission to the LTPP database. The first QC check was used on the input values. All the other QCs were used to check the output  $|E^*|$  predictions. In the following sections, each of these QC criteria is described. The work criterion is implied but not explicitly stated for each of these checks. The quality grading system referenced is different than the standard record status definition used in the LTPP database. For example, data assigned an “A” by the research team represent the highest quality data, whereas the LTPP convention assigns an “E” to the highest quality data. The research team established strict QC checks for these data to ensure that only the highest quality data were assigned an “A” grade. The data that did not achieve an “A” grade should be used with caution, and users should be fully aware that the data did not pass the QC check. All predictions are included in the database so users can determine whether or not the data are suitable for their needs. In addition, FHWA can revise the criteria used in the QC checks as deemed appropriate based on the opinions of their experts.

### 6.2.1 QC #1

QC #1 checks for a violation of the input range used in each model based on the input ranges of the calibration dataset, as seen in (see table 24). Figure 61 through figure 65 show example predictions of  $|E^*|$  in two sections where violations of the input criteria have been detected. This check is performed on a line-by-line basis, meaning that each time a modulus is predicted, the input parameters are checked. Lines that pass the QC check receive a grade of “A,” whereas those that do not pass the QC check receive a grade of “F.”

For the layers where  $|E^*|$  predictions are estimated using the  $M_R$  ANN model but QC #1 is violated, the mastercurve created appears visually continuous (see figure 61 and figure 62). The reason for this appearance is that the output of this model is the mastercurve itself. However, the output of the other two ANN models is the estimation of  $|E^*|$  under a specific condition. In this case, a violation of QC #1 may create a clear error in the mastercurve, as demonstrated in figure 63 through figure 65. The acceptable range of input parameters is shown for the three ANN models in table 24. These models do not estimate the information needed to create the mastercurve.

**Table 24. Input ranges of different ANN models.**

Model	Range	Parameter								
		$M_R$ 5 °C (GPa)	$M_R$ 25 °C (GPa)	$M_R$ 40 °C (GPa)	$f_R$ (Hz)	Viscosity ( $10^9$ P)	VMA (percent)	VFA (percent)	$ G^* $ (psi)	$\text{Log}( E^* )$ (psi)
MR	Min	4.8003	1.081	0.3789		0.01 25	9.51 34.64	32.82 95.07		
	Max	34.053	15.411	6.8637						
VV-grade <sup>1</sup>	Min				0.01	1.99E-06	9.51	32.82		3.52
	Max				25	2.70E+01	34.64	95.07		6.82
GV-PAR <sup>1</sup>	Min						9.51	32.82	2.93E-02	3.52
	Max						22.21	95.07	6.76E+05	6.81

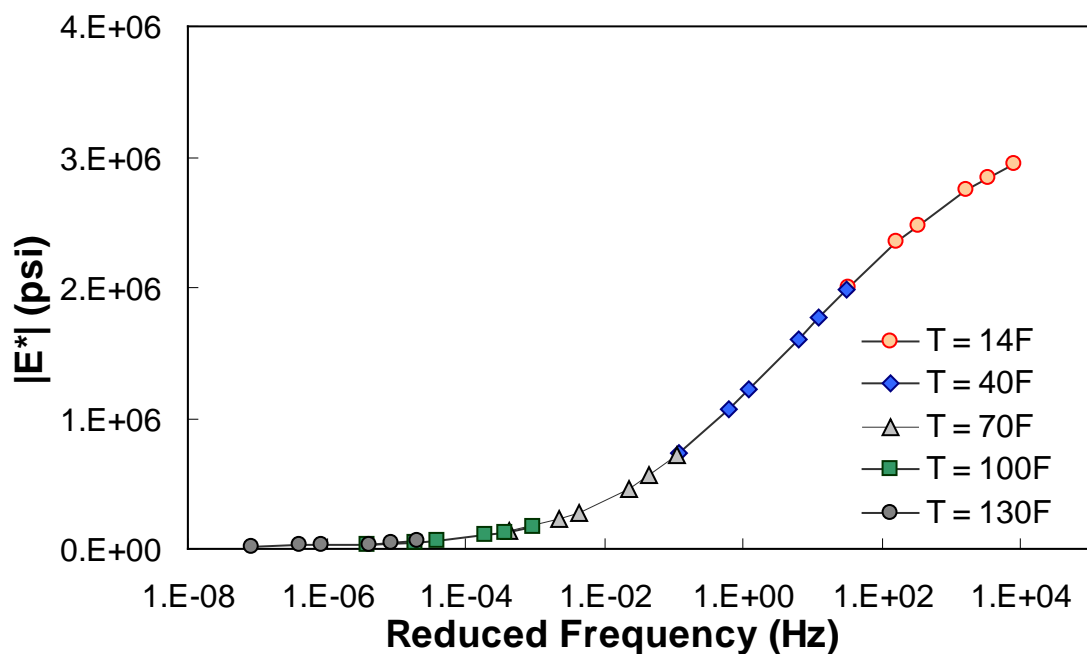
°C = (°F-32)/1.8

1 Pas = 10 P

1 psi = 6.86 kPa

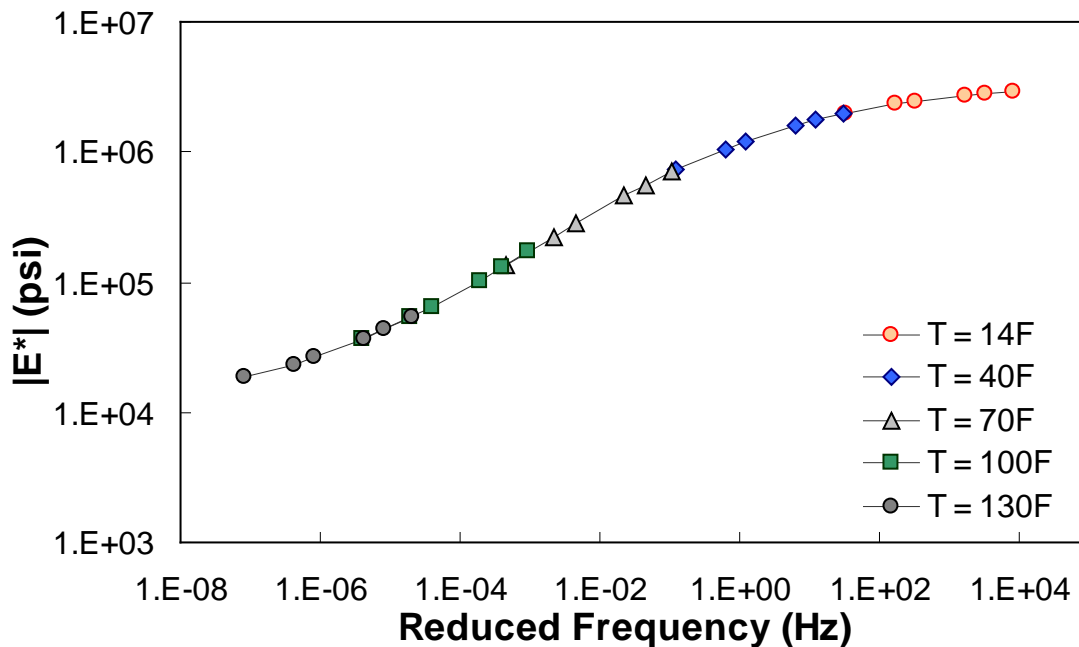
<sup>1</sup>Indicates that VV-grade and GV-PAR have the same range of input.

Note: Blank cells indicate that the input parameter is not required in the model.



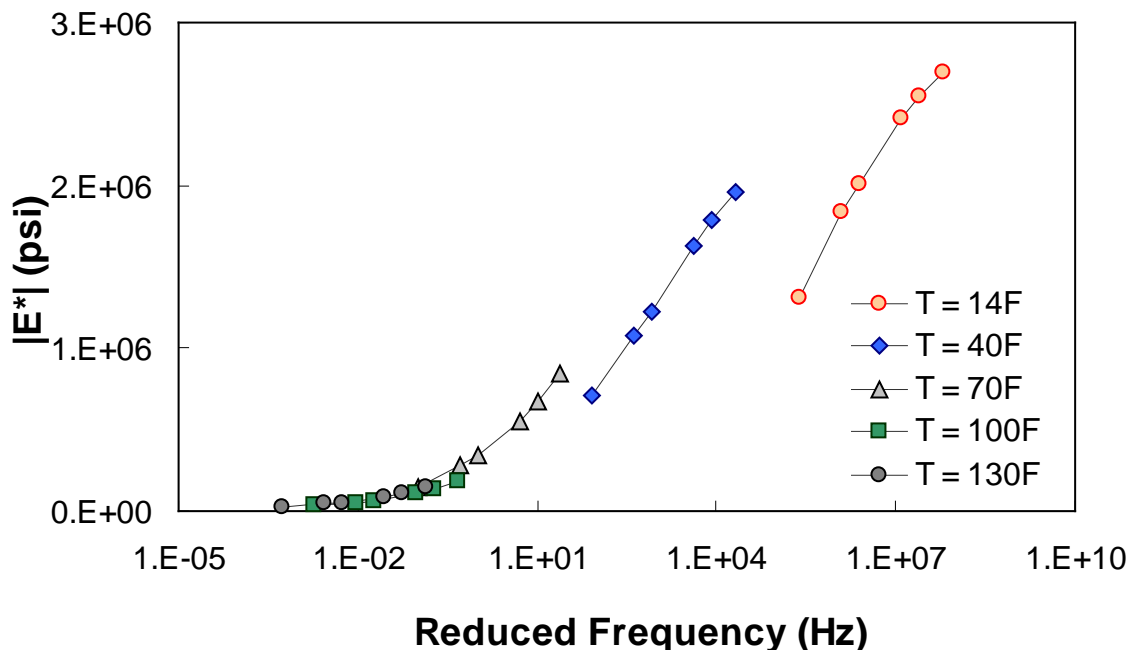
1 psi = 6.86 kPa

**Figure 61. Graph. Example of the effect of a violation of QC #1 for  $M_R$  ANN model in semi-log scale.**



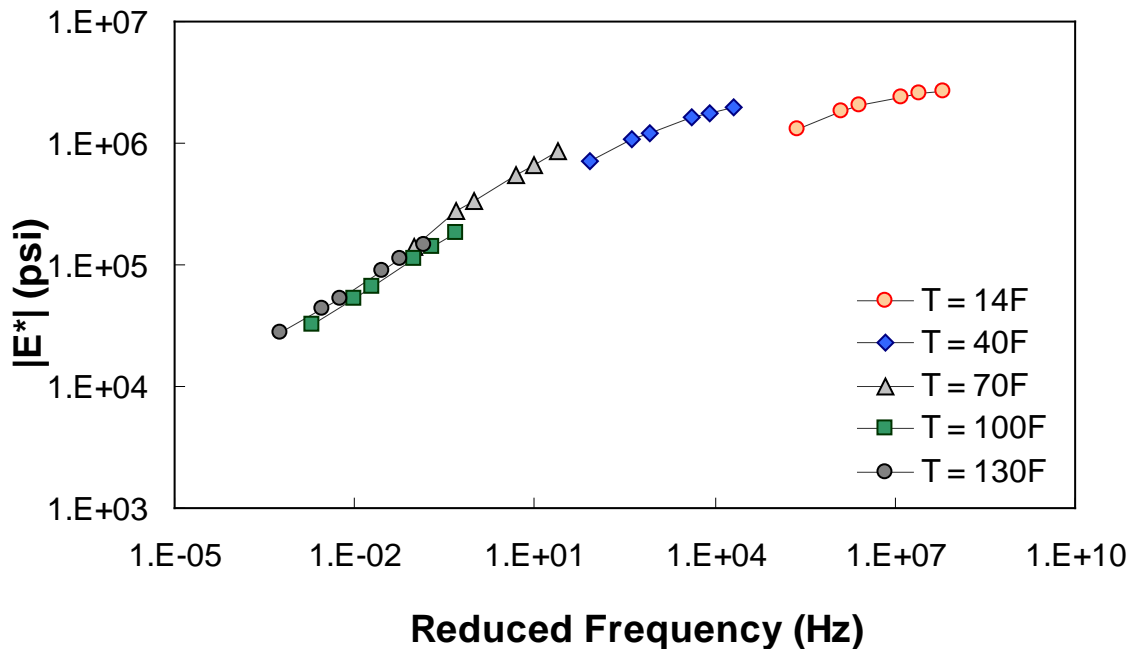
$1 \text{ psi} = 6.86 \text{ kPa}$

**Figure 62. Graph. Example of the effect of a violation of QC #1 for  $M_R$  ANN model in log-log scale.**



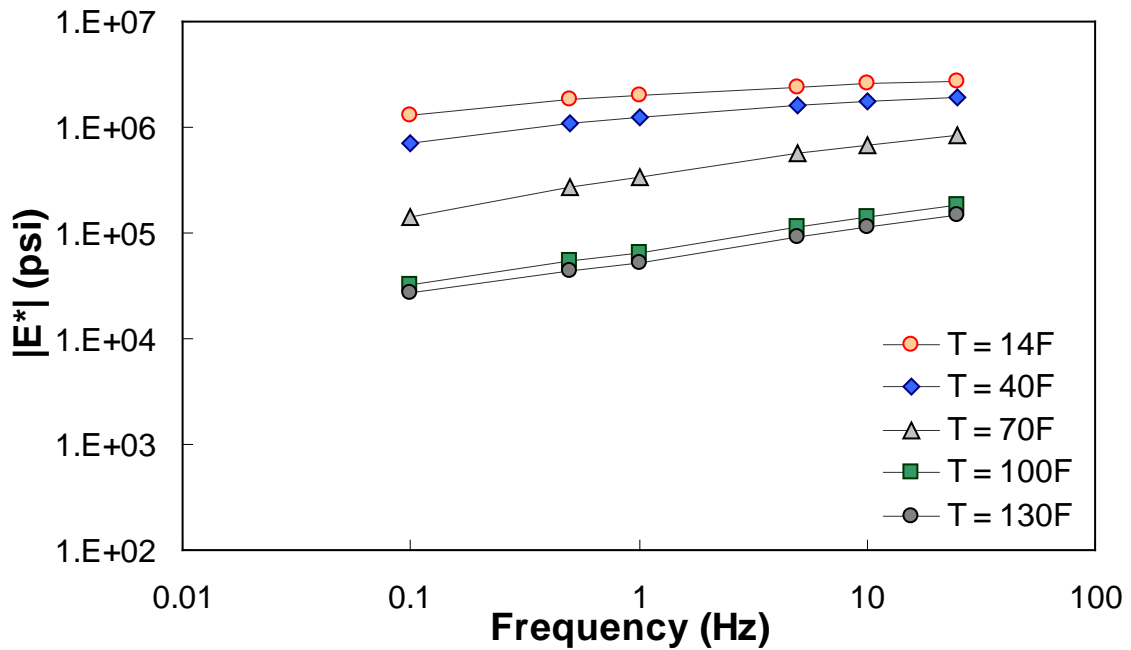
$1 \text{ psi} = 6.86 \text{ kPa}$

**Figure 63. Graph. Example of the effect of a violation of QC #1 for VV ANN model in semi-log scale.**



1 psi = 6.86 kPa

**Figure 64.** Graph. Example of the effect of a violation of QC #1 for VV ANN model in log-log scale.

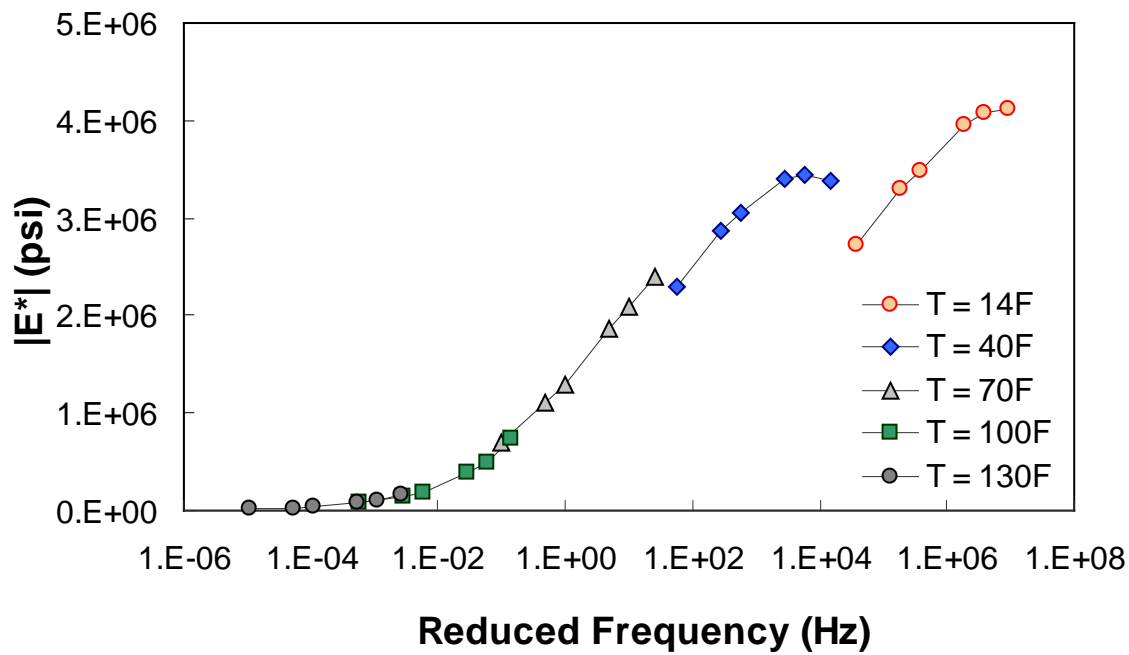


1 psi = 6.86 kPa

**Figure 65.** Graph. Example of the effect of a violation of QC #1 for VV ANN model unshifted data.

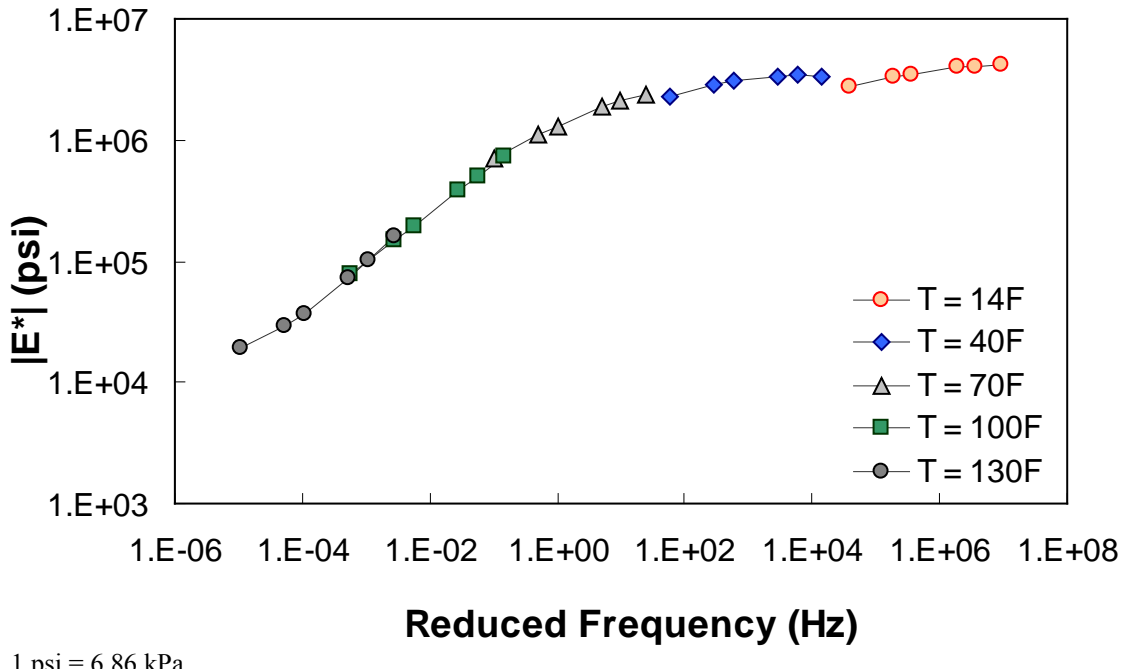
### 6.2.2 QC #2

QC #2 checks the trends of  $|E^*|$  as a function of temperature and frequency. It is expected that  $|E^*|$  decreases as the temperature increases and the loading frequency decreases. Figure 66 through figure 68 show sample cases of a QC #2 violation. In these examples, the predicted  $|E^*|$  value at 40 °F (4.4 °C) and 25 Hz is smaller than the predicted value at 40 °F (4.4 °C) and 10 Hz. Similar to QC #1, this QC check is performed line-by-line; the lines that pass receive a grade of “A,” and those that fail receive a grade of “F.”



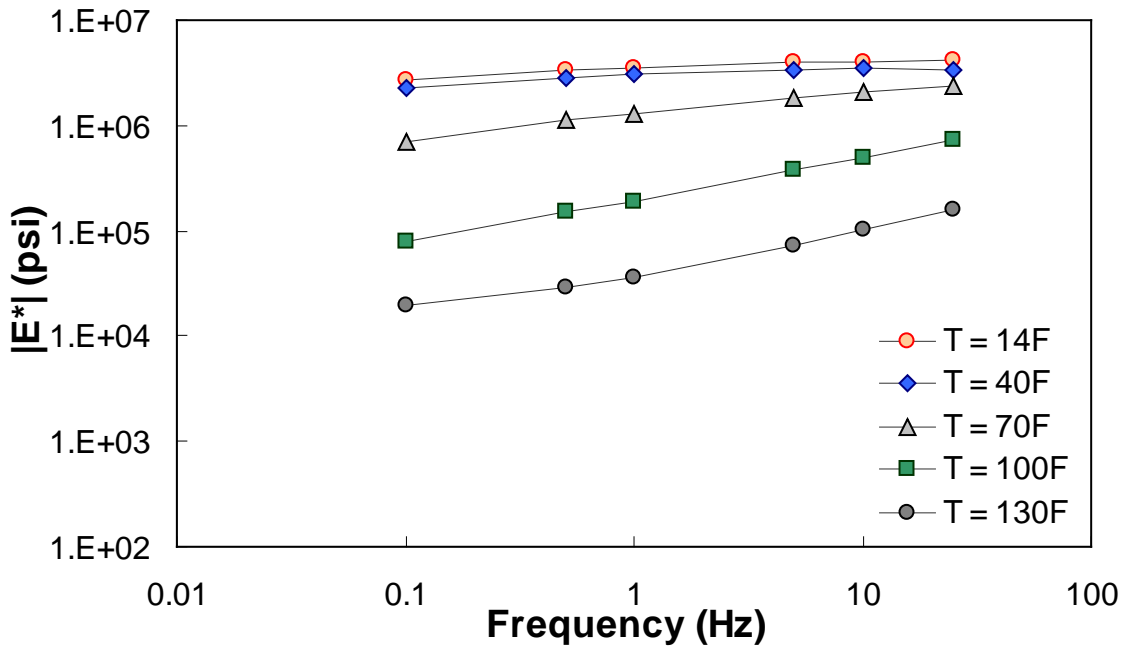
1 psi = 6.86 kPa

**Figure 66.** Graph. Example of the effect of a violation of QC #2 in semi-log scale.



1 psi = 6.86 kPa

**Figure 67. Graph. Example of the effect of a violation of QC #2 in log-log scale.**



1 psi = 6.86 kPa

**Figure 68. Graph. Example of the effect of a violation of QC #2 unshifted data.**

### 6.2.3 QC #3

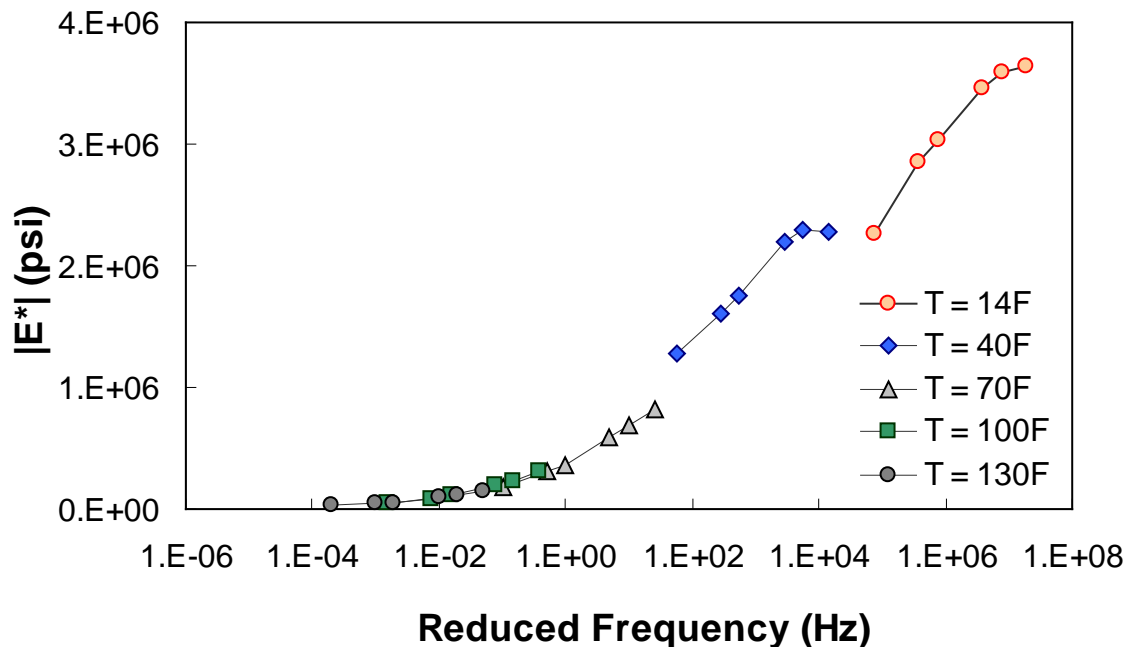
The typical percentage of difference between 0.1 Hz at one temperature and 25 Hz at the next warmest temperature is checked using QC #3. Equation 51 states the percentage of difference and a typical value of this term based on the available data in this study. Figure 69 through

figure 71 show the violation of QC #3 in one of the sections. For this particular section, a violation occurred between 40 and 70 °F (4.4 and 21.1 °C). For this sample case, at 0.1 Hz and 40 °F (4.4 °C), the modulus is equal to  $1.29 \times 10^6$  psi ( $8.85 \times 10^6$  kPa). At 25 Hz and 70 °F (21.1 °C), the modulus is equal to  $8.28 \times 10^5$  psi ( $56.8 \times 10^5$  kPa), which is a percentage difference of 55.4 percent.

$$\% \text{ Difference} = \frac{\text{LowerTemperature}@0.1\text{Hz} - \text{HigherTemperature}@25\text{Hz}}{\text{HigherTemperature}@25\text{Hz}} \quad (51)$$

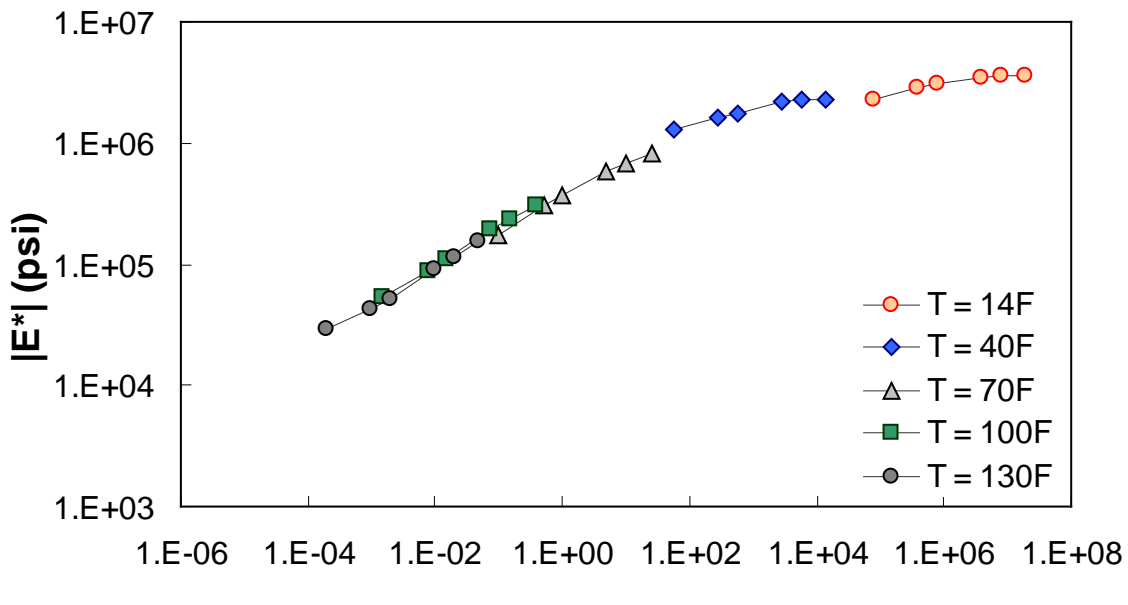
- From 14 to 40 °F (-10 to 4.4 °C): +25 percent, -25 percent.
- From 40 to 70 °F (4.4 to 21.1 °C): +50 percent, -75 percent.
- From 70 to 100 °F (21.1 to 37.7 °C): +50 percent, -75 percent.
- From 100 to 130 °F (37.7 to 54.4 °C): +50 percent, -75 percent.

Unlike the previous QC checks, QC #3 is performed on the basis of temperature. For example, if the percentage of difference between 14 and 40 °F (-10 and 4.4 °C) exceeds 25 percent, then all of the predictions at 14 °F (-10 °C) would receive a grade of “F.”



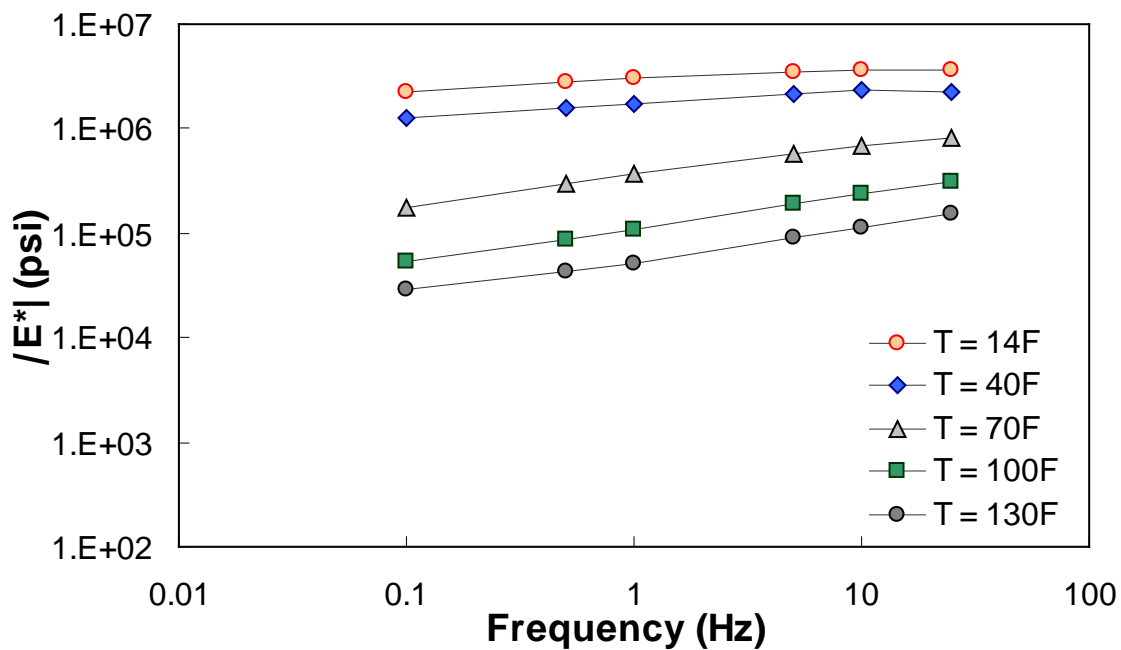
1 psi = 6.86 kPa

**Figure 69. Graph. Example of the effect of a violation of QC #3 in semi-log scale.**



1 psi = 6.86 kPa

**Figure 70. Graph.** Example of the effect of a violation of QC #3 in log-log scale.



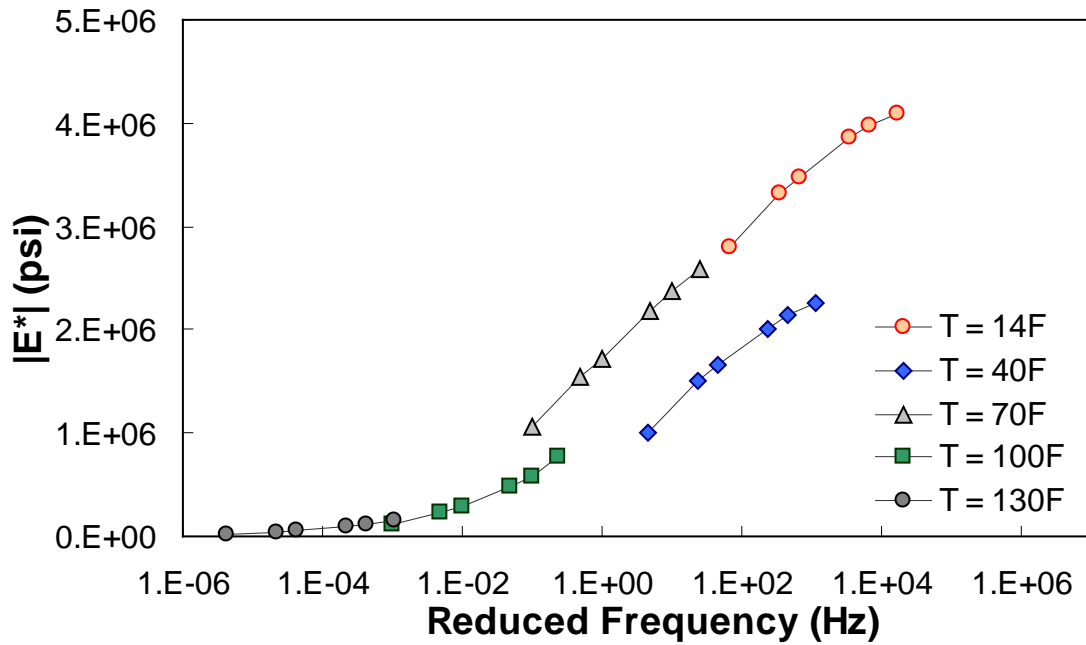
1 psi = 6.86 kPa

**Figure 71. Graph.** Example of the effect of a violation of QC #3 unshifted data.

#### 6.2.4 QC #4

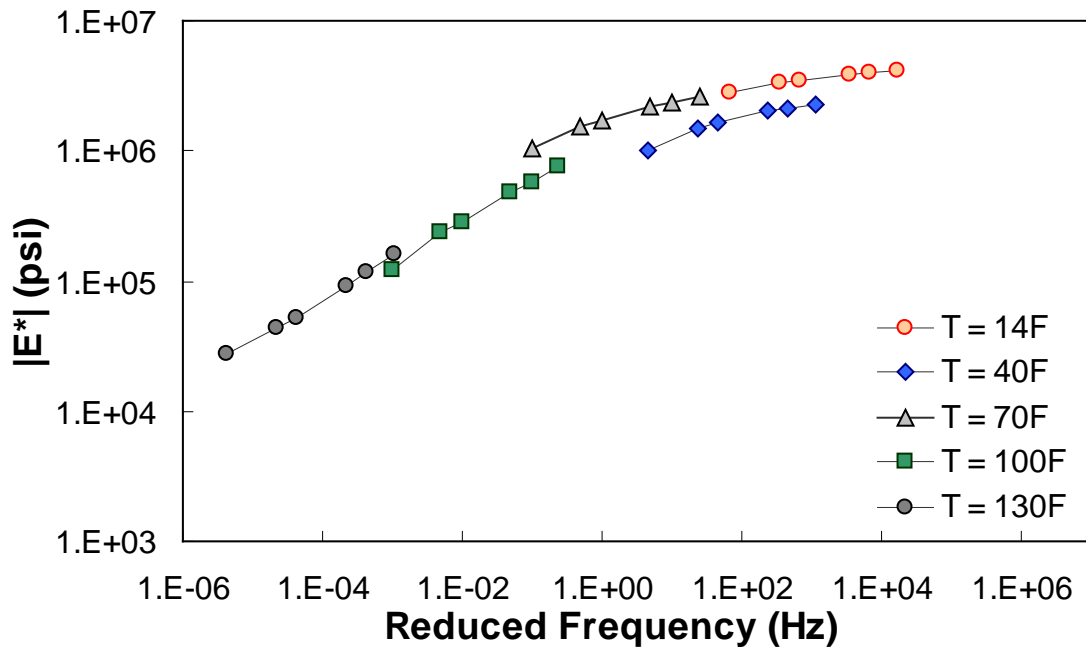
in QC #4, the difference in  $|E^*|$  values predicted between 0.1 Hz at one temperature and 0.1 Hz at the next warmest temperature is checked to see if appropriate trends with regard to temperature and modulus hold. Sample cases of QC #4 violation are shown in figure 72 through

figure 74. For the data in these figures,  $|E^*|$  at 0.1 Hz and 40 °F (4.4 °C) is smaller than  $|E^*|$  at 0.1 Hz and 70 °F (21.1 °C). In the case shown in these figures, this situation has led to a discontinuous mastercurve because the optimization algorithm becomes confused when the modulus does not decrease as the temperature increases. Similar to QC #3, QC #4 is applied on a temperature basis.



1 psi = 6.86 kPa

**Figure 72. Graph.** Example of the effect of a violation of QC #4 in semi-log scale.



1 psi = 6.86 kPa

**Figure 73. Graph.** Example of the effect of a violation of QC #4 in log-log scale.

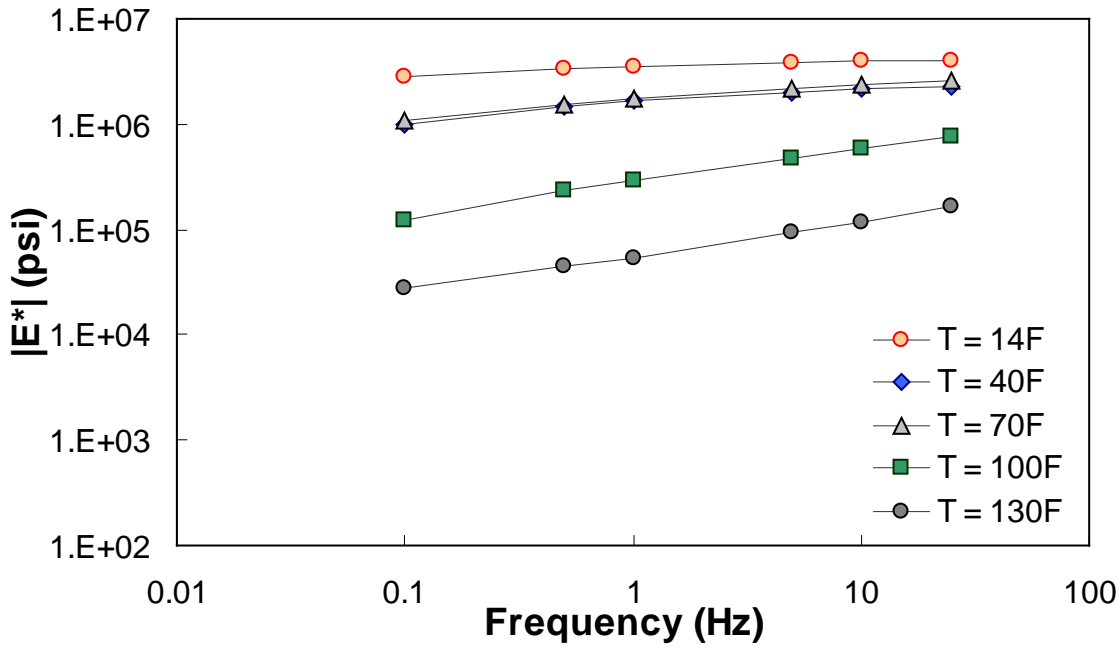


**Figure 74. Graph. Example of the effect of a violation of QC #4 unshifted data.**

### 6.2.5 QC #5

QC #5 checks the range of shift factor values in the output predictions against typical values. This check is used to indicate potential problems with the mastercurve generation process. The limits identified and subsequently used are as follows:

- At 14 °F (-10 °C):  $3 < \log(a_T) < 7$
- At 130 °F (54.4 °C):  $-5 < \log(a_T) < -2$

The output parameters of interest from the ANNACAP software are SHIFT\_FACTOR\_COEFFICIENT 1 ( $\alpha_1$ ), SHIFT\_FACTOR\_COEFFICIENT 2 ( $\alpha_2$ ), and SHIFT\_FACTOR\_COEFFICIENT 3 ( $\alpha_3$ ). The shift factor is computed using equation 52 as follows:

$$\log(a_T) = \alpha_1 T^2 + \alpha_2 T + \alpha_3 \quad (52)$$

Because the goal of this QC criterion is to judge the mastercurve generation process, only shift factor values at extreme temperatures need to be examined. Note that because the  $M_R$  ANN model predicts the mastercurve directly, any predictions made with this model will automatically pass QC #5 without the need for calculation. When this QC is not passed, the entire section (at all temperatures) receives a grade of “F.”

Figure 75 through figure 77 show violations of QC #5. In these cases, the shift factor at 14 °F (-10 °C) is equal to 7.03. This effect results in a visual discontinuity in the mastercurve between the 14- and 40-°F (-10- and 4.4-°C) datasets.

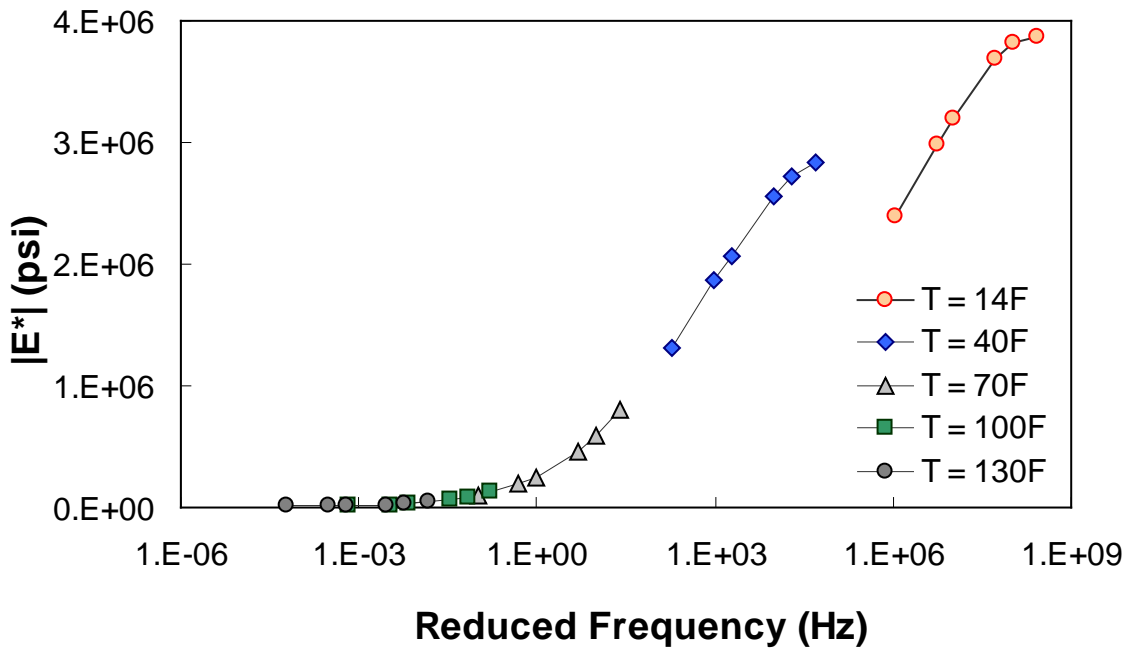


**Figure 75.** Graph. Example of the effect of a violation of QC #5 in semi-log scale.

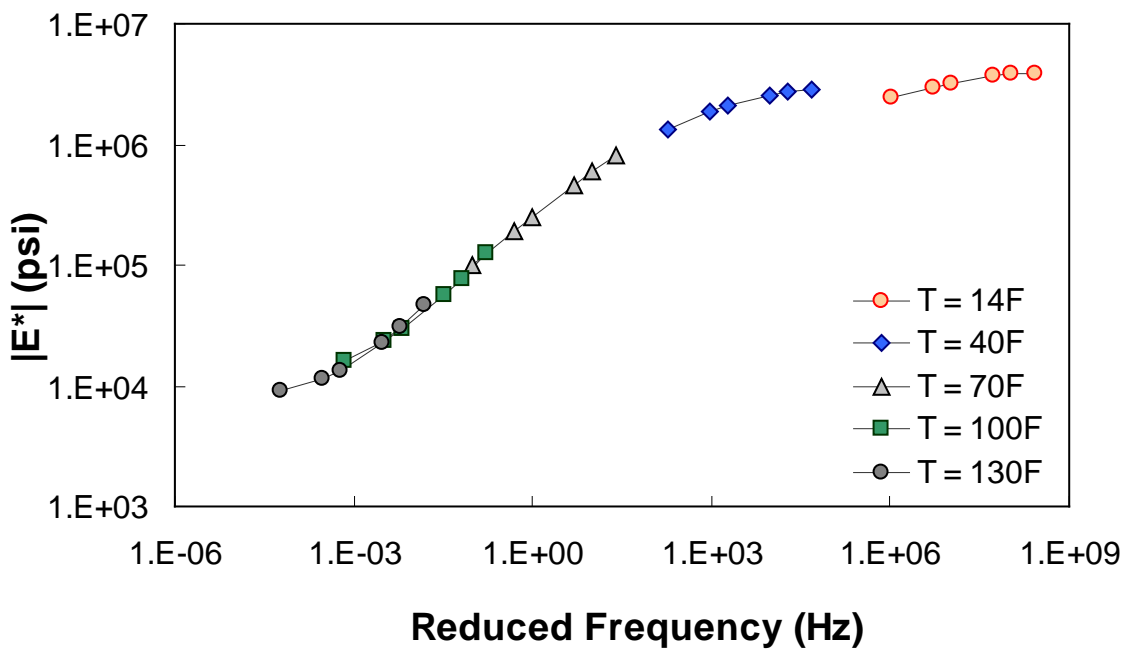
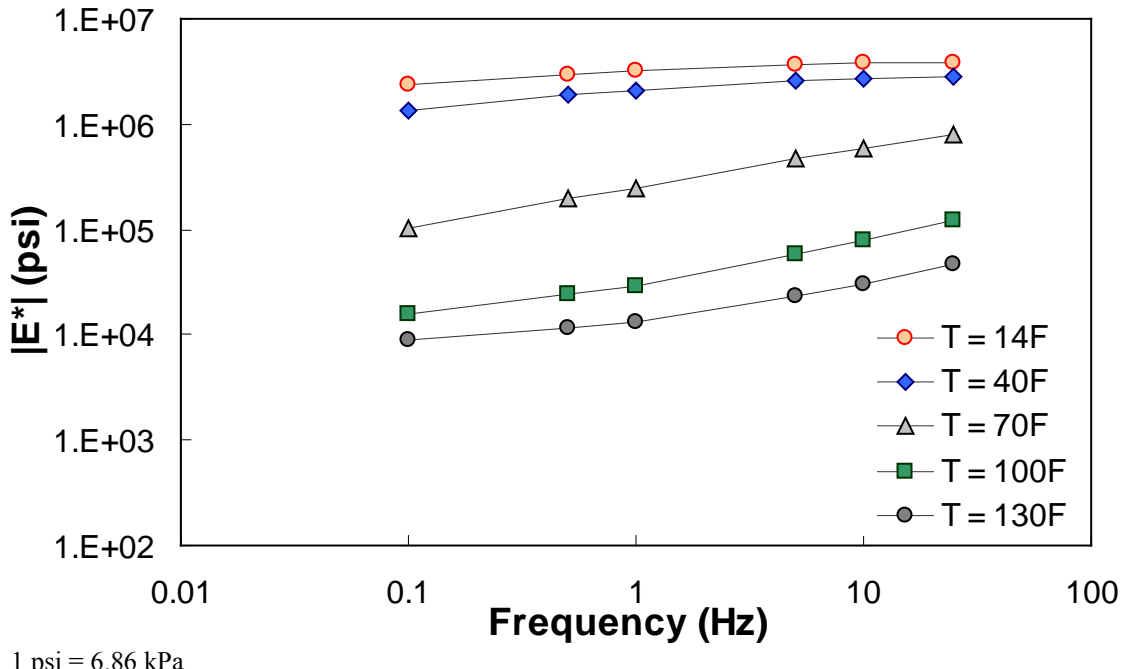


**Figure 76.** Graph. Example of the effect of a violation of QC #5 in log-log scale.



1 psi = 6.86 kPa

**Figure 77. Graph. Example of the effect of a violation of QC #5 unshifted data.**

### 6.2.6 QC #6

In an earlier version of the ANN models developed for this study, some cases had inputs within the calibration input range, but the  $|E^*|$  predictions obtained values of the limits of the calibration data. In some other cases,  $|E^*|$  did not change with varying temperature and frequency. QC #6 was expected to be the last QC check, but after improving the ANN models, the problem no longer exists. Nevertheless, the check is performed on the data. The limiting  $|E^*|$  values used to judge whether a given prediction passes this QC check are given in table 25. Like QC #1 and QC #2, this QC check is applied line-by-line.

**Table 25. Limiting  $|E^*|$  values used for QC #6.**

Model	Upper Limit (psi)	Lower Limit (psi)
$M_R$ ANN	N/A	N/A
VV ANN	5,888,437	3,311.311
GV ANN	6,456,542	3,311.311

1 psi = 6.86 kPa

N/A indicates that data are not available.

### 6.2.7 QC #7

Similar to QC #5, QC #7 is designed to judge the mastercurve generation process. Each time a mastercurve is generated, fitting statistics are computed. These statistics include the  $Se/Sy$  (of combined predictions), and  $R^2$ . According to the draft standard for mastercurve generation using AASHTO TP-62 data, the explained variance should be greater than 0.99, and the ratio of  $Se/Sy$  should be less than 0.05.<sup>(42)</sup> When these limits are exceeded, QC #7 is triggered, and the layer

fails. Because the  $M_R$  ANN model predicts the mastercurve directly, any predictions made with this model will automatically pass QC #7 without the need for calculation. Equations 53–55 are used to compute the necessary statistical parameters. Whenever this QC is violated, the entire section receives a grade of “F.”

$$S_e = \sqrt{\frac{1}{23} \sum_1^n \left[ (\log |E^*|_{ANN})_i - (\log |E^*|_{fit})_i \right]^2} \quad (53)$$

Where:

- 23 = Number of temperature/frequency combinations used minus the number of fitting parameters minus 1.
- $(\log |E^*|_{ANN})_i$  = Logarithm of the modulus determined from the ANN models at a particular temperature frequency combination.
- $(\log |E^*|_{fit})_i$  = Logarithm of the modulus determined from the optimized sigmoidal fit.

$$S_y = \sqrt{\frac{1}{29} \sum_1^n \left[ (\log |E^*|_{ANN})_i - (\log |E^*|_{avg})_i \right]^2} \quad (54)$$

Where:

- 29 = Number of temperature/frequency combinations used minus 1.
- $(\log |E^*|_{avg})_i$  = Logarithm of the average modulus determined from the ANN models for a given layer.

$$R^2 = 1 - \frac{(23)S_e^2}{(29)S_y^2} \quad (55)$$

### 6.3 CONTRACTOR JUDGMENT

The NCSU researchers used a combination of the above QC factors to judge the quality of the modulus prediction for an individual modulus prediction. If QCs #1, #3, #4, and #6 all pass, then the section receives a grade of “A.” If QC #1 fails but QCs #3, #4, and #6 all pass, then the modulus receives a grade of “C,” which means the predicted moduli are questionable. Otherwise, the modulus receives a grade of “F.”

### 6.4 CONTRACTOR MASTERCURVE JUDGMENT

QCs #5 and #7 are used to judge the quality of the calibrated mastercurve and shift factor function. When both QCs pass, the section receives a grade of “A,” but when both fail, the section receives a grade of “F.” If one passes and one fails, then the mastercurve and shift factor function values are questionable, and the section receives a grade of “C.”

### 6.5 PREDICTION STATISTICS

The LTPP database contains information for a total of 1,806 layers that meet the criteria described in section 3.4 of this report. These layers have binder data available at a combination

of different aging conditions including unaged or original-, RTFO-, PAV-, or field-aged. In the field-aged data, 2,223 records are available because some layers' properties may have been measured at different dates. The total resulting number of records is 7,641. Using the combined ANN models and requisite QC checks, modulus values were predicted for 363 records/layers in the original-aged level, 469 records/layers in the RTFO-aged level, 1 record/layer in the PAV level, and 503 records in the field-aged level. These numbers translate to predictions for 17.5 percent of the total number of records available. However, these records are distributed in such a way that a higher percentage of the layers have some sort of valid prediction. Of the 1,806 layers in the database, 1,010, or 56 percent, have a modulus prediction at some aging condition. Of these 1,010 layers, 615, or 34 percent of the total 1,806 layers, have completely reasonable predictions (i.e., an "A" grade), and 89, or 4.9 percent of the total 1,806 layers, have unreasonable predictions (i.e., an "F" grade). The remaining 306 layers (17 percent of the 1,806 layers) have questionable predictions (i.e., a "C" grade). Thus, the total percentage of layers with a completely valid or questionable prediction is 51 percent. Table 26 shows the summarized statistics of the population effort. Although it cannot be interpreted directly from this table, the majority of the valid records were populated using the  $M_R$  ANN model followed next by the VV-grade ANN model and the VV ANN model.

**Table 26. Statistics of LTPP data populated with  $|E^*|$ .**

Populated LTPP data	Aging Condition				<b>Total</b>
	<b>Original</b>	<b>RTFO</b>	<b>PAV</b>	<b>Field</b>	
Number of records	1,806	1,806	1,806	2,223	7,641
Number of populated records	363	469	1	503	1,336
Number of records by contractor individual judgment grade	Grade A	147	252	0	465
	Grade C	0	1	1	38
	Grade F	216	216	0	432
Number of records by contractor mastercurve judgment grade	Grade A	44	142	0	0
	Grade C	211	237	0	503
	Grade F	108	90	1	199
Populated records using $M_R$	5	0	0	503	508
Populated records using VV	358	59	0	0	417
Populated records using GV	0	0	1	0	1
Populated records using GV-PAR	0	2	0	0	2
Populated records using VV-grade	0	408	0	0	408
Number of populated layers					1,010
Number of layers with valid and questionable predictions					921
Number of layers with fully valid predictions					615
Number of layers with failed predictions					89

## 6.6 LTPP DATABASE ADDITIONS

As a result of this project, nine tables were included in the LTPP database to document the inputs used in the dynamic modulus models as well as resultant predictions.<sup>(20)</sup> The tables were added to the materials testing module (i.e., TST) of the LTPP database. Each table is described below. It should be noted that inputs from the LTPP database as well as outputs from the models are in

units that are consistent with popular convention, but both SI and English units are used in the tables.

- **TST\_ESTAR\_MASTER:** Identification information for all records in the ESTAR tables (see table 27 for format).
- **TST\_ESTAR\_MODULUS:**  $|E^*|$  predictions from the models described in the report (see table 28 for format).
- **TST\_ESTAR\_MODULUS\_COEFF:** Sigmodial and shift factor information generated from the  $|E^*|$  models (see table 29 for format).
- **TST\_ESTAR\_GSTAR\_INPUT:** Binder shear modulus information used as inputs into the GV ANN model (see table 30 for format).
- **TST\_ESTAR\_GSTAR\_CAM\_COEFF:** CAM coefficients used as inputs into the GV ANN model (see table 31 for format).
- **TST\_ESTAR\_VOLUM\_INPUT:** Volumetric properties used as inputs into the VV ANN model (see table 32 for format).
- **TST\_ESTAR\_VISC\_INPUT:** Binder viscosity information used as inputs into the VV ANN model (see table 33 for format).
- **TST\_ESTAR\_VISC\_MODEL\_COEFF:** A and VTS data generated from viscosity inputs for use in the VV ANN model (see table 34 for format).
- **TST\_ESTAR\_MR\_INPUT:**  $M_R$  data used as inputs into the  $M_R$  ANN model (see table 35 for format).

**Table 27. Structure and format of the TST\_ESTAR\_MASTER table.**

Field Name	Field Description
ESTAR_LINK	Generic key for linking ESTAR data
STATE_CODE	Numerical code for State or province. U.S. codes are consistent with Federal Information Processing Standards
SHRP_ID	Test section identification number assigned by LTPP program. Must be combined with STATE_CODE to be unique
LAYER_NO	Unique sequential number assigned to pavement layers starting with layer 1 as the deepest layer (subgrade)
PROJECT_ID	The four-character identifier for the SPS project used to identify elements of information which are common to all sections in that project
PROJECT_LAYER_CODE	Sequential alphabetic code assigned to identify group project-wide layers
PREDICTIVE_MODEL	Code indicating the predictive model used to generate ESTAR estimates
CONSTRUCTION_DATE	Construction date of the layer
SAMPLE_TYPE_ESTAR	Code indicating the aging condition of the samples used for inputs into the ESTAR predictive models
SAMPLE_DATE	Sampling date if field-aged
SAMPLE_AGE	Sample age if field-aged
RECORD_STATUS	Code indicating the general quality of the data as outlined, based on the level of QC checks described in the <i>Database User Reference Guide</i> <sup>(10)</sup>

**Table 28. Structure and format of the TST\_ESTAR\_MODULUS table.**

Field Name	Field Description
ESTAR_LINK	Generic key for linking ESTAR data
TEMPERATURE	Temperature of modulus prediction
FREQUENCY	Frequency of modulus prediction
ESTAR	Predicted dynamic modulus
RECORD_STATUS	Code indicating the general quality of the data as outlined, based on the level of QC checks described in the <i>Database User Reference Guide</i> <sup>(10)</sup>

**Table 29. Structure and format of the TST\_ESTAR\_MODULUS\_COEFF table.**

<b>Field Name</b>	<b>Field Description</b>
ESTAR_LINK	Generic key for linking ESTAR data
SIGMOIDAL_COEFF_1	Sigmoidal fitting function coefficient delta
SIGMOIDAL_COEFF_2	Sigmoidal fitting function coefficient alpha
SIGMOIDAL_COEFF_3	Sigmoidal fitting function coefficient beta
SIGMOIDAL_COEFF_4	Sigmoidal fitting function coefficient gamma
SHIFT_FACTOR_COEFF_1	Shift factor fitting function coefficient alpha 1
SHIFT_FACTOR_COEFF_2	Shift factor fitting function coefficient alpha 2
SHIFT_FACTOR_COEFF_3	Shift factor fitting function coefficient alpha 3
MASTERCURVE_QUALITY	Code indicating the general quality of the mastercurve generation process. Pass if explained variance is greater than 0.99 and ratio of standard error to standard deviation is less than 0.05
RECORD_STATUS	Code indicating the general quality of the data as outlined based on the level of QC checks described in the <i>Database User Reference Guide</i> <sup>(10)</sup>

**Table 30. Structure and format of the TST\_ESTAR\_GSTAR\_INPUT table.**

<b>Field Name</b>	<b>Field Description</b>
ESTAR_LINK	Generic key for linking ESTAR data
TEMPERATURE	Temperature of modulus prediction
FREQUENCY	Frequency of modulus prediction
GSTAR	Binder shear modulus used for $G^*$ ANN model
RECORD_STATUS	Code indicating the general quality of the data as outlined based on the level of QC checks described in the <i>Database User Reference Guide</i> <sup>(10)</sup>

**Table 31. Structure and format of the TST\_ESTAR\_GSTAR\_CAM\_COEFF table.**

<b>Field Name</b>	<b>Field Description</b>
ESTAR_LINK	Generic key for linking ESTAR data.
CAM_COEFF_1	CAM fitting function coefficient $G_g$
CAM_COEFF_2	CAM fitting function coefficient $w_c$
CAM_COEFF_3	CAM fitting function coefficient $k$
CAM_COEFF_4	CAM fitting function coefficient $m_e$
RECORD_STATUS	Code indicating the general quality of the data as outlined based on the level of QC checks described in the <i>Database User Reference Guide</i> <sup>(10)</sup>

**Table 32. Structure and format of the TST\_ESTAR\_VOLUM\_INPUT table.**

<b>Field Name</b>	<b>Field Description</b>
ESTAR_LINK	Generic key for linking ESTAR data
VMA	Voids in mineral aggregate as a percent of total volume
VFA	Voids filled with asphalt as a percent of VMA
RECORD_STATUS	Code indicating the general quality of the data as outlined, based on the level of QC checks described in the <i>Database User Reference Guide</i> <sup>(10)</sup>

**Table 33. Structure and format of the TST\_ESTAR\_VISC\_INPUT table.**

<b>Field Name</b>	<b>Field Description</b>
ESTAR_LINK	Generic key for linking ESTAR data
TEMPERATURE	Temperature of modulus prediction
VISCOSITY	Voids filled with asphalt as a percent of VMA
RECORD_STATUS	Code indicating the general quality of the data as outlined, based on the level of QC checks described in the <i>Database User Reference Guide</i> <sup>(10)</sup>

**Table 34. Structure and format of the TST\_ESTAR\_VISC\_MODEL\_COEFF table.**

<b>Field Name</b>	<b>Field Description</b>
ESTAR_LINK	Generic key for linking ESTAR data
VISC_A	Viscosity model intercept
VISC_VTS	Viscosity model slope
RECORD_STATUS	Code indicating the general quality of the data as outlined, based on the level of QC checks described in the <i>Database User Reference Guide</i> <sup>(10)</sup>

**Table 35. Structure and format of the TST\_ESTAR\_MR\_INPUT table.**

<b>Field Name</b>	<b>Field Description</b>
ESTAR_LINK	Generic key for linking ESTAR data
MR_5C	Resilient modulus at 5 °C
MR_25C	Resilient modulus at 25 °C
MR_40C	Resilient modulus at 40 °C
RECORD_STATUS	Code indicating the general quality of the data as outlined, based on the level of QC checks described in the <i>Database User Reference Guide</i> <sup>(10)</sup>

°C = (°F-32)/1.8

QC checks were developed to be applied to the LTPP database. These checks include many of the internal checks developed as part of this study as well as additional checks deemed appropriate. As such, the data available in the LTPP database have been subjected to both the research team's internal QC checks and the LTPP database QC checks. Figure 78 shows the ANN models and their appropriate input and output tables.

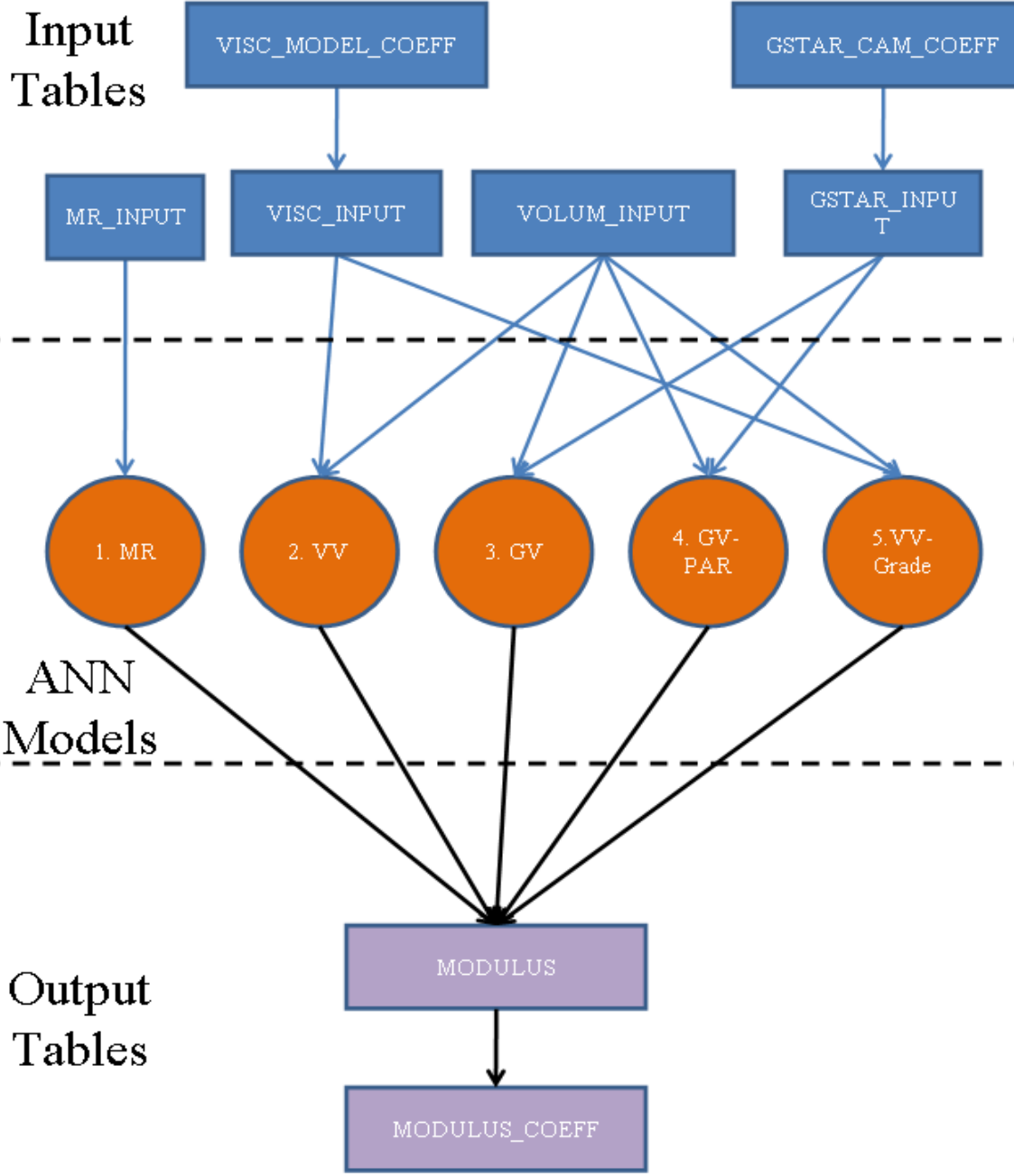


Figure 78. Illustration. ANN models and their appropriate input and output tables.

## 7.0 SUMMARY AND FUTURE WORK

Existing predictive equations, including the original Witczak equation (see equation 1), the modified Witczak equation (NCHRP 1-40D), the Hirsch model, and the law of mixtures parallel model were evaluated for accuracy and potential bias. (See references 2, 5, 6, and 7.) For fairness to each model, a database consisting of hundreds of mixtures and binders and thousands of single data points from projects across the United States was compiled and used in the evaluation. This effort showed that although each model has certain benefits, no single model is capable of highly accurate predictions over the complete range of necessary conditions. Furthermore, none of these predictive models could predict the  $|E^*|$  values when only the  $M_R$  was available. This final criterion is crucial because more layers had available  $M_R$  values than the information needed for the existing predictive models. Multiple models are necessary because the layers in the LTPP database are not uniform in their population of material properties. As a result, the research team developed ANN models that, through a pilot study, were shown to yield reasonable and accurate predictions for the complete range of conditions needed. This hierarchical approach thus allows a more complete population of  $|E^*|$  values.

In the end, three ANN models were developed. Each model differed in the required input parameters. The most accurate ANN model was found to utilize  $M_R$  as its primary input parameter. The other two models use mixture volumetric properties as well as a binder property as input variables. The VV ANN model uses the binder viscosity and input frequency, whereas the GV ANN model uses the binder  $|G^*|$  property. These models were extended to include conditions where perfect input values were not available, such as when  $|G^*|$  had been measured at warm temperatures for the RTFO-aged binder and measured at intermediate temperatures for the PAV binder or when only the binder grade was available. Statistical analysis and engineering judgment were utilized to rank the predictive models, with the  $M_R$  ANN model being the best, the VV ANN model being the second best, and the GV ANN model being the third best. Imperfect input conditions were also ranked below these three models.

The individual ANN models developed for this project have practical implications beyond the current study. The most direct use of these ANN models is the prediction of  $|E^*|$  values for MEPDG or other structural/performance analysis of AC pavements. They may be used in the same way that existing closed-form solutions are used. The advantage of using ANN models for this purpose is their improved accuracy when compared to existing closed-form solutions. The  $M_R$  ANN model developed in this project is the only available method for predicting  $|E^*|$  over the range of temperatures and frequencies needed for complete analysis. Agencies that have managed to compile large databases of  $M_R$  values may find such a tool useful in local calibration efforts.

The LTPP database was populated with  $|E^*|$  values at five temperatures and six frequencies by using the prioritized ANN models. This database contains information for a total of 1,806 layers. These layers have binder data available at a combination of different aging conditions, including unaged or original-, RTFO-, PAV-, or field-aged. In the field-aged data, 2,223 records are available because, for some layers, properties may have been measured at different dates. The total resulting number of records is 7,641. Using the combined ANN models and requisite QC checks, modulus values were predicted for 363 records/layers in the original-aged level,

469 records/layers in the RTFO-aged level, 1 record/layer in the PAV level, and 503 records in the field-aged level. These numbers translate to predictions for 17.5 percent of the total number of records available. However, these records are distributed in such a way that a higher percentage of the layers have some sort of valid prediction. Of the 1,806 layers in the database, 1,010, or 56 percent, have a modulus prediction at some aging condition. Of these 1,010 layers, 615, or 34 percent of the total 1,806 layers, have completely reasonable predictions (i.e., an “A” grade), and 89, or 4.9 percent of the total 1,806 layers, have unreasonable predictions (i.e., an “F” grade). The remaining 306 layers, 17 percent of the 1,806 layers, have questionable predictions (i.e., a “C” grade). Thus, the total percentage of layers with a completely valid or questionable prediction is 51 percent.

These populated values will allow users to develop a mastercurve for independent analysis or directly into MEPDG. In addition, mastercurve sigmoidal parameters and temperature shift factors were also computed and included in the population effort. The computed parameters are included in the computed parameter data submitted to FHWA.

The following tasks constitute suggested future research efforts:

- Development and/or refinement of a closed-form  $|E^*|$  predictive model to estimate the dynamic modulus values as a function of temperature and frequency. The insight gained with the current ANN models should aid in the development of such models.
- Development of individual temperature-based ANN or closed-form  $|E^*|$  models. By developing such models or the comprehensive closed-form model suggested in the future task listed above, a maximum of 306 of the layers that currently have a questionable modulus prediction could be populated with more accurate values.
- Performance of an indepth and comprehensive experimental study to gain better understanding of the differences between the moduli measured via the AMPT and TP-62 protocols.<sup>(8)</sup> Understanding the factors that have led to the clear differences found in the datasets compiled by each of these techniques could lead to more robust predictive models.

## APPENDIX A: PROCESSING ASPHALT BINDER VISCOSITY DATA

### A.1 INTRODUCTION

Until the advent of the Superpave<sup>TM</sup> mix design system in the early 1990s, the viscosity of asphalt binders was the key measure used in purchase specifications. As a result, many sections that are now reaching their design lives and, as a result, are included in the LTPP database, contain various measures of viscosity. Over the years, four primary types of viscosity measures have been adopted: (1) ring and ball temperature (R&BT), (2) penetration (at various temperatures), (3) absolute viscosity at 140 °F (60 °C), and (4) kinematic viscosity at 275 °F (135 °C). These measures have been used together or separately in various grading schemes. With the exception of penetration, these viscosity measures are beyond the range of temperature conditions typically needed for modulus prediction. As a result, a certain amount of processing the available data is necessary. In this appendix, the steps necessary to properly analyze available viscosity data are presented.

### A.2 TEMPERATURE SUSCEPTIBILITY RELATIONSHIP

Although the relationship between viscosity and temperature is highly nonlinear, it has been found that when proper transformations are made to temperature and viscosity, a linear relationship exists. This relationship is commonly referred to as the “A-VTS relationship.”<sup>(43)</sup> This relationship is shown schematically in figure 79 and mathematically in equation 56. The plateau region in figure 79 is based on arguments that are, in turn, based on the chemical structure of asphalt binder and suggest that the maximum viscosity for asphalt binder is  $2.7 \times 10^{12}$  cP ( $0.0027 \times 10^{12}$  Pas).<sup>(44)</sup> For the purposes of this report, this same limiting criterion was also adopted.

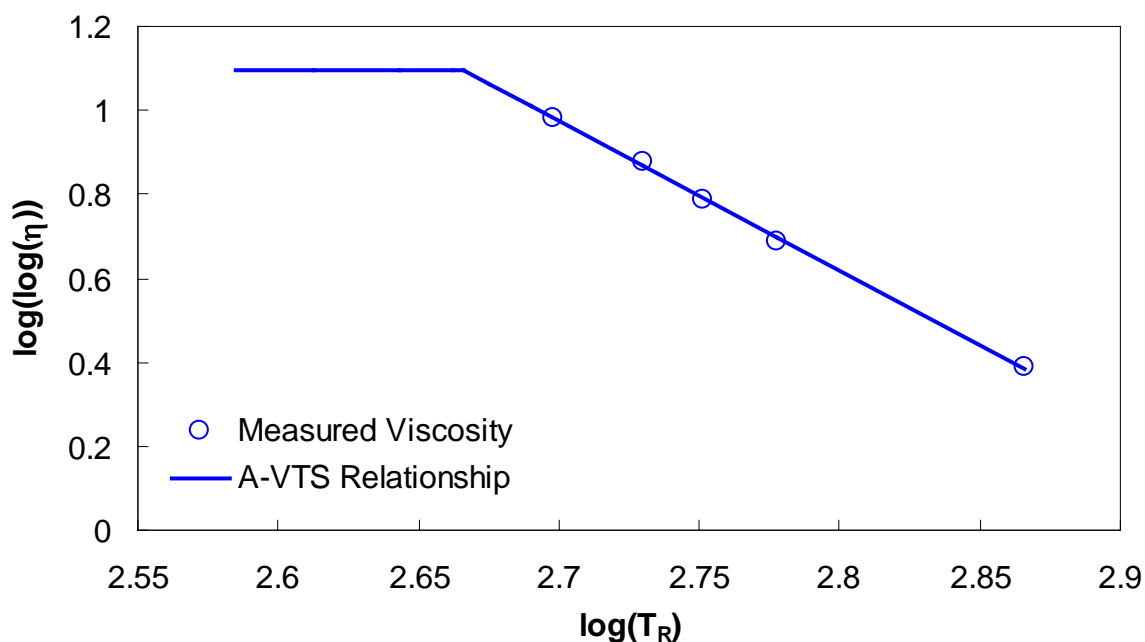


Figure 79. Graph. A-VTS relationship.

$$\log \log(\eta) = \begin{cases} A + VTS \log(T_R) & T_R > T_{critical} \\ 1.095 & T_R \leq T_{critical} \end{cases} \quad (56)^*$$

Where:

- $\eta$  = Viscosity (cP).
- $A$  = Intercept of temperature susceptibility relationship.
- $VTS$  = Slope of temperature susceptibility relationship.
- $T_R$  = Temperature in Rankine.
- $T_{critical}$  = Temperature in Rankine at which the viscosity is equal to  $2.7 \times 10^{12}$  cP ( $0.0027 \times 10^{12}$  Pas).

Because the A-VTS relationship is linear, only two of the four viscosity measures are needed to completely characterize the relationship. The following sections provide the equations necessary to convert the four measures to actual viscosity.

### A.3 R&BT TEMPERATURE

The softening point of asphalt binder as measured by AASHTO T53-08 is also known as R&BT.<sup>(45)</sup> According to literature on the topic, this temperature, measured in Fahrenheit, corresponds to the temperature at which asphalt binder has a viscosity of 13,000 P (1,300 Pas).<sup>(44)</sup>

### A.4 PENETRATION

The penetration number for asphalt binder is determined via AASHTO T49-07.<sup>(46)</sup> In this test, a 3.5-oz (100-g) needle is used to penetrate an asphalt sample for 5 s. The amount of penetration, measured in tenths of a millimeter, is the penetration number for the asphalt binder at the particular test temperature. The measurement temperature typically used for specification purposes is 77 °F (25 °C); however, other temperatures, including 39.2 and 115 °F (4 and 46 °C), may also be measured. Penetration values are converted to viscosity using the relationship suggested by Mirza and Witczak as seen in equation 57:<sup>(44)</sup>

$$\log \eta = 10.5012 - 2.2601 \log(PEN) + 0.00389 (\log(PEN))^2 \quad (57)$$

Where:

- $\eta$  = Viscosity (P).
- PEN = Penetration number at a given test temperature.

### A.5 ABSOLUTE VISCOSITY

The *absolute viscosity* is the viscosity of asphalt binder measured at 140 °F (60 °C) by AASHTO T202-03.<sup>(47)</sup> Because this quantity is typically reported in poise instead of centipoise, the only conversion needed is to multiply the given quantity by 100.

\*Equation modified July 27, 2015.

## A.6 KINEMATIC VISCOSITY

The kinematic viscosity of asphalt binder is determined at 275 °F (135 °C) via AASHTO T201-03.<sup>(48)</sup> Kinematic and absolute viscosities are related by the density of the medium under investigation. The relationship between these two quantities is shown in equation 58. For LTPP purposes, it is assumed that the density for all binders is equal to 0.6 oz/in<sup>3</sup> (1.03 g/cm<sup>3</sup>).

$$\eta = \nu * \rho \quad (58)$$

Where:

- $\eta$  = Absolute viscosity (cP).  
 $\nu$  = Kinematic viscosity (cSt).  
 $\rho$  = Density (oz/in<sup>3</sup> ((g/cm<sup>3</sup>)).

## A.7 EXAMPLE PROBLEM

For a given asphalt binder, the following properties are measured:

R&BT temperature = 104 °F (40 °C)

PEN at 39.2 °F (4 °C) = 19

PEN at 77.0 °F (25 °C) = 156

$\eta$  = 774 P (77.4 Pas)

$\nu$  = 266.1 centistokes (cSt)

Using these relationships, the viscosity is computed for different temperatures as follows:

39.2 °F (4 °C) =  $4.14 \times 10^9$  cP ( $0.00414 \times 10^9$  Pas)

77.0 °F (25 °C) =  $3.66 \times 10^7$  cP ( $0.00366 \times 10^7$  Pas)

104 °F (40 °C) =  $1.30 \times 10^6$  cP ( $0.0013 \times 10^6$  Pas)

140 °F (60 °C) =  $7.74 \times 10^5$  cP ( $0.00774 \times 10^5$  Pas)

275 °F (135 °C) =  $2.74 \times 10^2$  cP ( $0.00274 \times 10^2$  Pas)

After performing linear regression on these quantities, it is found that  $A = 10.599$ ,  $VTS = -3.5646$ , and  $T_{critical} = 464.8$  °R.

## A.8 TYPICAL VALUES FOR PURCHASE SPECIFICATION GRADE

As part of the NCHRP 1-37A effort, researchers compiled typical A and VTS values for different purchase specification grades.<sup>(2)</sup> These typical values include Superpave<sup>TM</sup> PG binders, AC viscosity-graded binders, and penetration-graded binders. Data were not compiled for all grades in use across the United States, but most grades were included. Because some of the LTPP layers fell in the category where the only binder information known was the grade, these relationships are considered important. In table 36, the A and VTS parameters are presented for the different grades reported in the MEPDG documentation.<sup>(2)</sup>

**Table 36. Relationship between asphalt binder grade and viscosity parameters.**

Asphalt Binder Grade	A	VTS	Asphalt Binder Grade	A	VTS
PG 46-34	11.5040	-3.9010	PG 70-28	9.7150	-3.2170
PG 46-40	10.1010	-3.3930	PG 70-34	8.9650	-2.9480
PG 46-46	8.7550	-2.9050	PG 70-40	8.1290	-2.6480
PG 52-10	13.3860	-4.5700	PG 76-10	10.0590	-3.3310
PG 52-16	13.3050	-4.5410	PG 76-16	10.0150	-3.3150
PG 52-22	12.7550	-4.3420	PG 76-22	9.7150	-3.2080
PG 52-28	11.8400	-4.0120	PG 76-28	9.2000	-3.0240
PG 52-34	10.7070	-3.6020	PG 76-34	8.5320	-2.7850
PG 52-40	9.4960	-3.1640	PG 82-10	9.5140	-3.1280
PG 52-46	8.3100	-2.7360	PG 82-16	9.4750	-3.1140
PG 58-10	12.3160	-4.1720	PG 82-22	9.2090	-3.0190
PG 58-16	12.2480	-4.1470	PG 82-28	8.7500	-2.8560
PG 58-22	11.7870	-3.9810	PG 82-34	8.1510	-2.6420
PG 58-28	11.0100	-3.7010	AC-2.5	11.5167	-3.8900
PG 58-34	10.0350	-3.3500	AC-5	11.2614	-3.7914
PG 58-40	8.9760	-2.9680	AC-10	11.0134	-3.6954
PG 64-10	11.4320	-3.8420	AC-20	10.7709	-3.6017
PG 64-16	11.3750	-3.8220	AC-3	10.6316	-3.5480
PG 64-22	10.9800	-3.6800	AC-40	10.5338	-3.5104
PG 64-28	10.3120	-3.4400	PEN 40-50	10.5254	-3.5047
PG 64-34	9.4610	-3.1340	PEN 60-70	10.6508	-3.5537
PG 64-40	8.5240	-2.7980	PEN 85-100	11.8232	-3.6210
PG 70-10	10.6900	-3.5660	PEN 120-150	11.0897	-3.7252
PG 70-16	10.6410	-3.5480	PEN 200-300	11.8107	-4.0068
PG 70-22	10.2990	-3.4260	—	—	—

— Indicate that no additional relationships exist.

## **APPENDIX B: PROCESSING ASPHALT BINDER SHEAR MODULUS DATA**

### **B.1 INTRODUCTION**

A potential shortcoming of the predictive models that rely on the binder  $|G^*|$  is the need for the moduli to fall within the complete range of conditions under which the material mixture modulus can be predicted. This range of conditions typically includes temperatures from 14 to 129.2 °F (-10 to 54 °C) and frequencies from 25 to 0.1 Hz. All of the possible combinations of these temperatures and frequencies should be known in order to effectively use the predictive equations for pavement design purposes. The specification data cover the necessary range, but four main problems arise in using the specification results to determine the material properties: (1) the availability of data at only a limited number of temperatures, (2) the evaluation of LVE properties at only a single frequency or time, (3) the mixture of time domain and frequency domain measurements, and (4) a mixture of characteristic behaviors under different aging conditions. It is possible to measure the material properties at a sufficient number of frequencies/times and temperatures to perform the appropriate analysis. However, this process is not part of standard agency practice and, therefore, is not included in the current LTPP database.

In this appendix, a combined phenomenological and mechanical approach is developed and presented. This approach, when coupled with a standard optimization technique, can be used with the existing specification test results to determine  $|G^*|$  over the necessary range. This approach provides sufficient information for  $|E^*|$  predictions without increasing the testing requirements. This analytical methodology, although more complicated than that typically used in agency offices, may be coded into a software package or a spreadsheet to allow easy, direct, and rapid characterization.

### **B.2 USE OF BBR DATA IN $|G^*|$ MASTERCURVE GENERATION**

In asphalt binder testing, two TPs are used to extract the LVE properties of the material. At high and intermediate temperatures, DSR is used, and at low temperatures, BBR is used. To determine the properties of a material over an entire range of in-service conditions, results from these two TPs must be combined. The purpose of this section is to present a method that combines these two outcomes into a single relationship.

A comparison of the mastercurve and the t-T superposition shift factor function development with and without BBR data is also presented. The methodology used for mastercurve and t-T shift factor function development using DSR and BBR data generally follows the method presented by Kim et al.<sup>(49)</sup> The method used herein differs from the Kim et al. method in that it makes more extensive use of optimization techniques.

### **B.3 ANALYSIS USING DSR MEASUREMENTS**

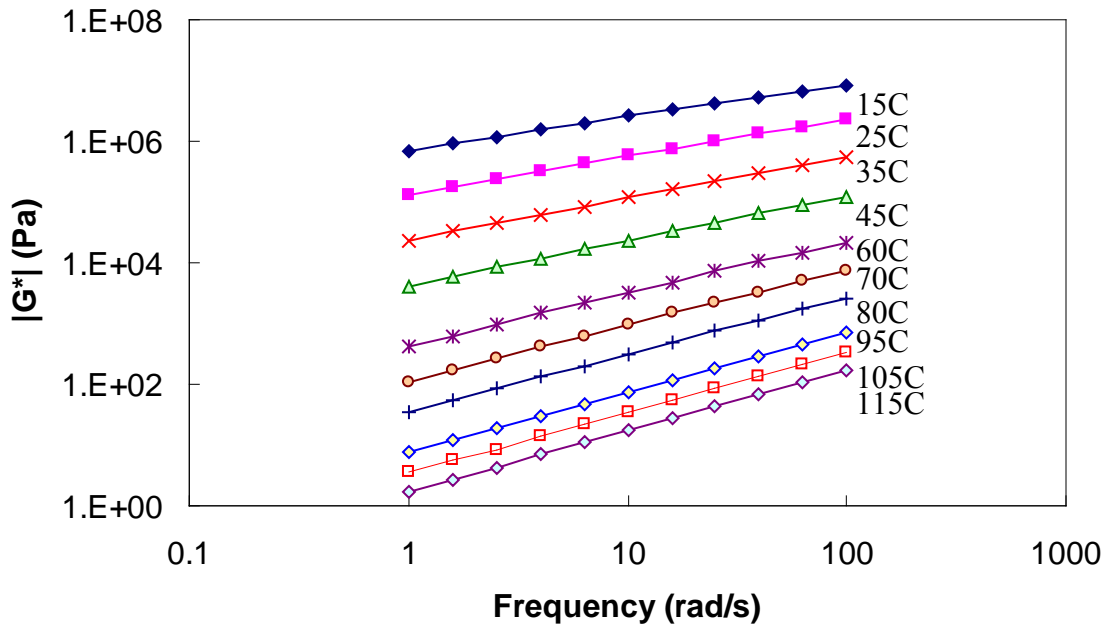
Significant literature exists on the development of mastercurves from DSR measurements. Stiffness values at multiple combinations of temperature and frequency, such as those shown in figure 80, are first determined via experimentation. The data are then horizontally shifted by temperature along the logarithmic frequency axis to form a continuous function (see figure 81). The amount of horizontal shift is the t-T shift factor for that particular temperature and the

shifted frequency is referred to as the “reduced frequency.” This operation is expressed mathematically in equation 59, and an example function is shown in figure 82.

$$a_T = \frac{\omega_{T_R}}{\omega_T} \quad (59)$$

Where:

- $a_T$  = Time-temperature shift factor.
- $\omega_T$  = Frequency at the physical temperature.
- $\omega_{TR}$  = Reduced frequency of  $\omega_T$  at the reference temperature.



$$^{\circ}\text{C} = (\text{^{\circ}\text{F}-32})/1.8$$

**Figure 80. Graph.  $|G^*|$  versus frequency curves at different temperatures.**

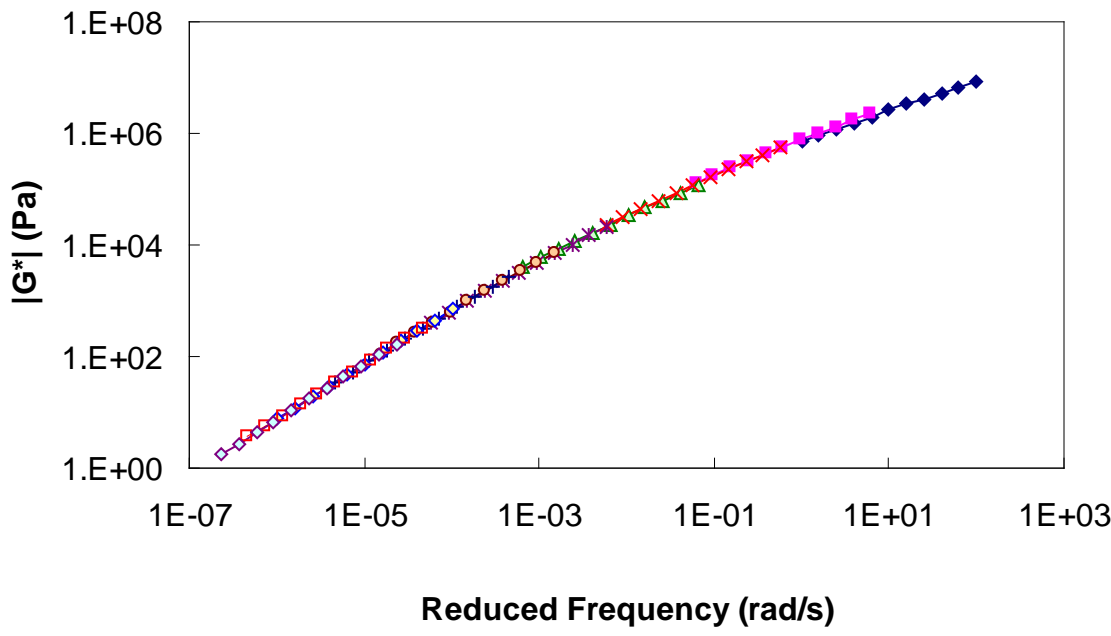


**Figure 81.** Graph.  $|G^*|$  versus reduced frequency mastercurve at 59 °F (15 °C).

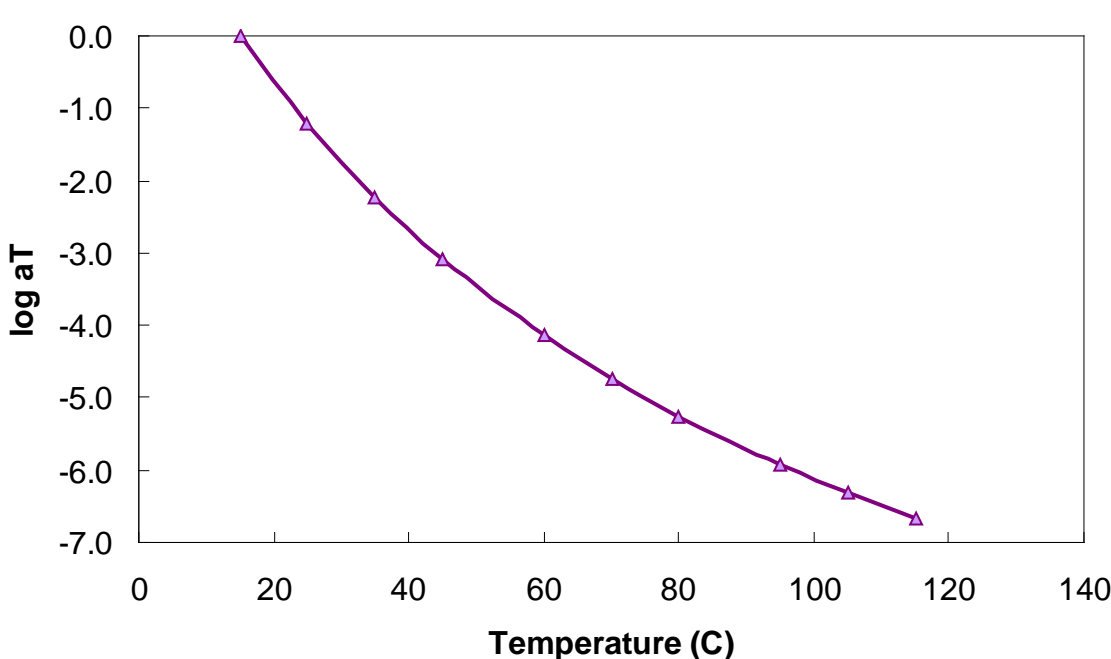


**Figure 82.** Graph. t-T shift factor function at 59 °F (15 °C).

Prior to desktop computers and optimization spreadsheet functions, the determination of the shift factors and the functional form comprised distinct steps. However, a current common technique is to assume some functional form for the mastercurve a priori and then optimize the coefficients of this function along with either the t-T shift factors directly or a function that relates these factors. Equation 60, which is an extension of the CAM model developed through the SHRP

program, is assumed for the mastercurve, and the Williams-Landel-Ferry (WLF) model is assumed for the t-T shift factor function (see equation 61). For all cases, 59 °F (15 °C) is taken as the reference temperature (i.e.,  $a_T = 1$  at 59 °F (15 °C)).

$$|G^*| = \frac{G_g}{\left(1 + \left(\frac{\omega_c}{\omega_R}\right)^k\right)^{m_e/k}} \quad (60)$$

Where:

- $G_g$  = Maximum shear modulus or glassy modulus (pascals).
- $\omega_R$  = Reduced frequency (rad/s).
- $\omega_c, m_e$ , and  $k$  = Fitting coefficients.

$$\log a_T = \frac{C_1(T - T_R)}{C_2 + T - T_R} \quad (61)$$

Where:

- $a_T$  = t-T shift factor at temperature T (°C).
- $T_R$  = Reference temperature (°C).
- $C_1$  and  $C_2$  = Fitting coefficients.

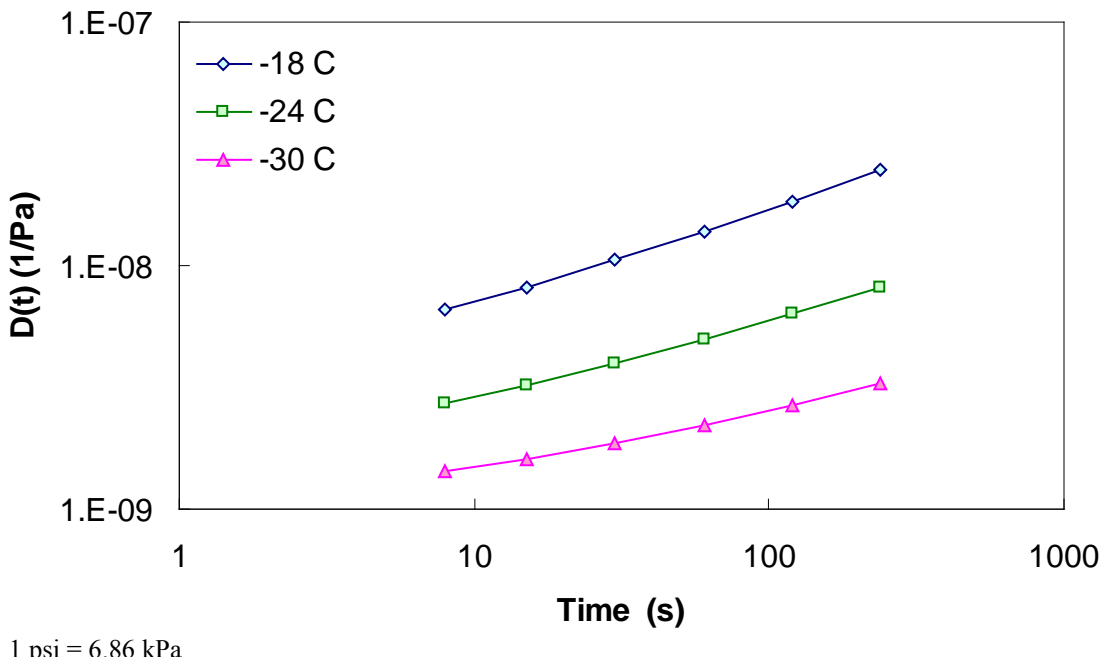
#### B.4 ANALYSIS WITH BBR MEASUREMENTS

To utilize the BBR data in  $|G^*$  mastercurve development, the data must be further processed because BBR measurements are taken in the time domain whereas DSR measurements are taken in the frequency domain. Also, BBR measurements are taken in the bending mode whereas DSR measurements are taken in the shear mode.

The PG specification defines *beam stiffness*,  $S(t)$ , as the inverse of creep compliance,  $D(t)$  (see equation 62). The creep compliance values of ALF AC5 at -22, -11.2, and -0.4 °F (-30, -24, and -18 °C) are calculated from the BBR stiffness values and plotted in figure 83. In a manner similar to the mastercurve development method mentioned previously, these curves are horizontally shifted to form a continuous curve. Note that because these measurements are made in the time domain, the reduced time is defined by equation 63.

$$S(t) = \frac{1}{D(t)} \quad (62)$$

$$t_{T_R} = \frac{t_T}{a_T} \quad (63)$$



1 psi = 6.86 kPa

**Figure 83. Graph.  $D(t)$  at different temperatures for ALF AC5 binder.**

For  $D(t)$ , a generalized power law (GPL) is assumed as seen in equation 64 as follows:

$$D(t) = D_0 + D_1 t_R^m \quad (64)$$

Where  $D_0$ ,  $D_1$ , and  $m$  are regression coefficients. In Kim et al., the determination of the coefficients in equation 64 is shown through a regression technique.<sup>(49)</sup> For the work presented here, the coefficients are determined via optimization using the Microsoft® Excel Solver function. The two techniques are compared in figure 84 and found to yield indistinguishable results. Note that for the BBR measurements, the t-T shift factors form a linear relationship with temperature as seen in equation 65 as follows:

$$\log a_{T,BBR} = C_3(T - T_R) \quad (65)$$

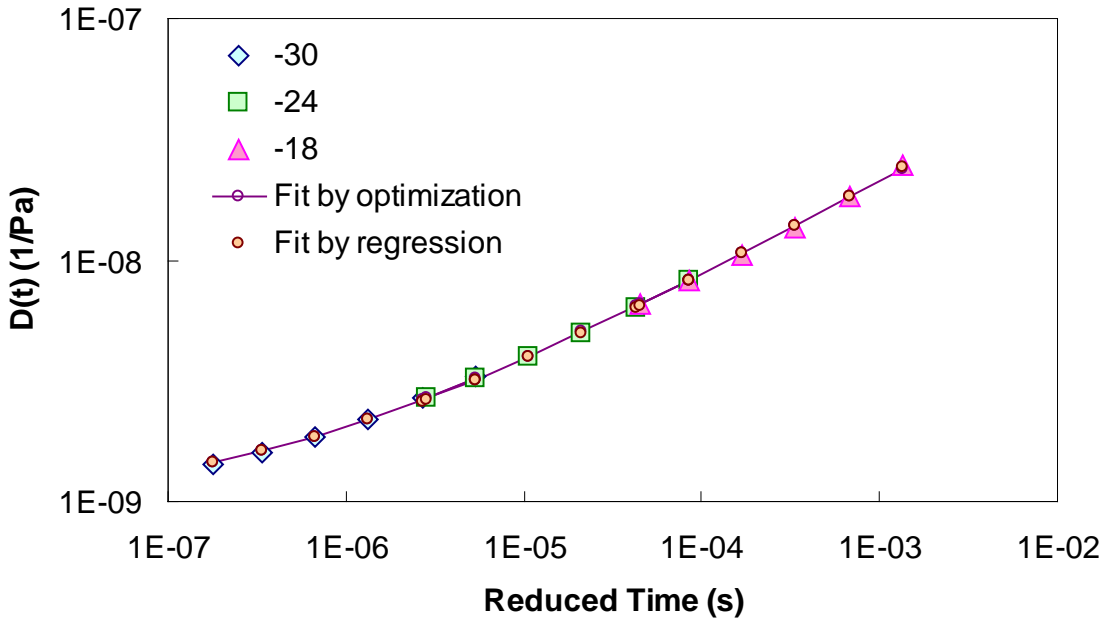


**Figure 84. Graph. Comparison of optimization and regression GPL characterization results.**

To use the BBR results with DSR measurements,  $D(t)$  must be converted to  $|G^*|$ . To make this conversion, the mathematical consequences of linear viscoelasticity and equation 64 along with equation 66 are utilized. Note that in this process, Poisson's ratio is assumed to be time-independent and has a value of 0.50.

$$|G^*| = \frac{1}{2(1+\nu)|D^*|} \quad (66)$$

In this equation,  $\nu$  is Poisson's ratio and  $|D^*|$  is the dynamic axial creep compliance. From linear viscoelasticity, this compliance can be determined by the following relationship:

$$|D^*| = \sqrt{(D')^2 + (D'')^2} \quad (67)$$

Where:

$D'$  = First vector component of  $|D^*|$ .

$D''$  = Second vector component of  $|D^*|$ .

Both are defined for the GPL in equations 68 and 69 as follows:

$$D' = D_0 + D_1 \Gamma(m+1) \omega_R^{-m} \cos\left(\frac{m\pi}{2}\right) \quad (68)$$

$$D'' = D_1 \Gamma(m+1) \omega_R^{-m} \sin\left(\frac{m\pi}{2}\right) \quad (69)$$

Although it is not necessary for this methodology, the frequencies at which the shear modulus is determined are consistent with LVE time-frequency equivalency principles. The equivalency is given in equation 70 as follows:

$$\omega_R = \frac{2}{\pi t_R} \quad (70)$$

## B.5 COMBINING DSR AND BBR ANALYSIS RESULTS

To utilize the BBR measurements for CAM model development and t-T shift factor determination, the Microsoft® Excel Solver optimization package is used. In this technique, the coefficients of the CAM model (see equation 60), the GPL model (see equation 64), the WLF equation for t-T shift factors above 32 °F (0 °C), and the t-T shift factor slope for temperatures below 32 °F (0 °C) are simultaneously optimized such that the objective function in equation 71 is minimized. The results from this optimization are shown in figure 85 and figure 86 for the WesTrack binder. Results of the characterization for all binders for a reference temperature of 59 °F (15 °C) are shown in table 37.

$$\begin{aligned} \text{Objective Function} = & \sum_{i=1}^M \left( \log(|G^*|_{DSR}) - \log(|G^*|_{CAM}) \right)_i^2 + \\ & \sum_{j=1}^N \left( \log(D(t)_{BBR}) - \log(D(t)_{GPL}) \right)_j^2 + \\ & \sum_{j=1}^N \left( \log(|G^*|_{BBR}) - \log(|G^*|_{CAM}) \right)_j^2 \end{aligned} \quad (71)$$

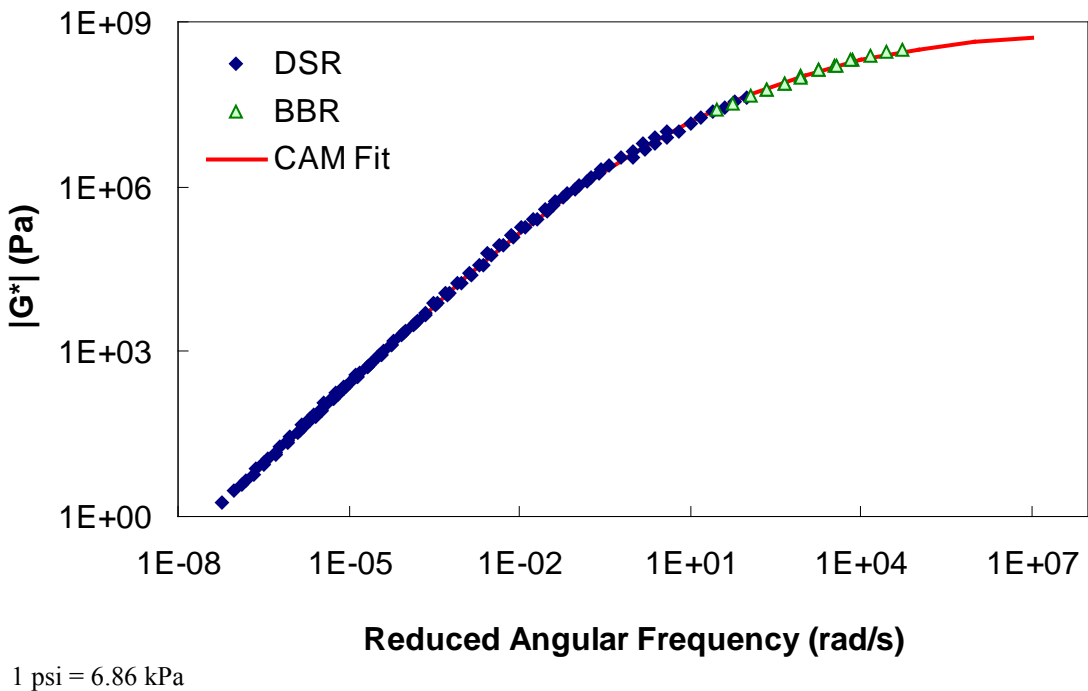


**Figure 85.** Graph.  $|G^*|$  mastercurve for the WesTrack binder at 59 °F (15 °C).

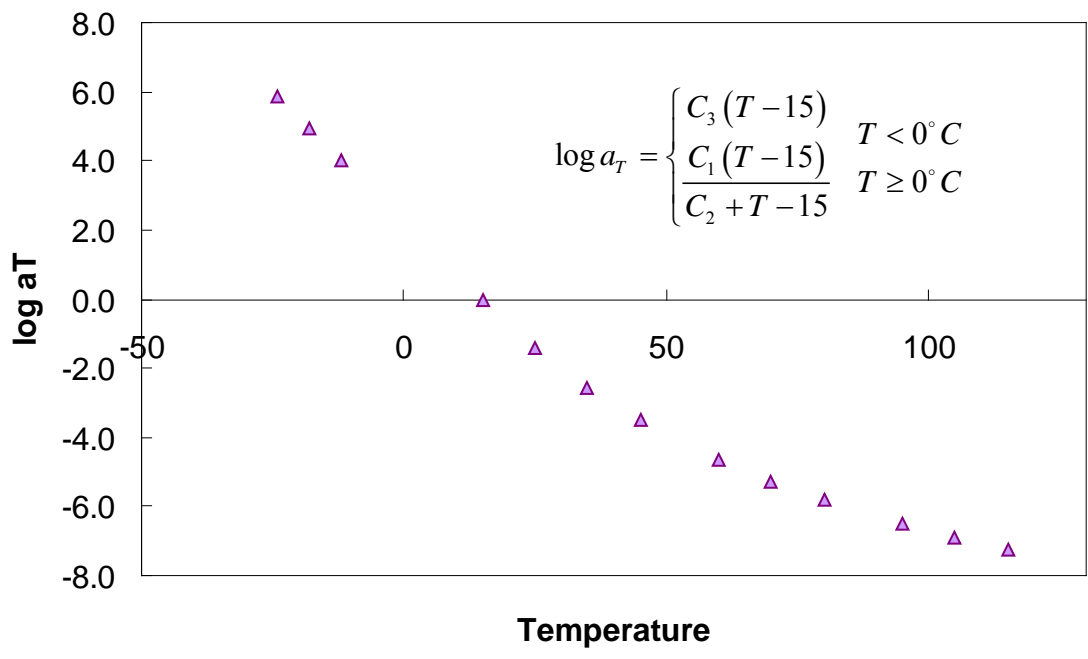


**Figure 86.** Graph. Optimized t-T shift function for WesTrack binder at 59 °F (15 °C).

**Table 37. Calibrated CAM model and t-T shift factor function coefficients using BBR data.**

Binder	CAM				t-T		
	$G_g$ (Pa)	$f_c$ (rad/s)	$k$	$m_e$	$C_1$	$C_2$	$C_3$
ALF AC5	3.60E+10	0.06	0.0777	1.4245	-13.4747	99.8914	-0.1447
ALF AC10	2.49E+10	0.09	0.0851	1.4299	-12.9868	90.7373	-0.1481
ALF AC20	1.81E+09	1.60	0.1278	1.1693	-13.6667	94.2261	-0.1520
ALF Novophalt	8.38E+08	0.60	0.1265	1.0477	-12.6598	80.6345	-0.1624
ALF Styrelf	8.35E+10	0.00	0.0622	1.2543	-15.5337	121.0536	-0.1525
MnRd. AC20	1.44E+09	0.54	0.1288	1.2208	-12.6909	77.2684	-0.1638
MnRd. Pen120-150	4.04E+10	0.11	0.0842	1.4556	-12.1122	78.8723	-0.1453
WesTrack	1.17E+09	0.60	0.1411	1.1828	-12.9616	73.4526	-0.1547

1 psi = 6.86 kPa

## B.6 COMPARISON OF RESULTS WITH AND WITHOUT BBR MEASUREMENTS

The methodology presented in the previous section has also been performed using only the DSR measurements. In this analysis, only the CAM model coefficients and WLF model coefficients are allowed to change, and the objective function is modified to that (see equation 72). The purpose of this analysis is to determine the effect of omitting BBR measurements when determining  $|G^*|$  values outside the DSR measured range. With this goal in mind, it is assumed that the analysis using BBR data represents the most accurate determination of the  $|G^*|$  mastercurve.

$$\text{Objective Function} = \sum_{i=1}^M \left( \log(|G^*|_{DSR}) - \log(|G^*|_{CAM}) \right)_i^2 \quad (72)$$

The calibrated CAM model coefficients and the t-T shift factor function coefficients for each of the binders are shown in table 38. A comparison of the values presented in table 37 and table 38 reveals no consistent trend. In some cases, the values from the calibrated model are higher than those from the BBR-calibrated models (higher  $G_g$  and  $k$  values and lower  $m_e$ ), whereas the opposite occurs in other models. In addition, the t-T shift factor function does not extrapolate well to lower temperatures when only DSR values are used in the calibration. An example of this behavior can be seen in figure 87. However, the figure shows that consistent results between the two characterization schemes occur at the DSR temperatures. To examine the effect of the extrapolation error, the GPL model is fitted to the BBR measurements, and the resulting overlap between the two datasets can be observed. When using the DSR-calibrated t-T shift factors, the BBR data are not continuous with the DSR data (see figure 88). This result suggests that the effect of extrapolating the t-T shift factor function is significant and may lead to errors.

**Table 38. Calibrated CAM model and t-T shift factor function coefficients omitting BBR data.**

Binder	CAM				t-T	
	$G_g$ (Pa)	$f_c$ (rad/s)	$k$	$m_e$	$C_1$	$C_2$
ALF AC5	5.24E+09	0.66	0.0976	1.2887	-13.2075	98.3537
ALF AC10	3.60E+10	0.62	0.0872	1.3514	-13.0002	92.7463
ALF AC20	1.25E+10	0.34	0.0968	1.2981	-14.0171	98.1479
ALF Novophalt	3.35E+07	1.74	0.3069	0.8552	-12.3904	79.8044
ALF Styrelft	4.52E+09	0.04	0.0824	1.1214	-14.8831	108.9959
MnRd. AC20	3.72E+10	0.57	0.0924	1.3303	-13.1226	86.8517
MnRd. Pen120-150	7.42E+10	0.90	0.0851	1.3752	-12.1104	80.9397
WesTrack	1.43E+08	4.33	0.2623	1.0068	-13.1142	81.7971

1 psi = 6.86 kPa

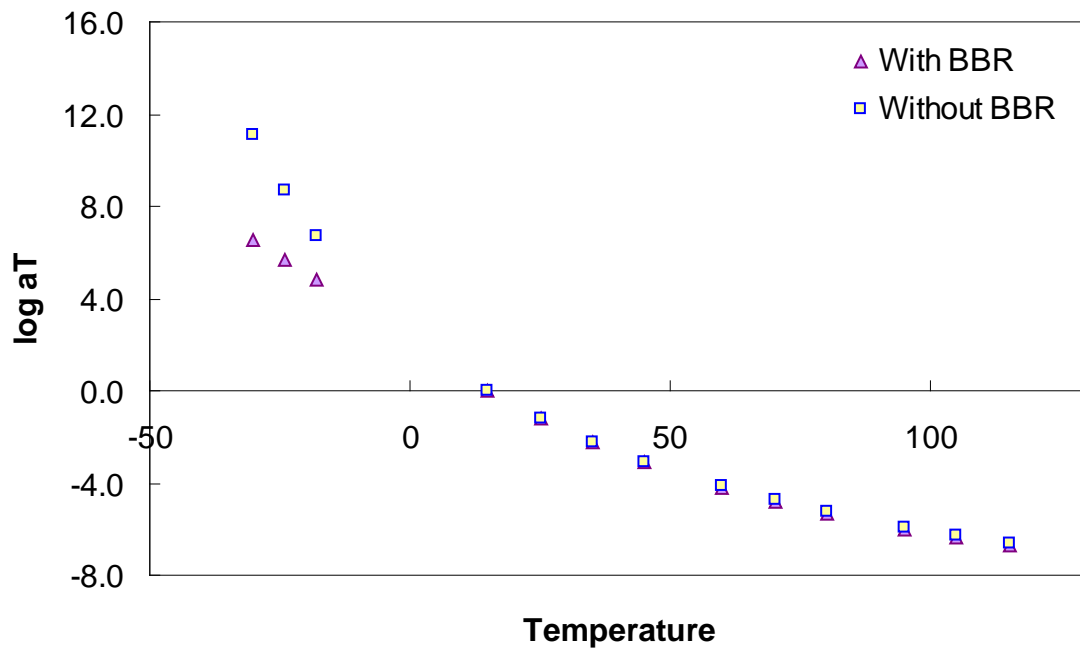


**Figure 87. Graph. Comparison of t-T shift factor functions calibrated with and without BBR data.**

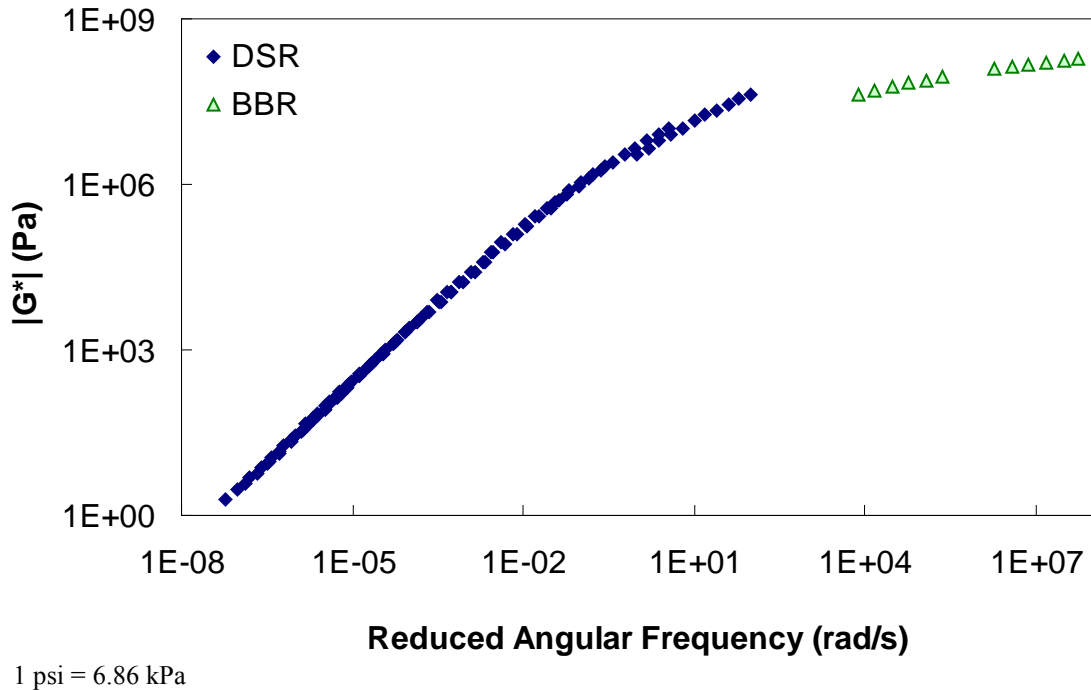


**Figure 88. Graph.**  $|G^*|$  mastercurve using t-T shift factor function calibrated without BBR data.

For the purposes of this report, the most critical information is found in the differences between these two techniques at TP-62 temperatures (14, 41, 68, 104, and 129.2 °F (-10, 5, 20, 40, and 54 °C)) and frequencies (25, 10, 5, 1, 0.5, and 0.1 Hz). To explore these conditions, the difference formula shown in equation 73 is utilized for  $|G^*|$  values that are predicted using the calibrated CAM models at the TP-62 temperatures and frequencies. The results are summarized in table 39 for each of the binders.

$$\%Diff = \frac{|G^*|_{with BBR} - |G^*|_{without BBR}}{|G^*|_{with BBR}} * 100 \quad (73)$$

**Table 39. Percentage of difference between BBR-calibrated and non-BBR-calibrated  $|G^*|$  at TP-62 temperatures and frequencies.**

Temperature (°C)	Frequency (Hz)	ALF AC5	ALF AC10	ALF AC20	ALF Novochip	ALF Styrene	MnRoad AC20	Pen 120-150	Wes Track
-10	25	-11.09	-153.94	-211.16	87.30	29.32	-629.40	-334.59	67.37
-10	10	-20.53	-162.36	-203.86	85.55	23.47	-589.44	-358.74	63.23
-10	5	-28.23	-169.15	-198.98	83.95	18.73	-561.10	-378.72	59.42
-10	1	-48.12	-186.48	-189.99	78.88	6.61	-501.81	-431.57	47.49
-10	0.5	-57.59	-194.67	-187.24	75.91	0.90	-479.17	-457.47	40.55
-10	0.1	-81.72	-215.54	-183.75	66.24	-13.55	-433.54	-526.17	18.18
5	25	16.83	-11.35	-29.59	72.25	20.04	-77.81	-13.86	54.92
5	10	14.07	-9.28	-22.56	67.17	15.44	-58.57	-10.94	50.21
5	5	12.09	-7.70	-17.75	62.64	11.89	-45.57	-8.76	46.44
5	1	7.96	-4.02	-8.19	49.60	3.57	-20.03	-3.78	37.54
5	0.5	6.42	-2.44	-4.73	42.92	-0.02	-10.83	-1.69	33.93
5	0.1	3.50	1.16	1.84	25.70	-8.25	7.00	2.98	27.26
20	25	3.60	-6.13	-3.81	21.12	9.08	-18.13	-5.92	1.89
20	10	2.11	-4.30	-0.90	10.85	5.61	-9.73	-3.60	-2.43
20	5	1.20	-2.94	0.90	3.71	3.09	-4.23	-1.91	-4.39
20	1	-0.15	0.06	3.86	-8.63	-2.32	6.09	1.75	-4.19
20	0.5	-0.40	1.28	4.63	-11.52	-4.42	9.61	3.21	-2.22
20	0.1	-0.24	3.92	5.42	-12.25	-8.72	15.95	6.27	5.47
40	25	-3.12	-2.17	3.73	-17.56	3.18	-1.44	-1.13	-20.55
40	10	-2.98	-0.87	3.76	-15.91	1.48	1.13	0.35	-15.26
40	5	-2.66	0.05	3.52	-13.42	0.38	2.60	1.37	-10.88
40	1	-1.30	1.90	2.23	-5.35	-1.53	4.65	3.36	-0.80
40	0.5	-0.49	2.56	1.41	-1.57	-2.06	5.01	4.04	3.10
40	0.1	1.78	3.78	-0.92	6.39	-2.69	4.89	5.22	10.41
54	25	-4.30	-0.72	3.71	-12.03	1.64	0.44	0.31	-11.80
54	10	-3.44	0.20	2.81	-7.08	0.87	1.07	1.28	-6.28
54	5	-2.64	0.81	1.97	-3.32	0.49	1.21	1.90	-2.54
54	1	-0.39	1.87	-0.37	4.40	0.19	0.58	2.90	4.19
54	0.5	0.70	2.18	-1.46	7.01	0.31	-0.02	3.14	6.13
54	0.1	3.38	2.48	-4.01	10.96	1.07	-1.99	3.22	8.28

°C = (°F-32)/1.8

The results in table 39 show that extreme errors may result when using only DSR measurements in the  $|G^*|$  mastercurve characterization. However, these errors are contained entirely within the low temperature range. At temperatures included in the DSR testing (greater than 59 °F (15 °C)), the errors are small. To place perspective on the differences shown in table 39, the mastercurves for the ALF AC5 and MnRoad Pen 120-150 binders are shown in figure 89 and figure 90, respectively. Note that the mastercurves themselves are calibrated well and that the observed errors are almost entirely related to the t-T shift factor errors (see figure 87). It is interesting to note that the two mastercurves that seem to have the poorest match (i.e., the WesTrack binder in figure 91) do not have the highest error. This result is due to the nature of the error definition and

also due to differences in the t-T shift factors obtained from the two characterization methods. This latter effect is seen in figure 89 through figure 91 where all the mastercurves change from an equivalent reduced frequency of 14 °F (-10 °C) and 25 Hz to 129.2 °F (54 °C) and 0.1 Hz. This effect is seen also in the t-T shift factor functions in figure 92 through figure 94.

Furthermore, equation 73 indicates that the error is defined in normal space, and figure 91 indicates that the magnitude of  $|G^*|$  is smaller for the Westrak binder than for the other binders. If the error is defined in logarithmic space, as seen in equation 74, the error is found to follow the graphical results more closely, as shown in table 40.

The results in figure 89 through figure 94, table 39, and table 40 affect the LTPP database population effort because BBR data are not currently available for any of the LTPP sections. In fact, the only data available in the LTPP database are DSR results at 10 rad/s and limited temperatures. A technique for considering these limited data is presented in the next section. However, these figures and tables reveal that without the BBR test results, the strength of the  $|E^*|$  predictive models, which rely on the  $|G^*|$ , would be severely limited at low temperatures.

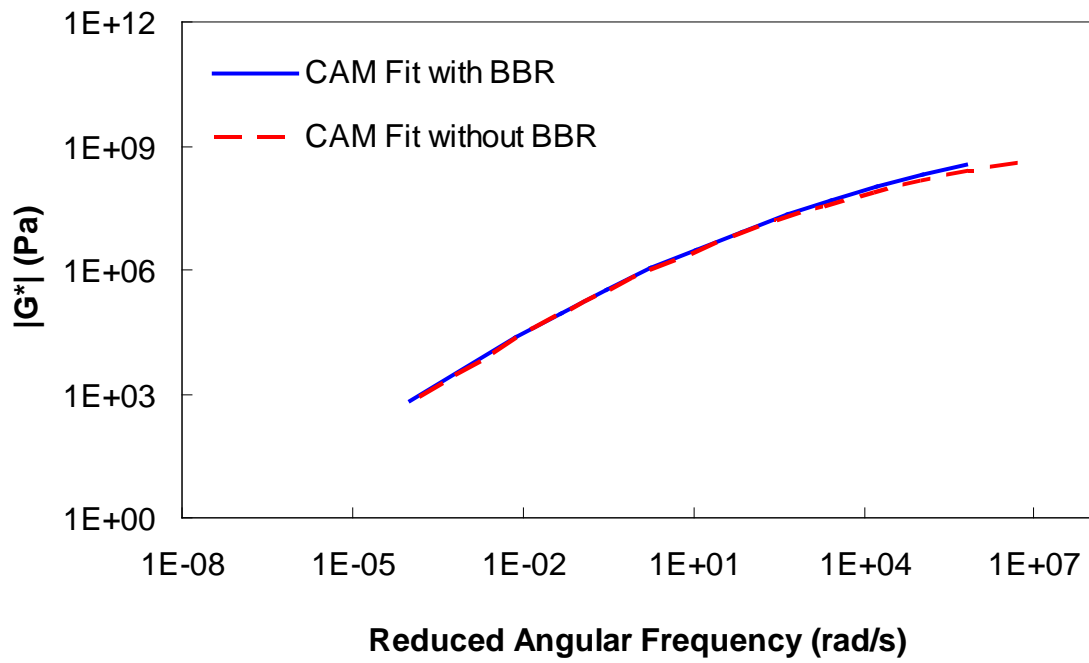


**Figure 89. Graph.  $|G^*|$  mastercurves characterized with and without BBR data for ALF AC5 binder.**

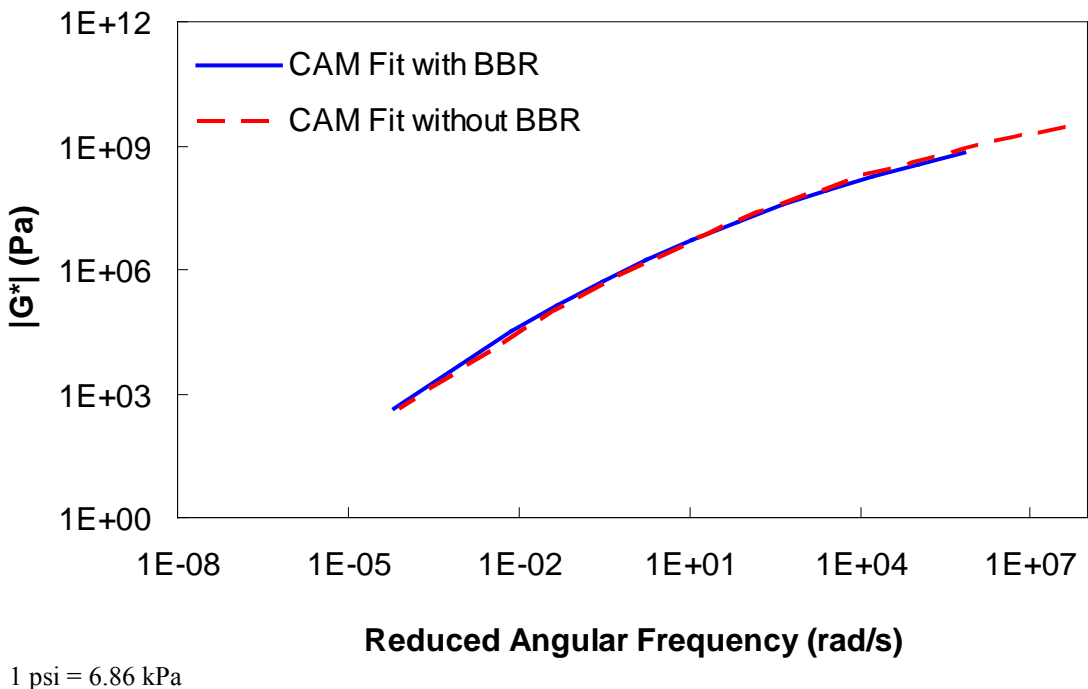


**Figure 90.** Graph.  $|G^*|$  mastercurves characterized with and without BBR data for the MnRoad Pen 120-150 binder.

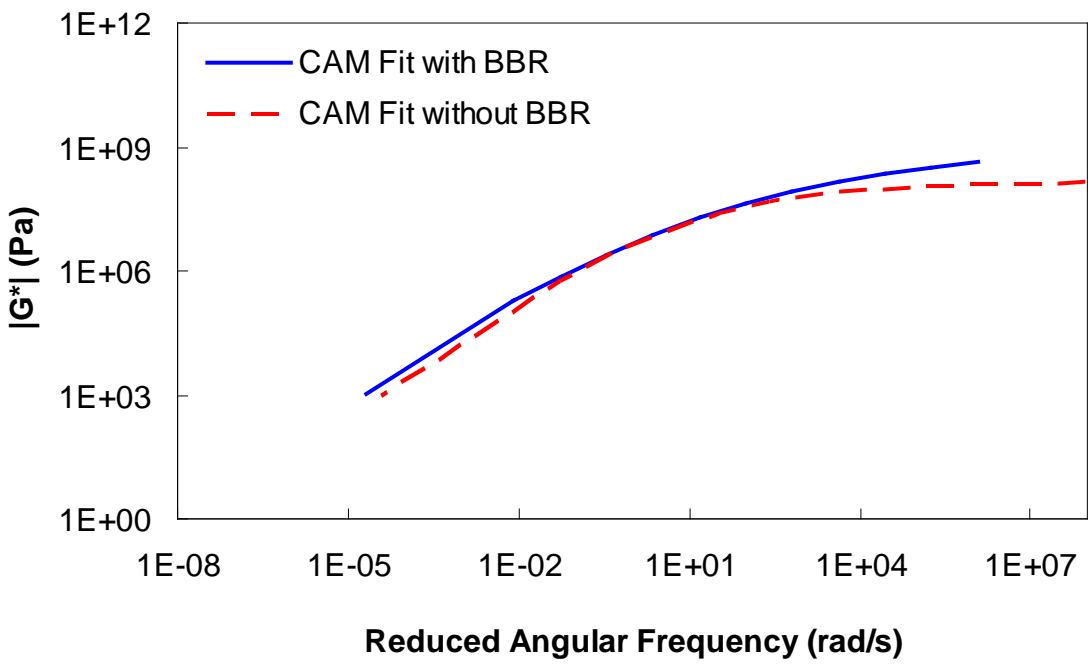


**Figure 91.** Graph.  $|G^*|$  mastercurves characterized with and without BBR data for the WesTrack binder.

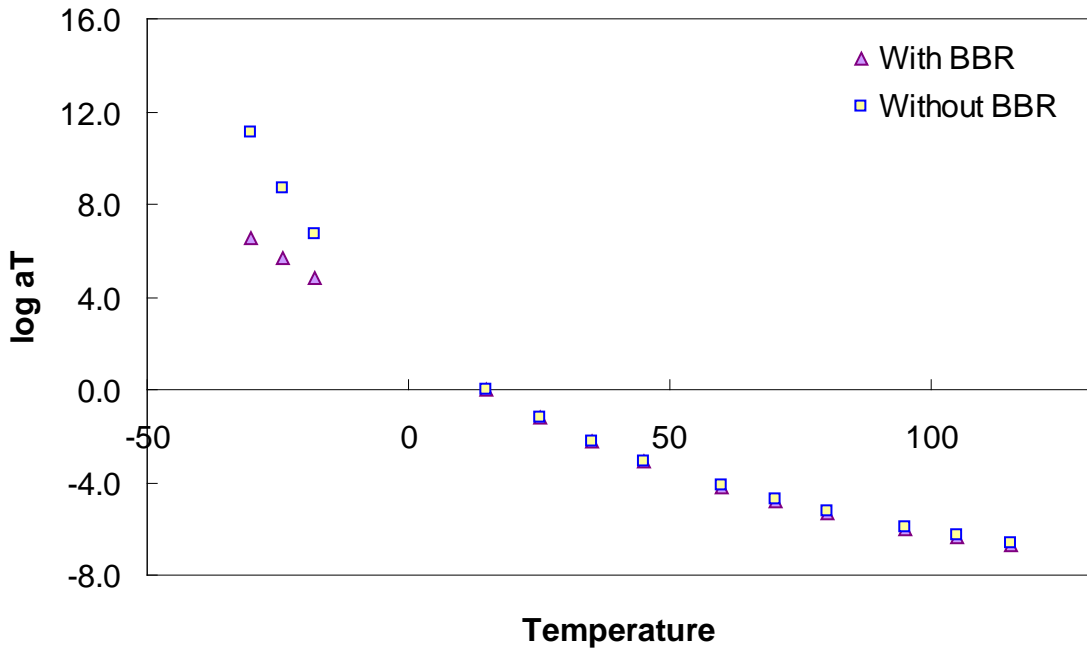


**Figure 92.** Graph. t-T shift factor function characterized with and without BBR data for the ALF AC5 binder.

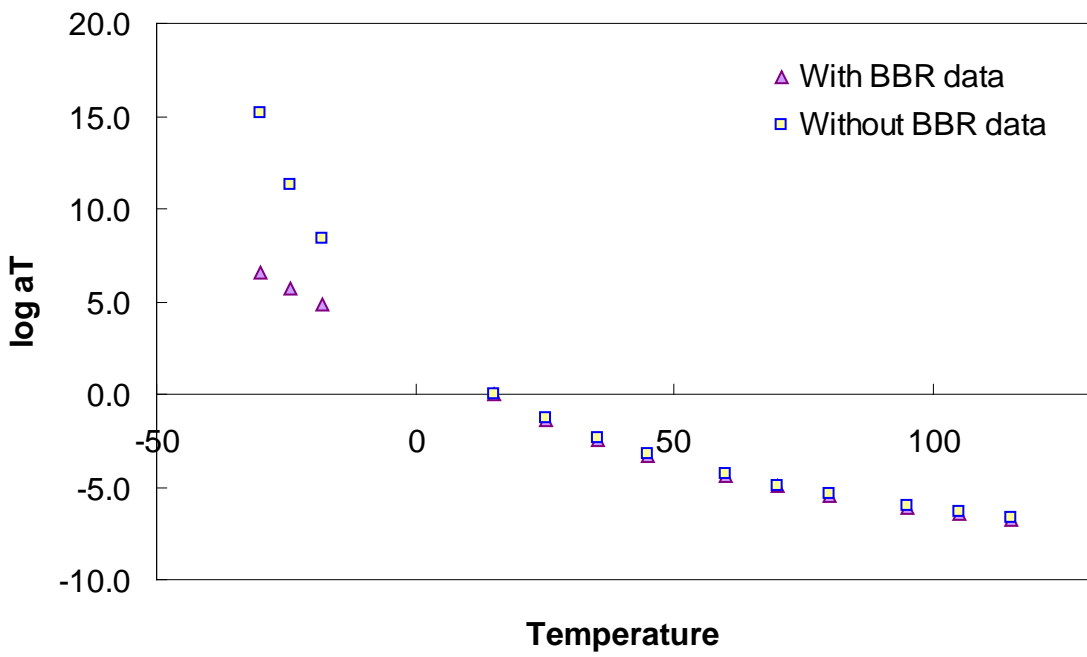
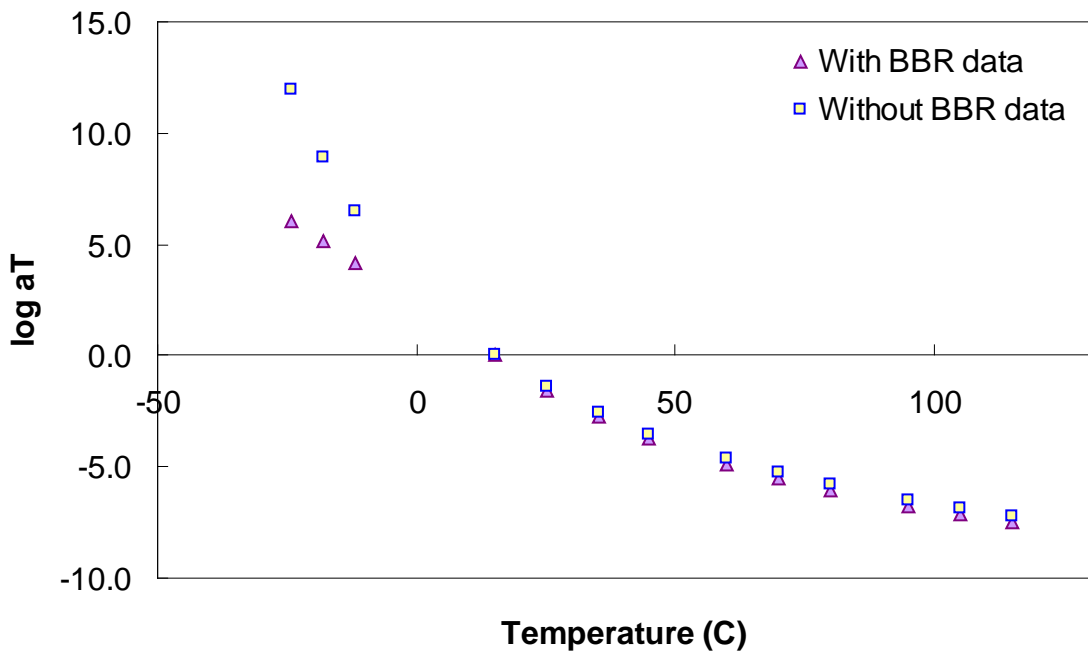


**Figure 93.** Graph. t-T shift factor function characterized with and without BBR data for the MnRoad Pen 120-150 binder.



$$^{\circ}\text{C} = (\text{ }^{\circ}\text{F}-32)/1.8$$

**Figure 94. Graph. t-T shift factor function characterized with and without BBR data for the WesTrack binder.**

$$\%Diff = \frac{\log(|G^*|_{with\ BBR}) - \log(|G^*|_{without\ BBR})}{\log(|G^*|_{with\ BBR})} * 100 \quad (74)$$

**Table 40. Percentage of log difference between BBR-calibrated and non-BBR-calibrated  $|G^*|$  at TP-62 temperatures and frequencies.**

Temperature (°C)	Frequency (Hz)	ALF AC5	ALF AC10	ALF AC20	ALF Novochip	ALF Styrene	MnRoad AC20	PEN 120-150	Wes Track
-10	25	-0.54	-4.06	-5.16	10.71	1.75	-8.35	-4.65	5.97
-10	10	-0.97	-4.24	-5.04	10.14	1.37	-8.01	-4.81	5.49
-10	5	-1.30	-4.39	-4.96	9.67	1.07	-7.75	-4.95	5.09
-10	1	-2.12	-4.76	-4.80	8.43	0.36	-7.14	-5.31	4.09
-10	0.5	-2.49	-4.94	-4.76	7.83	0.05	-6.89	-5.48	3.62
-10	0.1	-3.39	-5.40	-4.71	6.29	-0.70	-6.32	-5.92	2.44
5	25	1.03	-0.58	-1.39	6.96	1.24	-3.06	-0.69	4.17
5	10	0.86	-0.49	-1.11	6.12	0.95	-2.49	-0.56	3.69
5	5	0.75	-0.42	-0.90	5.47	0.73	-2.05	-0.46	3.34
5	1	0.50	-0.23	-0.45	3.91	0.22	-1.03	-0.21	2.58
5	0.5	0.41	-0.14	-0.27	3.24	0.00	-0.59	-0.10	2.30
5	0.1	0.23	0.07	0.11	1.78	-0.50	0.43	0.19	1.83
20	25	0.24	-0.37	-0.23	1.43	0.59	-1.00	-0.36	0.11
20	10	0.14	-0.27	-0.06	0.71	0.37	-0.57	-0.23	-0.15
20	5	0.08	-0.19	0.06	0.24	0.20	-0.26	-0.13	-0.27
20	1	-0.01	0.00	0.26	-0.55	-0.16	0.42	0.13	-0.27
20	0.5	-0.03	0.09	0.33	-0.74	-0.30	0.70	0.24	-0.15
20	0.1	-0.02	0.32	0.42	-0.83	-0.63	1.29	0.52	0.40
40	25	-0.24	-0.17	0.28	-1.15	0.23	-0.11	-0.09	-1.35
40	10	-0.24	-0.07	0.29	-1.09	0.11	0.09	0.03	-1.08
40	5	-0.23	0.00	0.28	-0.96	0.03	0.21	0.12	-0.82
40	1	-0.12	0.18	0.20	-0.43	-0.13	0.42	0.33	-0.07
40	0.5	-0.05	0.26	0.13	-0.13	-0.18	0.48	0.42	0.29
40	0.1	0.21	0.44	-0.10	0.63	-0.25	0.54	0.64	1.16
54	25	-0.38	-0.06	0.32	-0.91	0.13	0.04	0.03	-0.95
54	10	-0.33	0.02	0.26	-0.58	0.07	0.10	0.13	-0.55
54	5	-0.27	0.08	0.19	-0.29	0.04	0.12	0.20	-0.24
54	1	-0.05	0.22	-0.04	0.44	0.02	0.07	0.36	0.47
54	0.5	0.09	0.28	-0.17	0.75	0.03	0.00	0.42	0.75
54	0.1	0.53	0.39	-0.54	1.37	0.12	-0.29	0.53	1.25

°C = (°F-32)/1.8

## B.7 EXTRACTING FULL BINDER $|G^*|$ DATA FROM LIMITED ISOCHRONAL MEASUREMENTS

To fully utilize  $|G^*|$  in mixture  $|E^*|$  predictive models, a complete dataset is needed. This dataset must be complete because it must cover the temperature and frequency ranges over which the mixture modulus should be predicted. The full suite of Superpave™ binder specification tests covers this range; however, the data are inconsistent (i.e.,  $|G^*|$  from DSR, and  $S(t)$  and  $m$  from BBR) and require further processing for complete utilization. This section of the report presents

a method for analyzing standard PG binder characterization tests so that the results can provide a more complete dataset.

This method is currently under development by the research team and will be refined as a more complete picture of the available data is obtained. It is assumed that DSR (i.e.,  $|G^*|$ ) measurements taken at the standard frequency of 10 rad/s, or 1.67 Hz, at multiple temperatures are available. Results from Superpave™ BBR testing are not necessary in this methodology, but a theoretically justified technique for including such data in the process is shown and evaluated. Currently, such data are not available from the LTPP database; however, the methodology is evaluated nonetheless in case such characterization is included in future research efforts.

To extract a more complete dataset, an analytical expression for  $|G^*|$  as a function of frequency and temperature must be found. Because asphalt binder is thermorheologically simple, these two factors can be combined into a single parameter, known as “reduced frequency” and shown in equations 75 and 76. Note that although the nomenclature in this report represents frequency using  $\omega$ , which implies the unit is radians per second, the methodology is equally applicable to frequency in hertz.

$$|G^*|(T, \omega) = |G^*|(\omega_R) \quad (75)$$

$$\omega_R = \omega \times a_T \quad (76)$$

Where:

$\omega_R$  = Reduced frequency.

$a_T$  = t-T shift factor, which is a function of temperature.

This factor can be determined experimentally using results from a temperature and frequency sweep test, such as the test found in AASHTO TP-62.<sup>(8)</sup> From these tests, the t-T shift factor is determined by horizontally shifting the data at different temperatures until a smooth varying function results. This process is shown previously in this report and is only possible when measurements are taken at multiple frequencies and temperatures.

Measurements from a single-frequency temperature sweep test, such as Superpave™ DSR testing, cannot be used directly to extract these t-T shift factors by simple horizontal translations. This complication arises because the slope of the modulus-temperature relationship, a value that can be determined from single-frequency temperature sweep tests, is dependent on both the frequency and the temperature. Mathematically, this discrepancy can be expressed as follows:

$$\frac{\partial |G^*|}{\partial T} = \frac{\partial |G^*|}{\partial \log(\omega_R)} \frac{\partial \log(\omega_R)}{\partial T} \quad (77)$$

Where:

- $T$  = Temperature.
- $\omega_R$  = Reduced frequency.
- $\partial|G^*|/\partial T$  = Derivative of  $|G^*|$  with respect to time, known from Superpave<sup>TM</sup> DSR testing.

Direct determination is not possible using these measurements, but equation 77 can be solved analytically if functional forms for the t-T shift factor function and for  $|G^*|$  as a function of reduced frequency are known. In this methodology, the CAM model is assumed sufficient for the latter, and a secondary surrogate model along with the WLF equation is assumed for the logarithm of the former (note that two surrogate models are discussed in the following section). These functions are shown in equations 78 and 79, respectively.

$$|G^*| = \frac{G_g}{\left(1 + \left(\frac{\omega_c}{\omega_R}\right)^k\right)^{m_e/k}} \quad (78)$$

$$\log a_T = \frac{C_1(T - T_R)}{C_2 + T - T_R} \quad (79)$$

Where  $G_g$ ,  $\omega_c$ ,  $k$ ,  $C_1$ ,  $C_2$ , and  $C_3$  are fitting coefficients. Combining equations 76 and 79 yields the following analytical expression for reduced frequency:

$$\omega_R = \omega * 10^{\frac{C_1(T - T_R)}{C_2 + T - T_R}} \quad (80)$$

From equation 77, DSR measurements can be used directly to determine the left-hand side of the equation, and the right-hand side can be solved analytically. However, initial trials using this approach proved unsuccessful due to the large spacing between typical Superpave<sup>TM</sup> DSR measurements. Instead, a more direct approach that uses equation 78 was successful; however, it is necessary to first discuss the model used to predict the t-T shift factors.

## B.8 T-T SHIFT FACTOR SURROGATE MODEL DEVELOPMENT

Because no clear theoretical link was found between typical DSR measurements and the t-T shift factors, a phenomenological approach and a simple averaging approach were taken. As shown in the following sections, both approaches provide approximately the same accuracy; however, the final recommended procedure will be the subject of further investigation. Because it is important that this t-T shift factor function covers the range over which the mixture modulus would be predicted, only binders with BBR test data have been used. A list of these binders can be found in table 4. For each of these binders, the t-T shift factors were found from optimization fitting using the CAM and WLF equations.

### B.8.1 Phenomenological t-T Shift Factor Function Model

A similarity exists between the normalized shear modulus at 10 rad/s and the log shift factor function. Additionally, a similar relationship exists in the BBR test results at 60 s. These relationships are shown in figure 95 for the binders with BBR test data. For simplicity, both relationships are normalized to  $|G^*|$  at 10 rad/s at the chosen reference temperature. Because this value is taken as the reference condition and because BBR data are essentially DSR results at 0.01 rad/s ( $\omega=2/\pi t$ ), an apparent discontinuity is found in the BBR curve at the reference condition. To understand this discontinuity, it must be recognized that to obtain a given ratio larger than one from DSR test results, the test must be performed at a higher temperature than for a BBR test. This temperature effect is integral to the relationship shown in figure 95 for the DSR results. Because all of the BBR test results are obtained at the same time at 60 s, each is affected similarly, resulting in the discontinuity. However, the slope of this relationship stays much the same as seen in figure 96, where the offset discontinuity in the BBR data has been artificially removed.

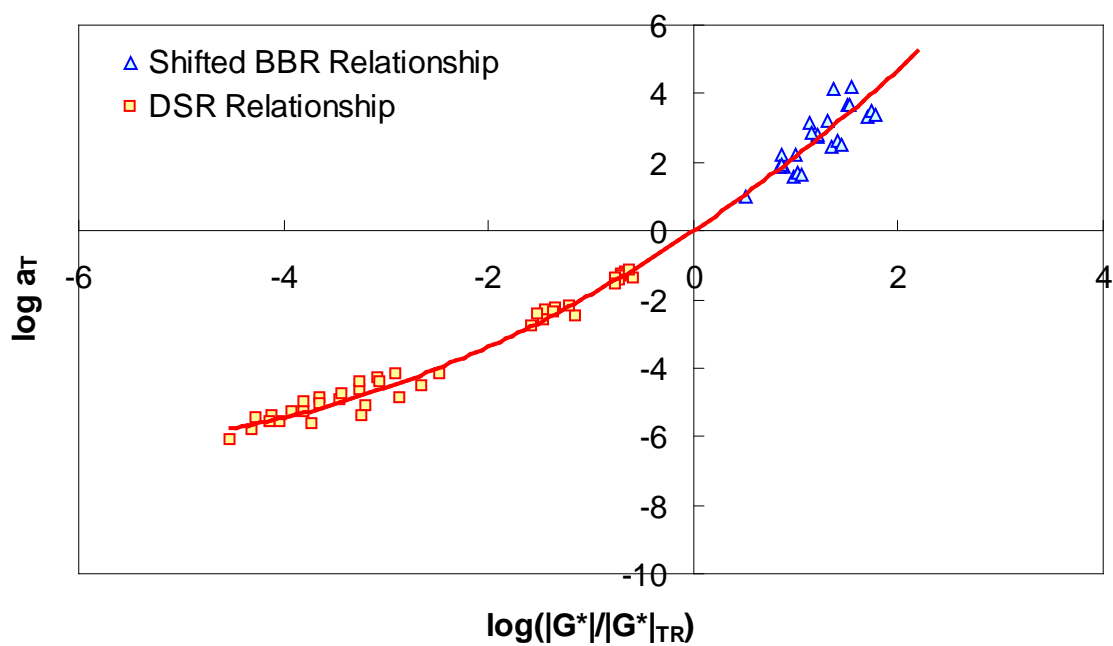
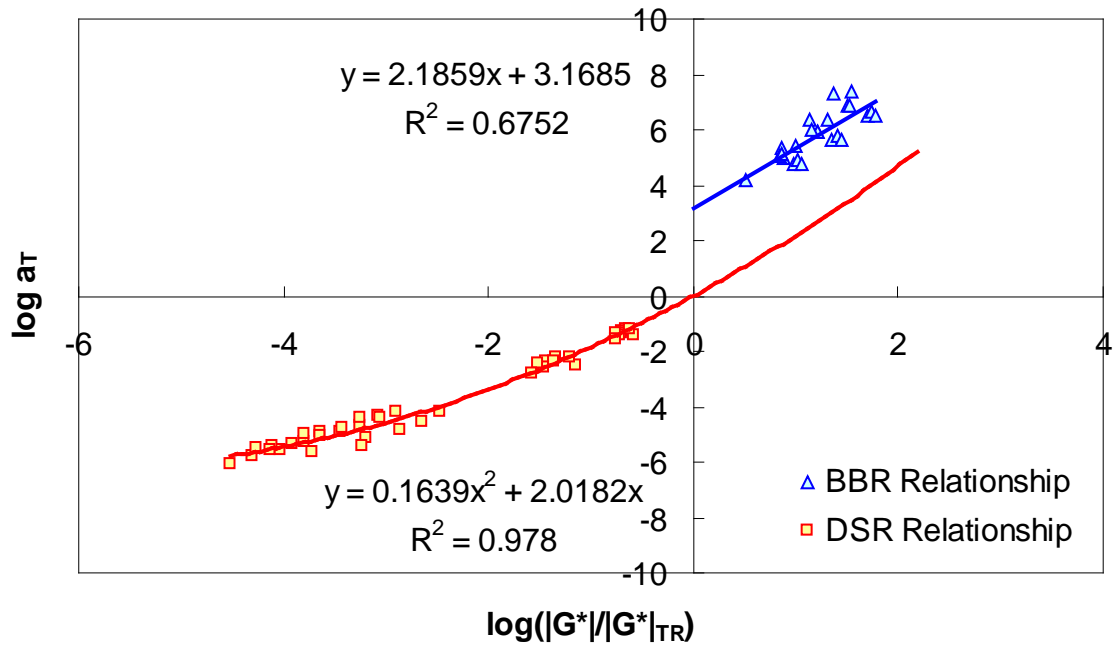
It should be noted that the relationships shown in figure 95 have been developed at a reference temperature of 59 °F (15 °C). If DSR measurements are taken at this temperature, then the relationship may be used directly. Alternatively,  $|G^*|$  at 59 °F (15 °C) may be interpolated if DSR measurements are taken near this temperature. Also, the relationship can be used even if the reference condition is not 59 °F (15 °C), although some error would be inevitable. However, the approach taken here recognizes that at around 59 °F (15 °C) (between 41 and 77 °F (5 and 25 °C)), the t-T shift factors are not significantly different. This relationship follows a second order polynomial, and its implications are shown in the calibrated t-T shift factor relationship shown in equations 81 and 82. The verification of these relationships is shown in figure 97 for FHWA mobile trailer and FHWA ALF binders, which were not included in the calibration process.

$$\log a_{T,DSR} = .1639(A)^2 + 2.0182 * (A) - (0.000638 * T_R^2 - 0.1469 * T_R + 2.06) \quad (81)$$

$$\log a_{T,BBR} = 2.1859(A) + 3.1685 - (0.000638 * T_R^2 - 0.1469 * T_R + 2.06) \quad (82)$$

Where:

$$A = \log\left(\frac{|G^*|}{|G^*|_{T_R}}\right) - 6.16 + 3.05\left(\sqrt{0.000418 * T_R^2 - 0.10 * T_R + 5.42}\right). \quad (83)$$



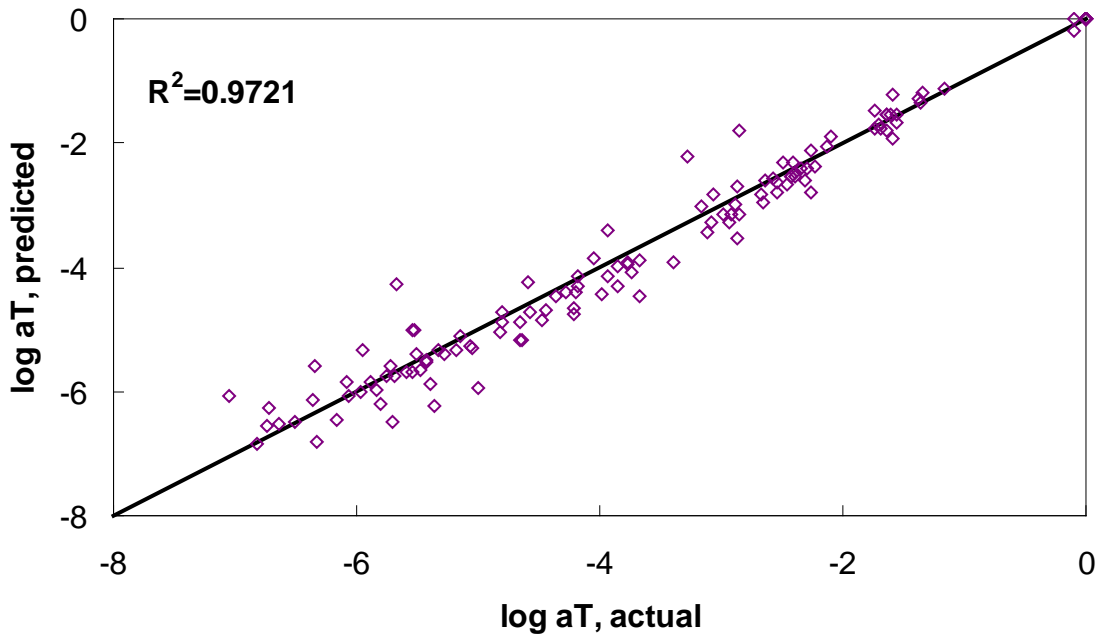
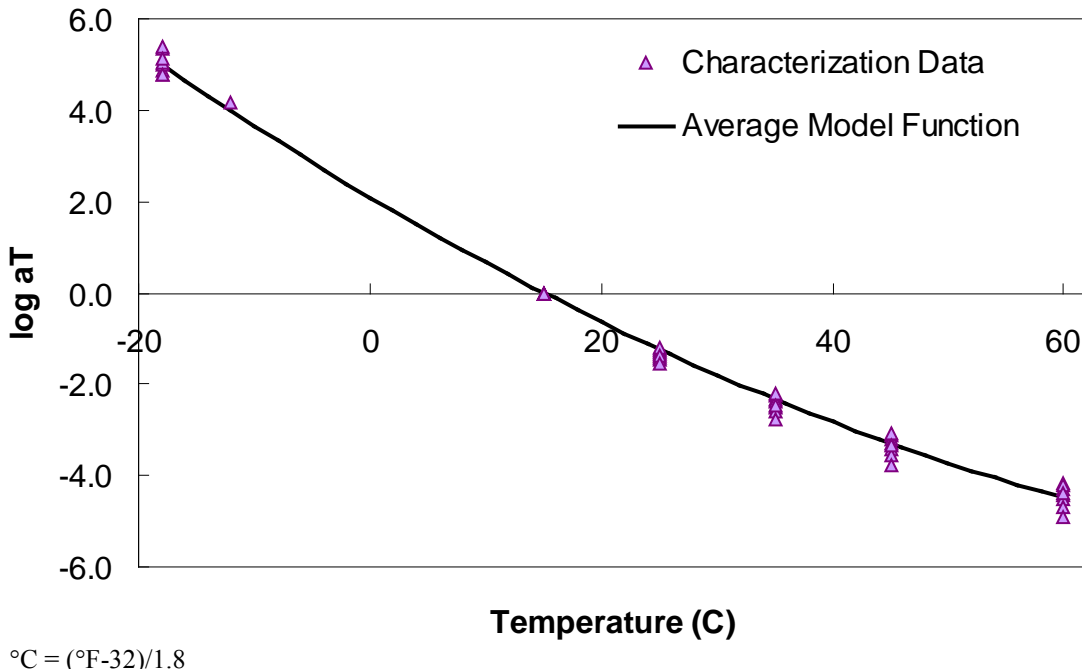


**Figure 97. Graph. t-T shift factor model verification with phenomenological model.**

### B.8.2 Use of Average t-T Shift Factor Function

A second, more simplistic approach has also shown promise. From the available binder databases, it was found that the t-T shift factor functions are somewhat similar across binder types. In this approach, the same binders used to develop the phenomenological model are processed to find an average representative shift factor function (see figure 98). The advantage of this approach is its simplicity as well as the fact that BBR test results are not needed to obtain a reasonable estimate of the t-T shift factor at low temperatures. Verification of this model is shown in figure 99. Comparing figure 99 to figure 97, it is observed that the average technique has a slightly improved  $R^2$  value. In addition, the average technique does not tend to show systematic underestimation of the phenomenological approach in the intermediate temperature ranges. However, in general, the effectiveness of the model does not appear to be significantly superior or inferior to the phenomenological approach. Both are evaluated in the subsequent sections.



$$^{\circ}\text{C} = (\text{^{\circ}\text{F}-32})/1.8$$

**Figure 98. Graph. Average t-T shift factor function.**

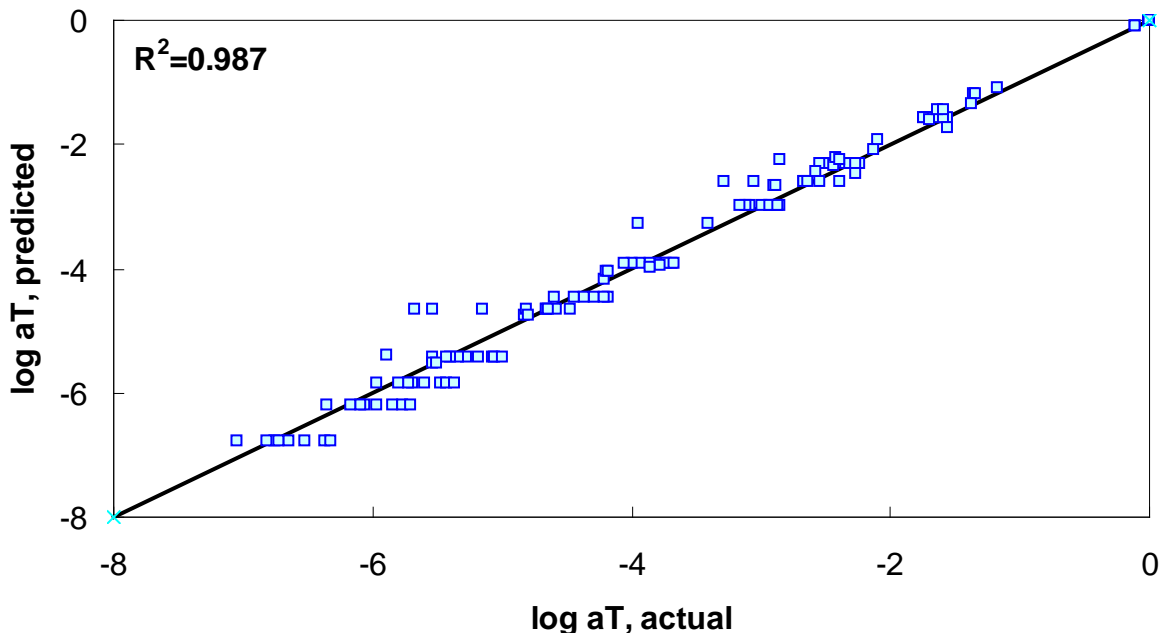


**Figure 99. Graph. t-T shift factor model verification with average function model.**

## B.9 INCLUSION OF BBR DATA IN MASTERCURVE GENERATION

Including Superpave<sup>TM</sup>-level BBR data in the optimization process is not as straightforward as the process that combines full DSR and BBR characterization. Complications arise due to the limited dataset that is available (typically only the beam stiffness term,  $S(t)$ , and  $m$  at 60 s for up to three temperatures). Therefore, to use the data as accurately as possible, a few approximate conversion and typical values need to be assumed. The process begins by observing from the

theory of linear viscoelasticity that  $S$  is actually the inverse of the uniaxial extensional  $D(t)$ . In order to convert to  $|G^*|$ , the uniaxial relaxation modulus,  $E(t)$ , must be found. Because it is possible that only a single BBR test result is available, the conversion technique must be capable of single-point conversion. For this purpose, the approximate relationship given in equation 84 is utilized as follows:

$$E(t) = \frac{\sin(n\pi)}{n\pi} \frac{1}{D(t)} = \frac{\sin(n\pi)}{n\pi} S(t) \quad (84)$$

Where  $n$  is equivalent to the  $m$ -value determined from the BBR test. After determining  $E(t)$ , the approximate interrelationship in equation 85 is used to convert from time-domain to frequency-domain functions as follows:

$$E(t) \approx E'(\omega) \Big|_{\omega=\frac{2}{\pi t}} \quad (85)$$

Where  $E'(\omega)$  is the storage modulus.  $E'(\omega)$  is then converted to the dynamic uniaxial modulus by using equation 86 as follows:

$$|E^*|(\omega) = \frac{E'(\omega)}{\cos(\phi)} \quad (86)$$

Where  $\phi$  is the phase angle in the material. Experience has found that this value is approximately 24 degrees under BBR test conditions. Therefore, the actual relationship used in this methodology is given by equation 87 as follows:

$$|E^*| = \frac{E'}{\cos(24)} = 1.095 * E' \quad (87)$$

Finally, to determine  $|G^*|$ , the mechanistic relationship between uniaxial and shear deformation shown in equation 88 is used. For this relationship, Poisson's ratio is assumed to be time-independent and to have a value of 0.5.

$$|G^*| = \frac{|E^*|}{2(1+\nu)} = \frac{|E^*|}{2(1+0.5)} = \frac{1}{3} |E^*| \quad (88)$$

Combining equations 84 through 87, the relationship between  $|G^*|$  and  $S(t)$  is given by equation 89, as follows:

$$|G^*|(\omega) = \frac{0.365 * \sin(n\pi)}{n\pi} S(t) \Big|_{t=\frac{2}{\pi t}} \quad (89)$$

In addition to calculating the shear stiffness values from beam stiffness and  $m$ -values, it is worthwhile to consider fitting the  $m$ -values. Recognizing that  $m$ -values are the derivative

of the logarithm of stiffness with respect to the logarithm of time and that simple multiplicative relationships are used to convert from frequency to time, the analytical expression for the  $m$ -value using the CAM model can be given by equation 90, as follows:

$$m_{calculated} = \frac{\partial \log |G^*|}{\partial \log \omega_R} = \frac{m_e \left( \frac{\omega_c}{\omega_R} \right)^k}{\left( 1 + \left( \frac{\omega_c}{\omega_R} \right)^k \right)} \quad (90)$$

## B.10 PAV- TO RTFO-AGING MODEL (PAR MODEL)

To develop a complete mastercurve from limited Superpave<sup>TM</sup> data, the conversion between PAV- and RTFO-aging conditions is necessary. This conversion is also needed in the LTPP database where  $|G^*|$  values are given in terms of RTFO- and PAV-aging conditions. It is noted that original  $|G^*|$  values are also available in the database. A similar approach could be used to convert from original (or field-aged) to RTFO. Currently, the more important conversion is from PAV to RTFO. To develop this relationship, the Witczak database binders listed in section 3.0 are used. In general, the relationship between  $|G^*|_{PAV}$  and  $|G^*|_{RTFO}$  is found to be dependent on temperature, frequency, and the chemical properties of the asphalt binder. Because none of the Superpave<sup>TM</sup> tests directly measure the chemical properties of the asphalt binder, the two primary factors in the PAR model are temperature and frequency. Although not a major factor, the Superpave<sup>TM</sup> high temperature grade is found to be a secondary factor and may indirectly capture some of the chemical composition effects.

The general form of the PAR model is shown in equation 91 where  $\kappa_T$  and  $\kappa_\omega$  are the temperature and frequency factors, respectively.

$$|G^*|_{RTFO} = \kappa |G^*|_{PAV} = \kappa_T \kappa_\omega |G^*|_{PAV} \quad (91)$$

In general,  $\kappa_T$  follows a second order polynomial relationship, with the minimum occurring near the high temperature PG (see figure 100). After calibrating  $\kappa_T$ ,  $\kappa_\omega$  is characterized. This relationship follows a power law relationship, with the parameters depending on the high temperature grade of the asphalt binder, as seen in figure 101. With these relationships in mind, equation 91 can be rewritten as equation 92 as follows:

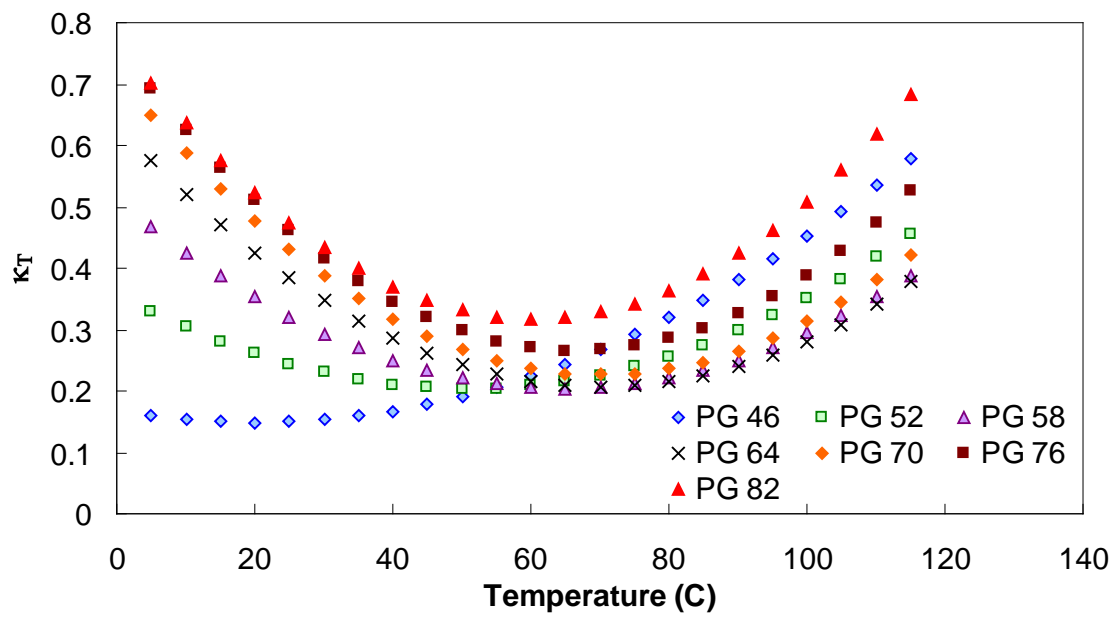
$$|G^*|_{RTFO} = (\beta_1 T^2 + \beta_2 T + \beta_3) (\gamma \omega^\tau) |G^*|_{PAV} \quad (92)$$

Where  $T$  is temperature. Each of the parameters in equation 92 follow a first or second order polynomial according to the high temperature PG of the binder. These parameters are summarized in table 41. The calibration dataset along with the calibrated model are shown according to high temperature PG in arithmetic and logarithmic spaces in figure 102 through figure 105. For model verification, a database of binders obtained from the FHWA mobile trailer and the binders used in the current FHWA ALF study are summarized in table 42. The

verification is shown in figure 106 and figure 107, and agreement is found between the model and actual data at all high temperature PG levels.

**Table 41. PAR model coefficient summary for Superpave<sup>TM</sup> high temperature grades.**

PG	$\beta_1$	$\beta_2$	$\beta_3$	$\gamma$	$\tau$	$\lambda_1$	$\lambda_2$	Number of Observations	R <sup>2</sup>
46	4.82E-05	-0.002	0.169	0.858	0.082	-0.039	0.062	Extrapolated	0.983
52	6.08E-05	-0.006	0.359	0.842	0.082	-0.043	0.180		
58	7.35E-05	-0.010	0.514	0.819	0.084	-0.047	0.281		
64	8.61E-05	-0.012	0.633	0.790	0.086	-0.050	0.363		
70	9.88E-05	-0.014	0.716	0.754	0.090	-0.053	0.428		
76	1.11E-04	-0.015	0.763	0.712	0.095	-0.056	0.474		
82	1.24E-04	-0.015	0.774	0.663	0.101	-0.058	0.503		
Unknown	8.21E-05	-0.011	0.641	0.787	0.082	-0.033	0.689	2013	0.945



$$^{\circ}\text{C} = (^{\circ}\text{F}-32)/1.8$$

**Figure 100. Graph. Effect of temperature on aging ratio of asphalt binder.**

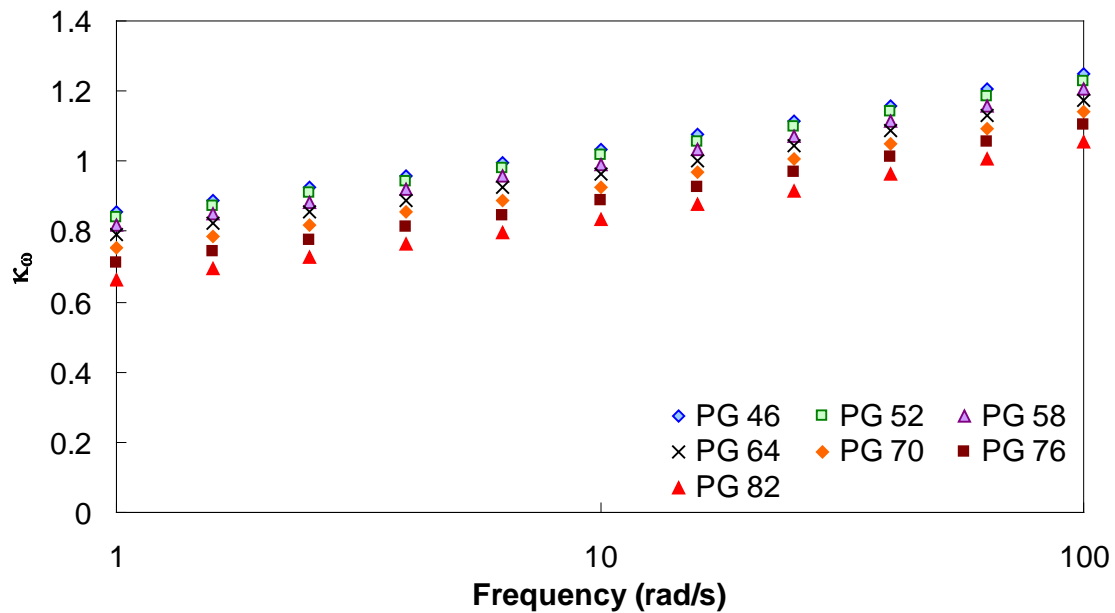
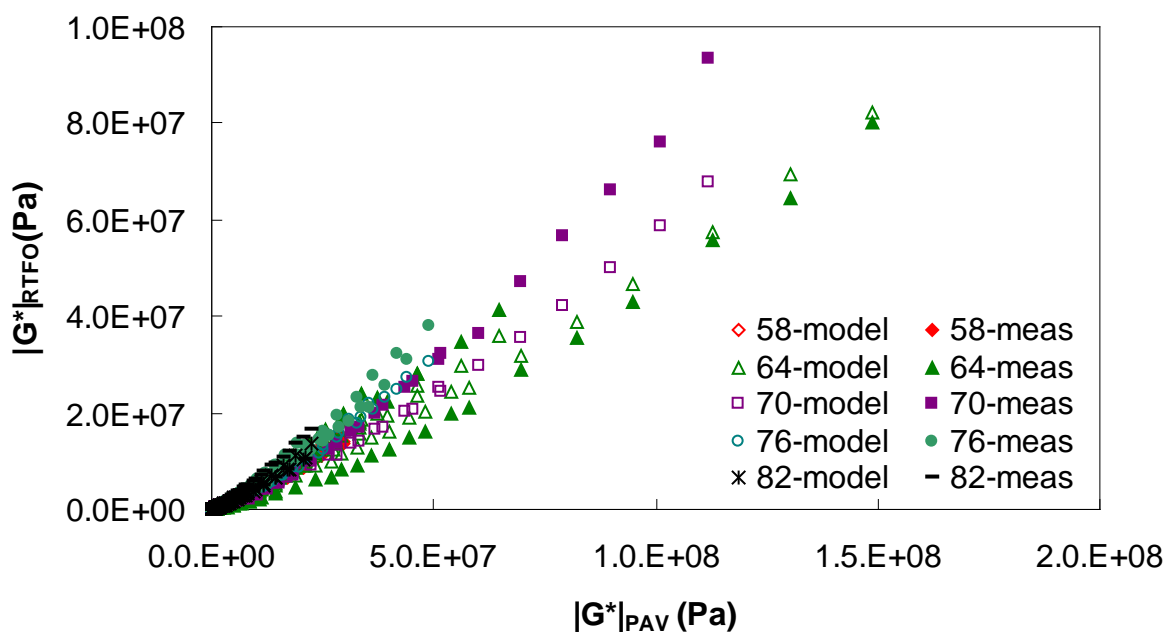
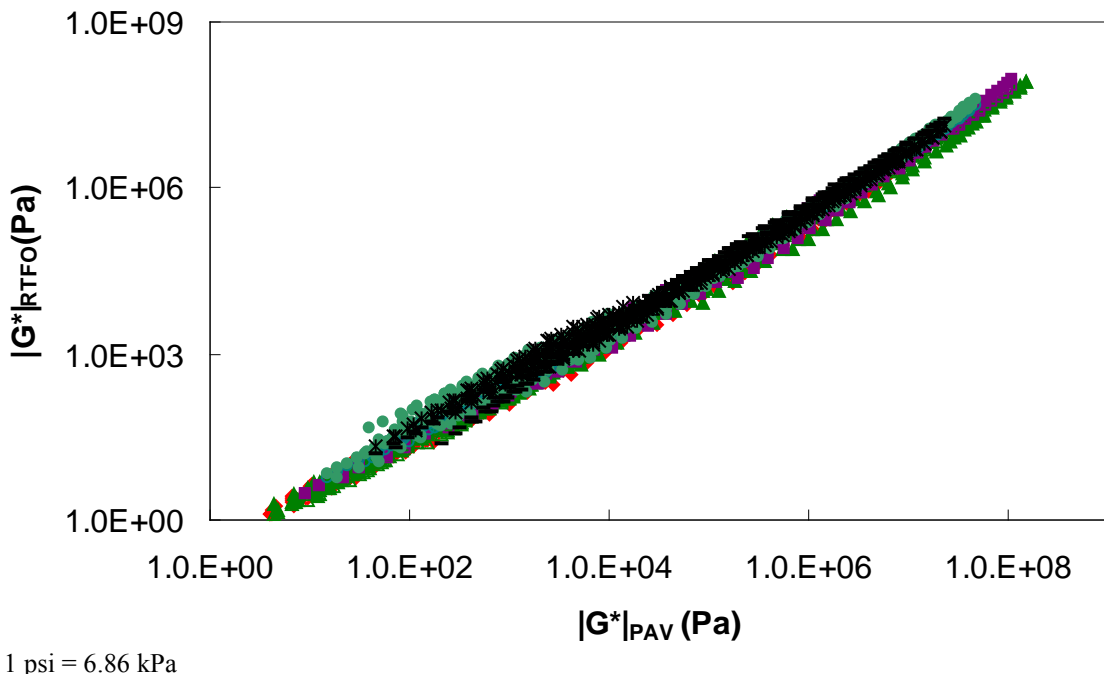


Figure 101. Graph. Effect of angular frequency on aging ratio of asphalt binder.



1 psi = 6.86 kPa

Figure 102. Graph. Calibrated PAR model in arithmetic scale.



**Figure 103. Graph. Calibrated PAR model in logarithmic scale.**

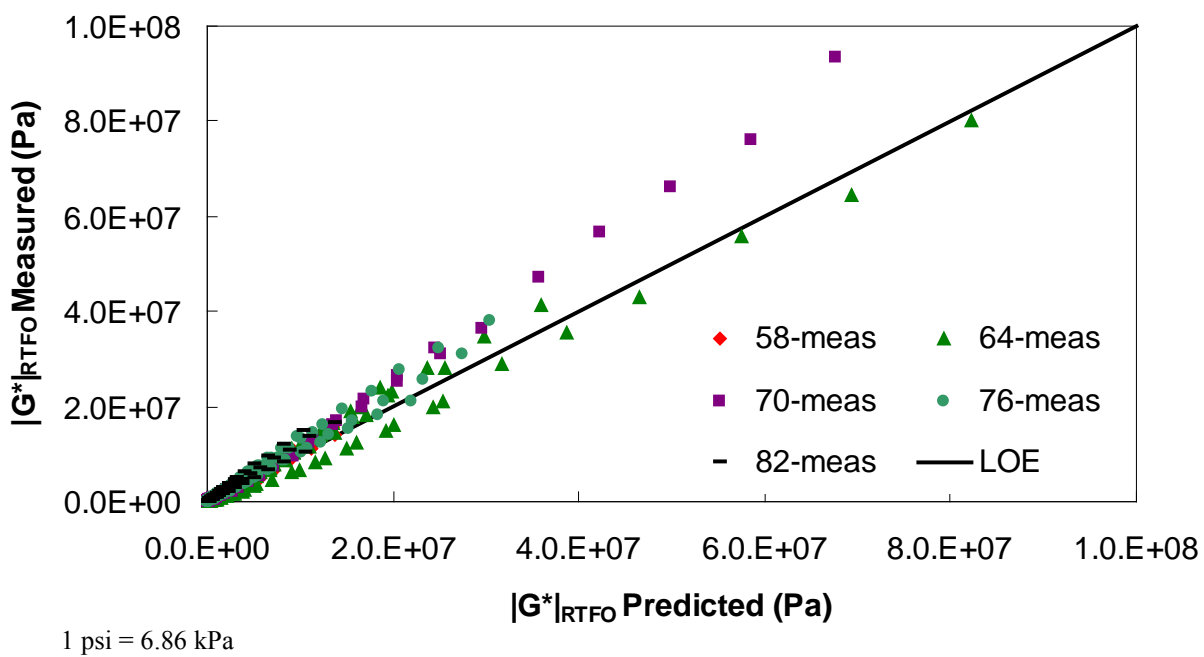


**Figure 104. Graph. Strength of PAR model in arithmetic scale.**

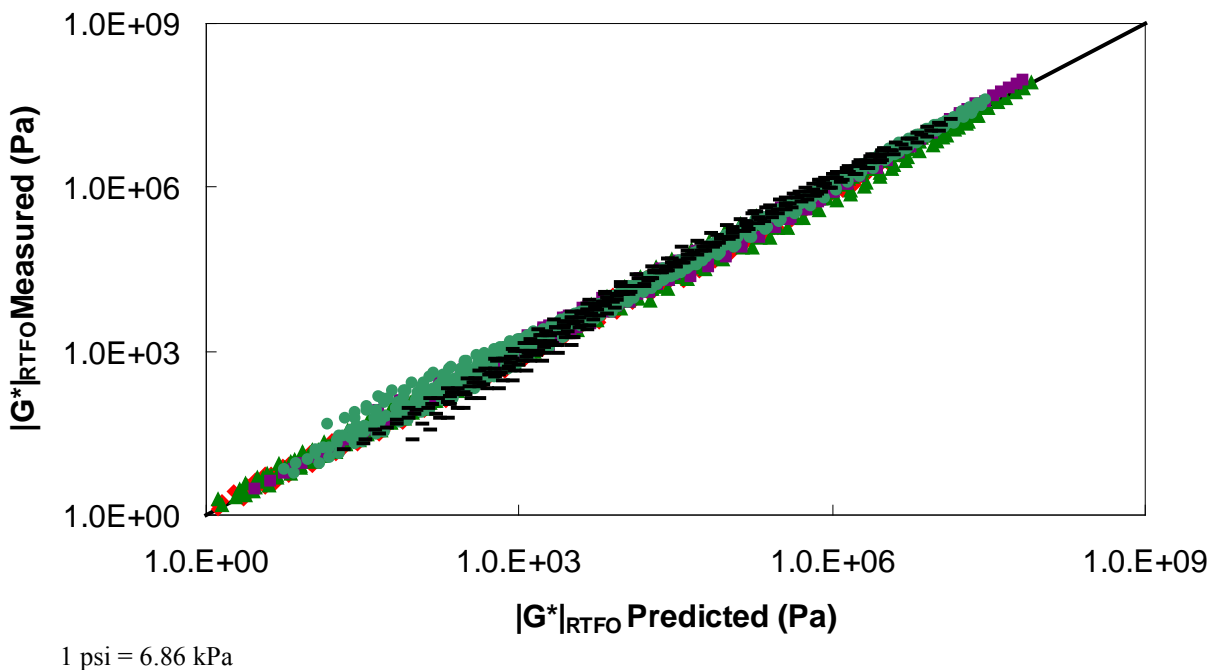


**Figure 105. Graph. Strength of PAR model in logarithmic scale.**

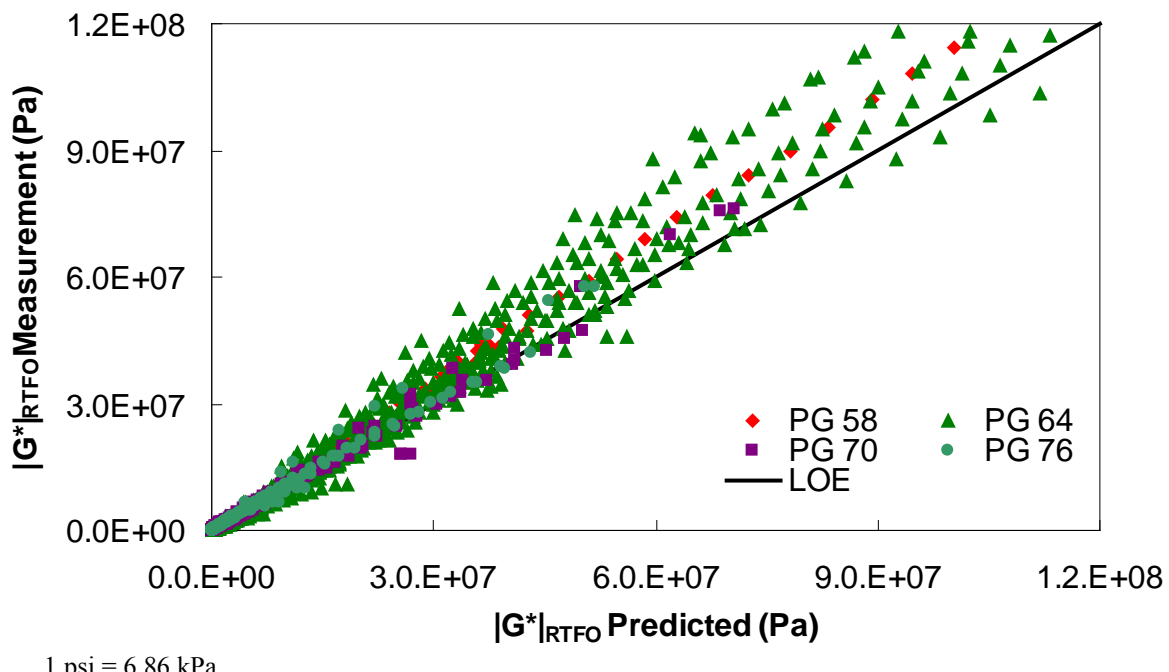


**Figure 106. Graph. PAR model verification in arithmetic logarithmic scale.**

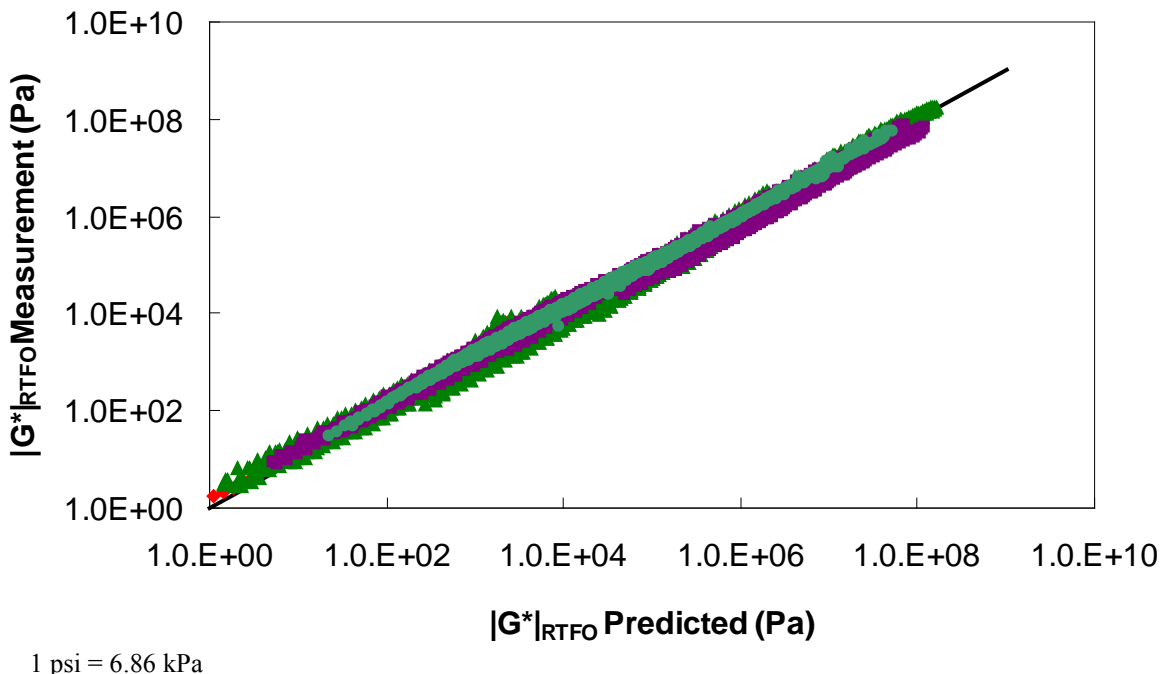
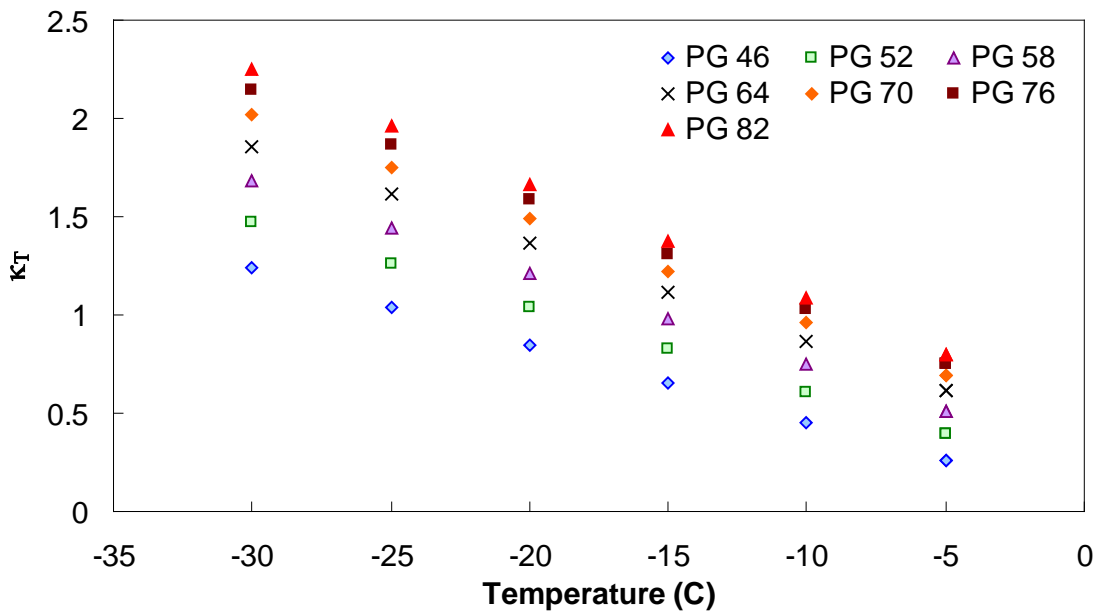


**Figure 107. Graph. PAR model verification in logarithmic scale.**

**Table 42. PAR model verification dataset summary.**

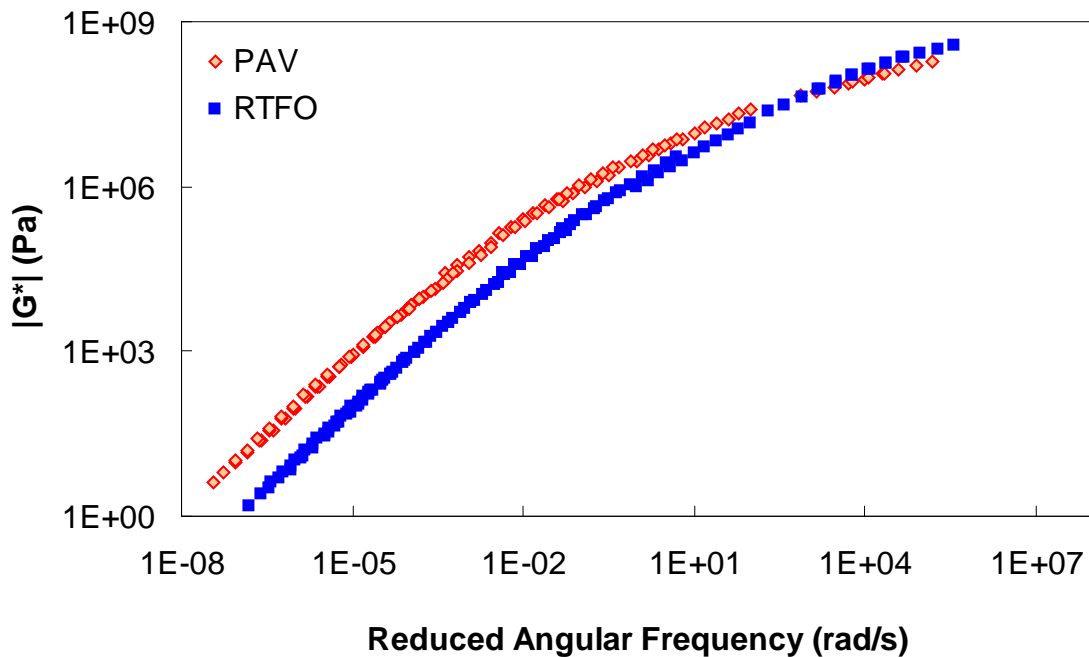
PG	Number of Observations	R <sup>2</sup>
52	297	0.702
58	605	0.981
64	2289	0.970
70	769	0.988
76	700	0.985

Because the DSR data extend only to 59 °F (15 °C), a second relationship must be calibrated for  $\kappa_T$  at temperatures consistent with the BBR test results. Such a relationship is calibrated by assuming  $\kappa_\omega$  is accurate for BBR conditions and then backcalculating  $\kappa_T$  from equation 91 and BBR test results under PAV and RTFO conditions. The results suggest that  $\kappa_T$  changes linearly with temperature under the BBR test conditions and that aging softens the material at the extremely high reduced-frequency region, as seen in figure 108. This observation is confirmed from  $|G^*|$  mastercurve analysis of the aforementioned binders and is believed to be the first of such an observation. An example of this analysis is shown for the ALF AC 10 binder in figure 109. Due to the limited database, this observation cannot be confirmed with certainty; rather,  $\kappa_T$  is treated as a fitting parameter, which, along with  $\kappa_\omega$ , approximates the effect of RTFO aging to PAV aging. The complete relationship between RTFO and PAV conditions for BBR tests is given in equation 93, and the parameters are summarized along with the other parameters in table 41. Finally, the calibrated BBR data model is shown in figure 110 and figure 111.



$$^{\circ}\text{C} = (\text{^{\circ}\text{F}-32})/1.8$$

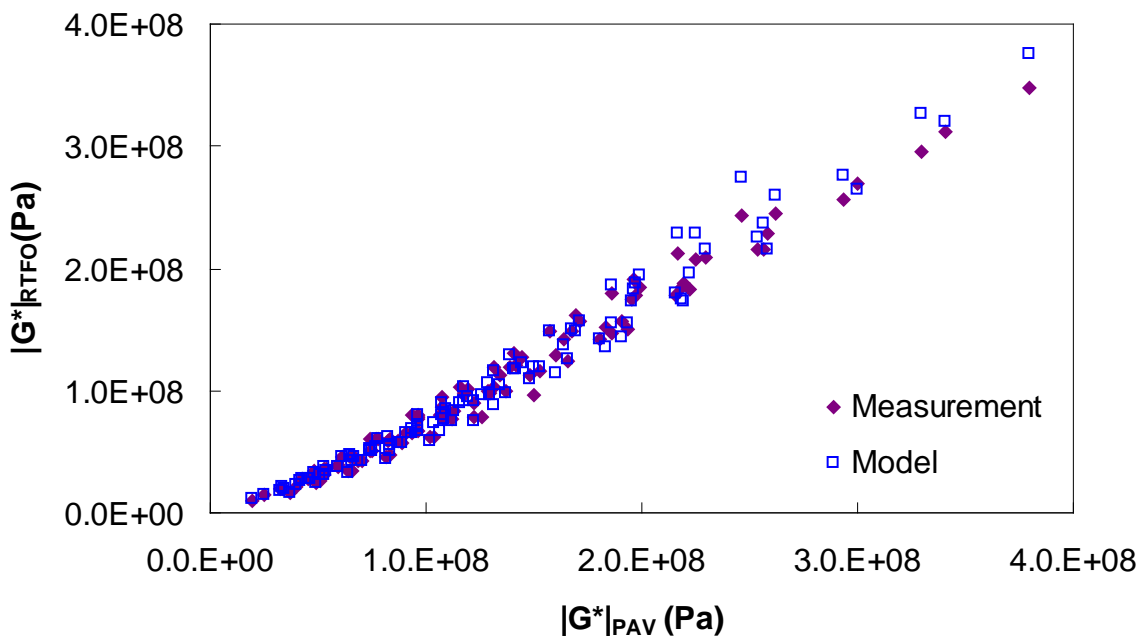
**Figure 108.** Graph. BBR-calibrated  $\kappa_T$  relationship.



$$1 \text{ psi} = 6.86 \text{ kPa}$$

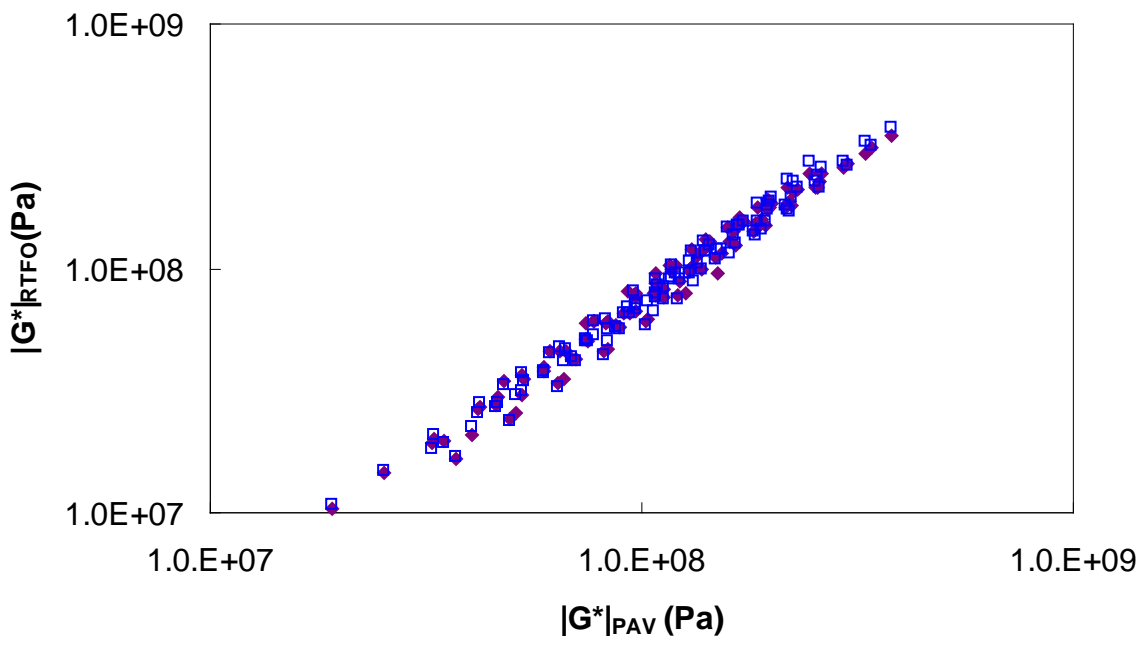
**Figure 109.** Graph. Comparison of  $|G^*|$  mastercurve analysis under PAV and RTFO conditions for ALF AC10 binder.

$$|G^*|_{RTFO} = (\lambda_1 T + \lambda_2) (\gamma \omega^\tau) |G^*|_{PAV} \quad (93)$$



$1 \text{ psi} = 6.86 \text{ kPa}$

**Figure 110. Graph. Calibrated PAR model for BBR conditions in arithmetic scale.**



$1 \text{ psi} = 6.86 \text{ kPa}$

**Figure 111. Graph. Calibrated PAR model for BBR conditions in logarithmic scale.**

## B.11 AGING EFFECT ON M-VALUE

To address the issue of aging effects on the  $m$ -value, the PAR model is used to derive the proper relationship. Consider that  $m$ ,  $n$ , the log-log slope of  $S(t)$ , and  $|G^*(\omega)|$  are close in absolute value at time-frequency equivalency points. In this case, the following equation is considered:

$$m = -\frac{\partial \log S}{\partial \log t} \approx \left. \frac{\partial \log |G^*|}{\partial \log \omega} \right|_{\omega=\frac{2}{\pi t}} \quad (94)$$

Which leads to the following equation:

$$m \approx \frac{\log |G^*|_1 - \log |G^*|_2}{\log \omega_1 - \log \omega_2} \quad (95)$$

Casting equation 95 for  $m_{RTFO}$  as follows:

$$m_{RTFO} \approx \frac{\log(|G^*|_{RTFO,1}) - \log(|G^*|_{RTFO,2})}{\log \omega_1 - \log \omega_2} \quad (96)$$

Applying equation 91 to equation 96 as follows:

$$m_{RTFO} \approx \frac{\log(|G^*|_{PAV,1} * \kappa_1) - \log(|G^*|_{PAV,2} * \kappa_2)}{\log \omega_1 - \log \omega_2} \quad (97)$$

Simplification leads to the following:

$$m_{RTFO} \approx m_{PAV} + \frac{\log(\kappa_1) - \log(\kappa_2)}{\log \omega_1 - \log \omega_2} \quad (98)$$

The second term in equation 98 can be solved analytically given the mathematical relationship for  $\kappa$  provided in equation 92. Performing the differentiation leads to the following:

$$m_{RTFO} \approx m_{PAV} + \frac{\tau}{\ln(10)} \quad (99)$$

Equation 99 is verified using the  $m$ -values for the binder data in the Witczak database, as shown in figure 112.

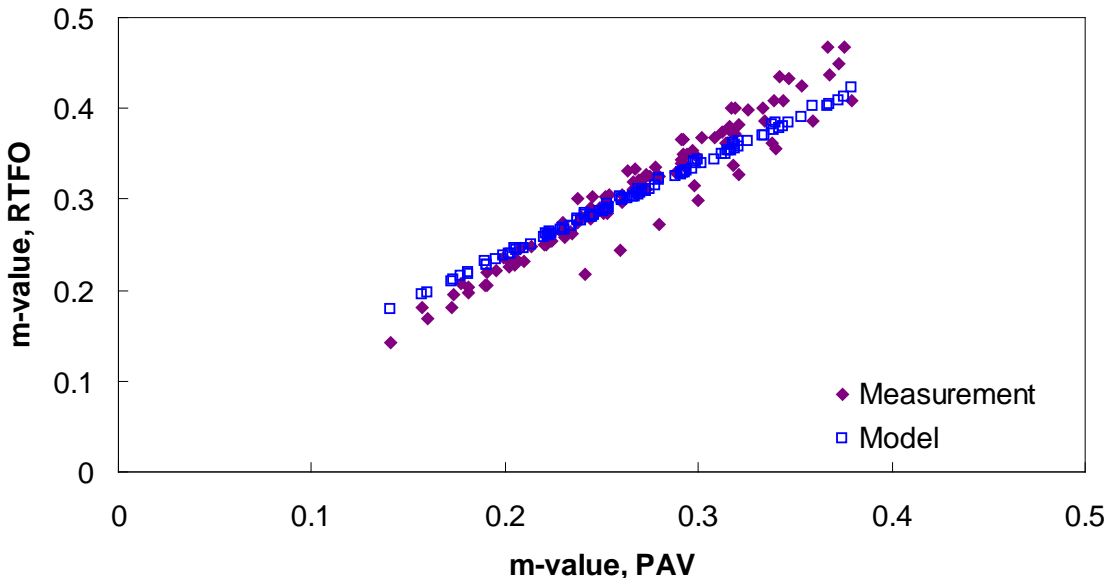


**Figure 112. Graph. Verification of  $m$ -value relationship.**

## B.12 VERIFICATION OF LIMITED DATA DEVELOPMENT

Verification of the mastercurve construction using only isochronal measurements is divided into three steps. The first verification level (divided into levels 1a and 1b) uses the Witczak binder data, which are also used in the shift factor function model development (i.e., the binder data in table 4 using available BBR measurements). However, this level is not considered true verification because the data were used in the calibration process. Instead, this level assesses the impact of model fitting errors. Levels 1a and 1b differ only in the use of the PAR model. Also, level 1 verification includes BBR data in the analysis process, which is not representative of the currently available LTPP database. However, the second two verification levels are representative of data in the current LTPP database. For sections that have the complete Superpave<sup>TM</sup> DSR suite, level 2 is the most representative. Sections without the complete high temperature characterization data are better represented by the level 3 verification. Note that for all sections, the phenomenological and average shift factor function models are used and presented.

### B.12.1 Level 1a Verification

The first check of these shifting principles consists of a circular check whereby the binders used in the previous section help determine the WLF and CAM model coefficients using only data that would typically be available for Superpave<sup>TM</sup> testing. For level 1a verification purposes, only RTFO data are used in the analysis; level 1b verification adds an aging model to account for the fact that Superpave<sup>TM</sup> testing consists of results under original-, RTFO-, and PAV-aged conditions. The steps taken in level 1a verification are as follows:

1. Find DSR results at 10 rad/s at 59, 77, 95, 140, 158, and 176 °F (15, 25, 35, 60, 70, and 80 °C).

2. Find BBR results at 60 s at either -22, -11.2, and -0.4 °F (-30, -24, and -18 °C) or at -11.2, -0.4, and 10.4 °F (-24, -18, and -12 °C).
3. Convert BBR results to  $|G^*|$  values using equation 89.
4. Determine the t-T shift factors via equations 81 and 82 or by using the average shift factor function.
5. Fit the t-T shift factors to the WLF model using equation 79.
6. Optimize the CAM model coefficients to minimize the error between the DSR and BBR results.

Typical analysis results are shown in figure 113 and figure 114. In general, the Superpave<sup>TM</sup> only data analysis results show good agreement with the full analysis results across all of the selected binders. The complete results of level 1a verification are summarized in figure 115 through figure 118 in both normal and logarithmic scales. Overall, the calibrated model fits the data well, with an overall average error of approximately 3.5 percent and a higher average absolute error at 14 percent. These error percentages are comparable for both of the t-T shift factor function models. The major difference between these two models appears to be the tendency of the average shift factor function model to underpredict the modulus values in the high region. Conversely, the average shift factor function tends to show a smaller spread in the prediction error.

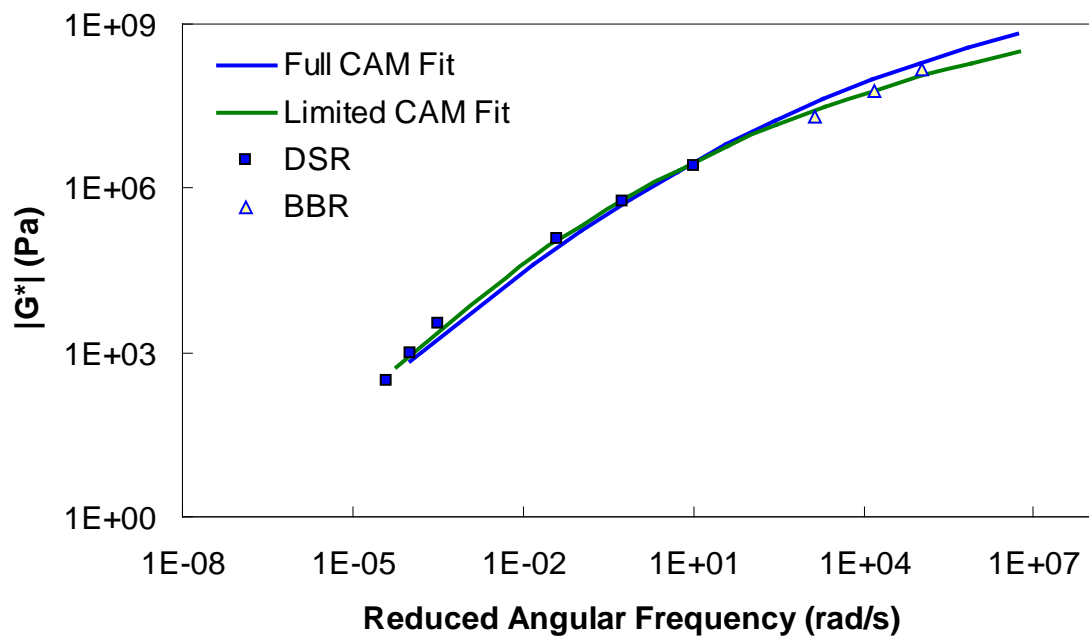
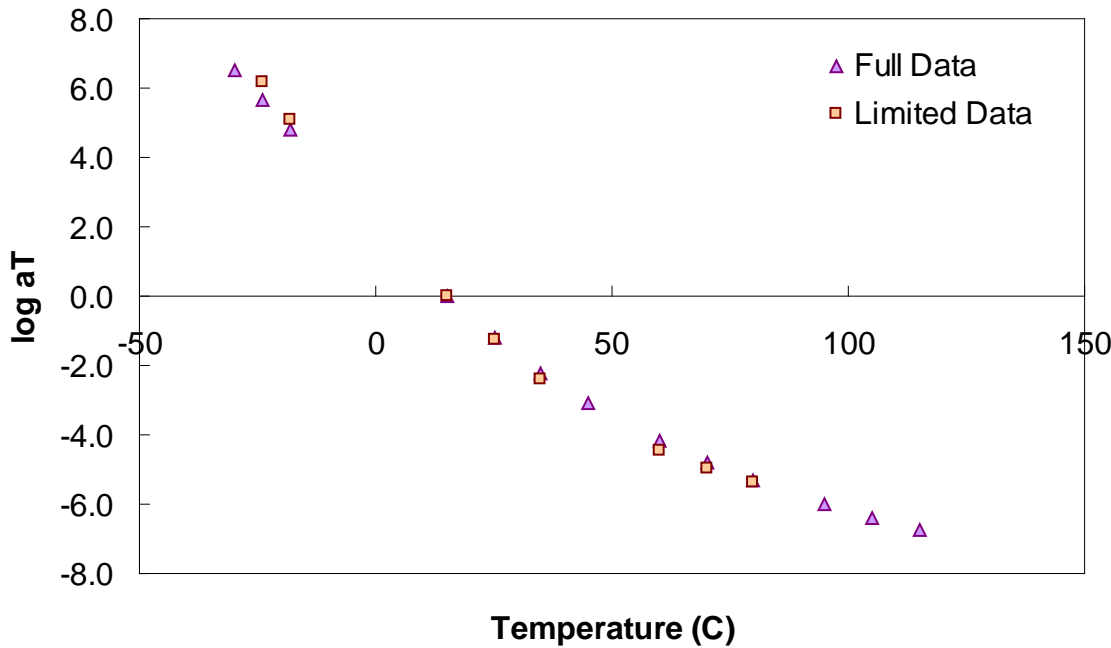


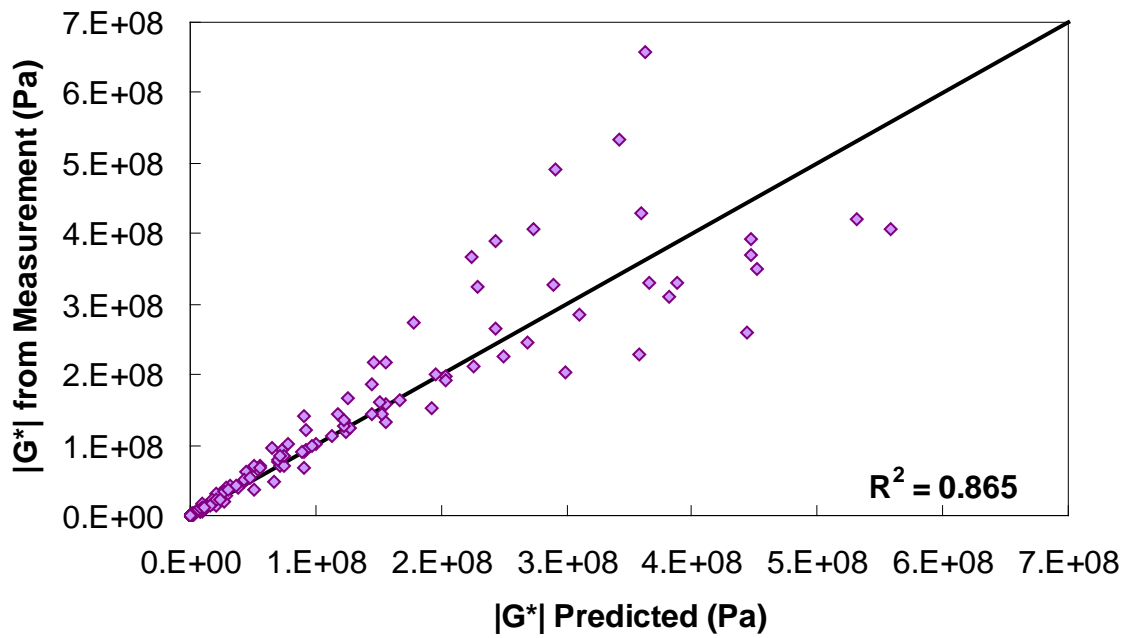
**Figure 113. Graph. Comparison of typical  $|G^*|$  mastercurves characterized using full database and Superpave<sup>TM</sup> only database.**

$$1 \text{ psi} = 6.86 \text{ kPa}$$



$$^{\circ}\text{C} = (^{\circ}\text{F}-32)/1.8$$

**Figure 114. Graph. Comparison of typical t-T shift factors characterized using full database and Superpave<sup>TM</sup> only database.**



$$1 \text{ psi} = 6.86 \text{ kPa}$$

**Figure 115. Graph. Level 1a verification of limited data analysis procedure in arithmetic scale using phenomenological shift factor function model.**

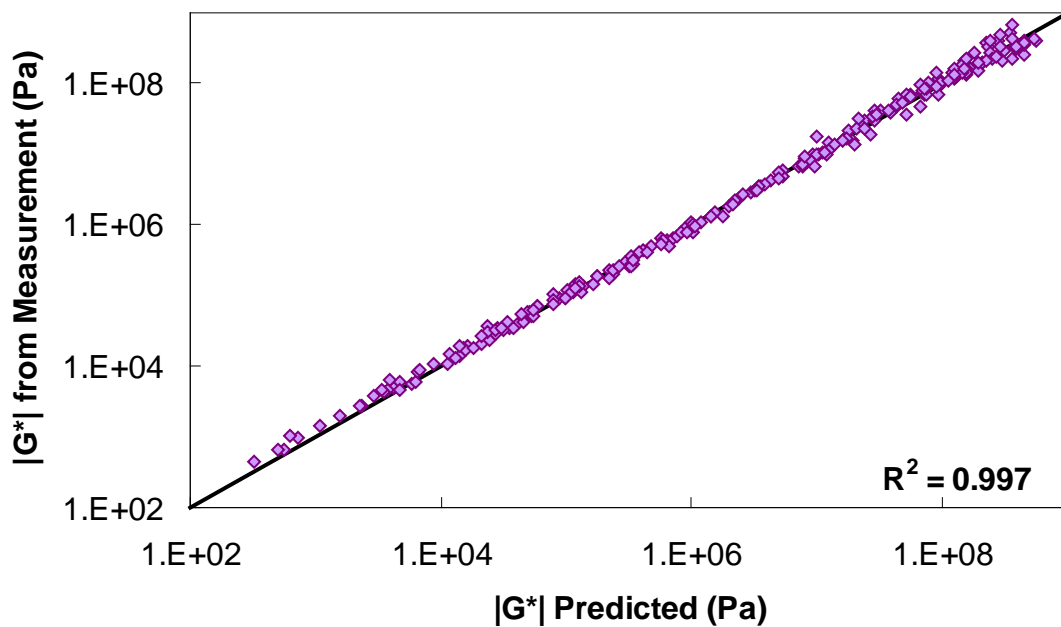


**Figure 116. Graph.** Level 1a verification of limited data analysis procedure in logarithmic scale using phenomenological shift factor function model.

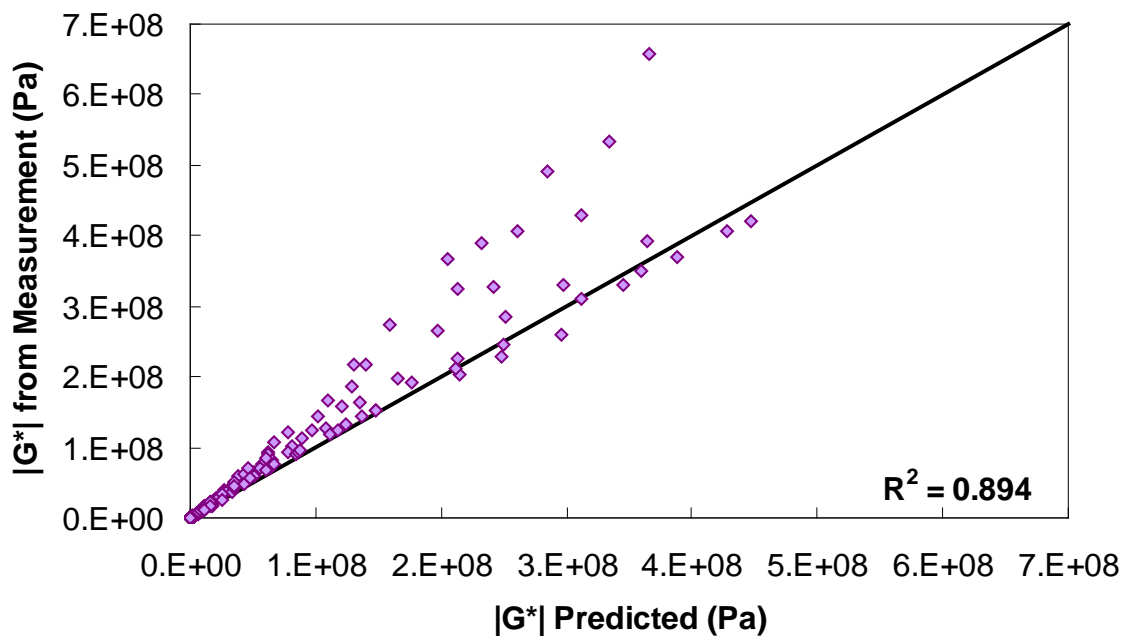


**Figure 117. Graph.** Level 1a verification of limited data analysis procedure in arithmetic scale using average shift factor function model.

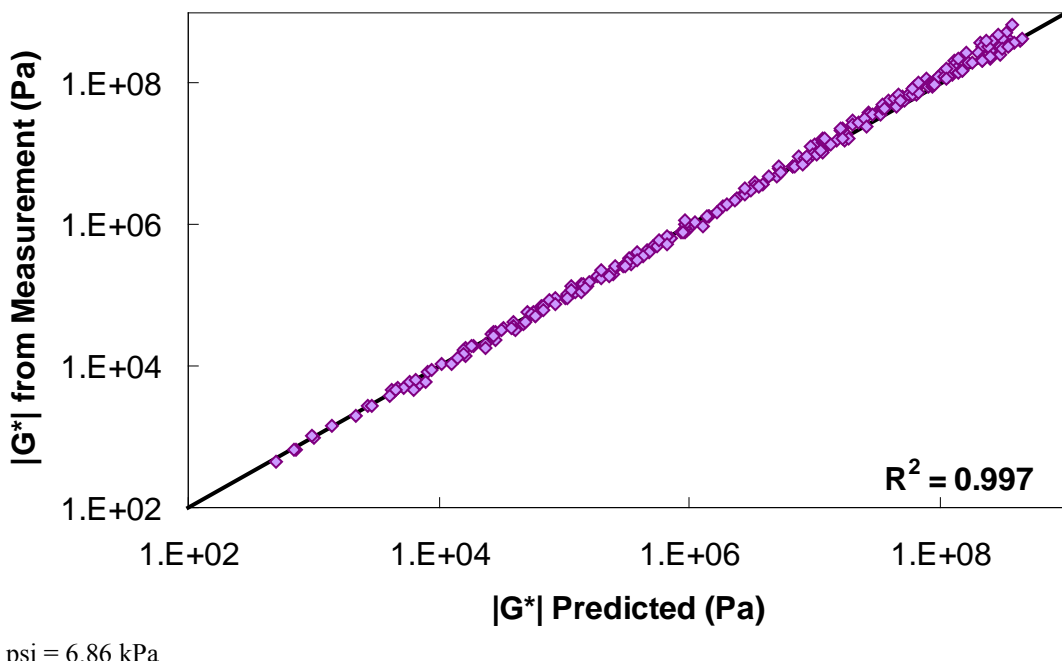


**Figure 118. Graph. Level 1a verification of limited data analysis procedure in logarithmic scale using average shift factor function model.**

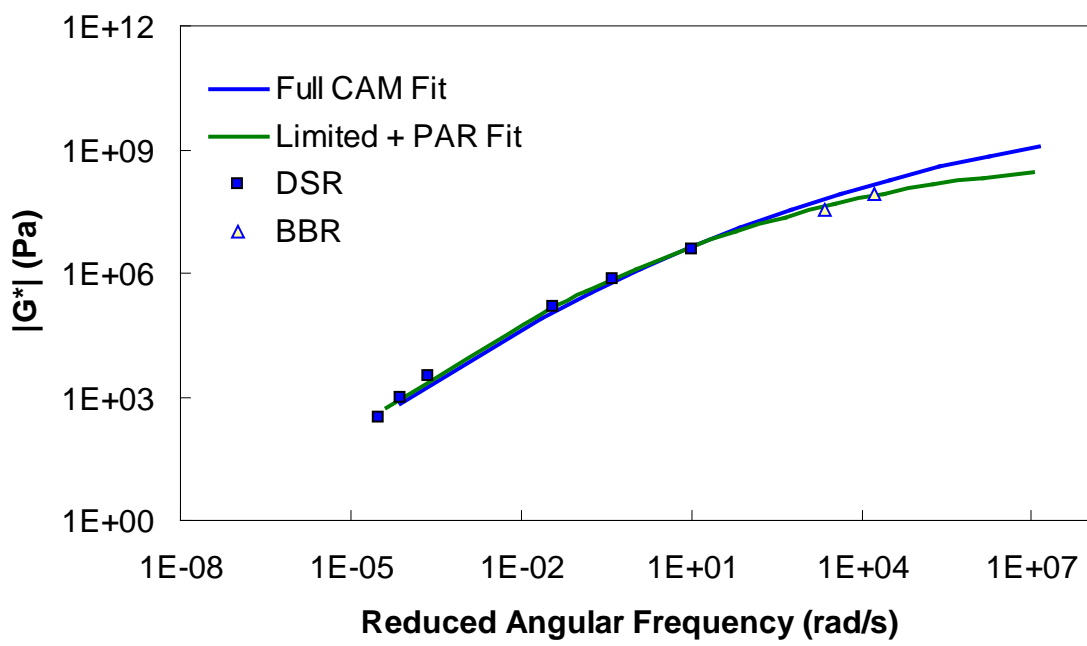
### B.12.2 Level 1b Verification

After verifying the limited data shifting procedure, attention is focused on Superpave<sup>TM</sup> testing on original-, RTFO-, and PAV-aged binders. Because the shear modulus data are desired under the RTFO conditions for the mixture  $|E^*|$  predictions and because most tests performed on the original-aged binder are also performed on the RTFO-aged binder, the primary model of interest is the relationship between the PAV and RTFO binders. Such a model would then be applied to the DSR tests at the intermediate temperatures and the BBR test results. The steps taken in level 1b verification are as follows:

1. Find DSR results under RTFO-aging conditions at 10 rad/s at 140, 158, and 176 °F (60, 70, and 80 °C).
2. Find DSR results under PAV-aging conditions at 10 rad/s at 59, 77, and 95 °F (15, 25, and 35 °C).
3. Find BBR results under PAV-aging conditions at 60 s at either -22, -11.2, and -0.4 °F (-30, -24, and -18 °C) or at -11.2, -0.4, and 10.4 °F (-24, -18, and -12 °C).
4. Apply the PAR model from equations 92 or 93 to predict RTFO values for intermediate temperature DSR results and BBR results.
5. Convert the BBR results to  $|G^*|$  values using equation 89.
6. Determine the t-T shift factors using equations 81 and 82 or via the average shift factor function.

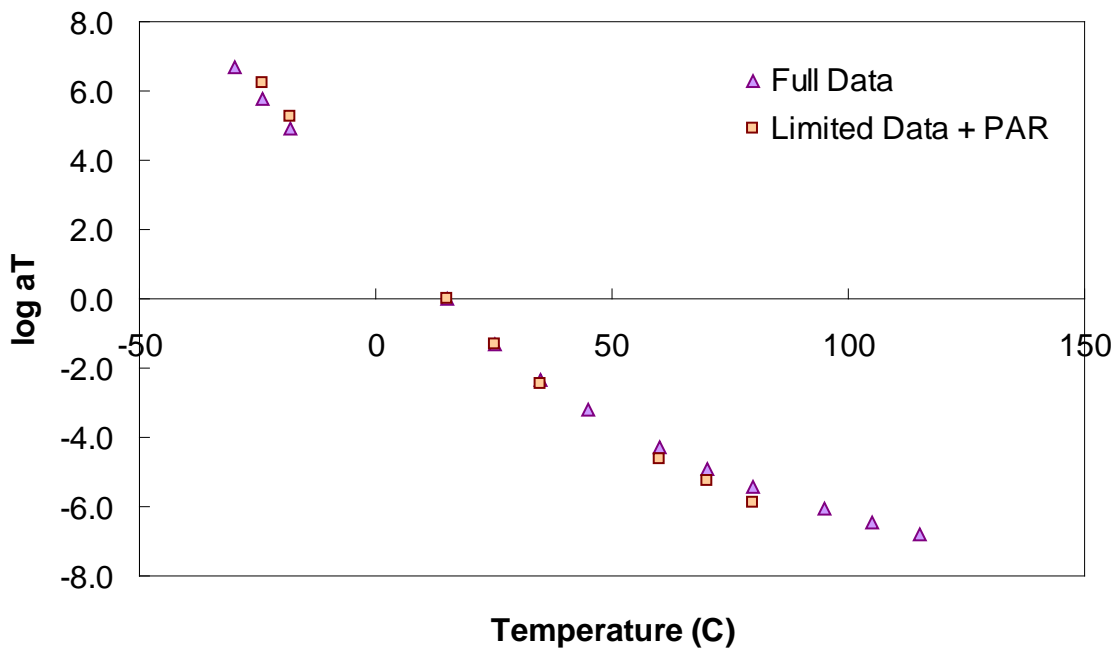
7. Fit the t-T shift factors to the WLF model using equation 79.
8. Optimize the CAM model coefficients to minimize the error between the DSR and BBR results.

Typical analysis results for this method are shown in figure 119 and figure 120. A slight decrease in the model strength is observed when compared to the level 1a verification, but in general, the Superpave™ only data analysis results show good agreement with the full analysis results across all of the selected binders. The complete results of level 1b verification are summarized in figure 121 and figure 122 for the phenomenological shift factor function model and in figure 123 and figure 124 for the average shift factor function in both normal and logarithmic scales. Overall, the calibrated model shows an approximately 13 percent error, with the average absolute error higher at 19 percent. As with level 1a verification, these numbers are comparable for both of the t-T shift factor function models. Also, these results tend to show a smaller variability with the average shift factor function model.



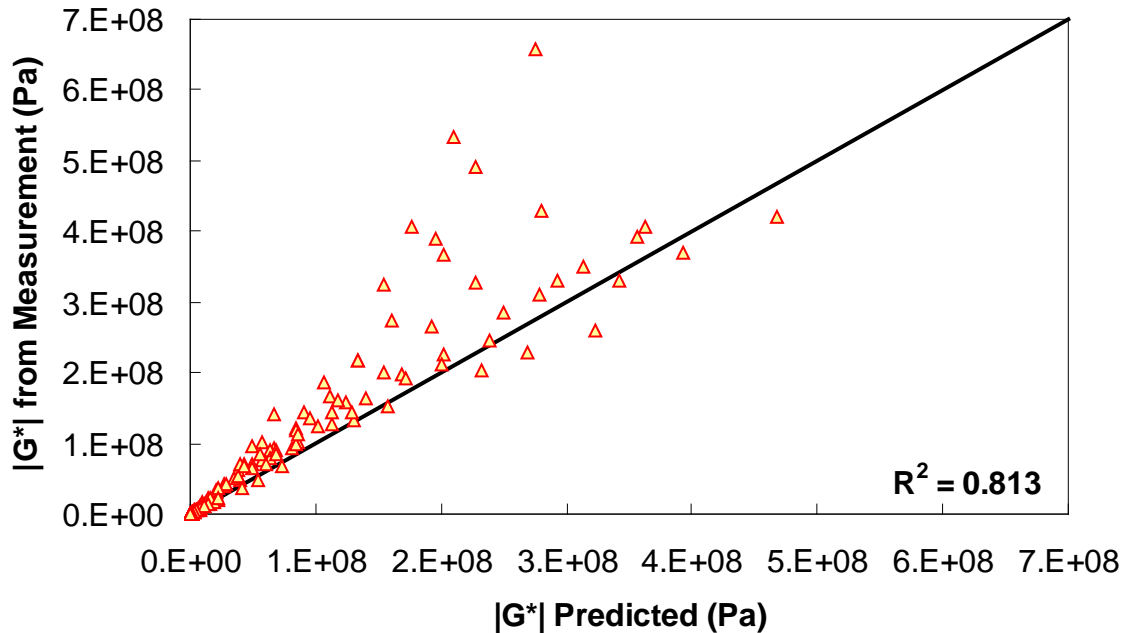
$1 \text{ psi} = 6.86 \text{ kPa}$

**Figure 119. Graph. Comparison of typical  $|G^*|$  mastercurve characterized using full database and Superpave™ only database plus PAR model.**



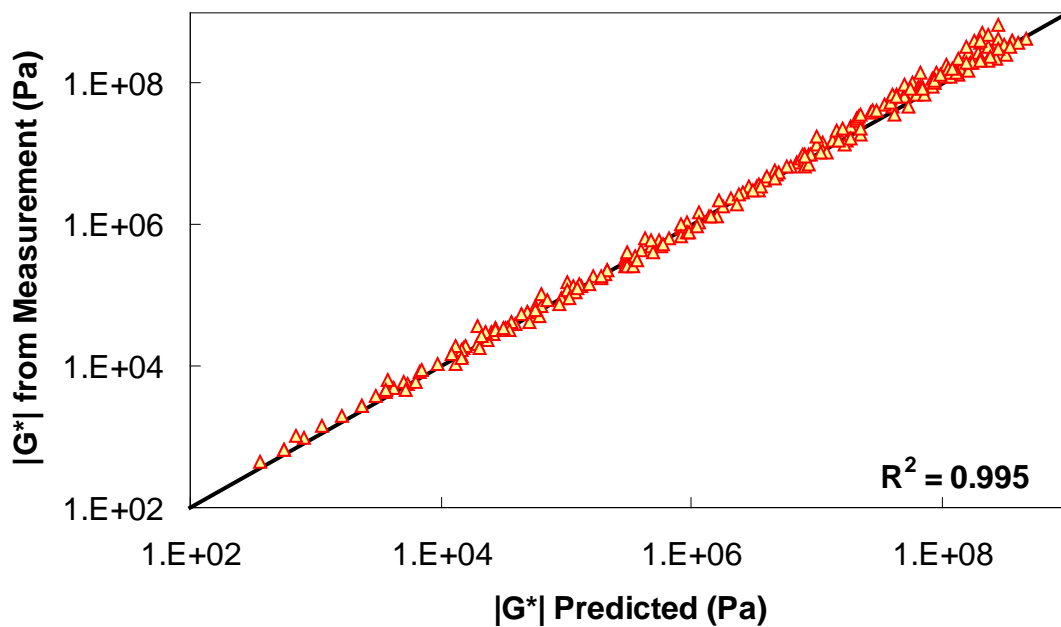
$$^{\circ}\text{C} = (\text{^{\circ}\text{F}-32})/1.8$$

**Figure 120.** Graph. Comparison of typical t-T shift factors characterized using full database and Superpave<sup>TM</sup> only database plus PAR model.



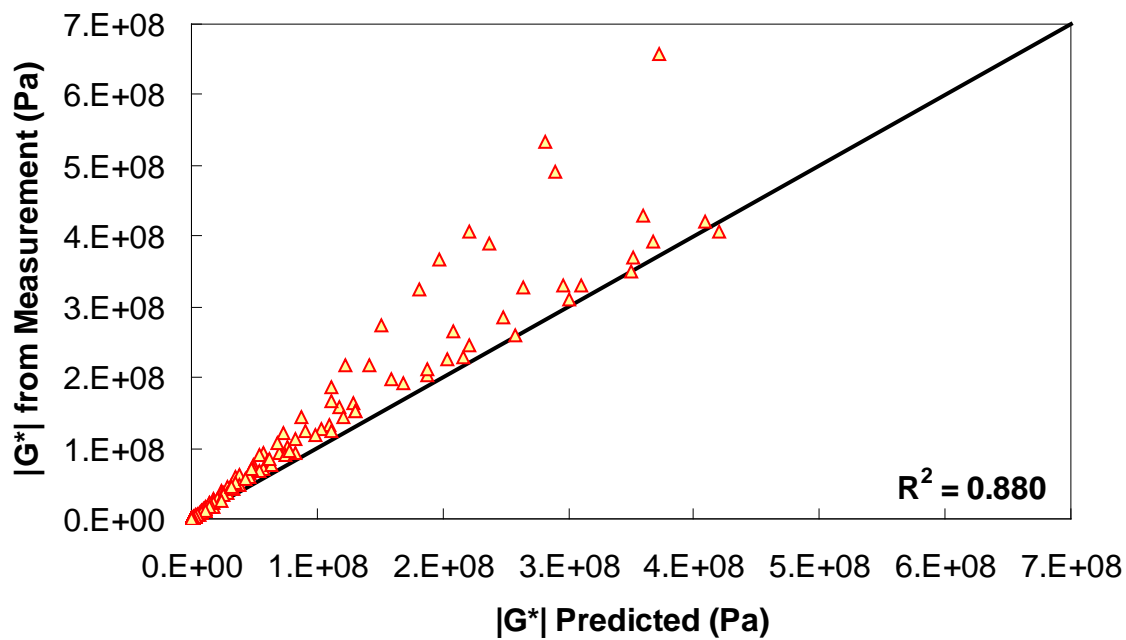
$$1 \text{ psi} = 6.86 \text{ kPa}$$

**Figure 121.** Graph. Level 1b verification of limited data analysis procedure in arithmetic scale using phenomenological shift factor function model.



1 psi = 6.86 kPa

**Figure 122. Graph. Level 1b verification of limited data analysis procedure in logarithmic scale using phenomenological shift factor function model.**



1 psi = 6.86 kPa

**Figure 123. Graph. Level 1b verification of limited data analysis procedure in arithmetic scale using average shift factor function model.**

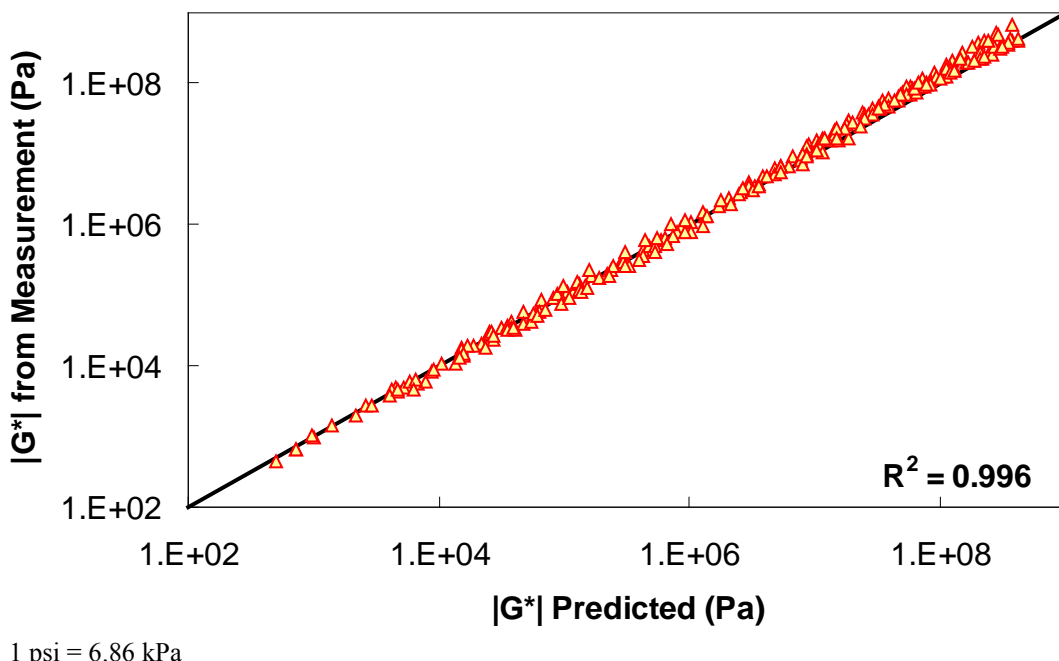


**Figure 124. Graph. Level 1b verification of limited data analysis procedure in logarithmic scale using average shift factor function model.**

### B.12.3 Level 2 Verification

Level 2 verification consists of data that have not been used in the development of either the PAR model or the t-T shift factor relationship. In addition, it consists of only DSR data, but the data cover the complete range expected in normal Superpave™ DSR characterization. A third level of verification that does not have the complete DSR data available is shown subsequently. The FHWA ALF study binders used previously to verify the PAR model are used for level 2 verification.

The steps taken in level 2 verification are as follows:

1. Find DSR results under RTFO-aging conditions at 10 rad/s at the two standard temperatures available that are closest to the high temperature PG of the binder—136.4 and 147.2 °F (58 and 64 °C), 147.2 and 168.8 °F (64 and 76 °C), or 147.2 and 179.6 °F (76 and 82 °C).
2. Find DSR results under PAV-aging conditions at 10 rad/s at 59, 77, and 95 °F (15, 25, and 35 °C).
3. Apply the PAR model from equation 92 to predict RTFO values for intermediate temperature DSR results.
4. Determine the t-T shift factors using equation 81 or by using the average shift factor function.
5. Fit the t-T shift factors to the WLF model using equation 79.

6. Optimize the CAM model coefficients to minimize the error in the DSR results.

The major difference between level 1 and 2 verification is the lack of BBR data in the process. Because it is shown earlier in this section that differences in  $|G^*|$  mastercurves can be large at temperatures below 41 °F (5 °C) when BBR data are not used for the calibration, only 41, 68, 105, and 129.2 °F (5, 20, 40, and 54 °C) data are used to analyze the differences in level 2 verification.

The results of level 2 verification are shown in figure 125 through figure 128. The model strength is good with an excellent coefficient of correlation. Both the average shift factor function and the phenomenological model show good results. The average function performs better in arithmetic space, and the phenomenological function appears to perform better in logarithmic space.

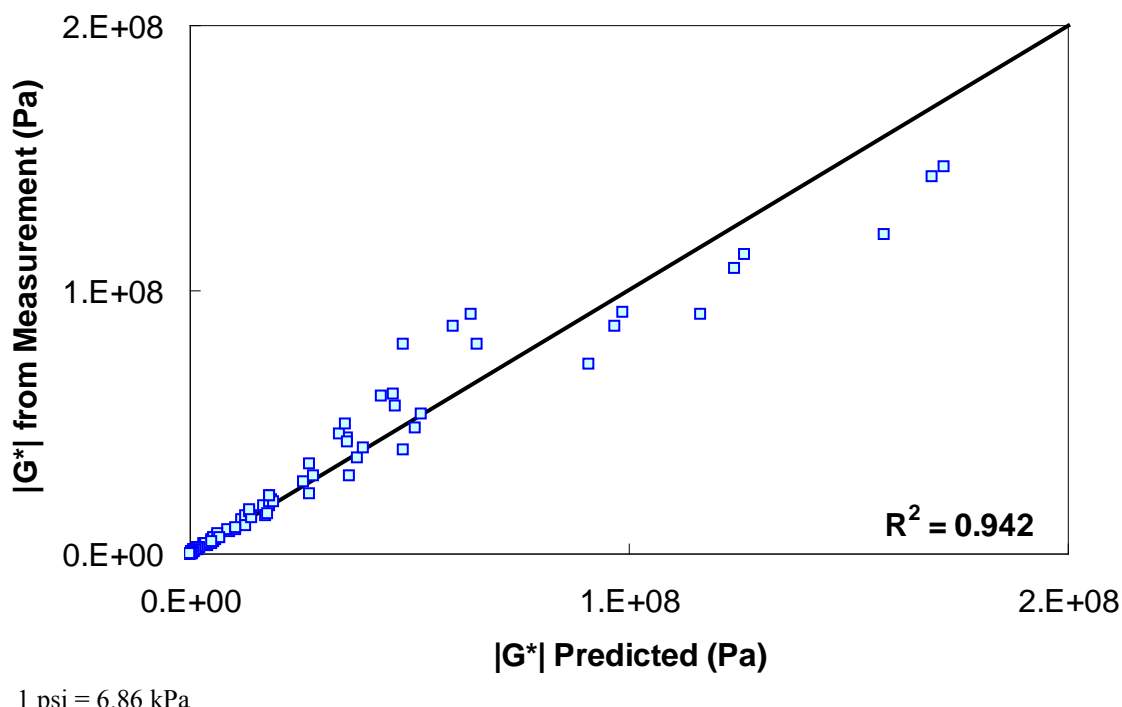
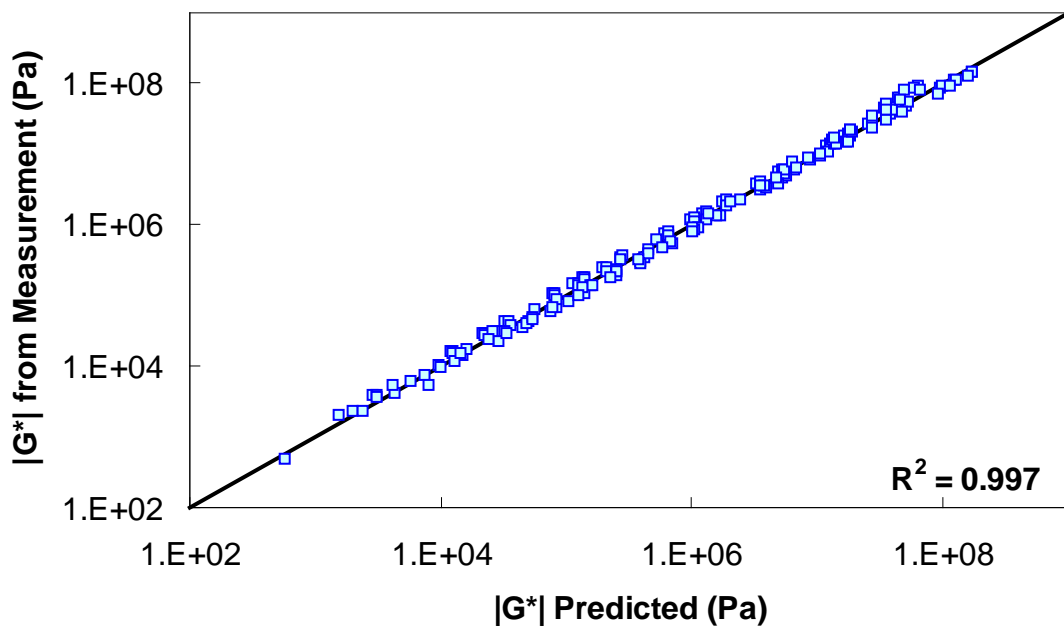
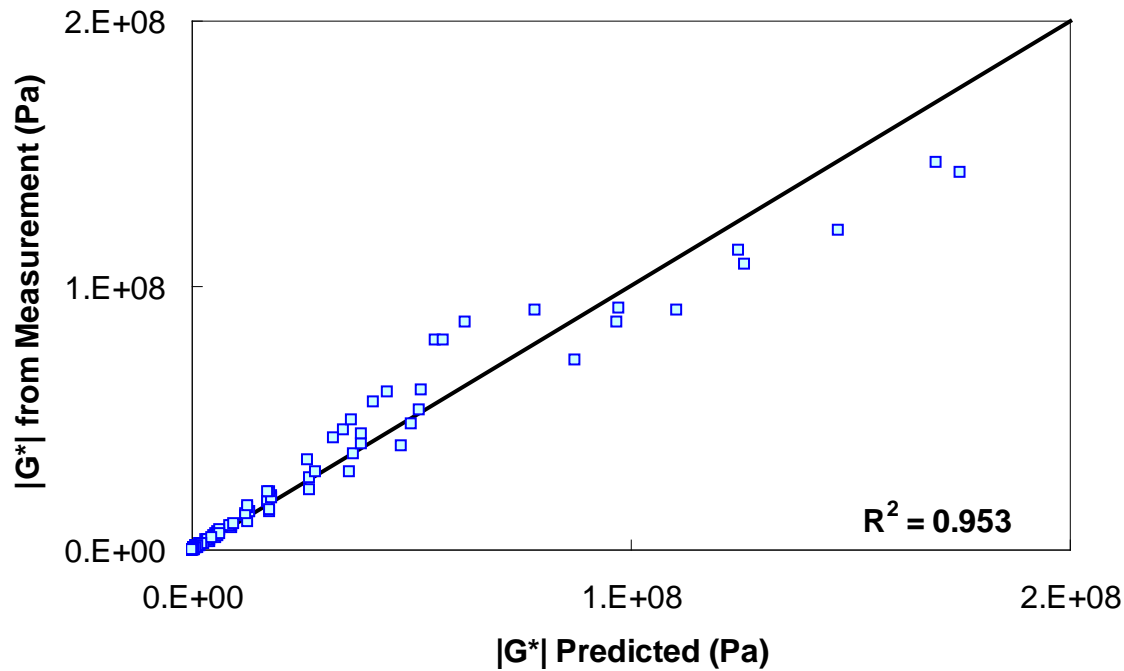


**Figure 125. Graph. Level 2 verification of limited data analysis procedure in arithmetic scale using phenomenological shift factor function model.**



1 psi = 6.86 kPa

**Figure 126.** Graph. Level 2 verification of limited data analysis procedure in logarithmic scale using phenomenological shift factor function model.



1 psi = 6.86 kPa

**Figure 127.** Graph. Level 2 verification of limited data analysis procedure in arithmetic scale using average shift factor function model.

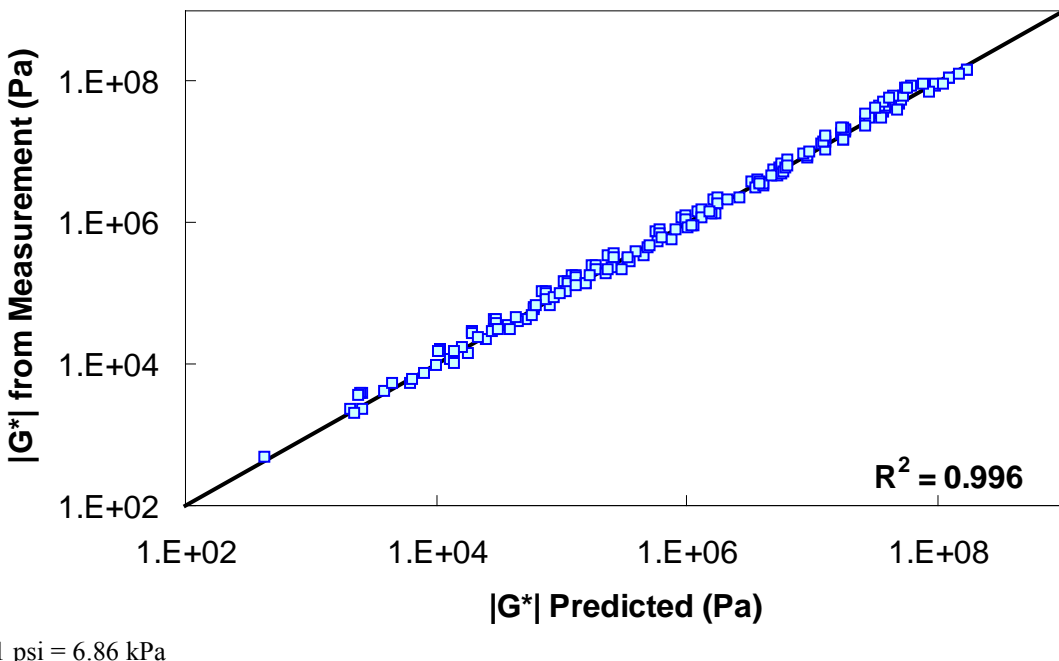


**Figure 128. Graph. Level 2 verification of limited data analysis procedure in logarithmic scale using average shift factor function model.**

#### B.12.4 Level 3 Verification

The final verification level considered in this report is the verification of the analysis procedure for DSR data that are not complete. Specifically, the data at high temperatures are assumed to be unavailable. For this purpose, the FHWA mobile trailer database outlined in table 42 is used. As with level 2 verification, BBR data are unavailable for calibration purposes, and 14 °F (-10 °C) data are not included in the verification process. Without available high temperature data, it is assumed that each binder receives its high temperature grade based on the RTFO-aged binder (i.e.,  $|G^*|/\sin(\delta) = 0.32$  psi (2.2 kPa) exactly at the high PG). In addition, it is known that asphalt binder has a phase angle of approximately 80 degrees at these high temperatures. These assumptions imply that  $|G^*|$  at the high temperature PG is 0.31 psi (2,166 Pa), which is used in the fitting process.

The steps taken in level 3 verification are as follows:

1. Find DSR results under PAV-aging conditions at 10 rad/s at the three coolest temperatures available for a given binder (see table 42).
2. Apply the PAR model using equation 92 to predict RTFO values for intermediate temperature DSR results.
3. Assume  $|G^*|$  under RTFO conditions at the high temperature PG to be 0.31 psi (2,166 Pa).
4. Determine the t-T shift factors using equation 81 or via the average shift factor function.
5. Fit the t-T shift factors to the WLF model using equation 79.

6. Optimize the CAM model coefficients to minimize the error in the DSR results.

The results of level 3 verification are shown in figure 129 through figure 132. From these figures, it is observed that this dataset shows a reduction in predictability compared to the level 2 analysis but improved predictability as measured by  $R^2$ . However, it should be noted that level 3 analysis does not include model data at 14 °F (-10 °C), while the two level 1 verification analyses do include these 14 °F (-10 °C) data.

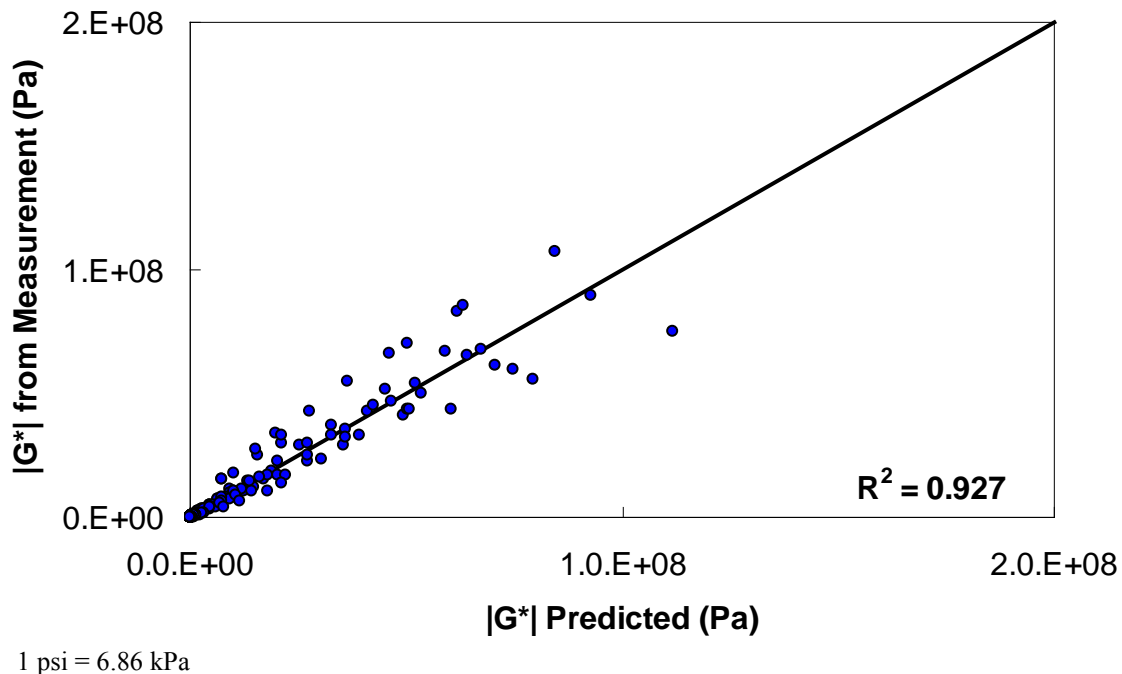


**Figure 129. Graph. Level 3 verification of limited data analysis procedure in arithmetic scale using phenomenological shift factor function model.**

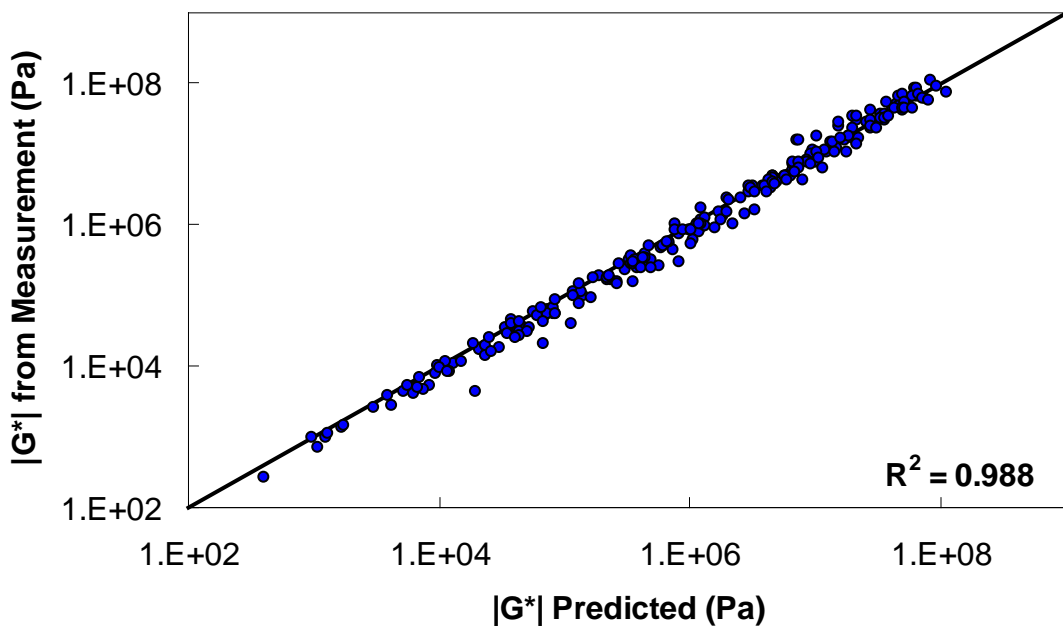


**Figure 130.** Graph. Level 3 verification of limited data analysis procedure in logarithmic scale using phenomenological shift factor function model.

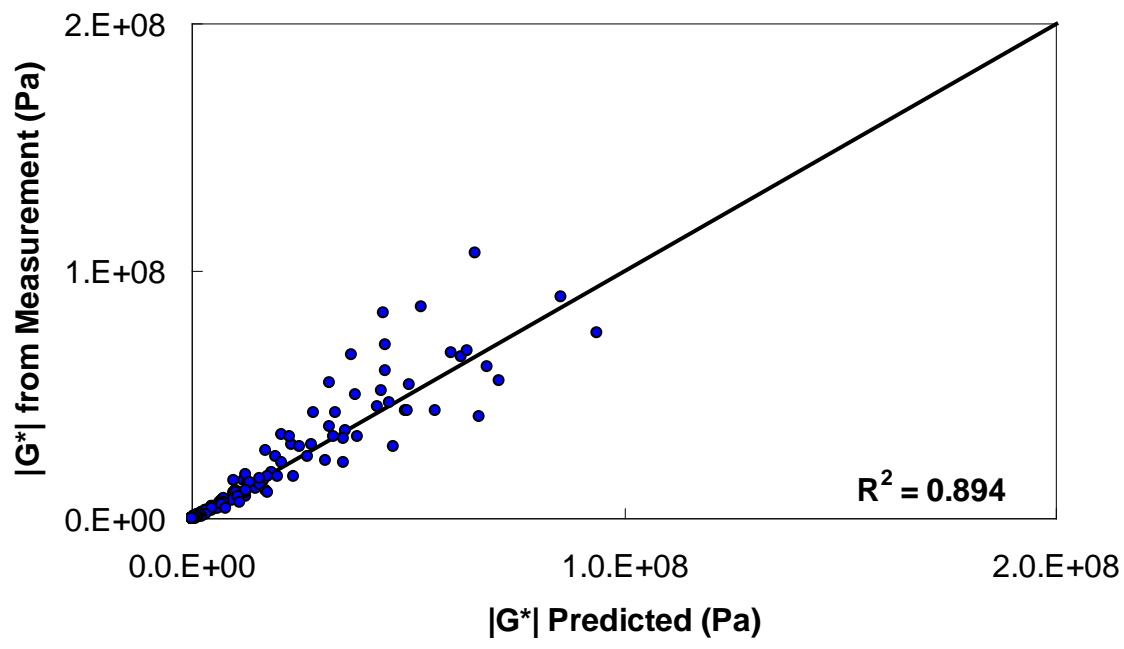


**Figure 131.** Graph. Level 3 verification of limited data analysis procedure in arithmetic scale using average shift factor function model.

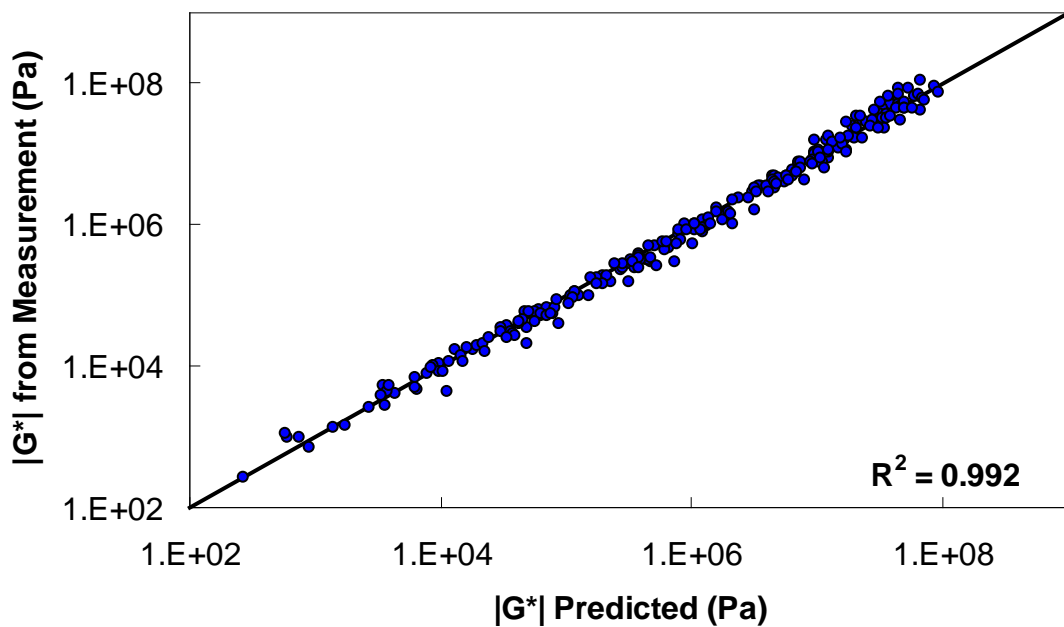


**Figure 132. Graph.** Level 3 verification of limited data analysis procedure in logarithmic scale using average shift factor function model.

## APPENDIX C: AMPT VERSUS TP-62

### C.1 EXPERIMENTAL VERIFICATION OF AMPT AND TP-62 DIFFERENCES

To assess differences in the measured moduli determined from the AMPT and TP-62 protocols, a joint study was carried out between researchers at the Turner-Fairbank Highway Research Center (TFHRC) and NCSU. For this study, TFHRC performed dynamic modulus testing on a mixture following the AMPT TP, and NCSU performed testing on the same mixture using the TP-62 protocol.<sup>(8)</sup> In both cases, three replicates have been tested. To reduce any variability not related to the equipment and protocols, all specimens were fabricated at NCSU and randomly sampled for either AMPT testing or TP-62 testing. The details of each testing protocol are summarized in table 43.

**Table 43. TP summary.**

<b>Factor</b>	<b>AMPT</b>	<b>TP-62</b>
Temperature (°F)	40, 70, 100, and 130	14, 40, 70, 100, and 130
Frequency (Hz)	20, 10, 5, 1, 0.5, and 0.1	25, 10, 5, 1, 0.5, and 0.1
Microstrain target	75–125	50–75
LVDT gauge length (mm)	70	100
Load direction	Bottom loading	Top loading
End treatment	Teflon®	Greased double latex membranes
Conditioning	External temperature chamber, then equalize in AMPT for 3 min	Equalize for 2.5–3.0 h in test machine
Rest period between frequencies (s)	0	300
Calculations	NCHRP 09-29 final 10 cycles <sup>(50)</sup>	NCHRP 09-29 final five cycles <sup>(50)</sup>

°C = (°F-32)/1.8

1 inch = 25.4 mm

The mixture used for this purpose is a 0.371-inch (9.5-mm) Superpave™ mixture typically used in North Carolina for surface courses. The gradation of this mixture is given in figure 133, and the relevant volumetric properties are summarized in table 44. All tests were conducted at 5.9 percent  $\pm$ 0.1 percent air void levels.

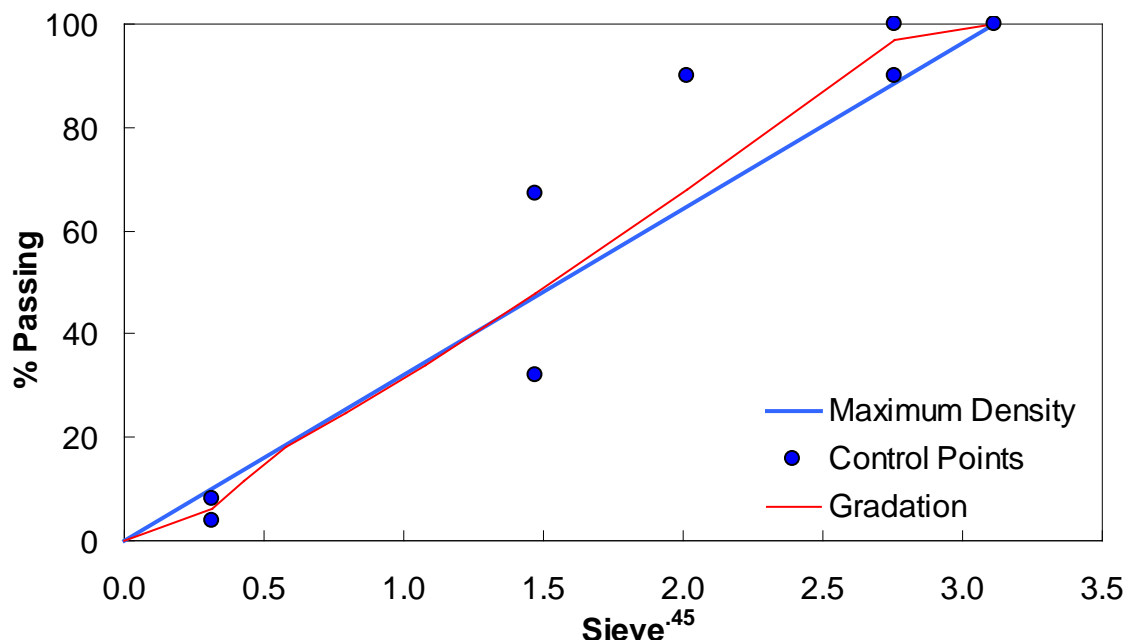
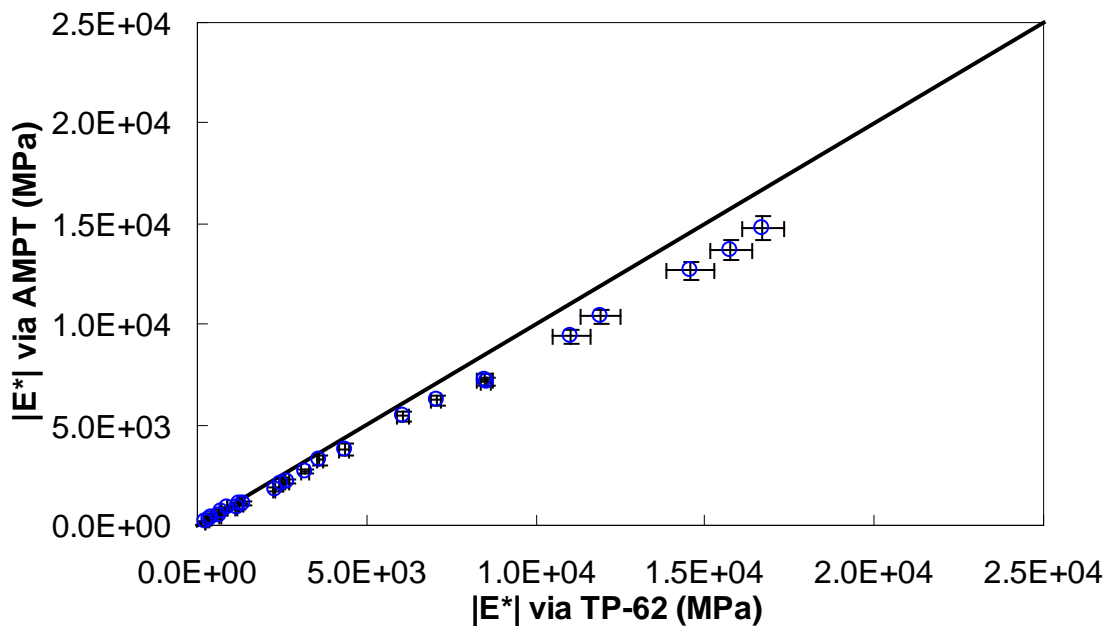


**Figure 133. Graph. Test mixture gradation.**

**Table 44. Test mixture volumetric properties.**

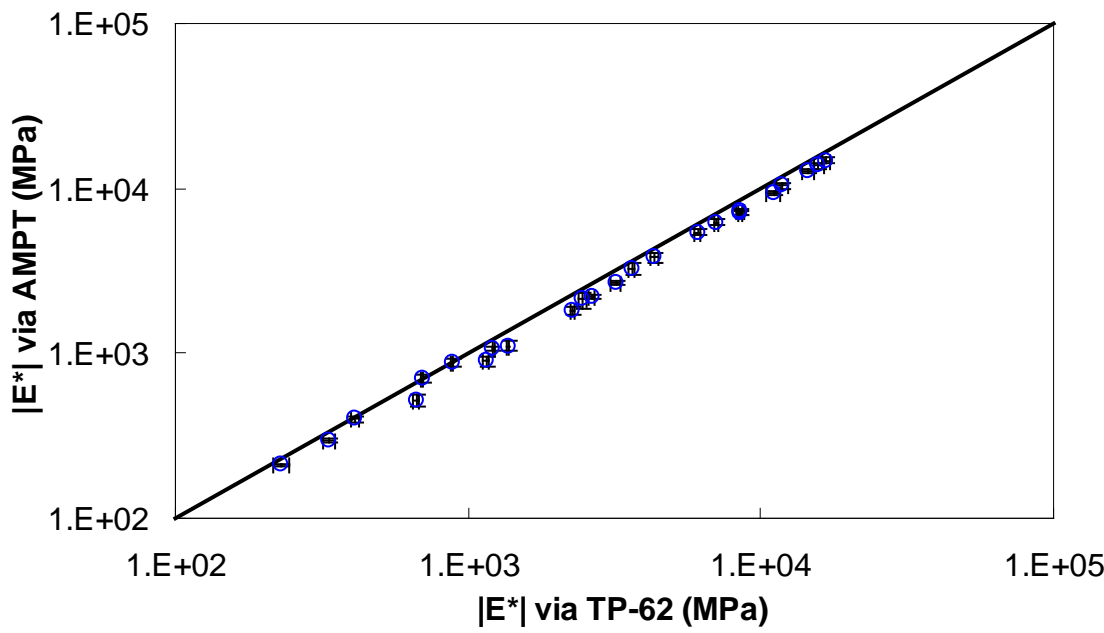
Volumetric Property	Mix Design	Test Samples
$V_a$ (percent)	3.8	5.9
VMA (percent)	15.6	17.5
VFA (percent)	75.7	66.2
Asphalt content (percent)	5.2	5.2
Percent effective binder content	4.9	4.9
Dust percentage	1.2	1.2
$G_{mm}$	2.616	2.616
Bulk specific gravity of the aggregate	2.828	2.828
Effective specific gravity of the aggregate	2.855	2.855
$G_b$	1.035	1.035

Results from the experimental study are summarized in figure 134 and figure 135, where the average dynamic moduli from the TP-62 protocol are plotted against the average moduli from the AMPT protocol. Error bars in these figures represent a single standard deviation from the mean. From these figures, it is observed that the AMPT test results are systematically lower than those from the TP-62 protocol; the difference between the two datasets is approximately 13 percent. Statistical analysis of these values using the step-down bootstrap method has also been performed. This method is used in lieu of multiple paired *t*-tests due to the effect of experimentwise error rates, which results in statistical errors when making multiple comparisons. Specifically, failing to account for this error rate increases the probability of finding significance when none is present. The statistical analysis results are shown by temperature and frequency in table 45. Note that in this table, the conditions under which the means are statistically similar are bold.



1 psi = 6.86 kPa

**Figure 134.** Graph. Comparison of  $|E^*$  measured via AMPT and TP-62 protocols in arithmetic scale.



1 psi = 6.86 kPa

**Figure 135.** Graph. Comparison of  $|E^*$  measured via AMPT and TP-62 protocols in logarithmic scale.

**Table 45. Statistical summary of AMPT and TP-62 test results.**

Temperature (°C)	Frequency (Hz)	E*  AMPT (psi)	E*  TP-62 (psi)	p-Value
4	25.00	2,145,226	2,420,540	0.032
4	10.00	1,989,606	2,284,746	0.020
4	5.00	1,838,144	2,111,129	0.030
4	1.00	1,503,747	1,726,774	0.026
4	0.50	1,359,729	1,601,117	0.019
4	0.10	1,050,375	1,234,431	0.023
21	25.00	1,030,409	1,237,696	0.020
21	10.00	899,831	1,022,446	0.023
21	5.00	785,545	881,347	0.025
21	1.00	550,882	628,569	0.033
21	0.50	468,842	524,847	<b>0.068</b>
21	0.10	306,841	358,120	<b>0.057</b>
37	25.00	385,448	464,233	0.008
37	10.00	318,540	384,219	0.010
37	5.00	263,476	330,282	0.002
37	1.00	160,938	198,110	0.008
37	0.50	130,346	167,580	0.005
37	0.10	75,190	96,587	0.011
54	25.00	153,735	177,050	0.003
54	10.00	127,039	128,097	<b>0.801</b>
54	5.00	102,669	101,164	<b>0.672</b>
54	1.00	58,086	59,737	<b>0.377</b>
54	0.50	42,997	48,863	0.022
54	0.10	23,863	33,547	0.005

 $^{\circ}\text{C} = (\text{°F}-32)/1.8$ 

1 psi = 6.86 kPa

Note: Bold text indicates conditions where means are statistically similar.

## C.2 COMPARISON OF AMPT AND TP-62 PROTOCOLS WITH THE AVAILABLE DATABASE

To assess the differences observed between the two  $|E^*|$  measurement protocols, a more comprehensive analysis was performed using the databases available in this study. The two AMPT and TP-62 databases were segregated based on the temperatures at which the  $|E^*|$  values were measured. Because these two databases cover different ranges of parameters, it is useful to examine the distribution of the relevant parameters for the two databases. Figure 136 through figure 157 present the distribution and range of each parameter in the two databases. In figure 158 through figure 162, the measured  $|E^*|$  data points available for some specific temperatures for each type of database are shown by frequency. Based on observations from these figures and the difference equation shown in equation 100, differences between the databases containing AMPT and TP-62 measurements are evident, as can be seen in table 46.

$$\%Difference = \frac{|E^*|_{TP-62} - |E^*|_{AMPT}}{|E^*|_{TP-62}} * 100 \quad (100)$$

Based on this description, the following differences are observed at each temperature:

- 40 °F (4.4 °C): 43.63 percent.
- 70 °F (21.1 °C): 57.84 percent.
- 100 °F (37.8 °C): 61.95 percent.
- 129 °F (53.9 °C): 46.26 percent.
- 130 °F (54.4 °C): 57.83 percent.

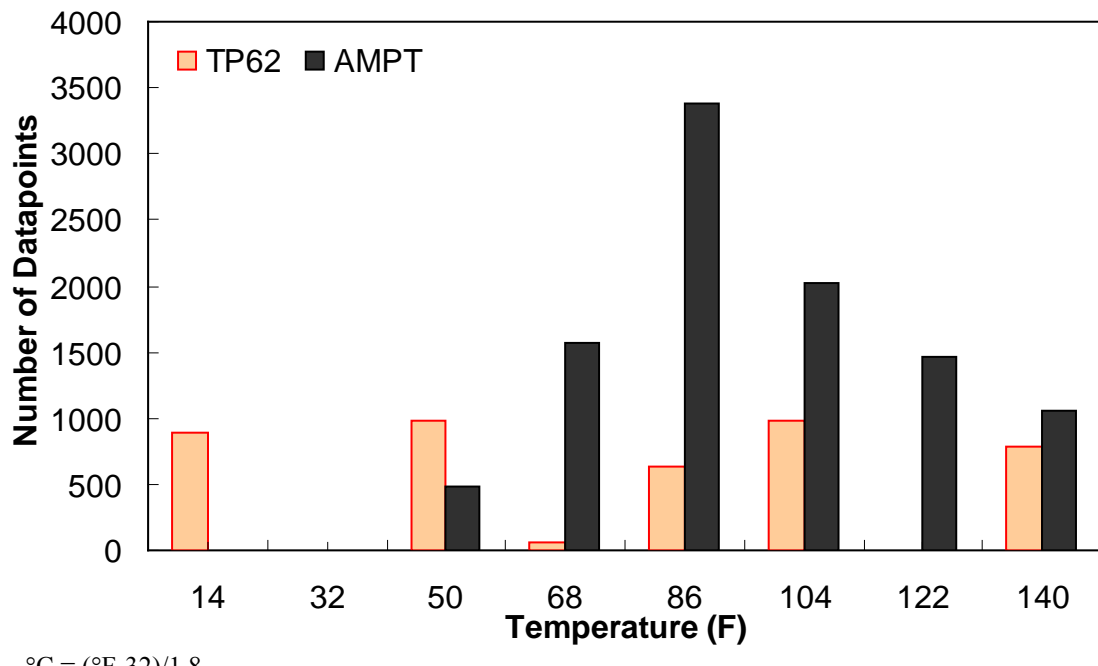


**Figure 136. Graph. Frequency distribution of temperature in AMPT versus TP-62 databases.**

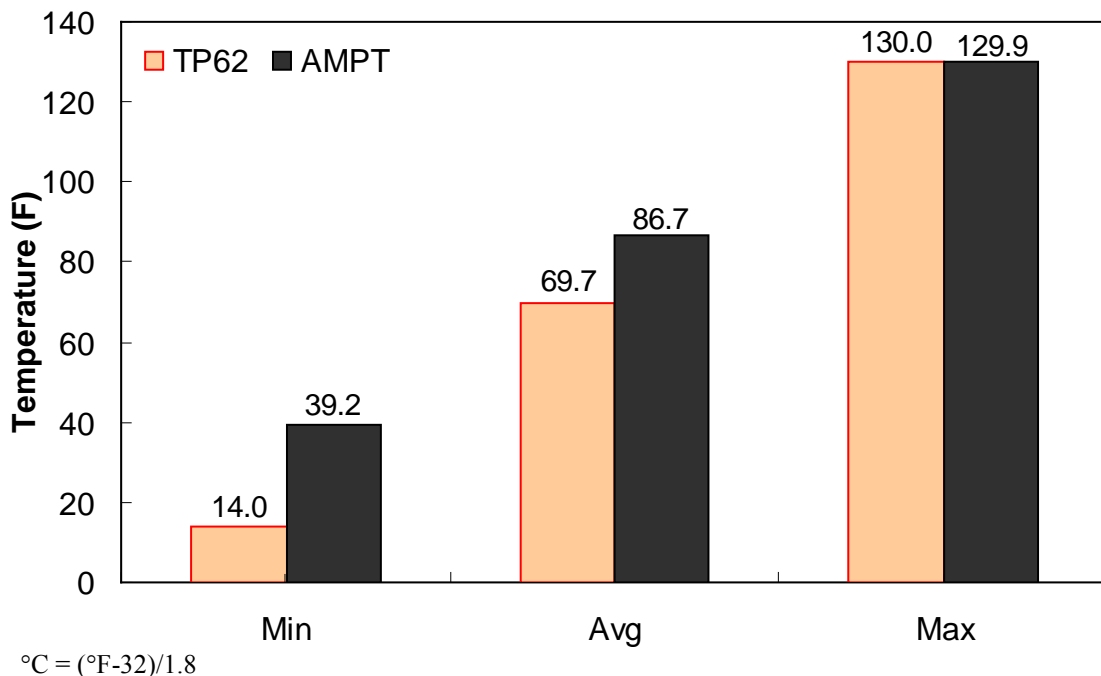


**Figure 137. Graph. Range of temperature in AMPT versus TP-62 databases.**

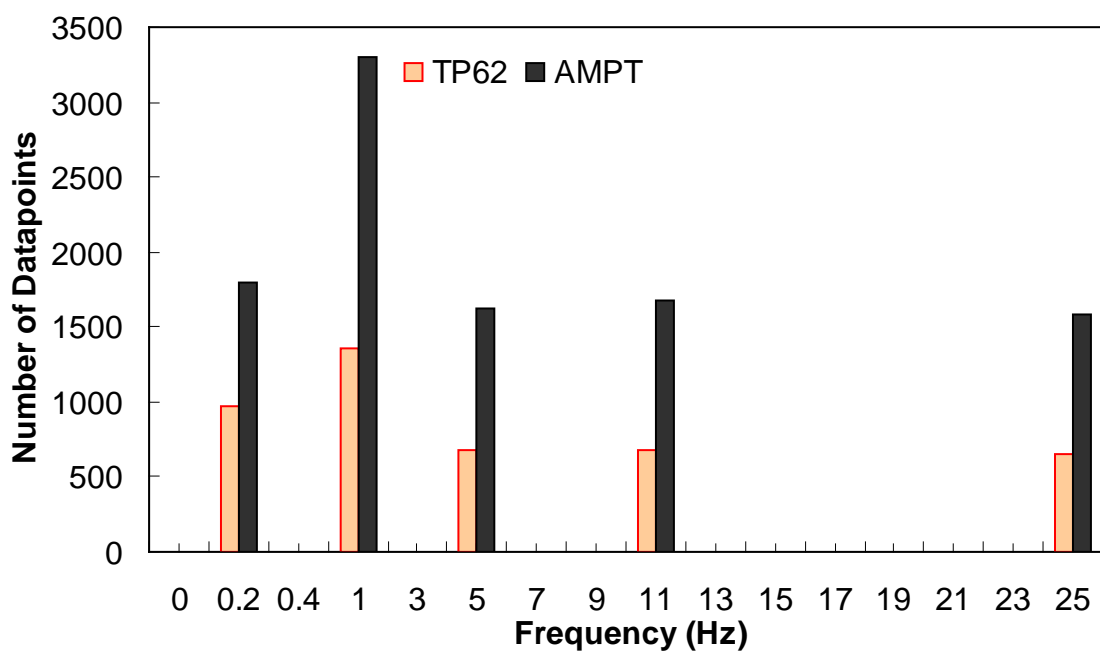


**Figure 138. Graph. Frequency distribution of frequency in AMPT versus TP-62 databases.**

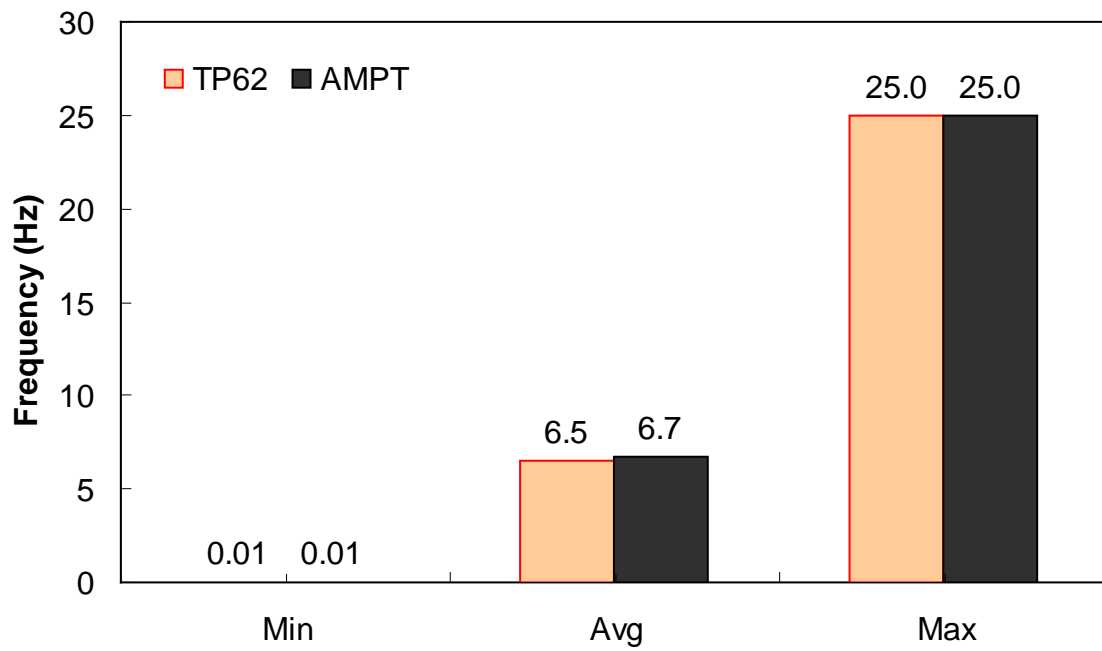


**Figure 139. Graph. Range of loading frequency in AMPT versus TP-62 databases.**

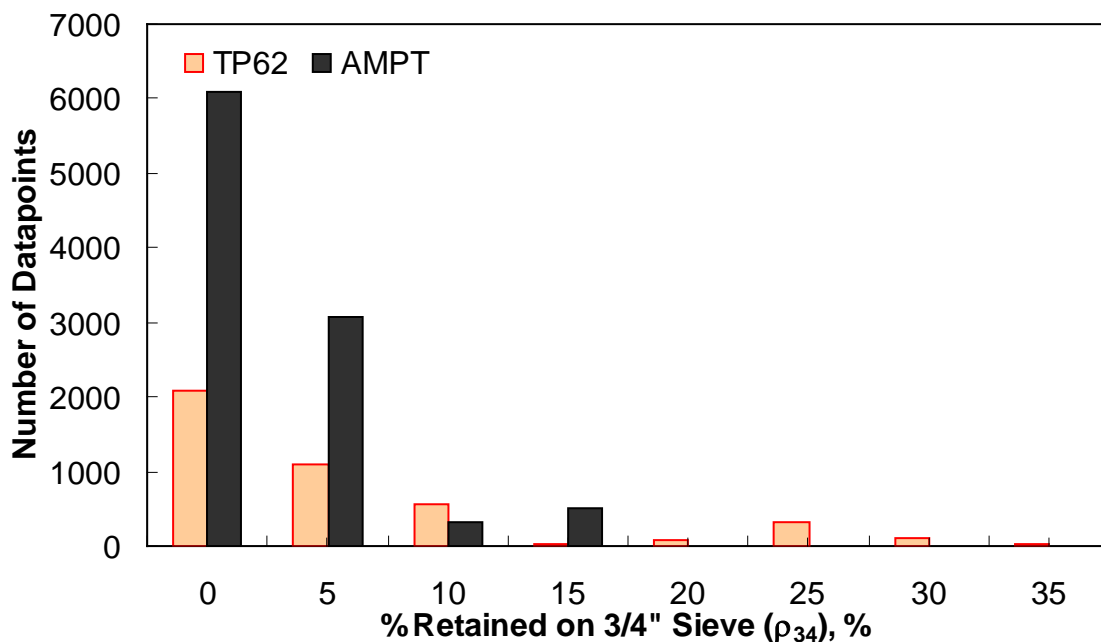


**Figure 140. Graph. Frequency distribution of percentage retained on  $\frac{3}{4}$ -inch (19.05-mm) sieve ( $\rho_{34}$ ) in AMPT versus TP-62 databases.**

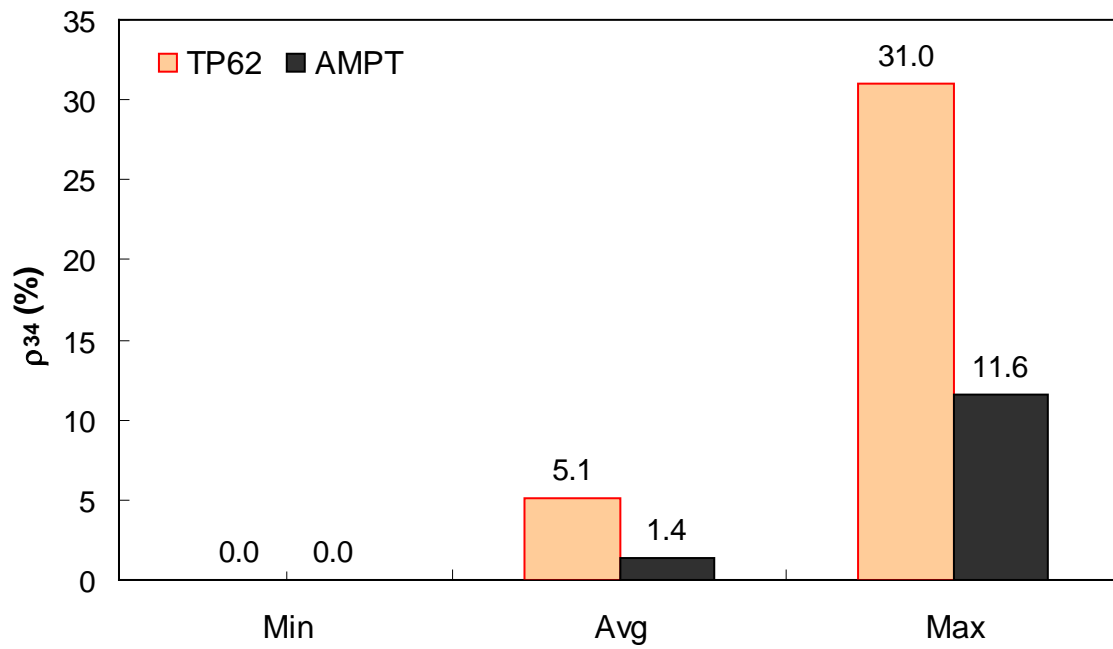


**Figure 141.** Graph. Range of percentage retained on  $\frac{3}{4}$ -inch (19.05-mm) sieve ( $\rho_{34}$ ) in AMPT versus TP-62 databases.

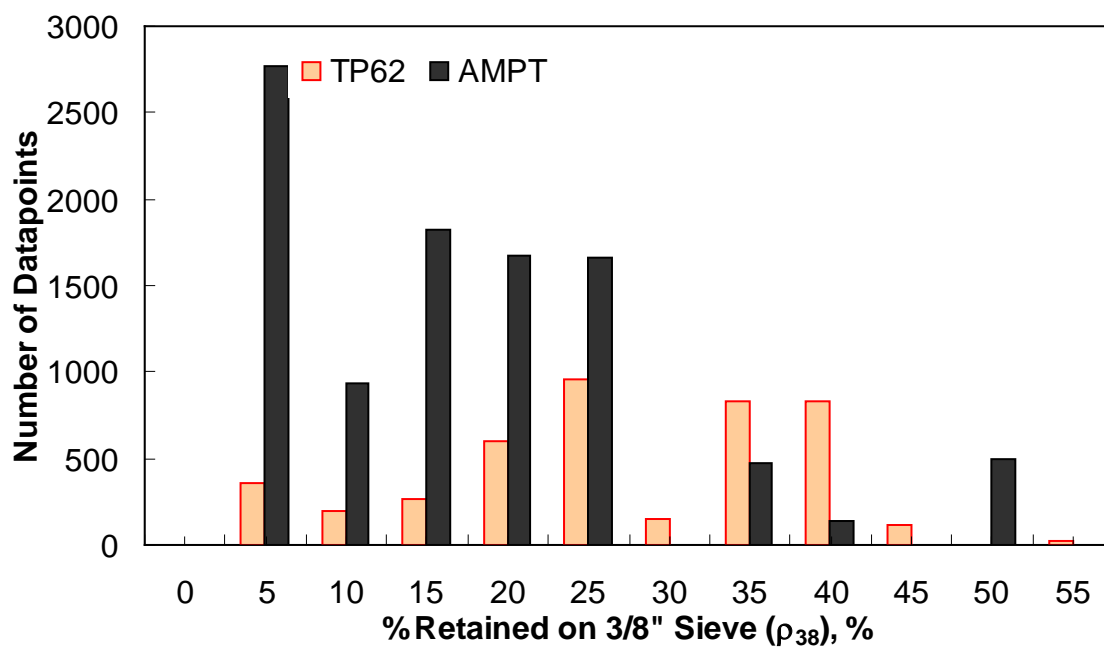


**Figure 142.** Graph. Frequency distribution of percentage retained on  $\frac{3}{8}$ -inch (9.56-mm) sieve ( $\rho_{38}$ ) in AMPT versus TP-62 databases.

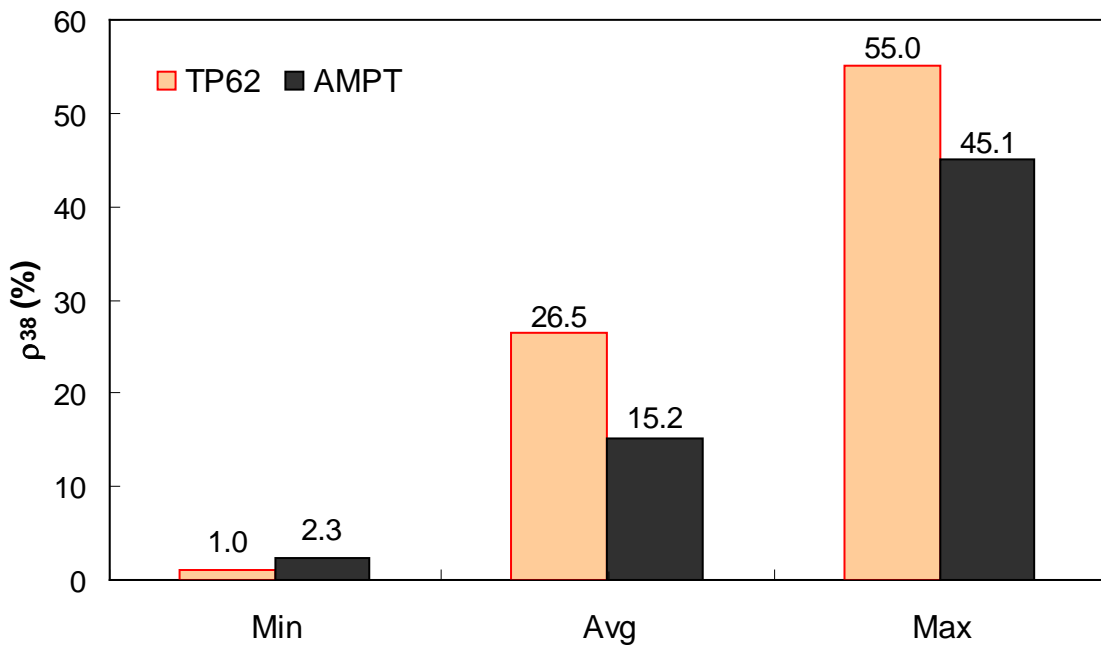


**Figure 143.** Graph. Range of percentage retained on  $\frac{3}{8}$ -inch (9.56-mm) sieve ( $\rho_{38}$ ) in AMPT versus TP-62 databases.

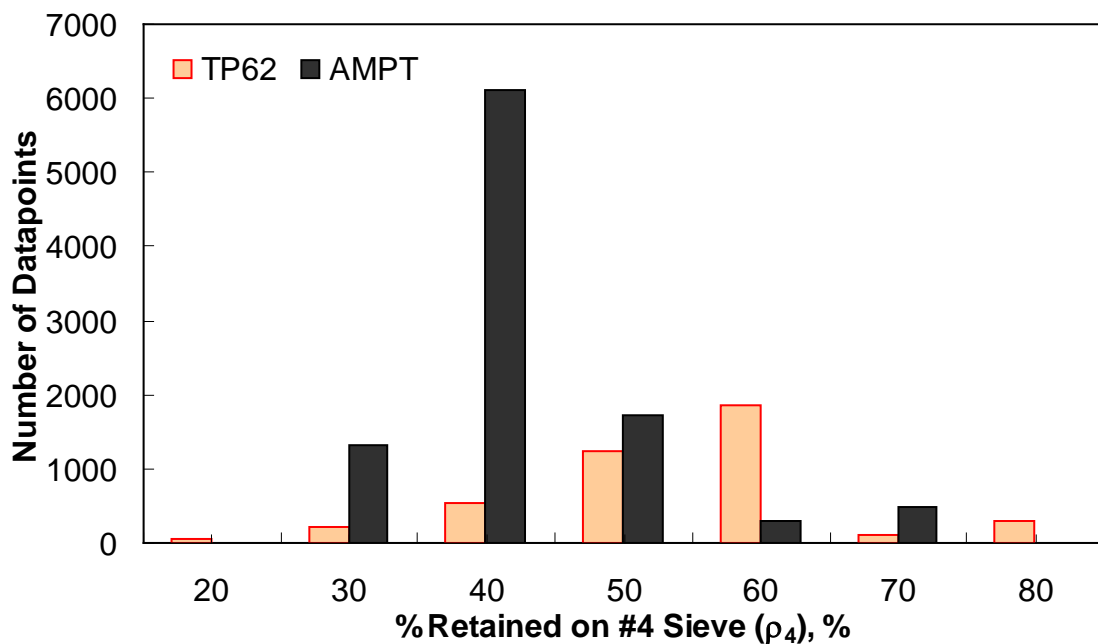


**Figure 144.** Graph. Frequency distribution of percentage retained on #4 sieve ( $\rho_4$ ) in AMPT versus TP-62 databases.

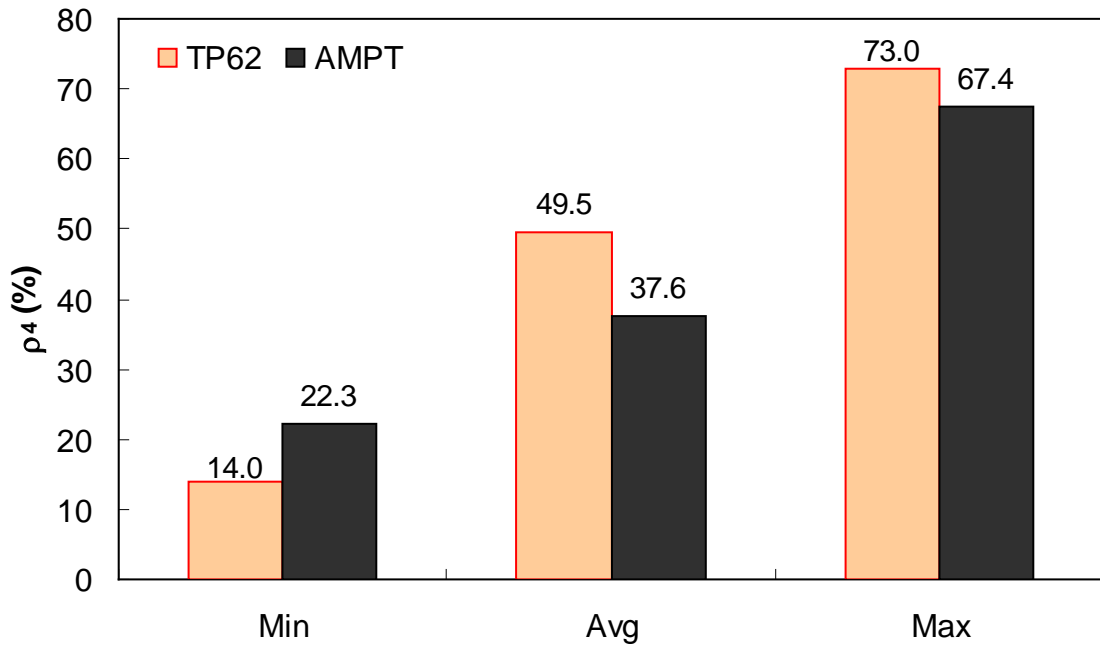


**Figure 145.** Graph. Range of percentage retained on #4 sieve ( $\rho_4$ ) in AMPT versus TP-62 databases.

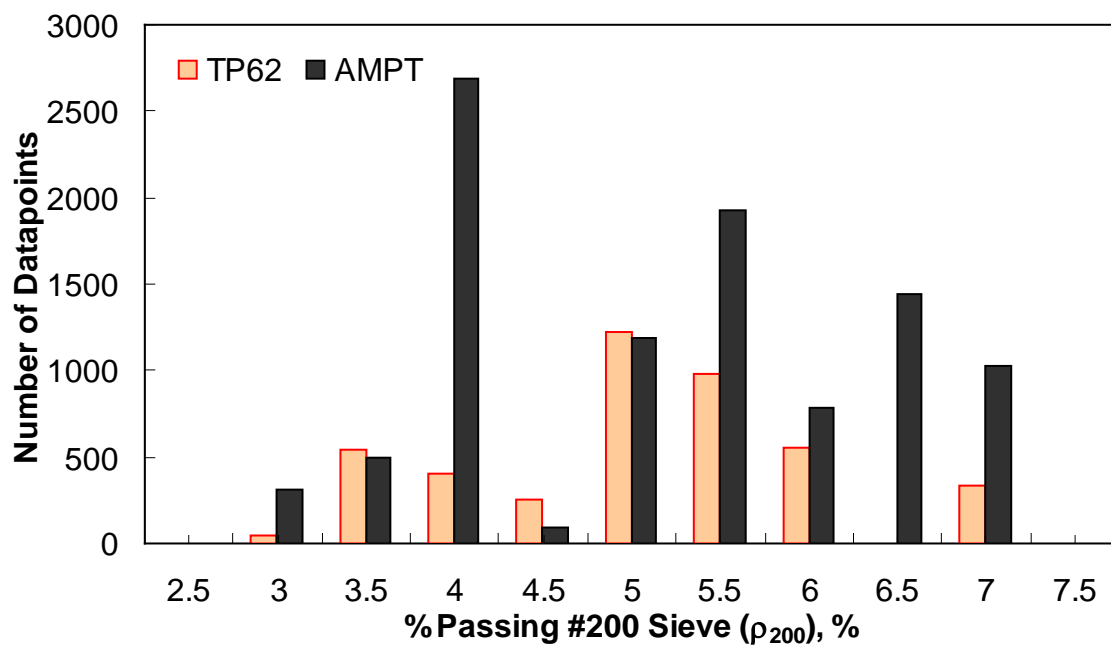


**Figure 146.** Graph. Frequency distribution of percentage passing #200 sieve ( $\rho_{200}$ ) in AMPT versus TP-62 databases.

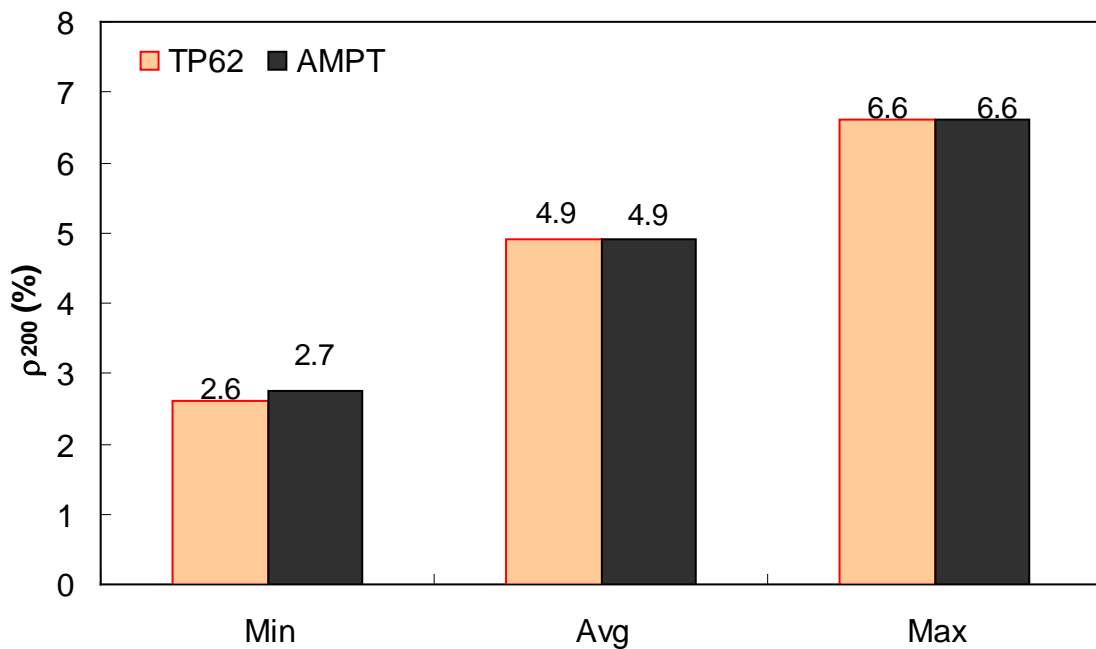


**Figure 147.** Graph. Range of percentage passing #200 sieve ( $\rho_{200}$ ) in AMPT versus TP-62 databases.

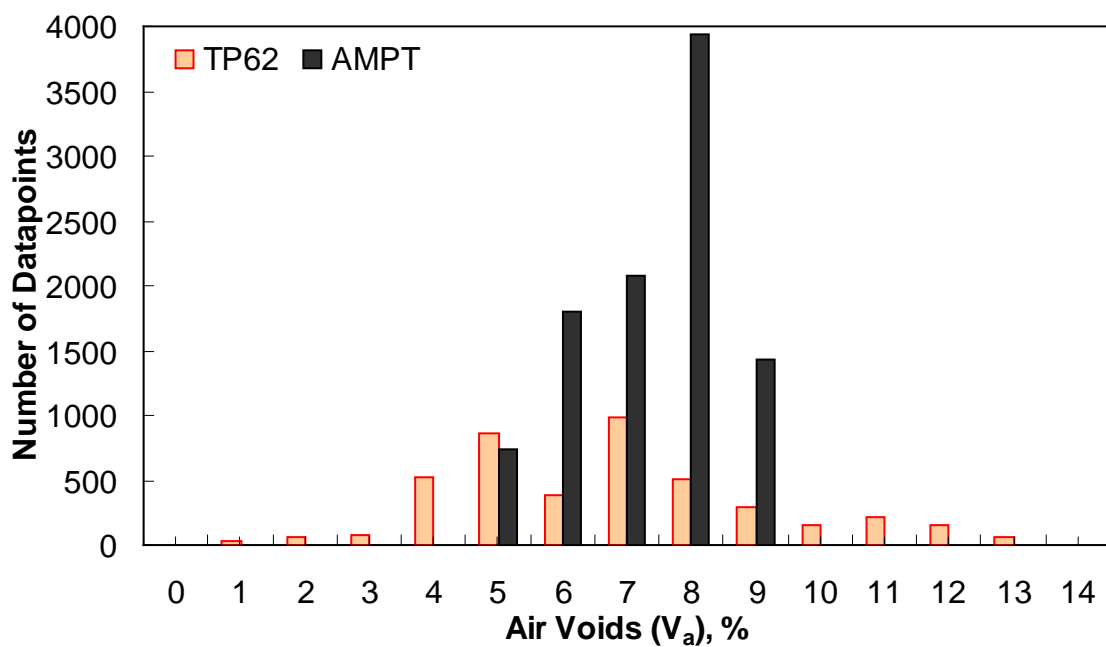


**Figure 148.** Graph. Frequency distribution of specimen air voids in AMPT versus TP-62 databases.

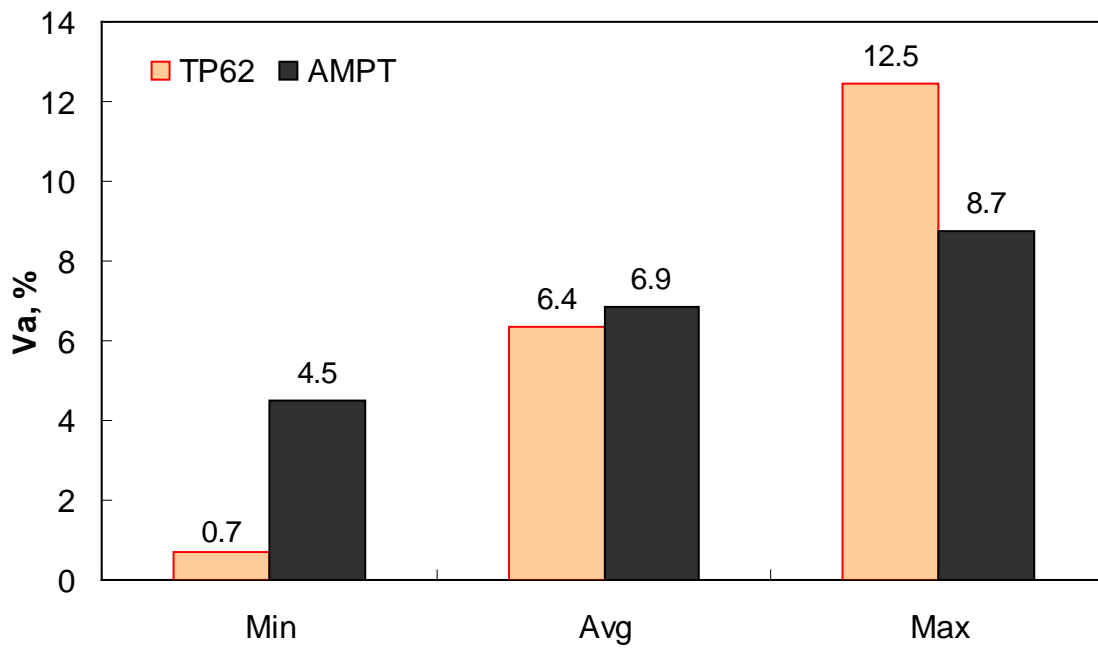


**Figure 149. Graph. Range of specimen air voids in AMPT versus TP-62 databases.**

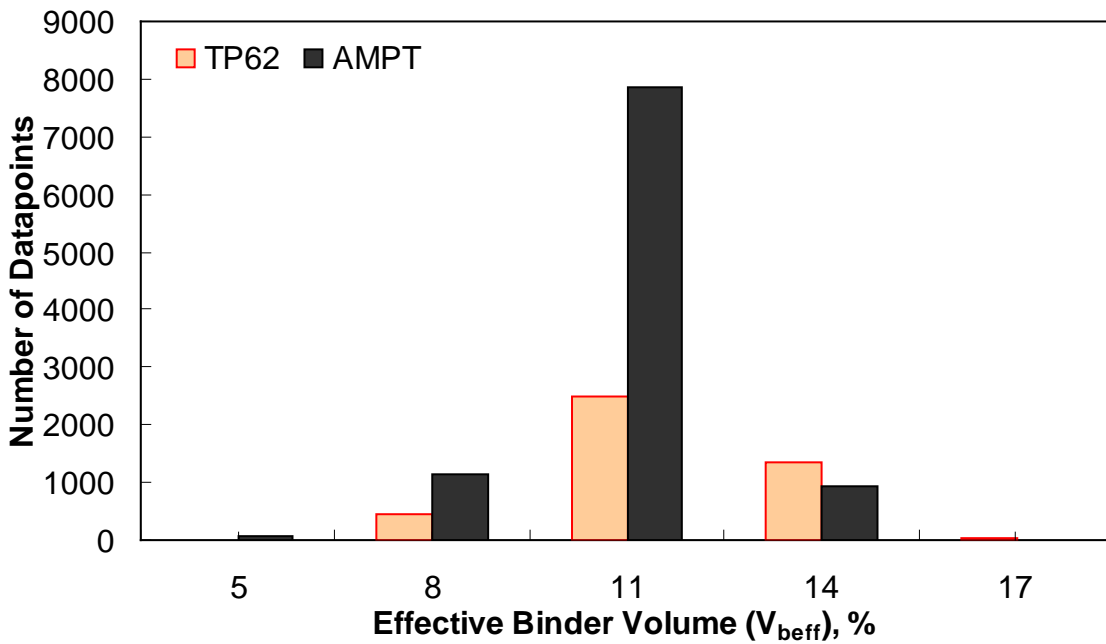


**Figure 150. Graph. Frequency distribution of effective binder volume in AMPT versus TP-62 databases.**

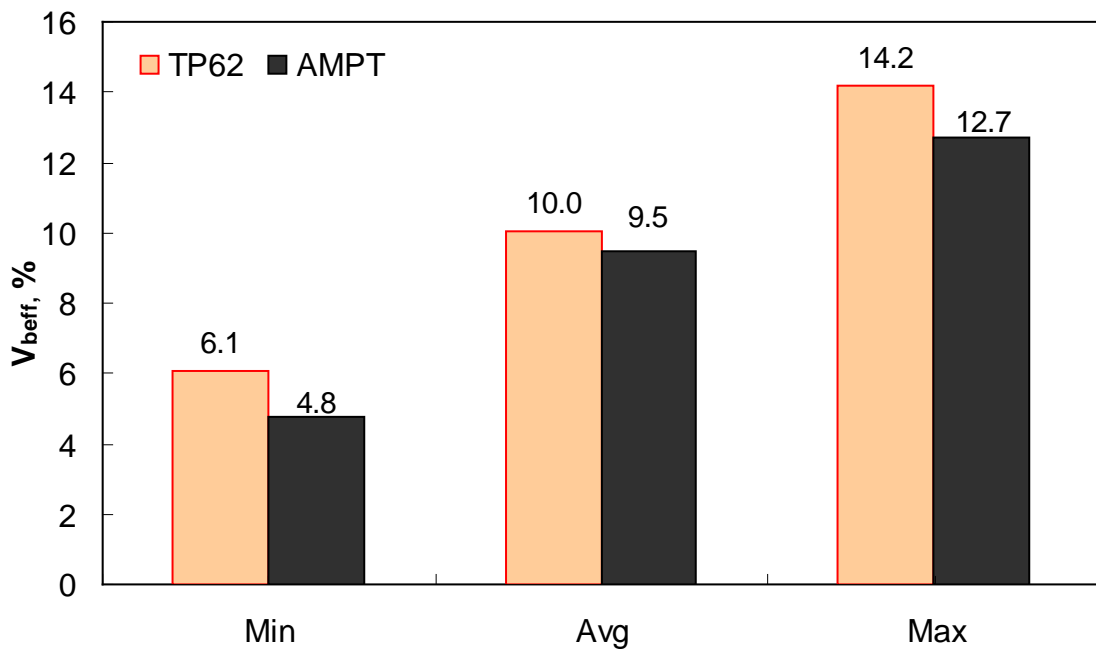


**Figure 151. Graph. Range of effective binder volume in AMPT versus TP-62 databases.**

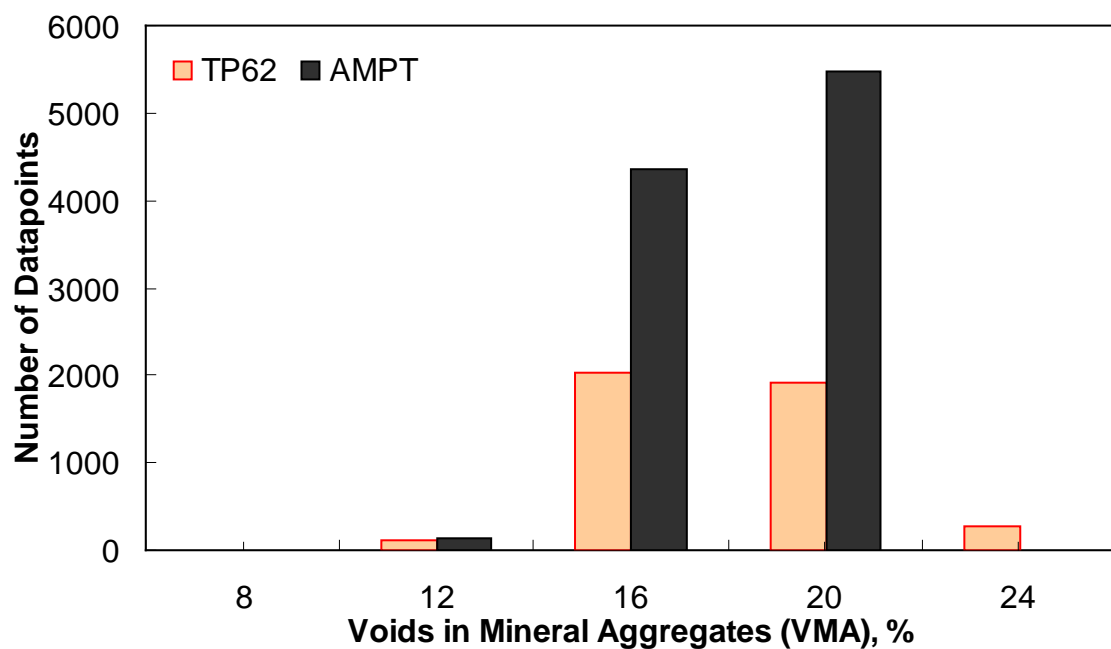


**Figure 152. Graph. Frequency distribution of VMA in AMPT versus TP-62 databases.**

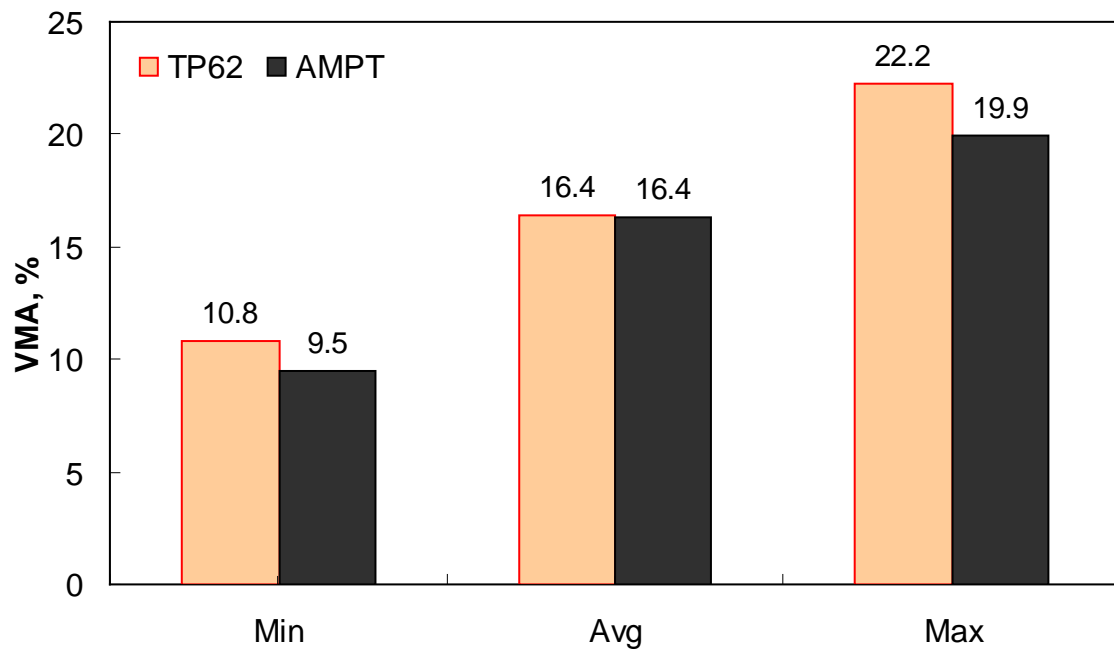


**Figure 153.** Graph. Range of VMA in AMPT versus TP-62 databases.

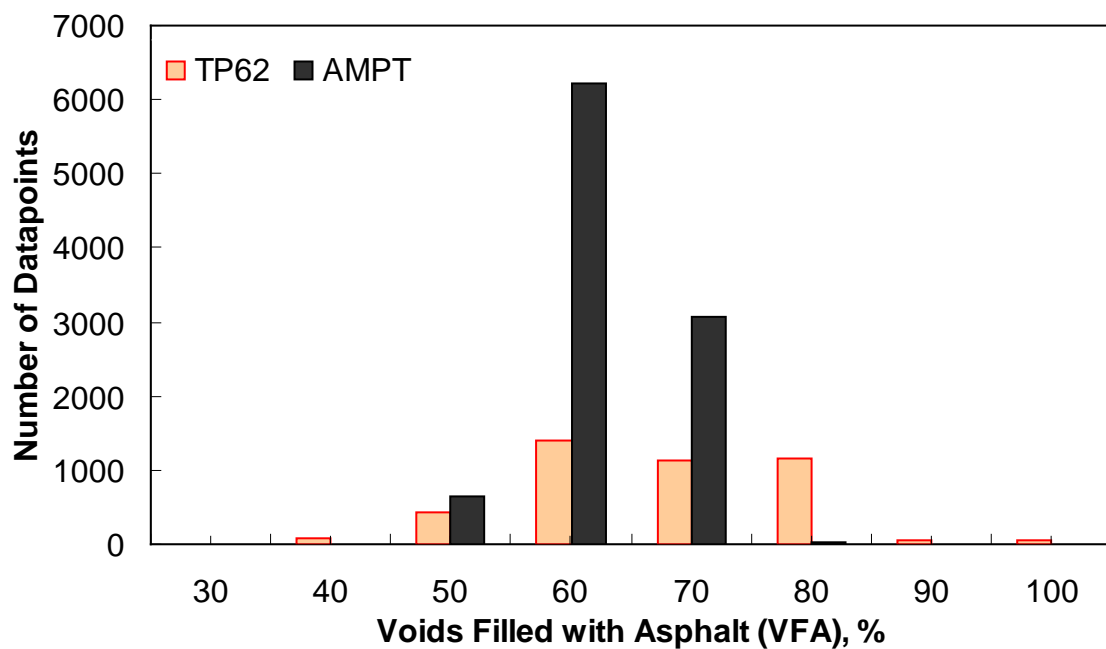


**Figure 154.** Graph. Frequency distribution of VFA in AMPT versus TP-62 databases.

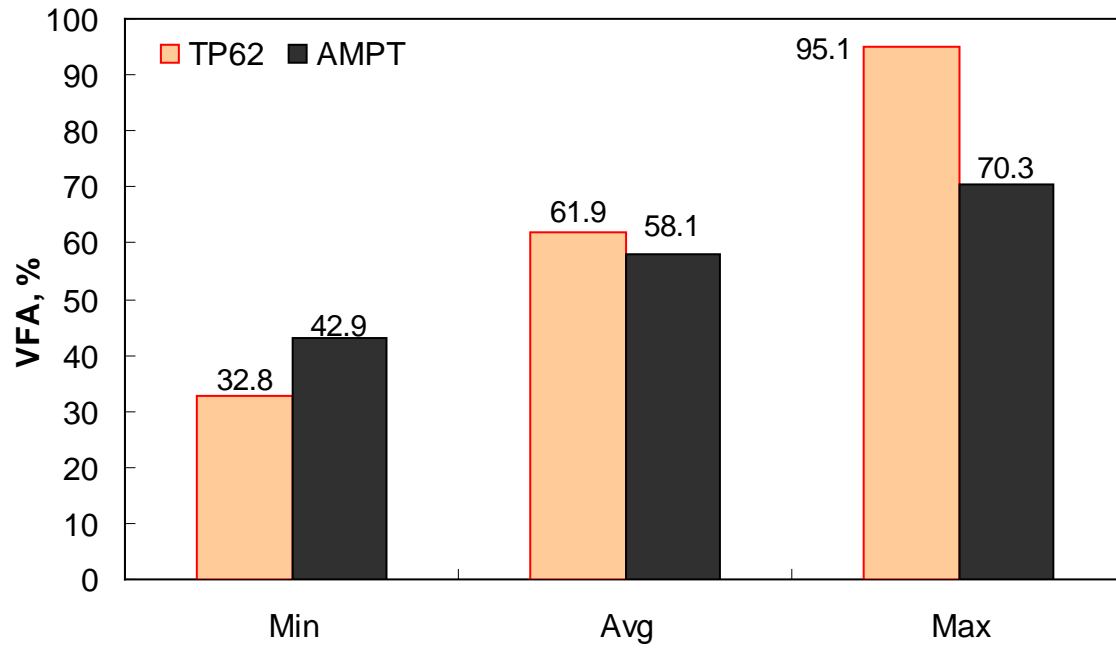


**Figure 155. Graph. Range of VFA in AMPT versus TP-62 databases.**

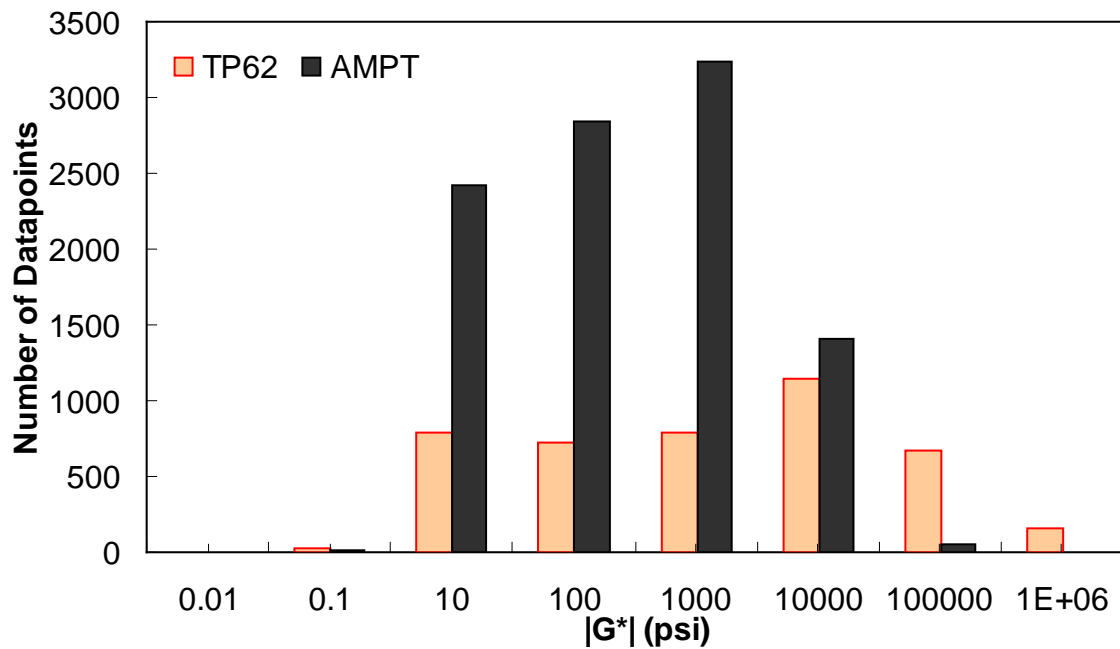


**Figure 156. Graph. Frequency distribution of |G\*| in AMPT versus TP-62 databases.**

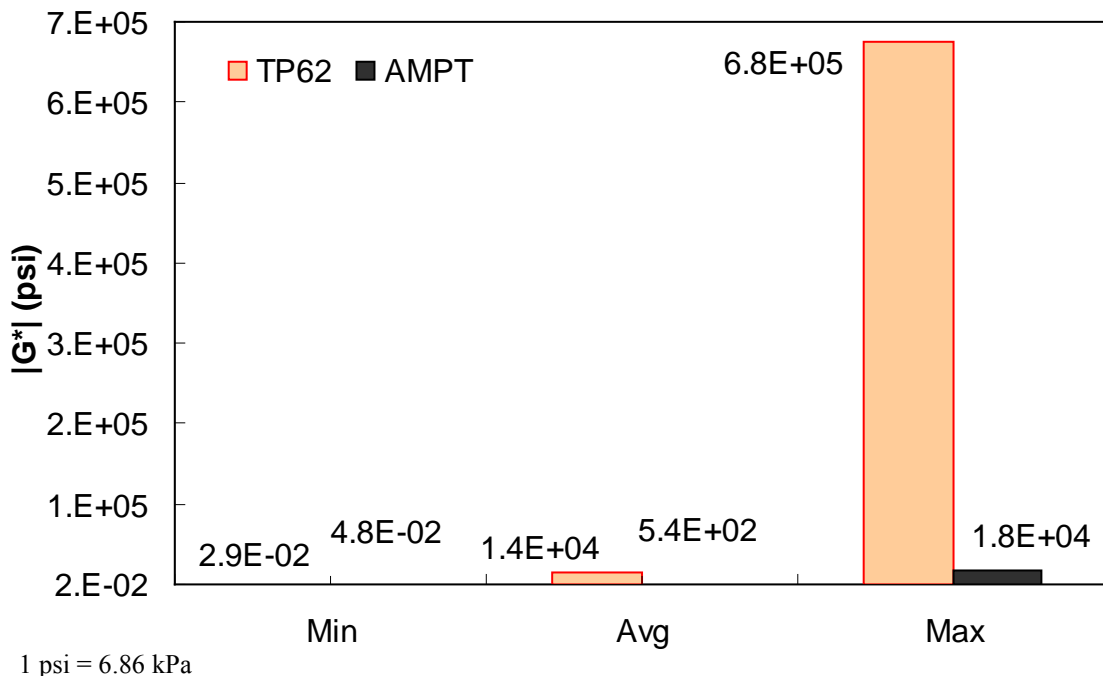


**Figure 157. Range of  $|G^*$  in AMPT versus TP-62 databases.**

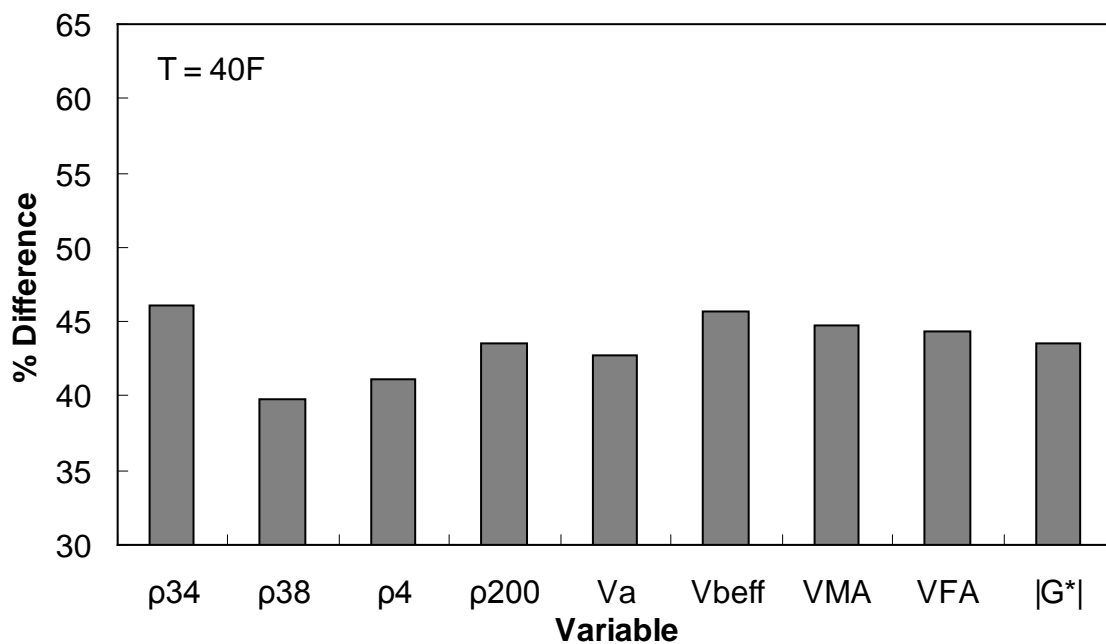


**Figure 158. Graph. Percentage of difference between AMPT versus TP-62 databases based on similar ranges of different variables at 39.9 °F (4.4 °C).**

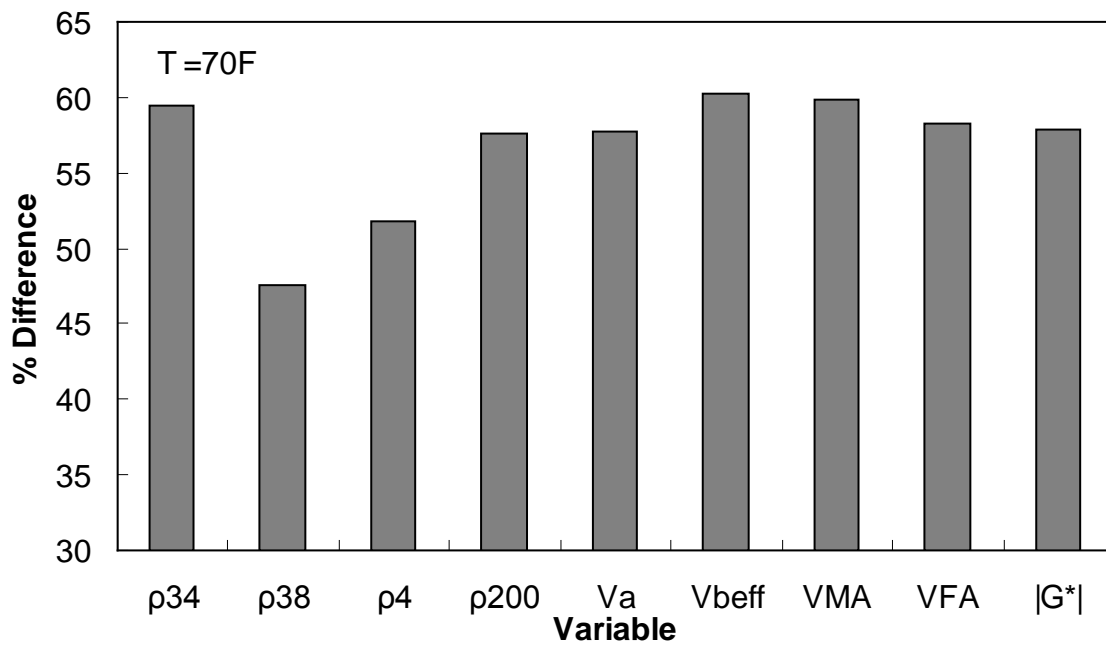


**Figure 159. Graph. Percentage of difference between AMPT versus TP-62 databases based on similar ranges of different variables at 69.9 °F (21.1 °C).**

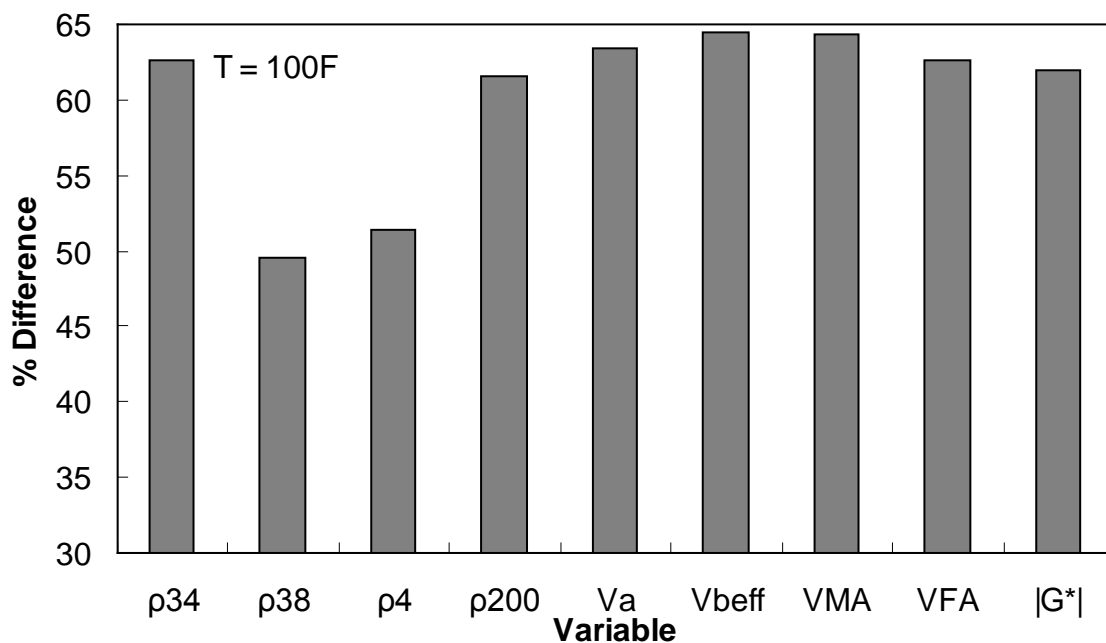


**Figure 160. Graph. Percentage of difference between AMPT versus TP-62 databases based on similar ranges of different variables at 100 °F (37.8 °C).**

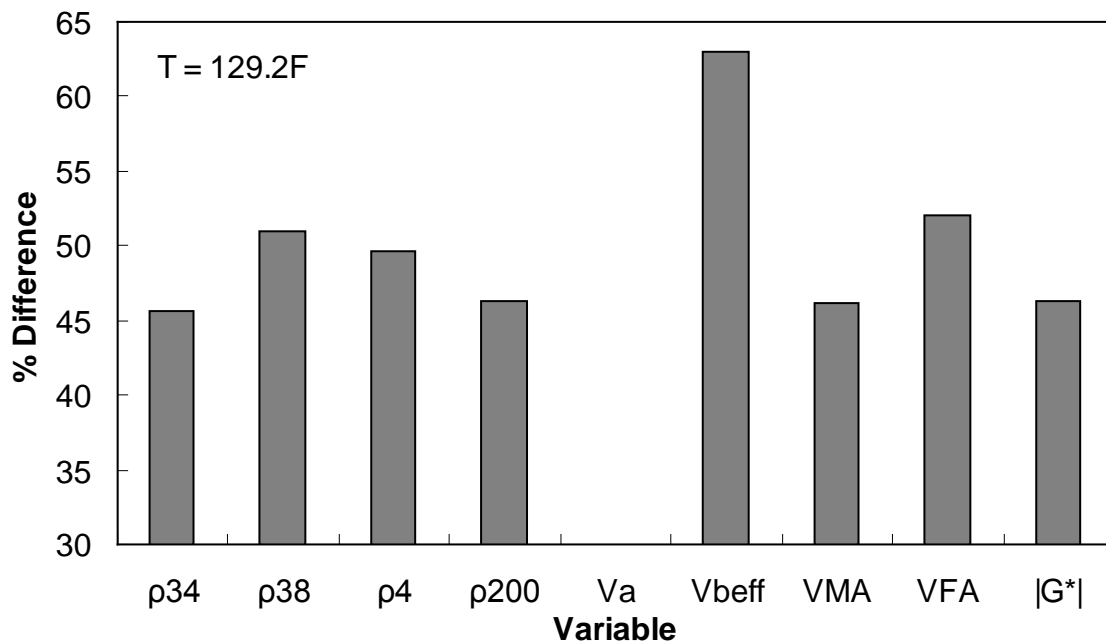


**Figure 161. Graph. Percentage of difference between AMPT versus TP-62 databases based on similar ranges of different variables at 129.2 °F (54.0 °C).**

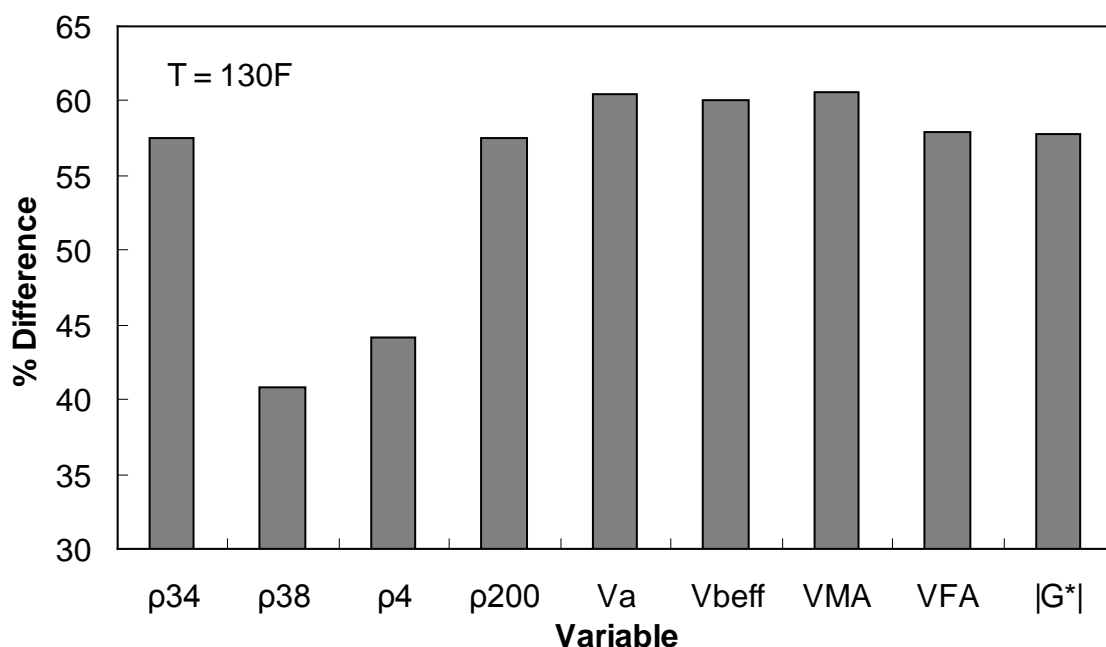


**Figure 162. Graph. Percentage of difference between AMPT versus TP-62 databases based on similar ranges of different variables at 129.9 °F (54.4 °C).**

**Table 46. Percentage of difference between AMPT versus TP-62 database based on similar ranges of different variables.**

Temp (°F)	<b>0 ≤ ρ<sub>34</sub> ≤ 15</b>	<b>5 ≤ ρ<sub>38</sub> ≤ 50</b>	<b>30 ≤ ρ<sub>4</sub> ≤ 70</b>	<b>3 ≤ ρ<sub>200</sub> ≤ 7</b>	<b>5 ≤ V<sub>a</sub> ≤ 9</b>	<b>8 ≤ V<sub>b<sub>eff</sub></sub> ≤ 14</b>	<b>12 ≤ VMA ≤ 20</b>	<b>50 ≤ VFA ≤ 80</b>	<b>1e-2 ≤  G*  ≤ 1e5</b>
40	46.08	39.80	41.14	43.54	42.75	45.65	44.81	44.29	43.60
70	59.39	47.54	51.74	57.66	57.67	60.23	59.91	58.32	57.84
100	62.63	49.53	51.35	61.61	63.38	64.49	64.36	62.66	61.95
129	45.60	51.02	49.65	46.26	N.A	63.01	46.16	52.09	46.26
130	57.55	40.76	44.14	57.46	60.50	59.99	60.54	57.93	57.83

°C = (°F-32)/1.8

Similar ranges of each variable have been considered for each temperature, and the percentage of error has been calculated based on the difference of average TP-62 versus AMPT |E\*| measurements for the corresponding temperature.

### C.3 EVALUATION OF AMPT VERSUS TP-62 PROTOCOLS USING ANN MODEL

A preliminary study was conducted to determine the feasibility and predictability of the ANN modeling technique relative to the existing models. This feasibility study was first conducted based on |G\*| because more existing closed-form models use this parameter as their primary input parameter. The ANN models used in this preliminary study are not the final models suggested by the research team, but they are similar in form and validation. To ensure full coverage of the expected conditions, the most recent Witczak database with available measured |G\*| data and a portion of the dataset obtained at NCSU with support from the NCDOT were utilized as the TP-62 training database. Also, appropriate portions of the FHWA mobile trailer database and the WRI database (from Kansas and Nevada sites) were considered as the AMPT training database (see table 47).<sup>(51,52)</sup> New parameters were not identified through this study. Instead, only those that have been used in the modified Witczak model are incorporated. For verification purposes, three different sets of independent databases were used (see table 48). As a corollary to this study, an additional ANN model was trained that uses the Hirsch model input parameters. The results from this model are given in this section, as well.

**Table 47. Summary of database used for training ANN models.**

<b>Type of Database</b>	<b>AMPT</b>		<b>TP-62</b>		<b>Total</b>
	<b>FHWA I</b>	<b>WRI</b>	<b>Witczak</b>	<b>NCDOT I</b>	
Number of mixtures	409	24	106	24	563
Number of data points	7,827	500	3,180	644	12,151
Number of binders	13	8	17	5	43
Number of gradation variations	13	12	13	19	57
Number of volumetric variations	256	13	98	24	391

Note: FHWA I consists of the mixtures from 12 States in the FHWA mobile trailer database.

**Table 48. Summary of the database used for verification of ANN models.**

Type of Database	AMPT		TP-62	Total
	FHWA II	Citgo		
Number of mixtures	84	8	12	104
Number of data points	1,652	168	338	2,158
Number of binders	3	2	3	8
Number of gradation variations	3	1	12	16
number of volumetric variations	75	1	12	88

Note: FHWA II consists of the mixtures from three States in the FHWA mobile trailer database with the following site IDs: 1-IA0358, 2-WA0463, and 3-KS464.

It should be noted that the two TPs, AMPT and TP-62, were used to measure the  $|E^*|$  values in the various databases. To illustrate any possible differences between the two protocols, three different ANNs were developed using the Witczak-based input parameters, as shown in table 49. G-GR pANN was trained using data from both the AMPT and TP-62 protocols, whereas AMPT pANN and TP-62 pANN models were trained using the data from AMPT only and TP-62 only. Table 49 summarizes the databases used to train and verify the ANNs.

**Table 49. Description of the developed ANN Models and their validation statistics.**

Model	Data Used in ANN Training		Description	Reference Scale	Statistical Parameters for Training Data	Statistical Parameters for Verification Data		
	AMPT	TP-62				FHWA II	NCDOT II	Citgo
G-GR pANN	FHWA I	Witczak	ANNs trained with modified Witczak parameters	Arithmetic	$Se/Sy = 0.29$ $R^2 = 0.92$	$Se/Sy = 0.38$ $R^2 = 0.86$	$Se/Sy = 0.33$ $R^2 = 0.97$	$Se/Sy = 0.52$ $R^2 = 0.94$
	WRI	NCDOT I		Log	$Se/Sy = 0.15$ $R^2 = 0.98$	$Se/Sy = 0.35$ $R^2 = 0.91$	$Se/Sy = 0.27$ $R^2 = 0.96$	$Se/Sy = 0.59$ $R^2 = 0.96$
	FHWA I			Arithmetic	$Se/Sy = 0.24$ $R^2 = 0.94$	$Se/Sy = 0.36$ $R^2 = 0.91$	$Se/Sy = 0.63$ $R^2 = 0.87$	$Se/Sy = 0.37$ $R^2 = 0.88$
	WRI			Log	$Se/Sy = 0.16$ $R^2 = 0.97$	$Se/Sy = 0.38$ $R^2 = 0.90$	$Se/Sy = 0.60$ $R^2 = 0.89$	$Se/Sy = 0.48$ $R^2 = 0.91$
TP-62 pANN		Witczak		Arithmetic	$Se/Sy = 0.34$ $R^2 = 0.88$	$Se/Sy = 2.08$ $R^2 = 0.77$	$Se/Sy = 0.24$ $R^2 = 0.95$	$Se/Sy = 1.20$ $R^2 = 0.97$
		NCDOT I		Log	$Se/Sy = 0.18$ $R^2 = 0.97$	$Se/Sy = 0.99$ $R^2 = 0.82$	$Se/Sy = 0.27$ $R^2 = 0.93$	$Se/Sy = 0.53$ $R^2 = 0.99$
Modified Witczak Model				Arithmetic		$Se/Sy = 0.92$ $R^2 = 0.91$	$Se/Sy = 0.71$ $R^2 = 0.91$	$Se/Sy = 0.64$ $R^2 = 0.98$
				Log		$Se/Sy = 0.58$ $R^2 = 0.92$	$Se/Sy = 0.19$ $R^2 = 0.98$	$Se/Sy = 0.26$ $R^2 = 0.99$
Hirsch Model				Arithmetic		$Se/Sy = 0.30$ $R^2 = 0.92$	$Se/Sy = 0.47$ $R^2 = 0.97$	$Se/Sy = 0.11$ $R^2 = 0.99$
				Log		$Se/Sy = 0.39$ $R^2 = 0.92$	$Se/Sy = 0.26$ $R^2 = 0.97$	$Se/Sy = 0.09$ $R^2 = 0.99$
Al-Khateeb Model				Arithmetic		$Se/Sy = 0.48$ $R^2 = 0.89$	$Se/Sy = 0.55$ $R^2 = 0.93$	$Se/Sy = 0.36$ $R^2 = 0.93$
				Log		$Se/Sy = 0.43$ $R^2 = 0.92$	$Se/Sy = 0.40$ $R^2 = 0.93$	$Se/Sy = 0.17$ $R^2 = 0.97$

Note: Blank cells indicate information is not applicable.

The ANN models perform well, as shown in figure 163 to figure 180, which display the prediction accuracies of the different models for the combined AMPT and TP-62 data (figure 163 to figure 168), TP-62 data only (figure 169 to figure 174), and AMPT data only (figure 175 to figure 180). Also, these three groups of figures show the prediction accuracies of the ANNs separately. In these three figures, the type of data (i.e., AMPT versus TP-62) used in the ANN training matches the type of data used in the verification (e.g., figure 163 shows the prediction accuracy of the G-GR pANN model trained with the combined AMPT and TP-62 data on the combined AMPT and TP-62 data, etc.). It is noted that the data used in these figures were not included in the ANN training.

Figure 181 through figure 204 further demonstrate the differences between the AMPT and the TP-62 data and their effect on the prediction accuracies of the different ANNs. FHWA II data used in figure 181 through figure 188 are obtained using the AMPT protocol. The TP-62 pANN model trained with the TP-62 data and the modified Witczak model overpredict the measured  $|E^*|$  values. Figure 189 through figure 196 present the prediction results for the NCDOT II data, which were measured using the TP-62 protocol. These figures illustrate the opposite effect on the prediction bias, that is, the effect of using the TP-62 data in the ANN training and predicting the AMPT data. In this case, the AMPT pANN model, trained using the AMPT data, underpredicts the  $|E^*|$  values. The G-GR pANN model provides a promising ANN-based  $|E^*|$  model, and the TP-62 pANN model shows good predictions without any significant bias. With the exception of the Citgo dataset, the G-GR pANN model provides high goodness of fit and correlation, as seen in table 49. The promising feature of the G-GR pANN model is that it improves the bias of  $|E^*|$  predictions, particularly at high and low temperatures. This new ANN model is more sensitive to, and thus more likely to capture, the changes in volumetric parameters than all the other existing predictive models.

The findings from figure 163 to figure 204 are summarized as follows:

- The  $|E^*|$  values measured by the AMPT protocol seem to be slightly different from those measured by the TP-62 protocol. The  $|E^*|$  predictive models developed using the  $|E^*|$  values measured by the TP-62 overpredict the  $|E^*|$  values measured by the AMPT.
- Overall, the G-GR pANN model, trained with the combination of the AMPT and TP-62 data, shows excellent statistics in terms of high accuracy and low bias, especially at extremely high and low temperatures.

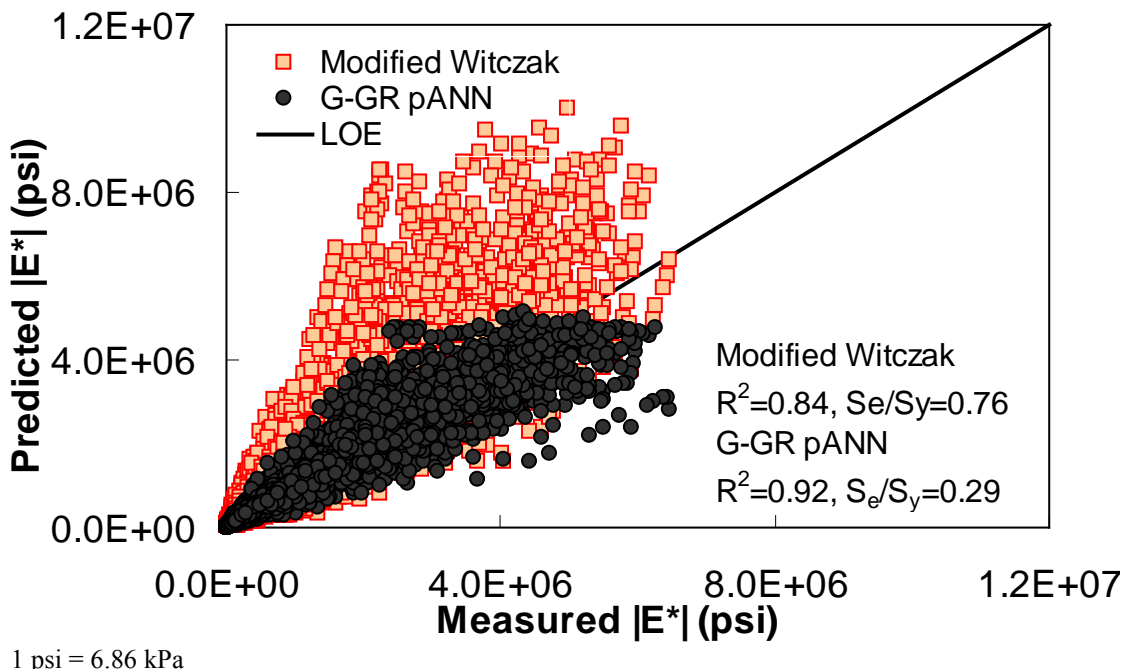


**Figure 163.** Graph. Prediction of the combination of AMPT and TP-62 data using the modified Witczak and G-GR pANN models in arithmetic scale.

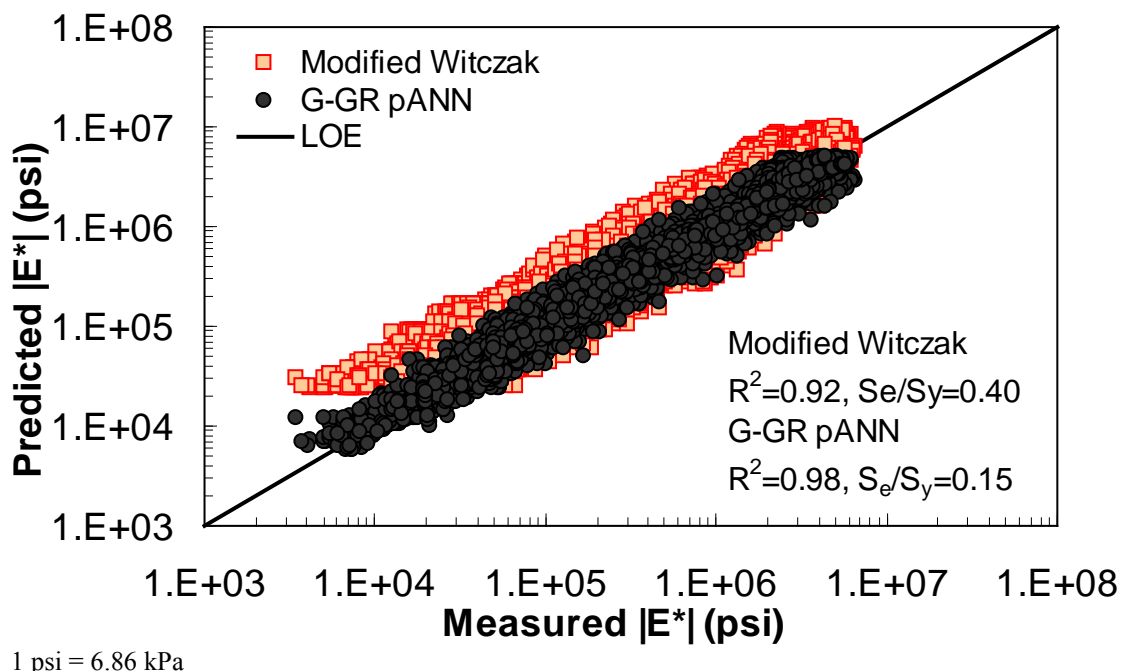


**Figure 164.** Graph. Prediction of the combination of AMPT and TP-62 data using the modified Witczak and G-GR pANN models in logarithmic scale.

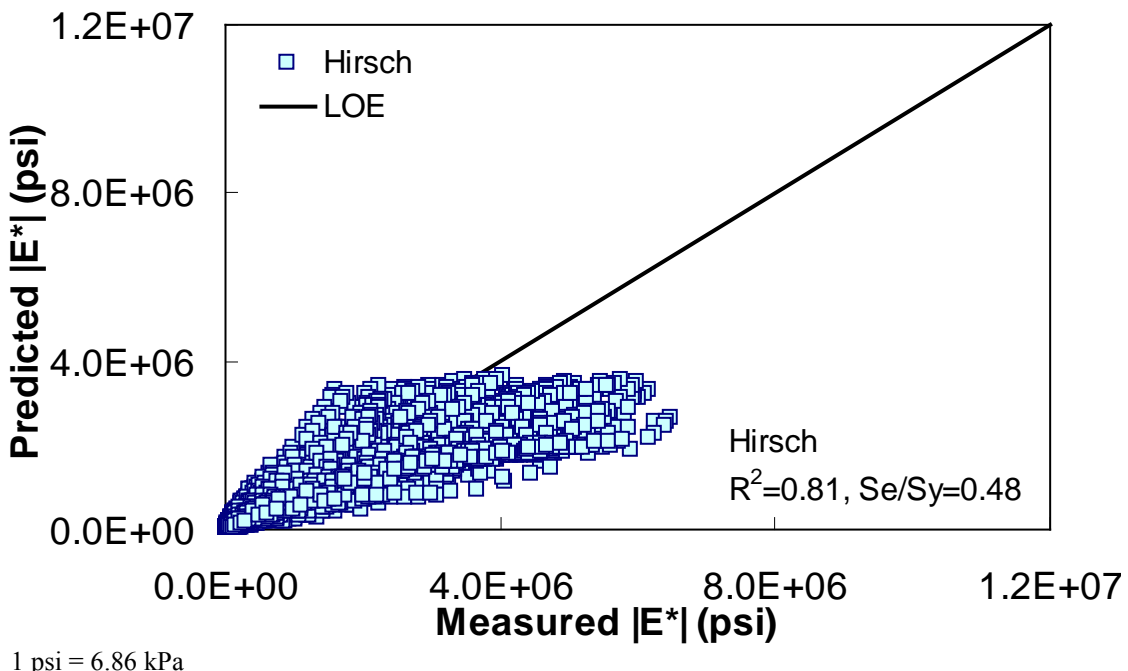


**Figure 165. Graph. Prediction of the combination of AMPT and TP-62 data using the Hirsch model in arithmetic scale.**

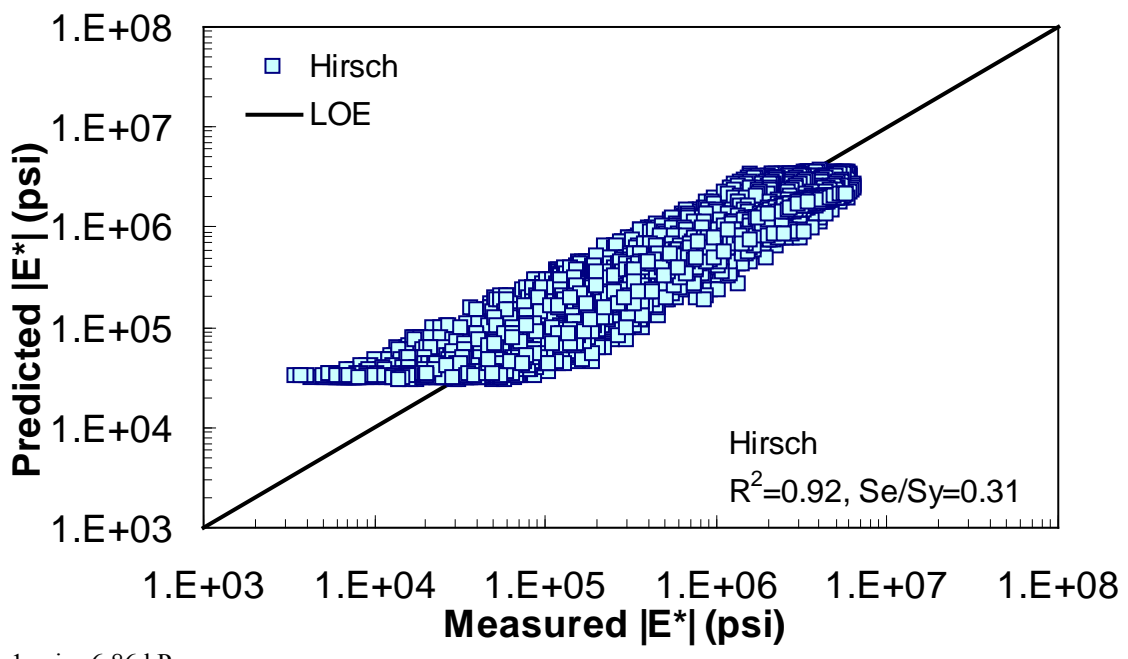


**Figure 166. Graph. Prediction of the combination of AMPT and TP-62 data using the Hirsch model in logarithmic scale.**

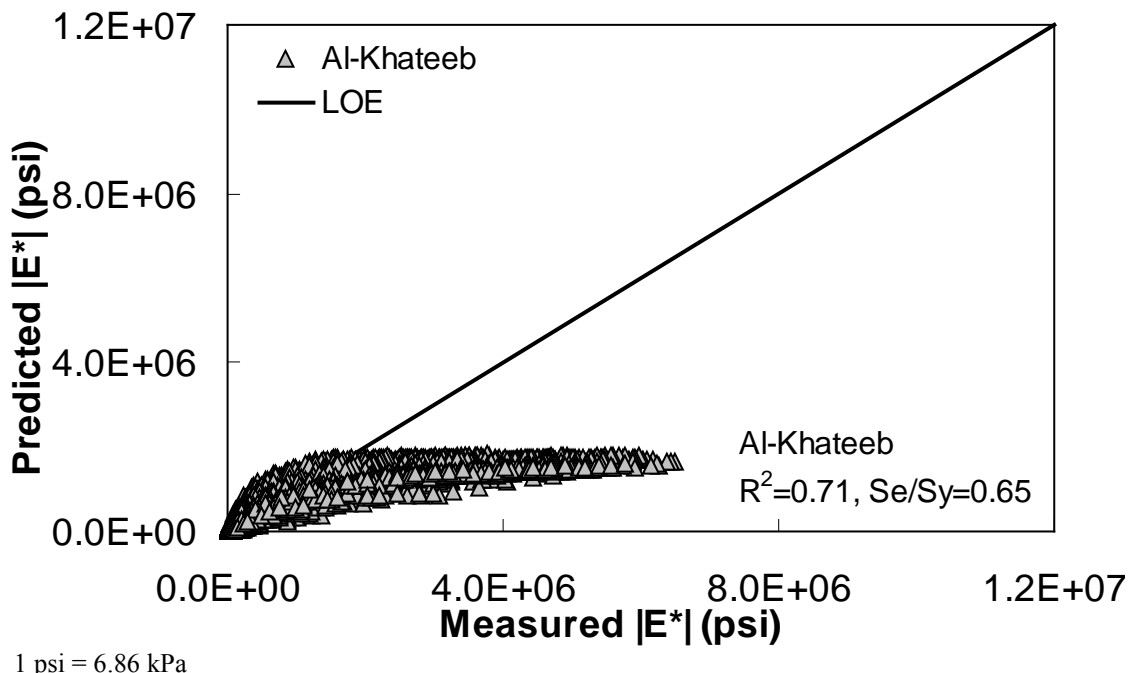


**Figure 167. Graph. Prediction of the combination of AMPT and TP-62 data using the Al-Khateeb model in arithmetic scale.**

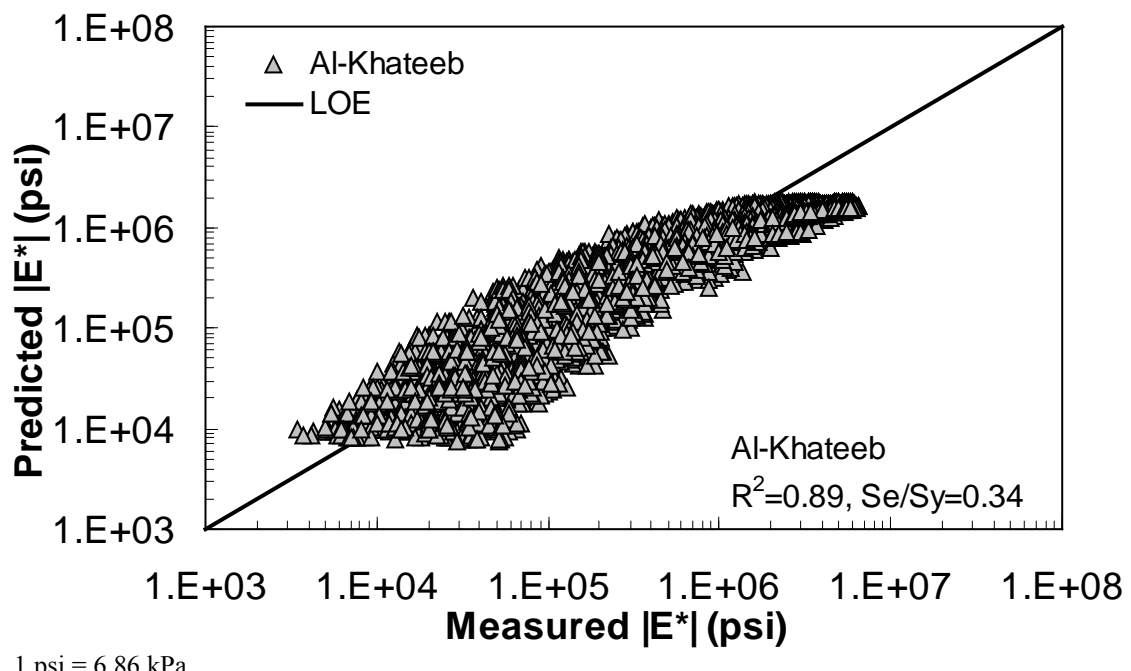


**Figure 168. Graph. Prediction of the combination of AMPT and TP-62 data using the Al-Khateeb model in logarithmic scale.**

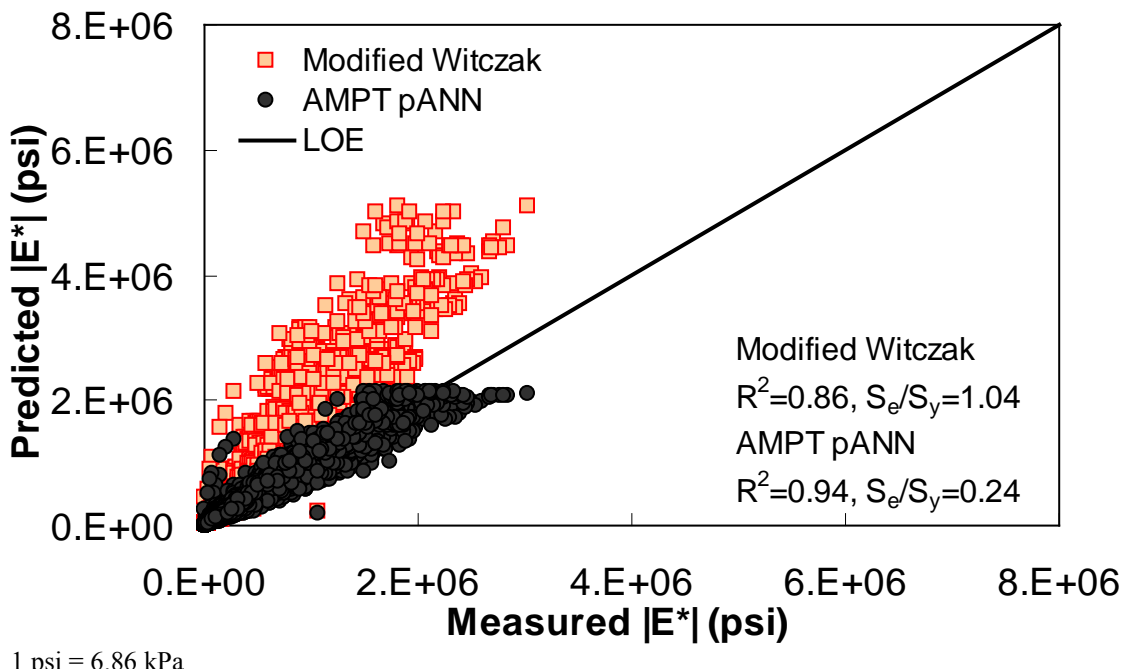


**Figure 169. Graph. Prediction of the AMPT data using the modified Witczak and AMPT pANN models in arithmetic scale.**

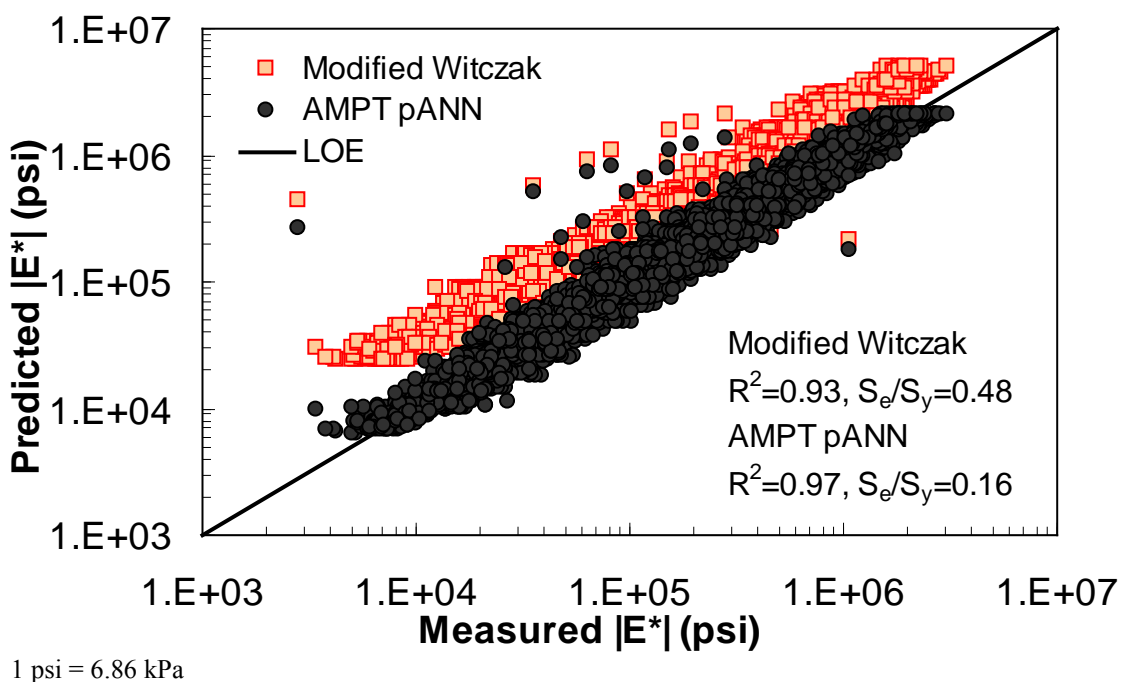


**Figure 170. Graph. Prediction of the AMPT data using the modified Witczak and AMPT pANN models in logarithmic scale.**

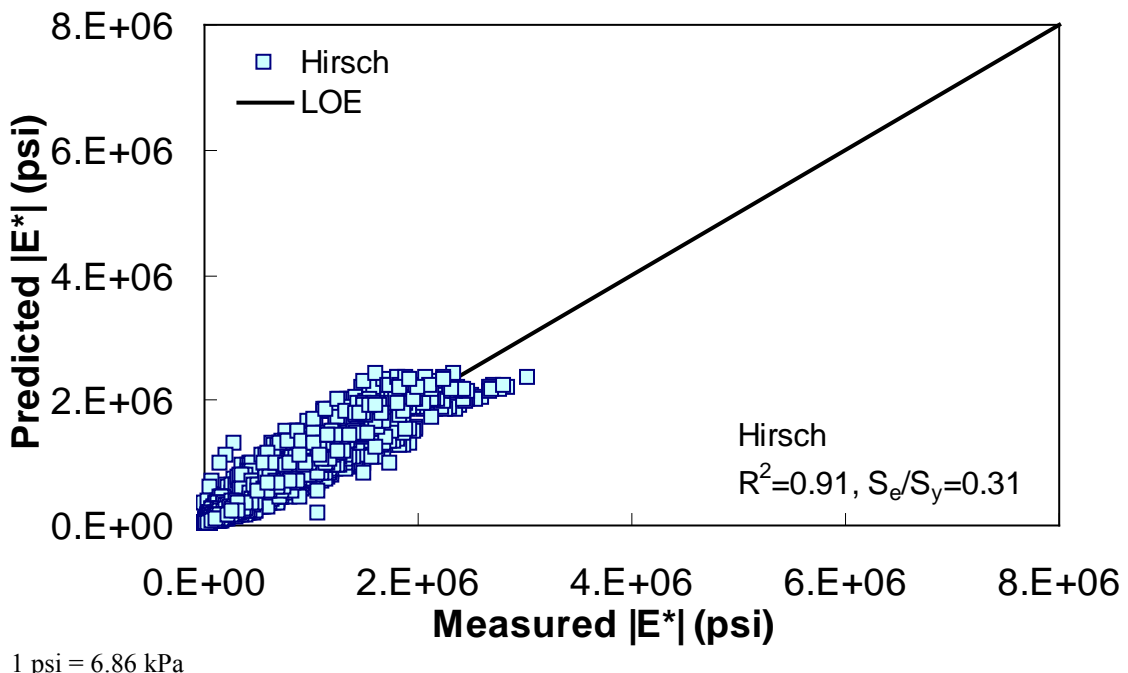


**Figure 171. Graph. Prediction of the AMPT data using the Hirsch model in arithmetic scale.**

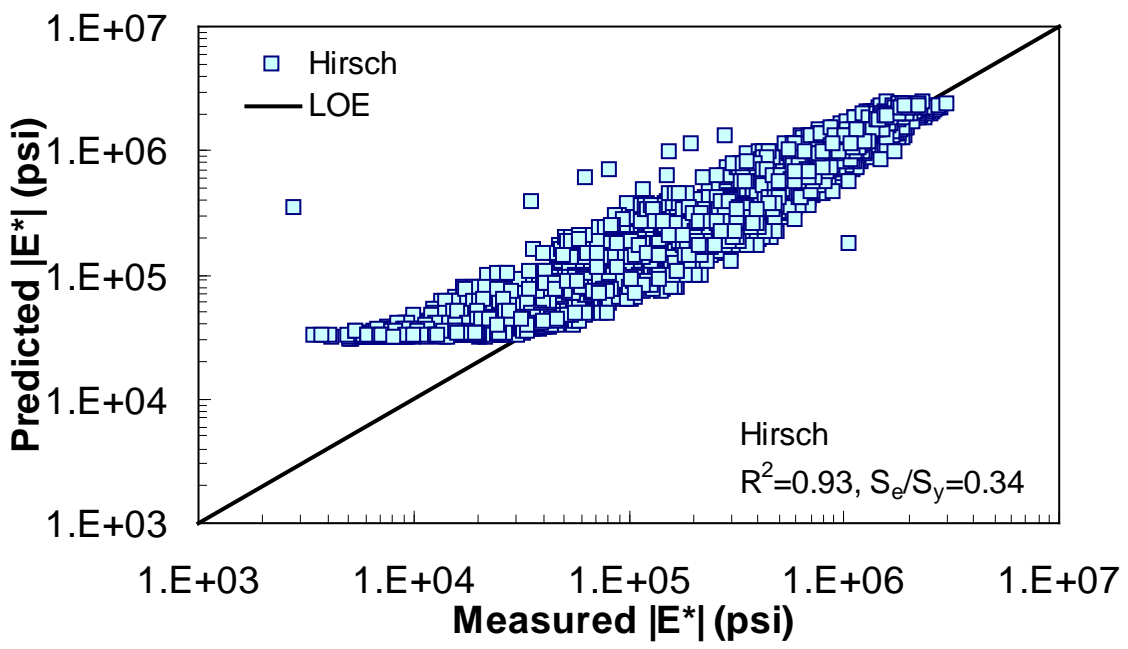


**Figure 172. Graph. Prediction of the AMPT data using the Hirsch model in logarithmic scale.**

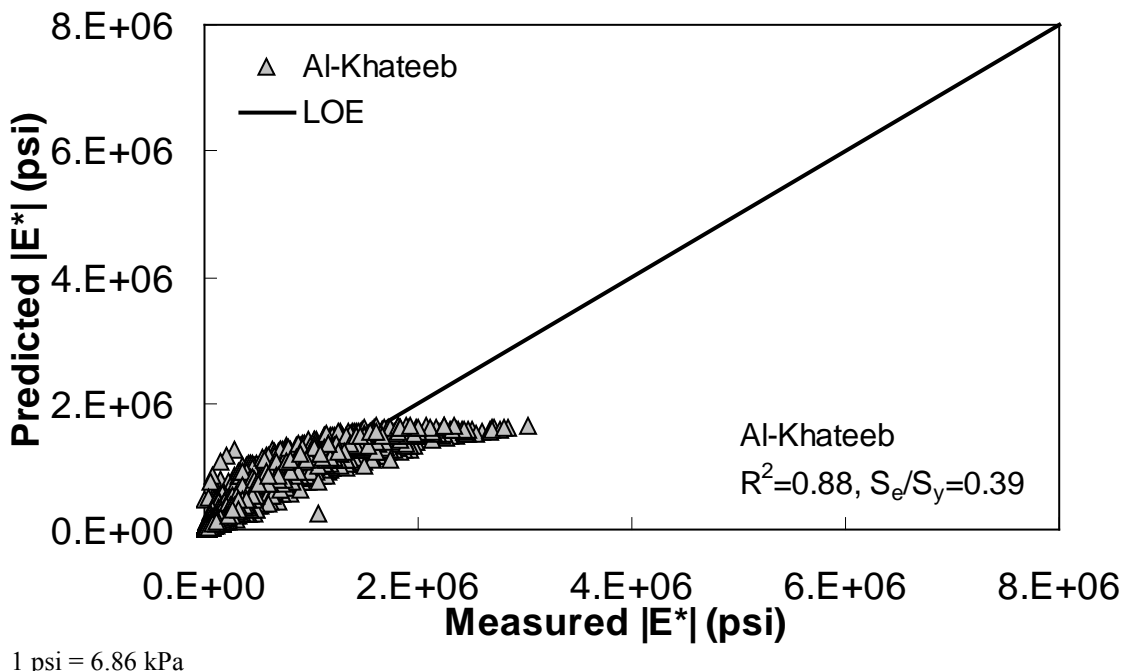


**Figure 173.** Graph. Prediction of the AMPT data using the Al-Khateeb model in arithmetic scale.

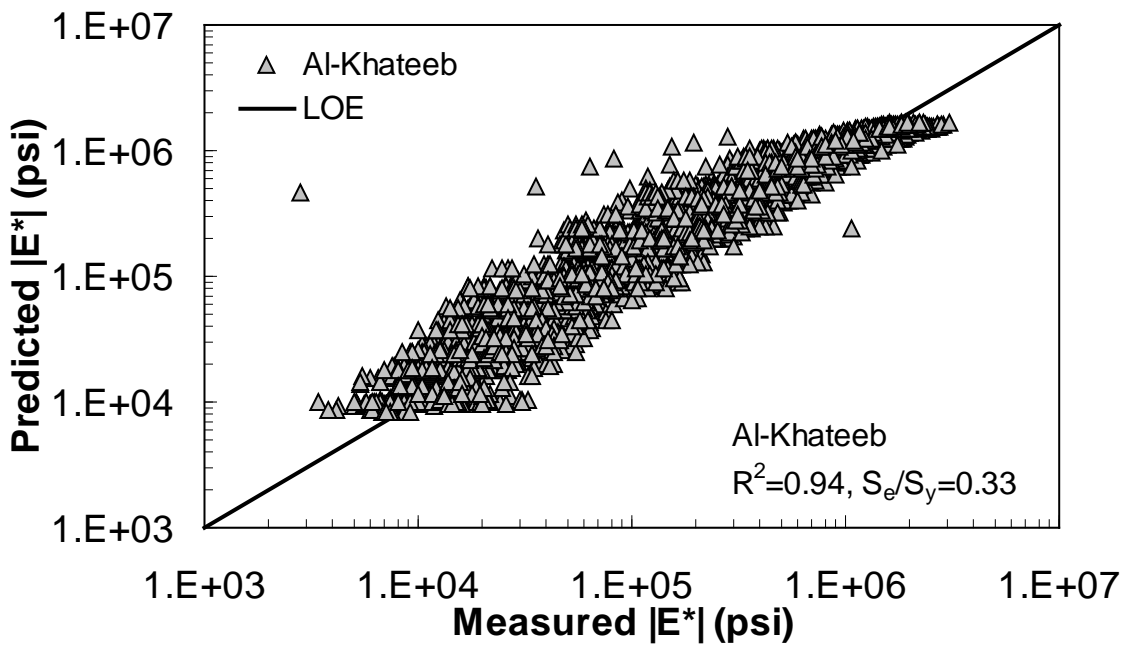


**Figure 174.** Graph. Prediction of the AMPT data using the Al-Khateeb model in logarithmic scale.

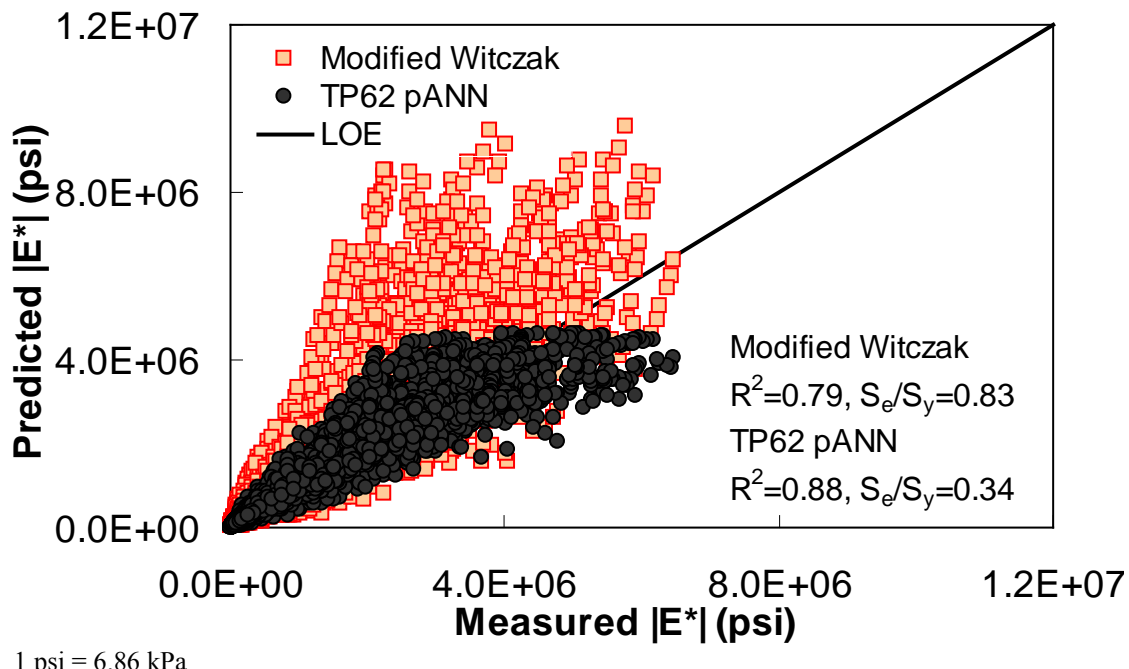


**Figure 175. Graph. Prediction of the TP-62 data using the modified Witczak and TP-62 pANN models in arithmetic scale.**

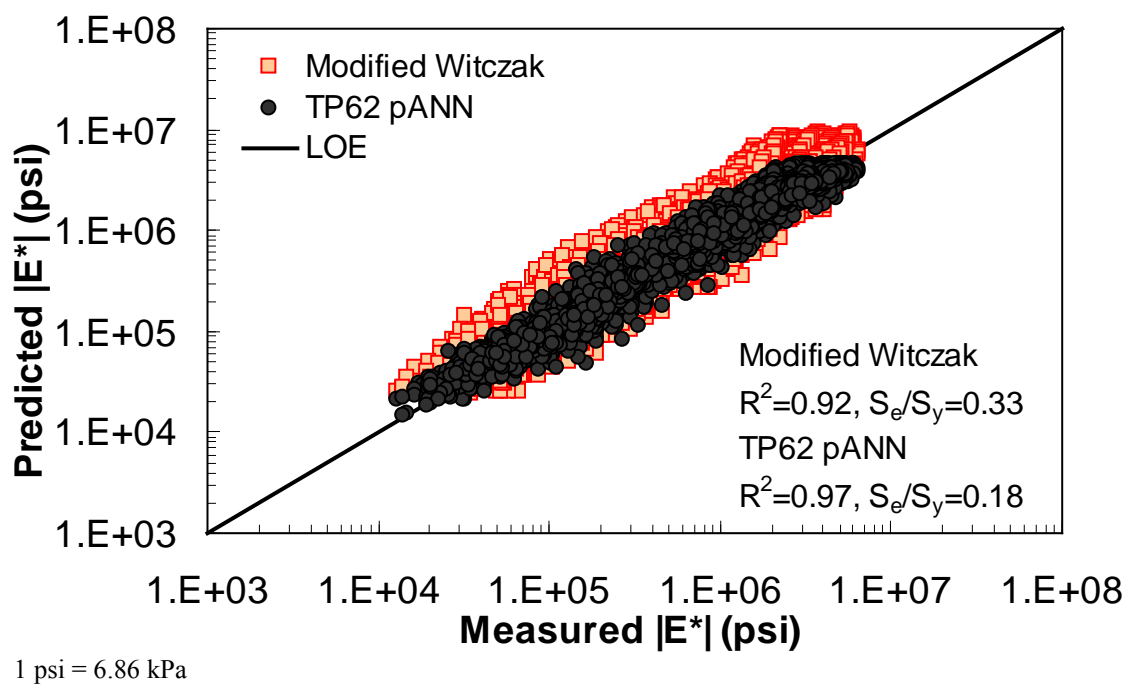
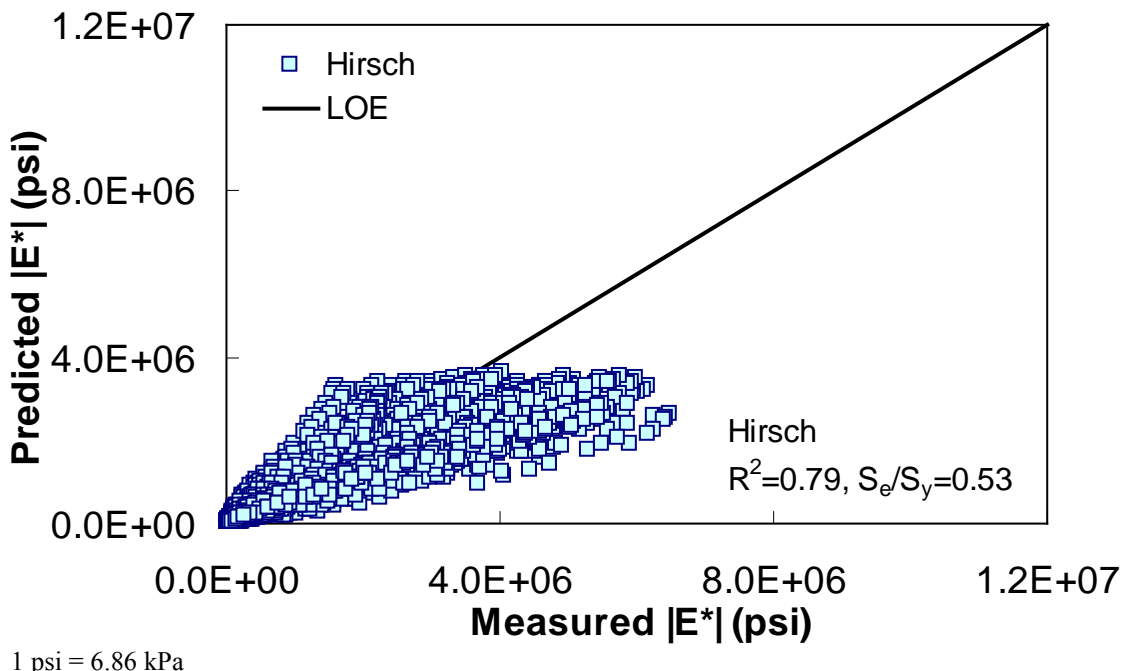
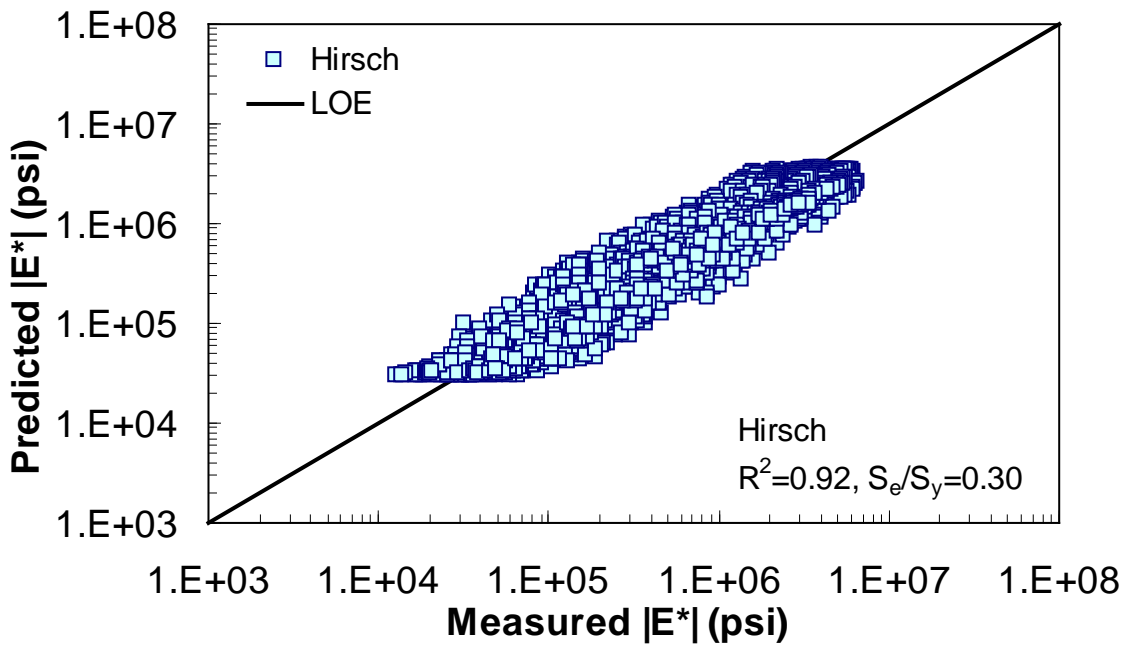


**Figure 176. Graph. Prediction of the TP-62 data using the modified Witczak and TP-62 pANN models in logarithmic scale.**



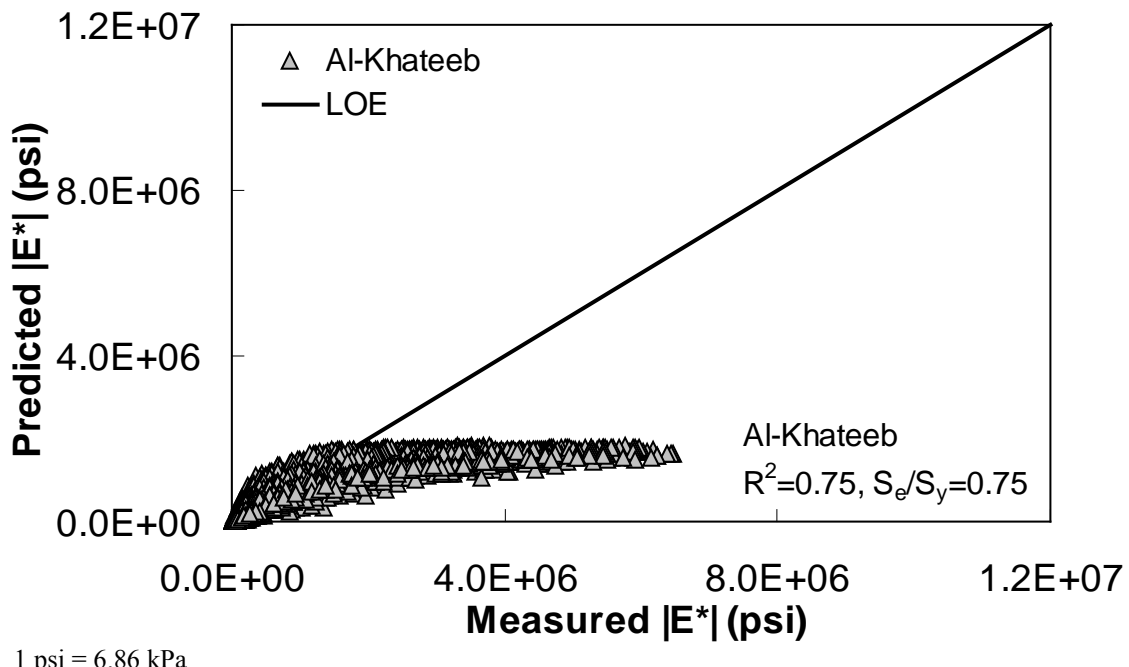
1 psi = 6.86 kPa

**Figure 177. Graph. Prediction of the TP-62 data using the Hirsch model in arithmetic scale.**



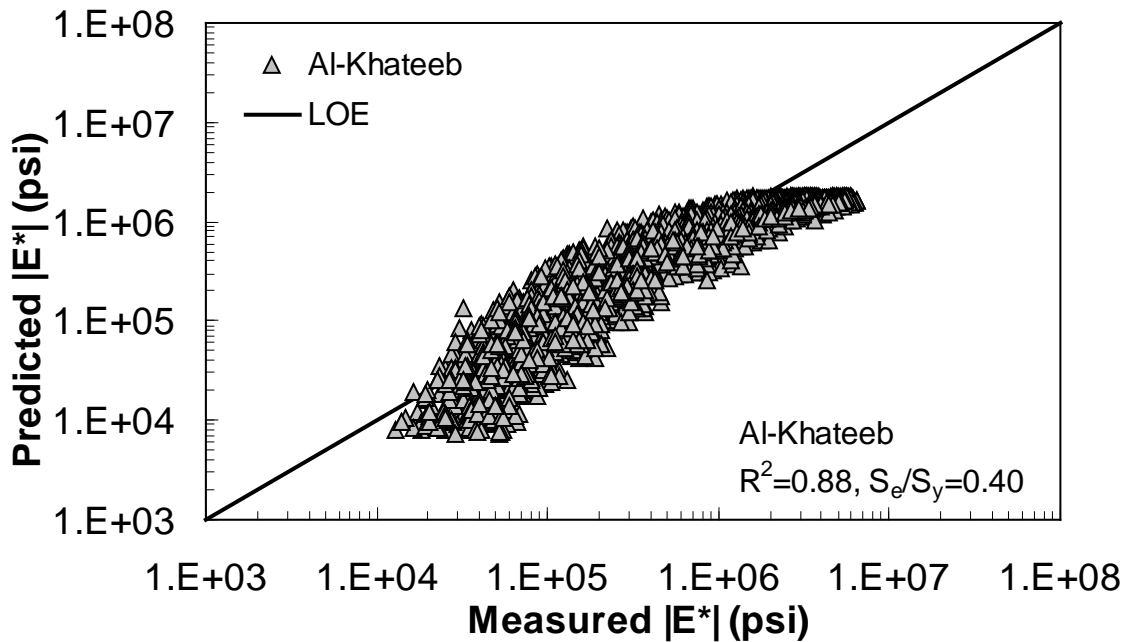
1 psi = 6.86 kPa

**Figure 178. Graph. Prediction of the TP-62 data using the Hirsch model in logarithmic scale.**



1 psi = 6.86 kPa

**Figure 179. Graph. Prediction of the TP-62 data using the Al-Khateeb model in arithmetic scale.**



1 psi = 6.86 kPa

**Figure 180. Graph. Prediction of the TP-62 data using the Al-Khateeb model in logarithmic scale.**

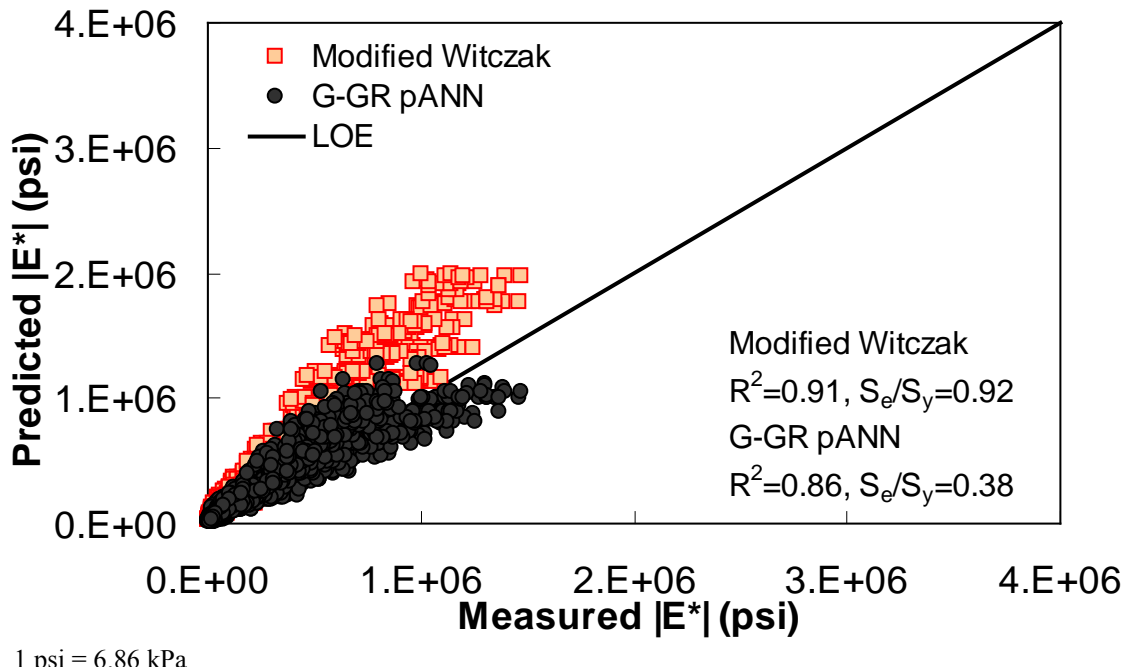


**Figure 181. Graph. Prediction of the FHWA II data using the modified Witczak and G-GR pANN models in arithmetic scale.**

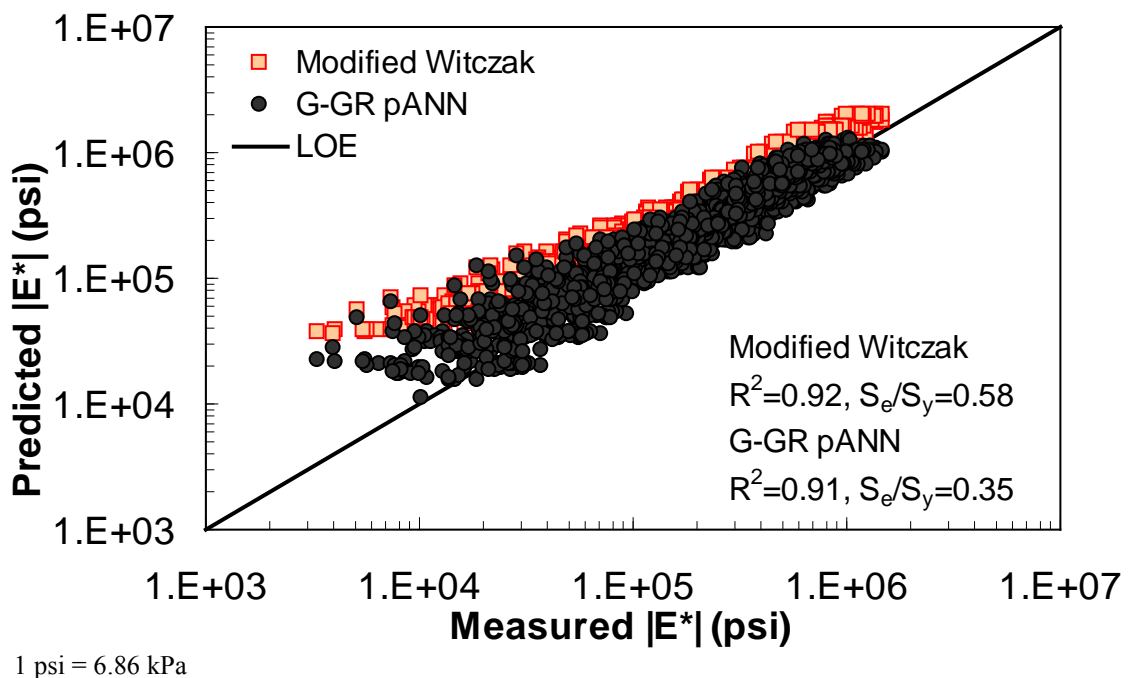


**Figure 182. Graph. Prediction of the FHWA II data using the modified Witczak and G-GR pANN models in logarithmic scale.**

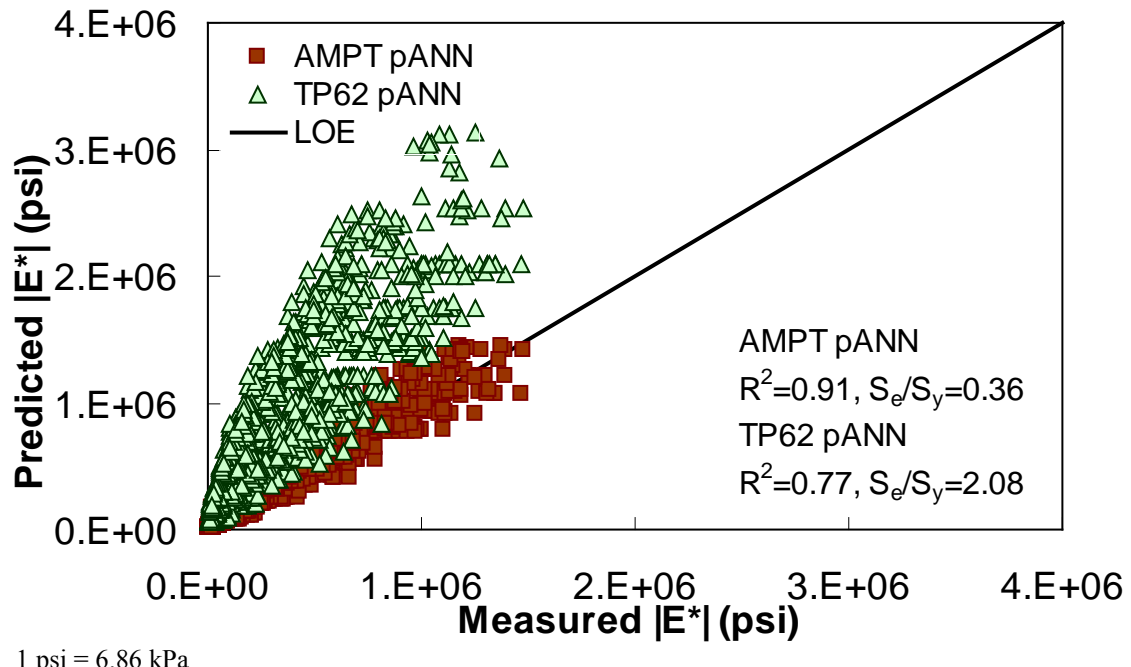


**Figure 183. Graph. Prediction of the FHWA II data using the AMPT pANN and TP-62 pANN models in arithmetic scale.**

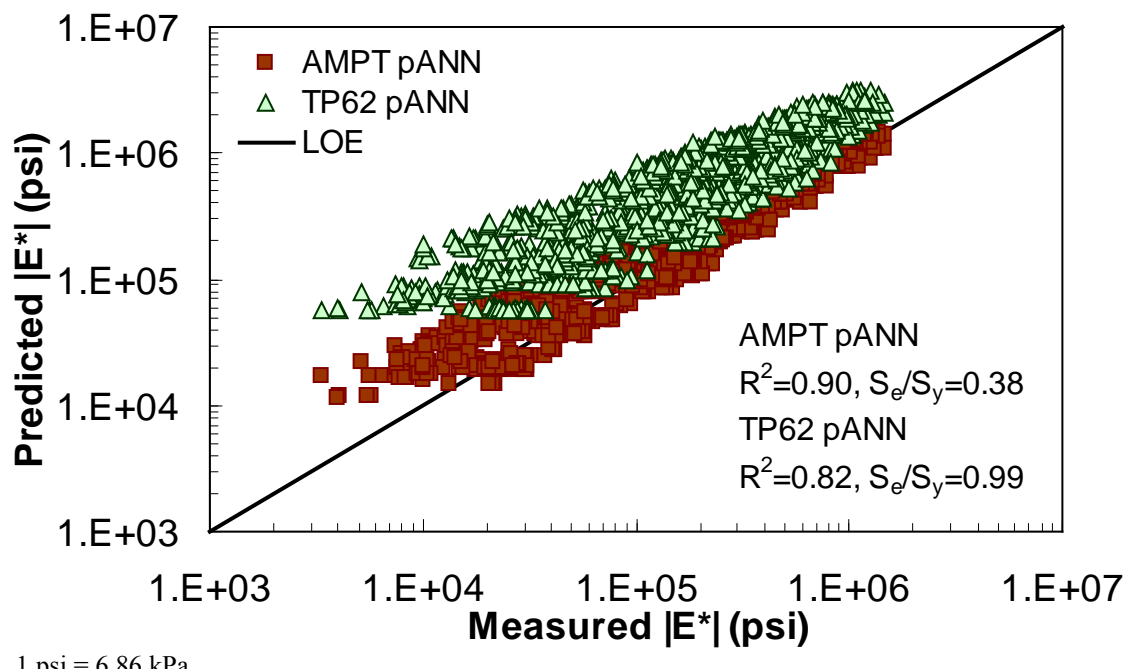
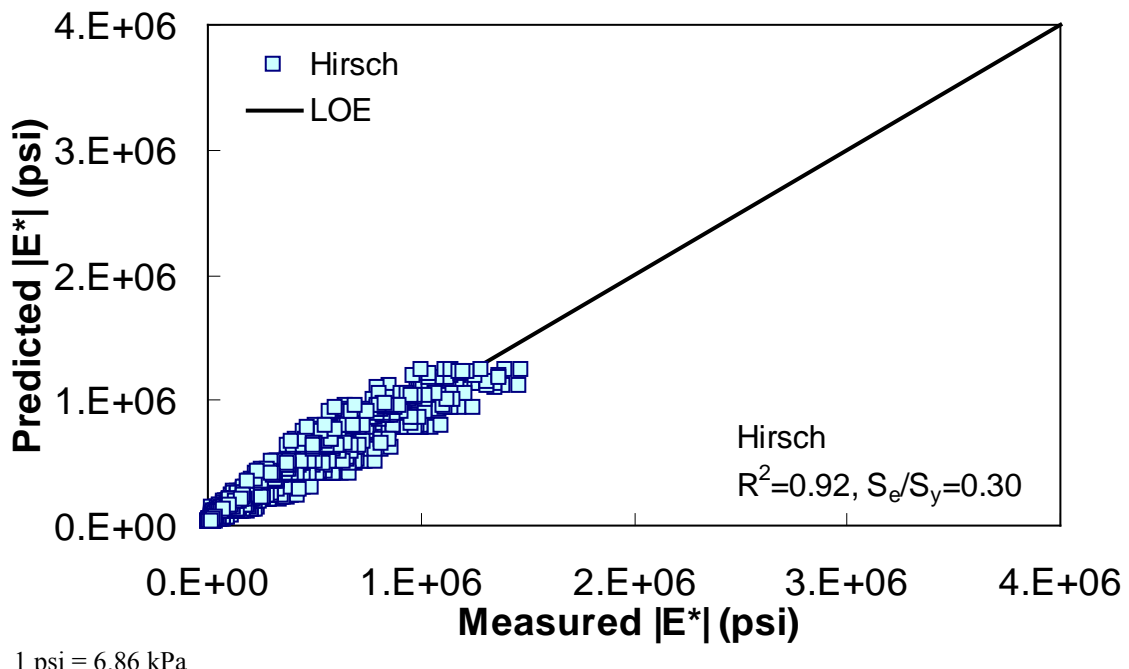
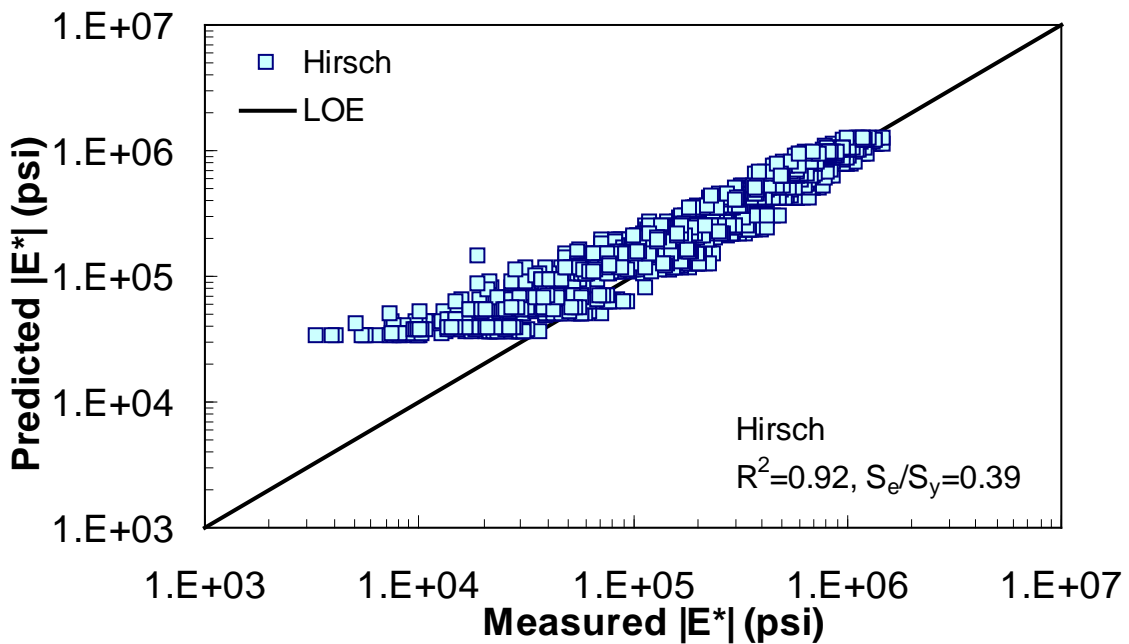


**Figure 184. Graph. Prediction of the FHWA II data using the AMPT pANN and TP-62 pANN models in logarithmic scale.**



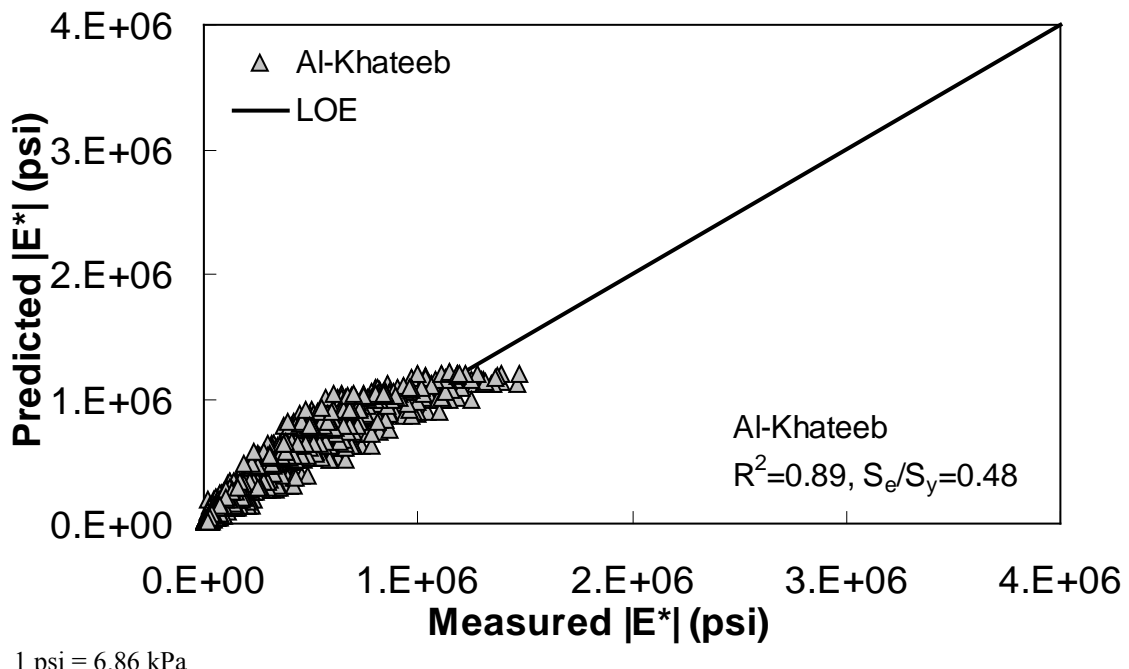
1 psi = 6.86 kPa

**Figure 185.** Graph. Prediction of the FHWA II data using the Hirsch model in arithmetic scale.



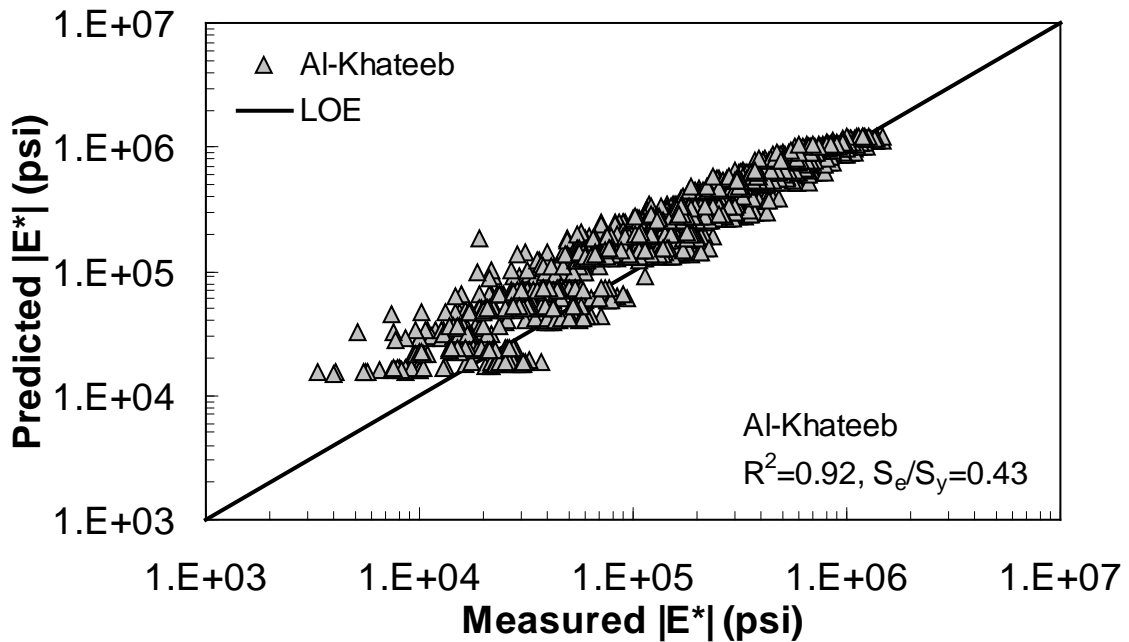
1 psi = 6.86 kPa

**Figure 186.** Graph. Prediction of the FHWA II data using the Hirsch model in logarithmic scale.



1 psi = 6.86 kPa

**Figure 187. Graph. Prediction of the FHWA II data using the Al-Khateeb model in arithmetic scale.**



1 psi = 6.86 kPa

**Figure 188. Graph. Prediction of the FHWA II data using the Al-Khateeb model in logarithmic scale.**

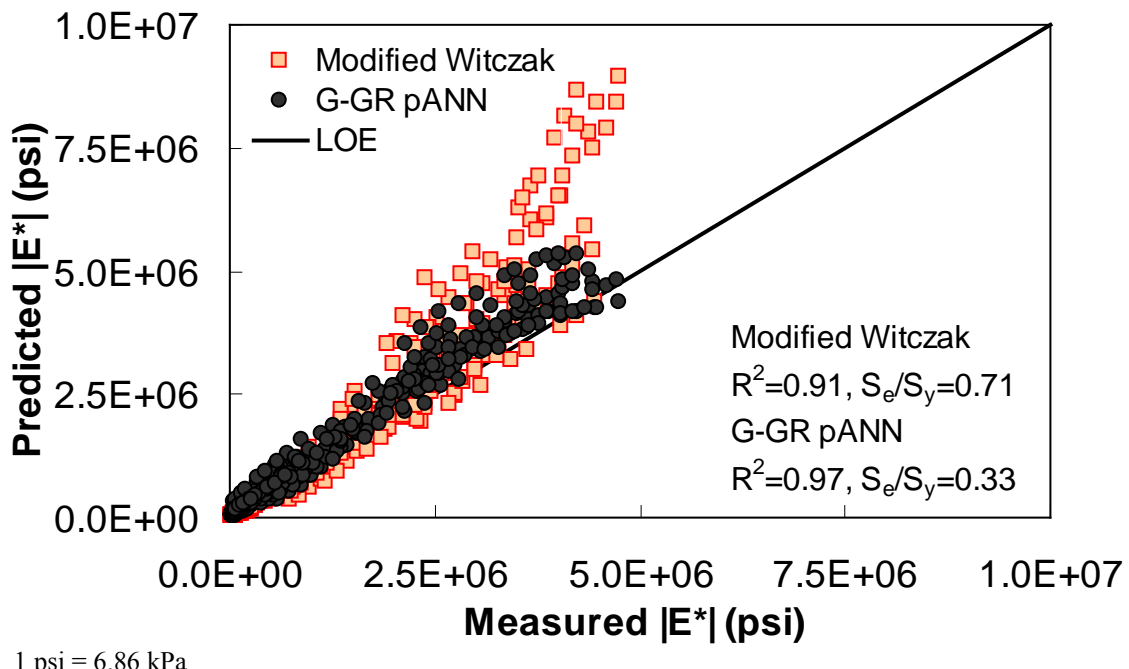


**Figure 189. Graph. Prediction of the NCDOT II data using the modified Witczak and G-GR pANN models in arithmetic scale.**

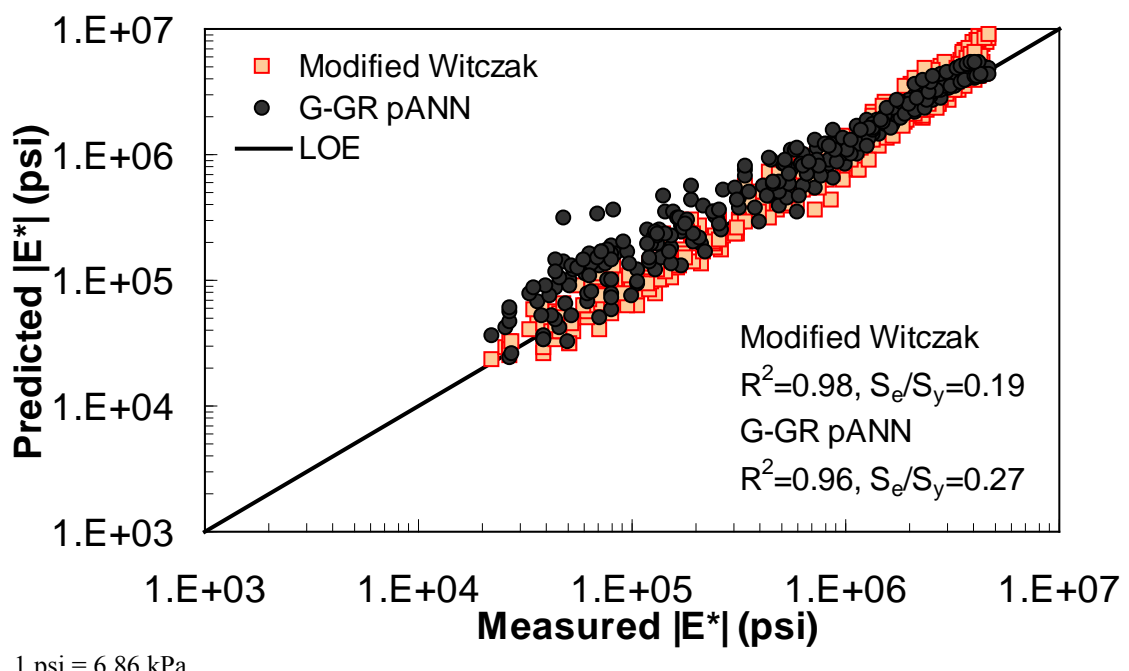


**Figure 190. Graph. Prediction of the NCDOT II data using the modified Witczak and G-GR pANN models in logarithmic scale.**

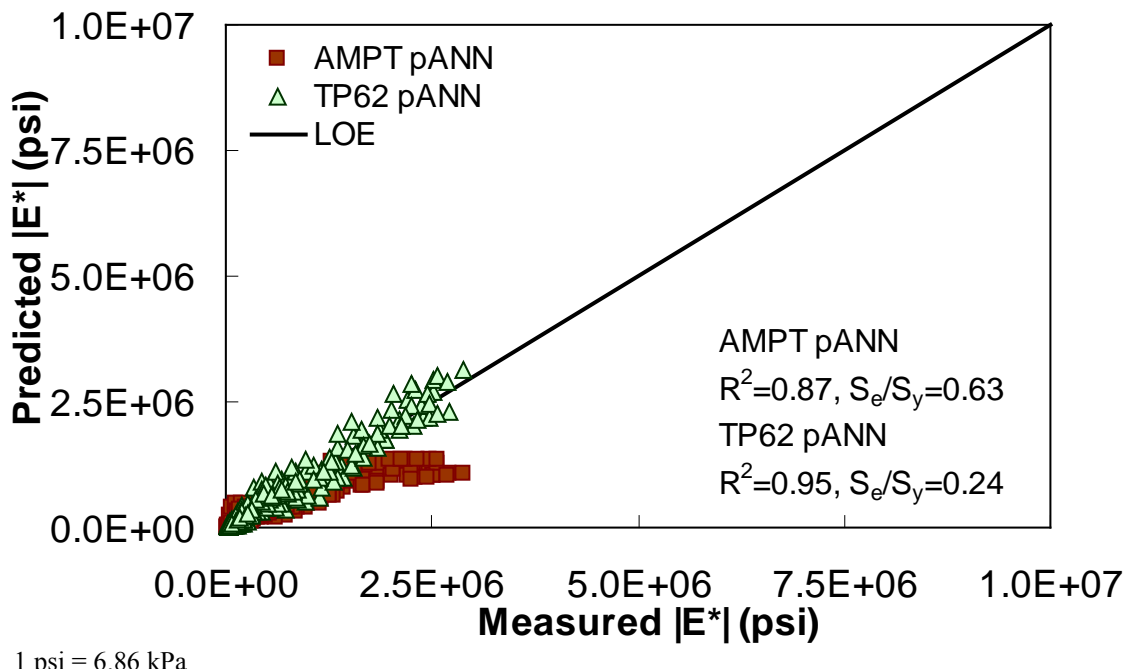


**Figure 191.** Graph. Prediction of the NCDOT II data using the AMPT pANN and TP-62 pANN models in arithmetic scale.

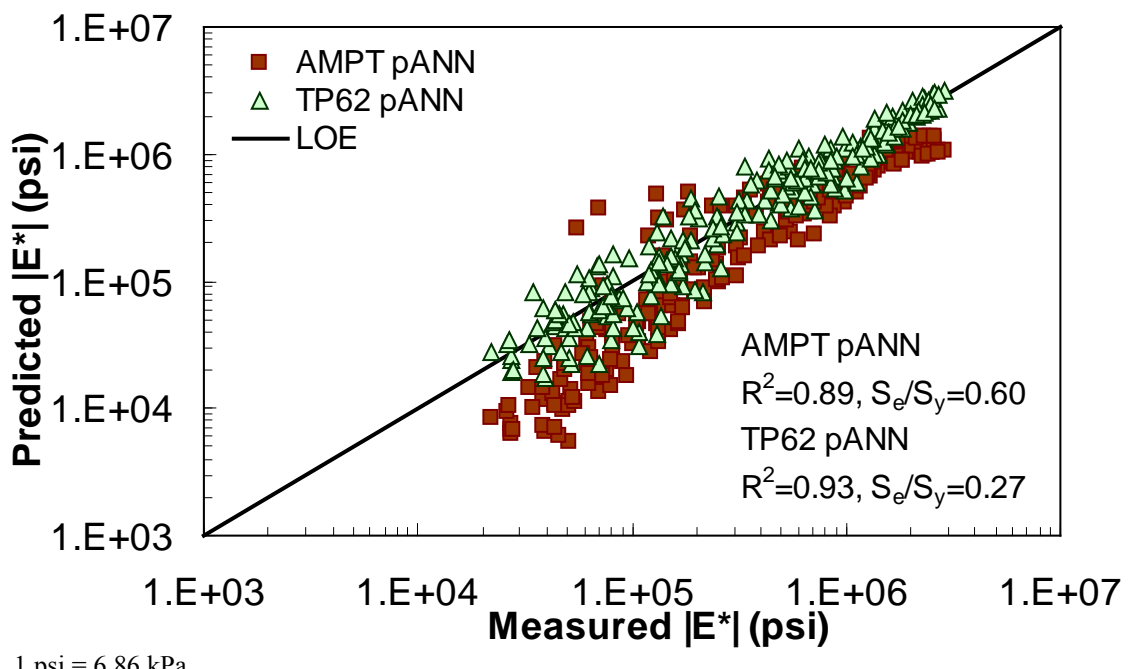
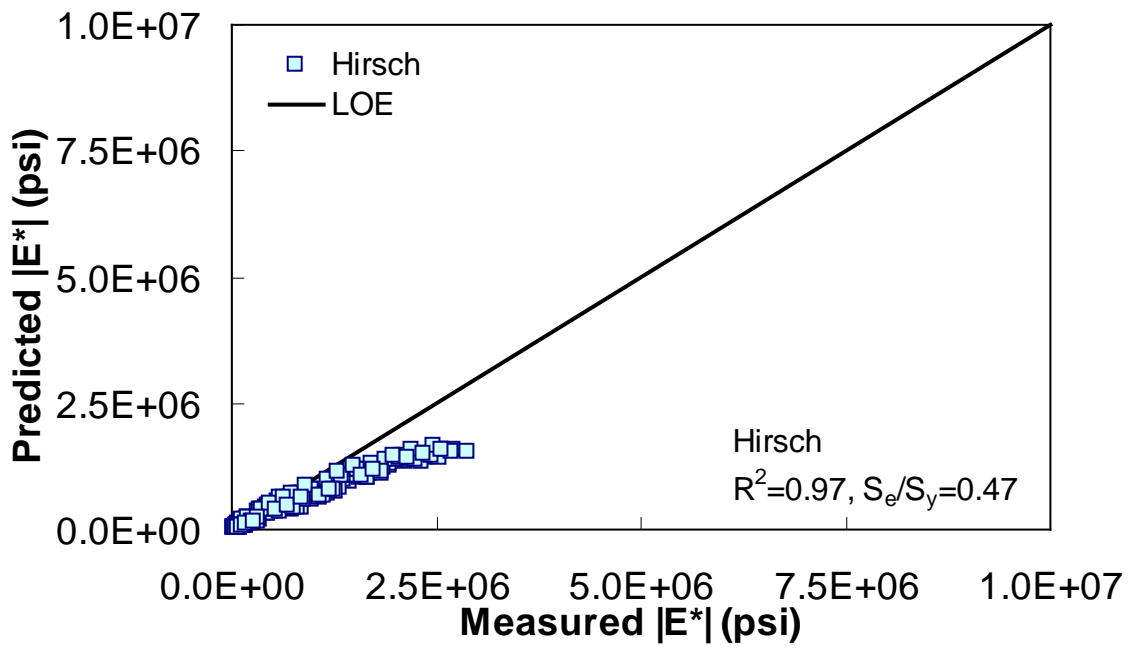
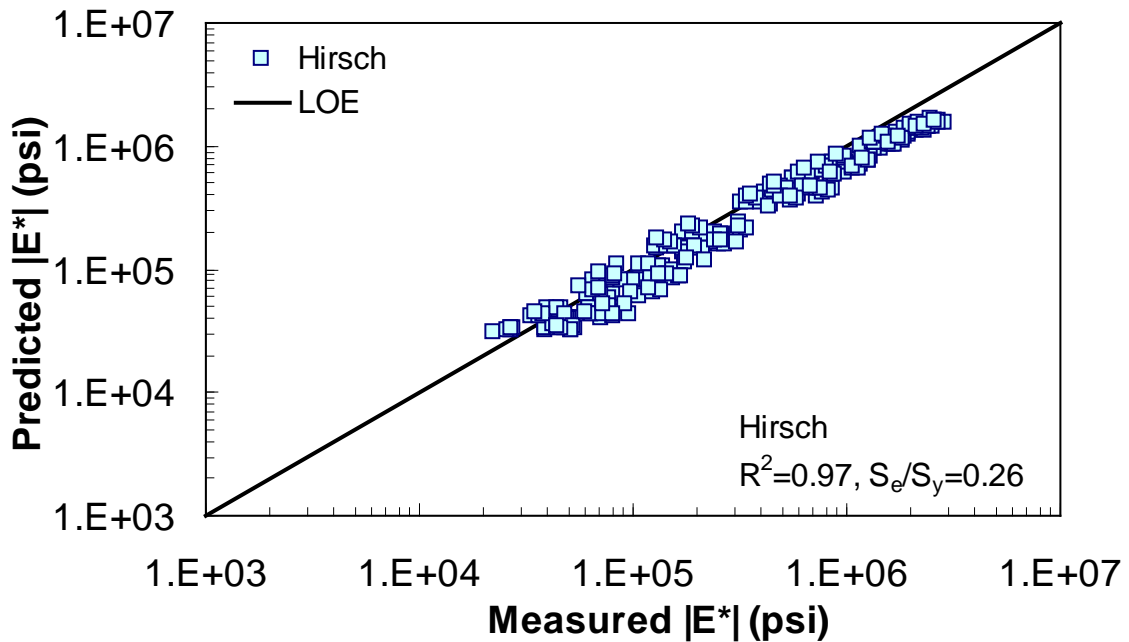


**Figure 192.** Graph. Prediction of the NCDOT II data using the AMPT pANN and TP-62 pANN models in logarithmic scale.



1 psi = 6.86 kPa

**Figure 193. Graph. Prediction of the NCDOT II data using the Hirsch model in arithmetic scale.**



1 psi = 6.86 kPa

**Figure 194. Graph. Prediction of the NCDOT II data using the Hirsch model in logarithmic scale.**

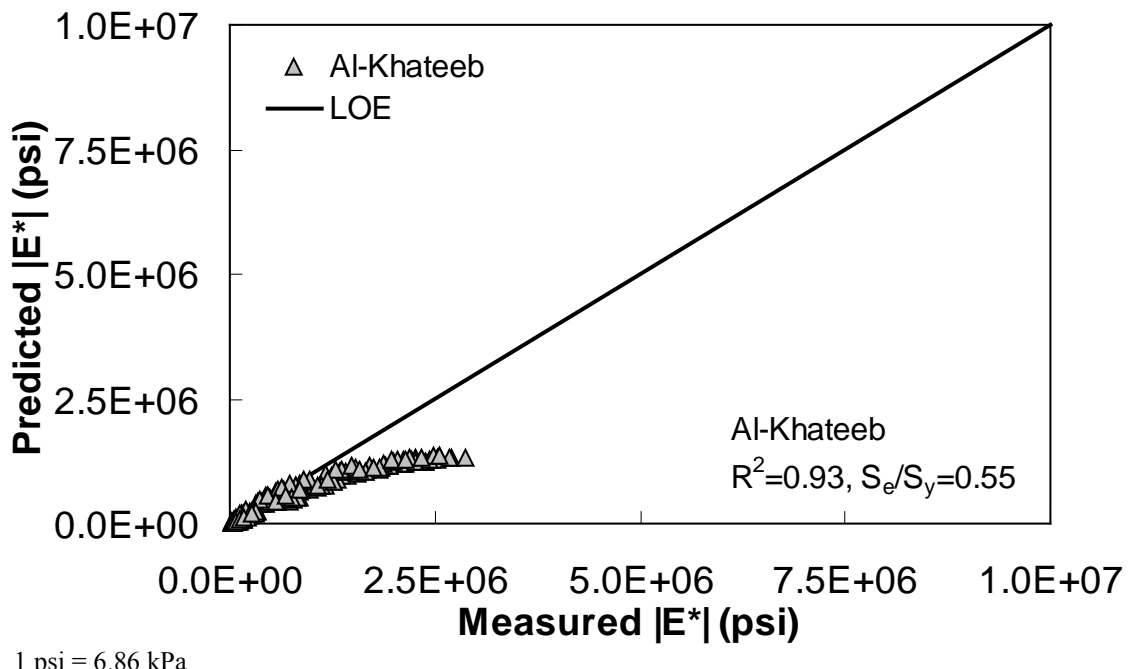


**Figure 195.** Graph. Prediction of the NCDOT II data using the Al-Khateeb model in arithmetic scale.

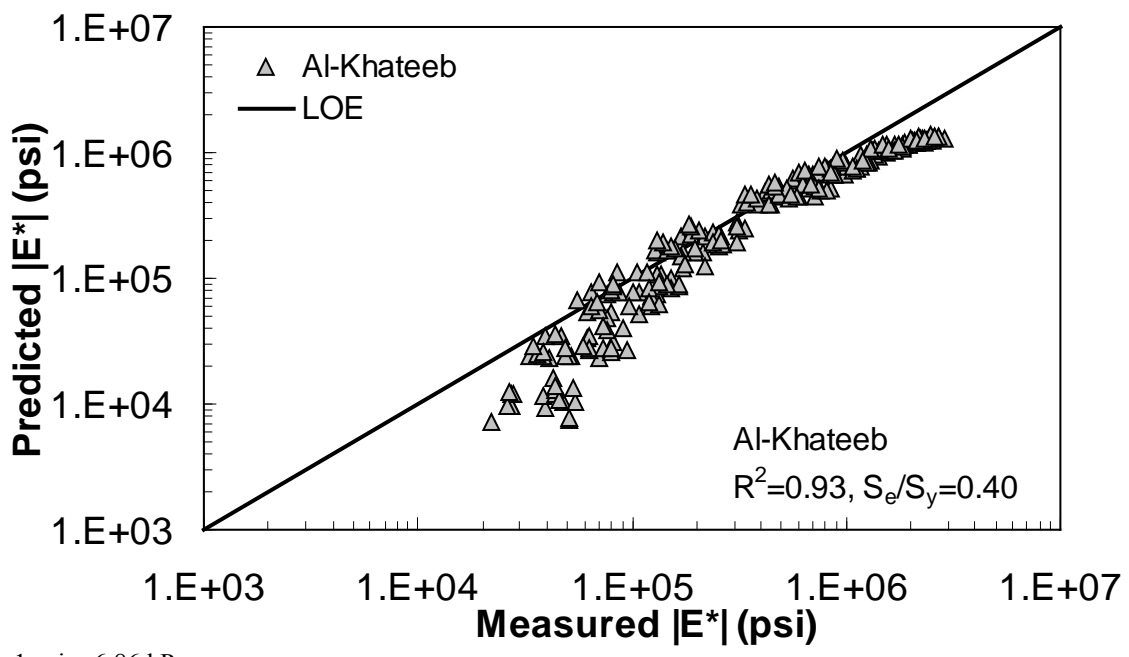


**Figure 196.** Graph. Prediction of the NCDOT II data using the Al-Khateeb model in logarithmic scale.

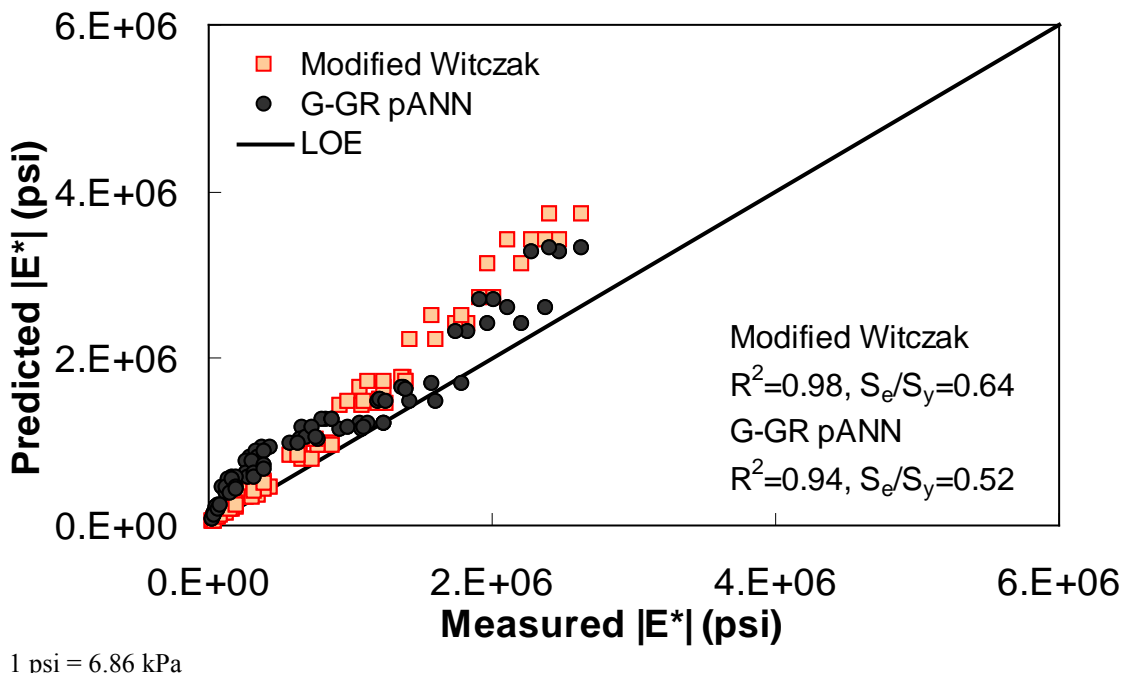


**Figure 197. Graph. Prediction of the Citgo data using the modified Witczak and G-GR pANN models in arithmetic scale.**

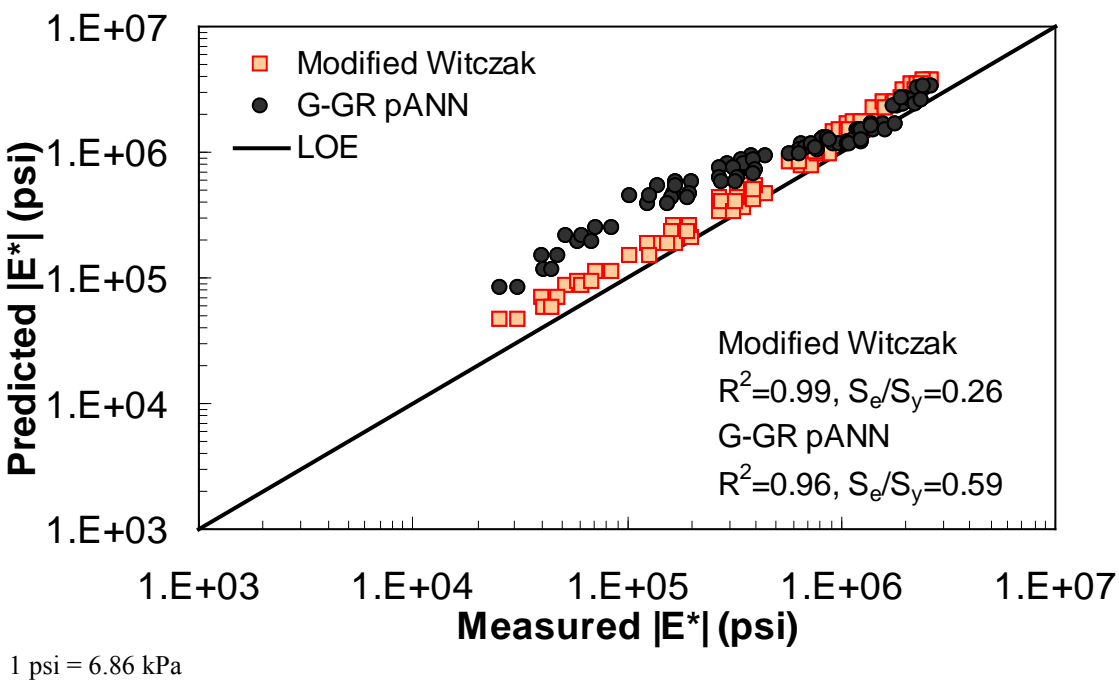


**Figure 198. Graph. Prediction of the Citgo data using the modified Witczak and G-GR pANN models in logarithmic scale.**

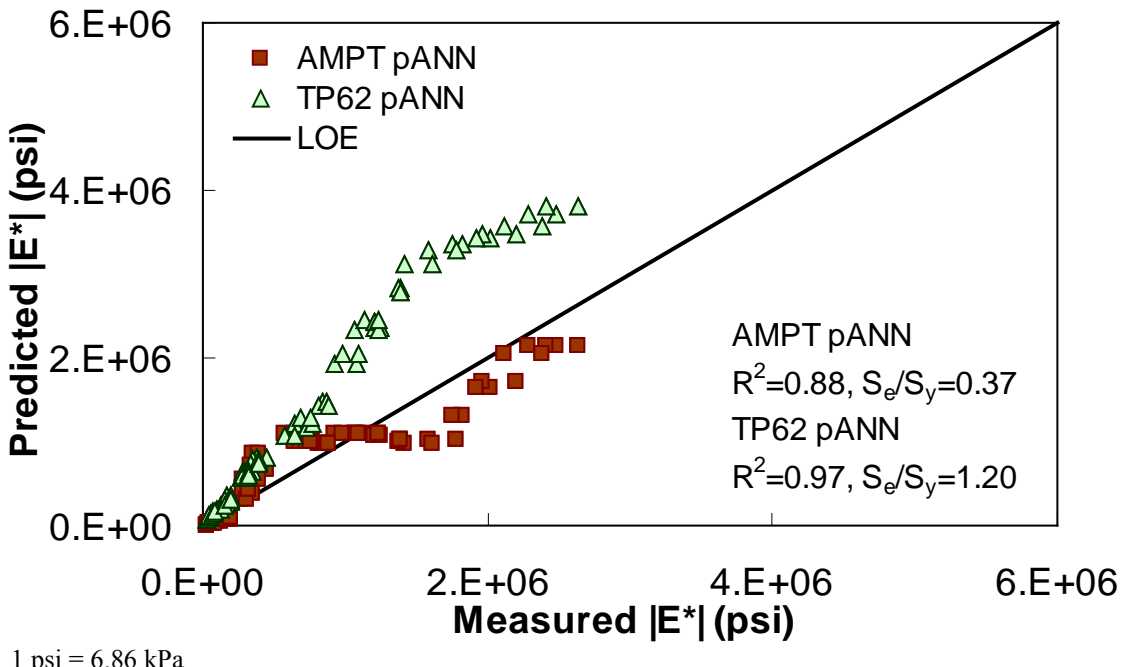


**Figure 199. Graph. Prediction of the Citgo data using the AMPT pANN and TP-62 pANN models in arithmetic scale.**

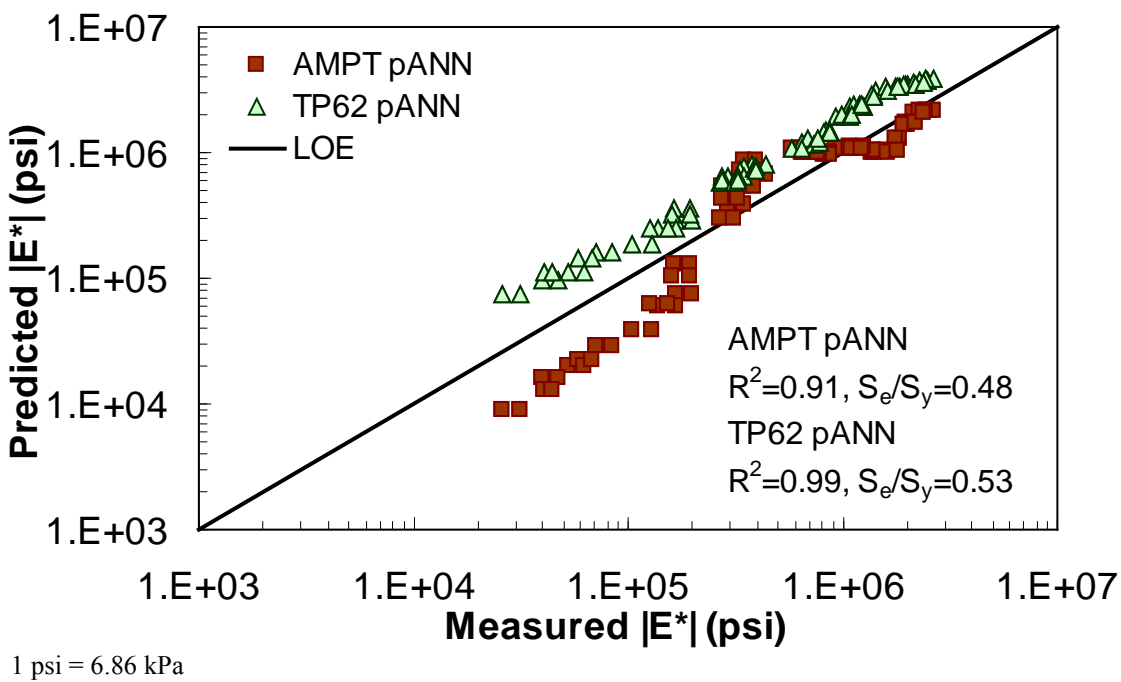


**Figure 200. Graph. Prediction of the Citgo data using the AMPT pANN and TP-62 pANN models in logarithmic scale.**

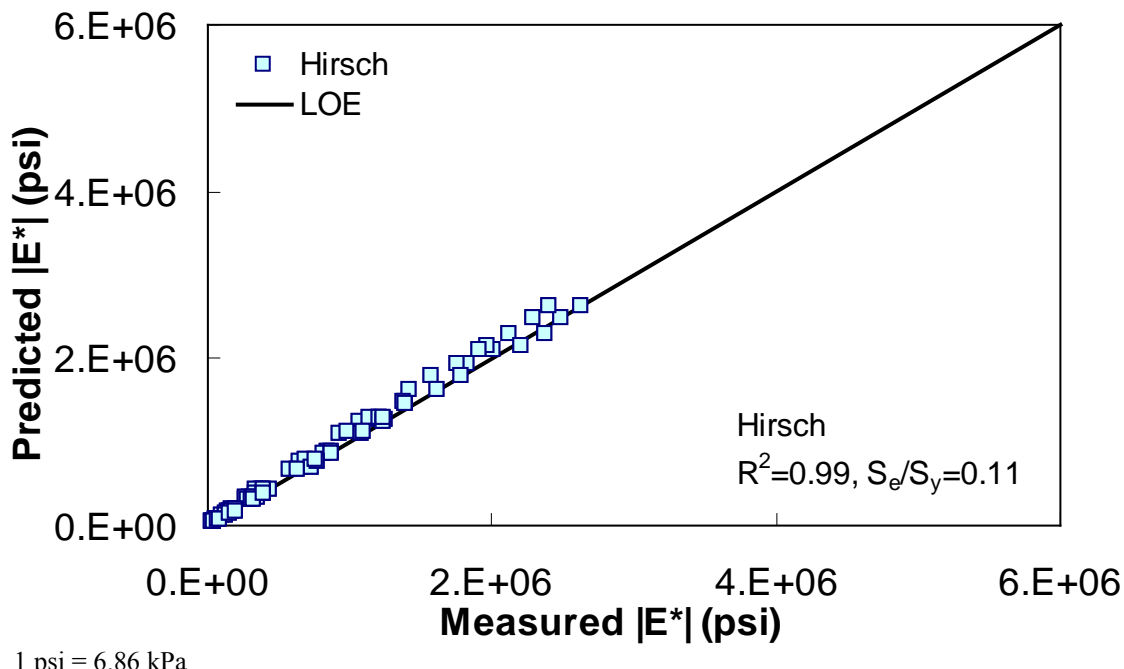


**Figure 201. Graph. Prediction of the Citgo data using the Hirsch model in arithmetic scale.**

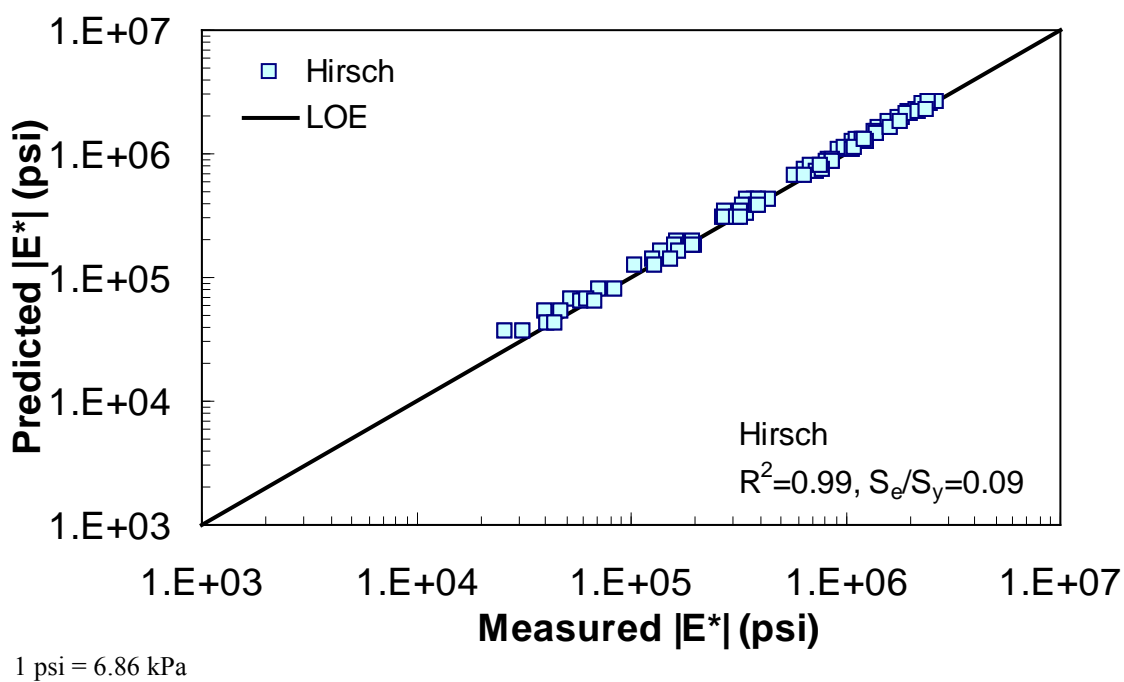
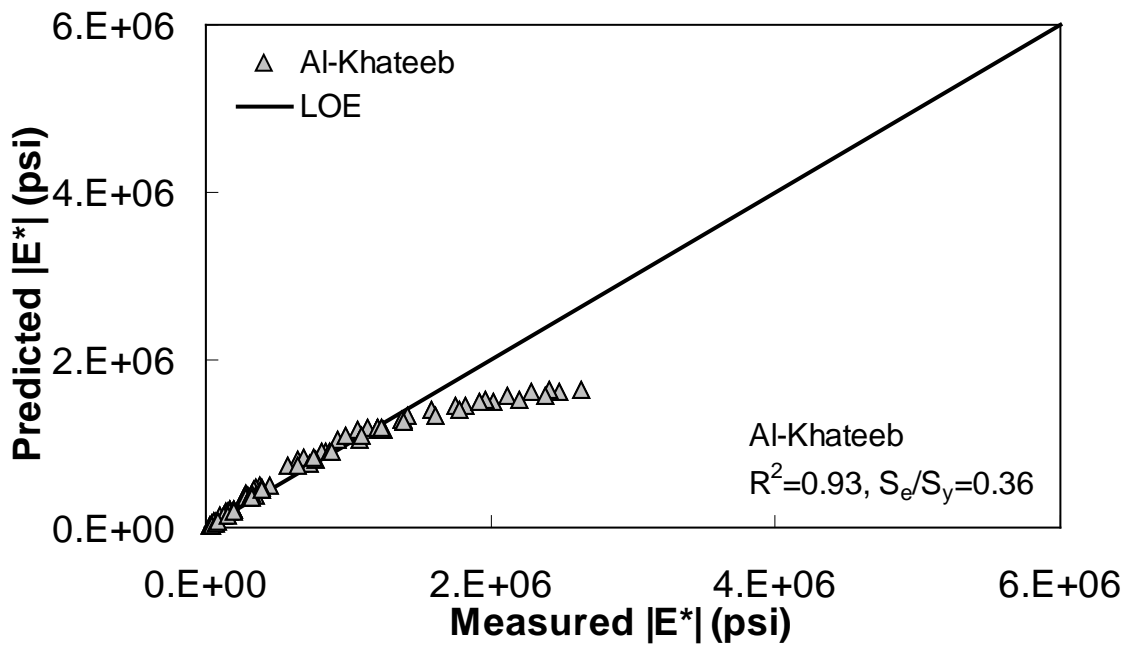
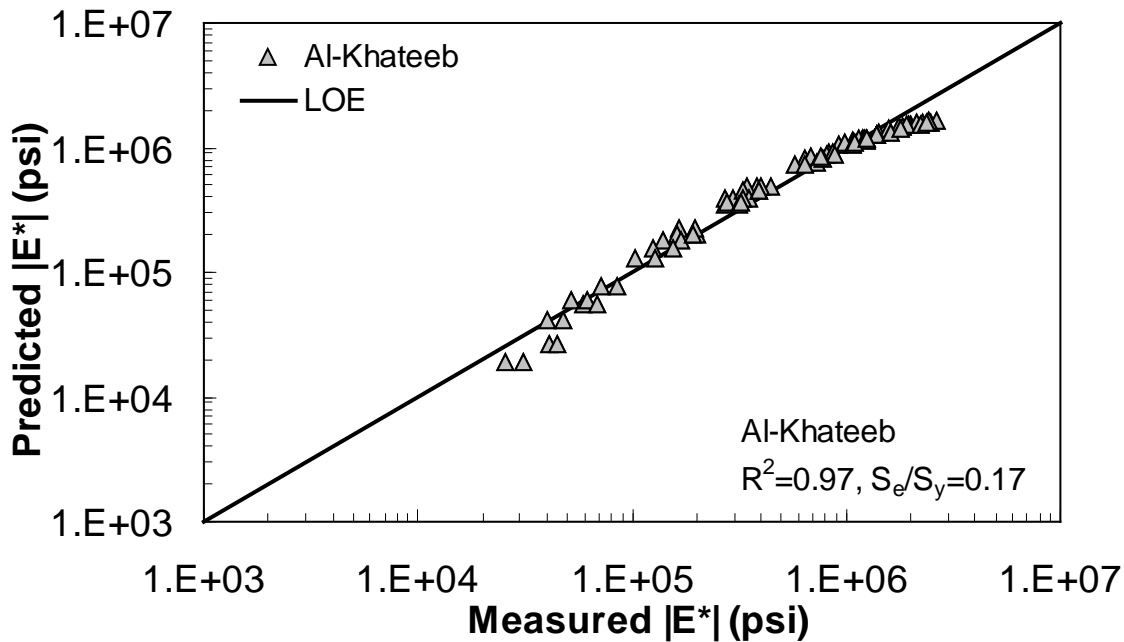


**Figure 202. Graph. Prediction of the Citgo data using the Hirsch model in logarithmic scale.**



1 psi = 6.86 kPa

**Figure 203. Graph. Prediction of the Citgo data using the Al-Khateeb model in arithmetic scale.**



1 psi = 6.86 kPa

**Figure 204. Graph. Prediction of the Citgo data using the Al-Khateeb model in logarithmic scale.**



## APPENDIX D: ANN MODEL FACTORS

### D.1 INTRODUCTION

The ANN model developed herein contains a mapping ANN architecture and is based on supervised learning. In the developed network, the learning method used is a feed forward back propagation, which is one of the best known types of ANN models. The sigmoidal function, which is shown in equation 101, was chosen as the transfer function. After an indepth investigation of network configurations, it was found that the three-layer network with equal nodes in the first two layers is the most appropriate configuration. All three ANN models share some basic functions, which are shown in equations 101–105. Equations specific to the  $M_R$  ANN are equations 106–108, and equations specific to the GV ANN and VV ANN models are equations 109–111. For equations 101–111, it should be understood that when a single index is used, it indicates an array. When dual indices are used, they represent a matrix with the first letter indicating the values in the row and the second letter indicating the values in the column. Index  $i$  represents the number of input parameters, index  $k$  represents the number of nodes in the first hidden layer, and index  $j$  represents the number of nodes in the second hidden layer. For the  $M_R$  ANN,  $l$  represents the number of output values. All inputs are scaled to have a value between -1 and 1. The normalization equation is shown in equation 112. Also, note that the  $M_R$  model produces coefficients for the sigmoidal function and is provided in equation 113. The units of the prediction are in megapascals as compared to pounds per square inch, which has been used elsewhere in this report.

$$f(T) = \frac{2}{1 + e^{-2T}} - 1 \quad (101)$$

$$H_k^1 = B_k^1 + \sum_{i=1}^m W_{ik}^1 \hat{P}_i \quad (102)$$

$$\hat{H}_k^1 = f(H_k^1) \quad (103)$$

$$H_j^2 = B_j^2 + \sum_{k=1}^n \hat{H}_k^1 W_{kj}^2 \quad (104)$$

$$\hat{H}_j^2 = f(H_j^2) \quad (105)$$

$$H_l^3 = B_l^0 + \sum_{j=1}^n \hat{H}_j^2 W_{jl}^3 \quad (106)$$

$$\hat{H}_l^3 = f(H_l^3) \quad (107)$$

$$Sig_l = (\hat{H}_l^3 + 1) \frac{((Sig_l)_{\max} - (Sig_l)_{\min})}{2} + (Sig_l)_{\min} \quad (108)$$

$$H^3 = B^0 + \sum_{j=1}^n \hat{H}_j^2 W_j^3 \quad (109)$$

$$\hat{H}^3 = f(H^3) \quad (110)$$

$$\log |E^*| = (\hat{H}^3 + 1) \frac{(\log |E^*|_{\max} - \log |E^*|_{\min})}{2} + \log |E^*|_{\min} \quad (111)$$

Where:

- $T$  = The placeholder variable.
- $f(T)$  = The transfer function.
- $H_k^1$  = The value of the nodes at the first hidden layer.
- $\hat{H}_k^1$  = The transferred value of the nodes at the first hidden layer.
- $H_j^2$  = The value of the nodes at the second hidden layer.
- $\hat{H}_j^2$  = The transferred value of the nodes at the second hidden layer.
- $H_l^3$  = The value of output node  $l$  ( $M_R$  ANN).
- $H^3$  = The value of the output node (GV ANN and VV ANN).
- $\hat{H}_l^3$  = The transferred value of the output node  $l$ , normalized output ( $M_R$  ANN).
- $\hat{H}^3$  = The transferred value of the output node, normalized output (GV ANN and VV ANN).
- $P_i$  = The input variables.
- $W_{ik}^1$  = The weight factors for the first hidden layer.
- $W_{kj}^2$  = The weight factors for the second hidden layer.
- $B_k^1$  = The bias factors for the first layer.
- $B_j^2$  = The bias factors for the second layer.
- $B_l^0$  = The bias factors for the outer layer ( $M_R$  ANN).
- $B^0$  = The bias factor for the outer layer (GV ANN and VV ANN).
- $(Sig_l)_{\max}$  = Maximum value for sigmoidal coefficient  $l$  in the trained data ( $M_R$  ANN).
- $(Sig_l)_{\min}$  = Minimum value for sigmoidal coefficient  $l$  in the trained data ( $M_R$  ANN).
- $\log |E^*|_{\max}$  = Maximum  $\log |E^*|$  of the trained data (GV ANN and VV ANN).
- $\log |E^*|_{\min}$  = Minimum  $\log |E^*|$  of the trained data (GV ANN and VV ANN).
- $m$  = The number of nodes in the first hidden layer (see table 21).
- $n$  = The number of nodes in the second hidden layer (see table 21).

$$\hat{P}_i = \frac{2(P_i - MIN_i)}{(MAX_i - MIN_i)} - 1 \quad (112)$$

Where:

- $P_i$  = Given input variable,  $i$ .
- $\hat{P}_i$  = Normalized value for given input variable,  $i$ .
- $MIN_i$  = Minimum value of  $i$  in calibration dataset.
- $MAX_i$  = Maximum value of  $i$  in the calibration dataset.

$$\log|E^*| = Sig_1 + \frac{Sig_2}{1 + \frac{1}{e^{Sig_3 + Sig_4 * \log(f_R)}}} \quad (113)$$

Where:

- $f_R$  = Reduced frequency (hertz).
- $Sig_1$  = First sigmoidal function coefficient.
- $Sig_2$  = Second sigmoidal function coefficient.
- $Sig_3$  = Third sigmoidal function coefficient.
- $Sig_4$  = Fourth sigmoidal function coefficient.

Three ANN models have been developed from this architecture: (1)  $M_R$  ANN, (2) VV ANN, and (3)  $|G^*|$  ANN. In the following sections, the value of the weight factors, bias factors, input parameters, and normalization parameters are given for each of these models.

## D.2 $M_R$ ANN

$$P_i = [M_R^5 \quad M_R^{25} \quad M_R^{40} \quad \alpha_1 \quad \alpha_2 \quad \alpha_3] \quad (114)$$

Where:

- $M_R^5$  = Resilient modulus at 41 °F (5 °C) (megapascals).
- $M_R^{25}$  = Resilient modulus at 77 °F (25 °C) (megapascals).
- $M_R^{40}$  = Resilient modulus at 104 °F (40 °C) (megapascals).
- $\alpha_1$  = Shift factor coefficient 1 (0.0007).
- $\alpha_2$  = Shift factor coefficient 2 (-0.1646).
- $\alpha_3$  = Shift factor coefficient 3 (0.806).

**Table 50.**  $W_{ik}^{-1}$  matrix elements for  $M_R$  ANN (part 1).

Element <i>k</i>	Element <i>i</i>		
	1	2	3
1	-0.00200156589300513	0.00128692125170315	0.00284438217881075
2	0.28516256606761700	0.49118675435971600	-0.01820933290109810
3	-0.13012155717600300	0.07853842949381770	0.17680064334424700
4	-0.29231959611729100	0.17617282979184900	0.39775504273252700
5	-1.41445013310154000	6.44297995264973000	-1.77482643703439000
6	-0.21241167223734400	0.12821712282974400	0.28884600944520300
7	0.03400370099657090	-0.02101635307328680	-0.04672053052579720
8	0.09548185985586570	-0.05752189953709870	-0.13026426280596500
9	0.32507208708348800	-0.19505459789439700	-0.44164369167303300
10	0.28899439562768500	1.14183643175563000	1.48347522466600000
11	-0.98864001747551200	-2.86851244653187000	-3.23450809016547000
12	1.62092571912098000	-4.58381702398853000	2.21293392742914000

**Table 51.**  $W_{ik}^{-1}$  matrix elements for  $M_R$  ANN (part 2).

Element <i>k</i>	Element <i>i</i>		
	4	5	6
1	-712.8628402976380000	9.83219882009042000	-1.94319401017490000
2	753.53741515309100000	7.67671366971338000	-0.84350062295273200
3	-1093.068754047720000	9.23892947309088000	0.14382032104724800
4	-1129.557247424060000	-1.50590848559491000	-0.66955349262730300
5	-1.83158558608035000	3.97456523446851000	7.12208818273337000
6	-839.5292060420890000	8.73889517406220000	0.67603083268390200
7	755.74883976821200000	-12.71270279414850000	-1.34117207352107000
8	847.61568238744000000	-12.59290188069720000	-0.47503813284310300
9	410.33781806362100000	-7.80175950866107000	-2.36148957427579000
10	-805.5026910683050000	-4.21610143211805000	4.07885029040178000
11	471.04240973832900000	13.45559381618210000	-3.61642908665572000
12	28.37591023338010000	12.28550446563640000	0.70805040715617700

**Table 52.**  $B_k^1$  vector elements for  $M_R$  ANN (transposed for convenience).

Element $k$	$B^1$
1	6.17091399170251000
2	7.71811183199239000
3	5.04220257285617000
4	1.36211474573909000
5	1.27586815658043000
6	1.24112853958781000
7	-0.55920953360997600
8	-1.54793233282465000
9	-2.38955526082692000
10	-5.31749985483251000
11	6.04452696422904000
12	2.43088472177158000

**Table 53.**  $W_{kj}^2$  matrix elements for  $M_R$  ANN (part 1).

Element $j$	Element k			
	1	2	3	4
1	-1.27212265453448000	0.98941325757367200	-1.90058367559899000	-1.69308092227318000
2	2.24917988742036000	-1.47046066978322000	2.81430927085362000	2.35680695833274000
3	0.90938132410845800	-1.87010703846175000	1.72113608938929000	0.53365095186003000
4	0.71420875730581000	-2.02463155580309000	1.24092642037176000	-0.75971225627055200
5	1.02573805084948000	-5.05227027803185000	-0.50811201125450400	0.12398342947210100
6	2.87344198982080000	1.1825109019882500	1.83686226283920000	1.07343492432610000
7	-6.84673965801500000	8.75898275822440000	-6.07092164029969000	-5.61770119661654000
8	-0.27215636118304200	-0.71265020644285800	0.10337231975487200	-0.50732389147556800
9	-1.24280778319817000	-0.42688724228155600	-1.49197352443203000	-1.1916709449455000
10	-0.87186156614646800	-0.55253243107747700	0.01014336151285740	-1.38109064819317000
11	5.05262125180162000	-3.58899791830666000	5.32477118646701000	6.08771475391962000
12	1.94315627250074000	-11.72058718677100000	1.02780825311488000	-0.07727872946434780

**Table 54.**  $W_{kj}^2$  matrix elements for  $M_R$  ANN (part 2).

Element <i>j</i>	Element <i>k</i>			
	5	6	7	8
1	1.72171850082868000	-1.22361303255407000	0.26380146379060500	1.59052924999161000
2	-0.69983955029987400	2.15750218152474000	-2.72092291591448000	-2.56417332772541000
3	5.68303374707809000	-0.22567435819557400	-0.38683461689596400	-1.33743701004047000
4	-5.29792907293055000	-0.79868120409271800	0.56639895589096100	-0.15145370730044200
5	-6.9600412768491900	-0.25943738604012600	-0.07507398274261910	-0.60082153969042900
6	-6.90406457489009000	0.66048638607472900	-0.74734595052120800	-1.77757048725853000
7	14.28996210073420000	-4.93956480500064000	5.47678679301124000	5.04474379279507000
8	5.33401793234324000	-0.67814558115517500	1.35435682469839000	0.67517616517050400
9	6.13017525412482000	-0.25895030883091000	0.76688050726348400	0.59567627875874100
10	-4.52656667316437000	-0.61198000964802400	0.66990865283891800	1.79648574970781000
11	61.00473788943800000	5.94808205391293000	-6.49782178526526000	-5.63585227166289000
12	-0.74313876146962200	-0.49502882731012100	-0.04343884290084600	0.43382323116577400

**Table 55.**  $W_{kj}^2$  matrix elements for  $M_R$  ANN (part 3).

Element <i>j</i>	Element <i>k</i>			
	9	10	11	12
1	1.28982526693395000	-1.36139827942535000	0.81242090814931100	0.75421177520166000
2	-1.98856516178736000	2.88665638759158000	-2.22345527946482000	47.32908703710720000
3	-1.46019991113224000	0.83288304533622300	-0.18737329755176000	7.94189735755131000
4	-0.62488286109702500	0.99358597783727000	-1.80707863873754000	-1.51697406306899000
5	-0.53491093234660500	0.03718852912964090	0.50412006696695100	-2.27324267108375000
6	-1.75495744905123000	0.04848011387017500	0.65137190325020200	-19.45130367879080000
7	6.34621810767813000	-4.33945264323816000	8.48179242696090000	-55.79280738270100000
8	-0.02703184429355360	-1.38007437316169000	-2.03641139073515000	7.15173377918400000
9	0.18219945071653500	-0.43950447308134000	0.88864139595275200	17.00276947159220000
10	0.18331101506990700	-1.29082311881848000	0.17907218849290100	0.00442335303199802
11	-4.70890802094776000	5.58102070625218000	-4.42512396747533000	34.44356640107110000
12	-0.58348656053904200	11.76004227042600000	-18.62573141905100000	40.36522874277380000

**Table 56.**  $B_j^2$  vector elements for  $M_R$  ANN (transposed for convenience).

Element <i>j</i>	$B^2$
1	0.69029100571690900
2	24.78083328475230000
3	-14.21641765871200000
4	0.59454387354854500
5	0.83441149973420900
6	2.00770642875969000
7	-6.80461833224959000
8	-3.04506035154618000
9	-2.81699338543501000
10	-0.01908957707522740
11	-23.82659200096020000
12	-2.84950882850698000

**Table 57.**  $W_{jl}^3$  vector elements for  $M_R$  ANN (part 1).

Element <i>l</i>	Element <i>j</i>			
	1	2	3	4
1	1.55631817035049000	-6.71717964044816000	5.52866041884021000	-23.13533591138010000
2	-2.10815560445854000	5.53651802240772000	-4.20046449739353000	13.84767577640070000
3	10.42186407217690000	1.07658778061795000	-1.00952254919933000	1.35728376824998000
4	12.53270054290200000	-2.82666156182142000	0.36140292673336200	11.63883002692080000

**Table 58.**  $W_{jl}^3$  vector elements for  $M_R$  ANN (part 2).

Element <i>l</i>	Element <i>j</i>			
	5	6	7	8
1	7.89233240566186000	3.41508482981355000	0.23067944090008000	-6.35835335516061000
2	-4.35253958227055000	-4.33105623723765000	-0.23450370767118300	4.90555584894330000
3	-0.53624851772844700	4.26302489876063000	0.18477243720173400	0.95437352582270800
4	-5.27378018192719000	12.58074218873790000	0.30883922900382400	-0.81566323458280500

**Table 59.**  $W_{ji}^3$  vector elements for  $M_R$  ANN (part 3).

Element <i>l</i>	Element <i>j</i>			
	9	10	11	12
1	3.12448098517872000	7.76943031096589000	0.16915092735543200	17.81482352191000000
2	-4.10144987129725000	-8.41207948330685000	-0.13394241862122600	-14.80599826102690000
3	4.33224573662362000	-12.80943716195050000	0.05065733872668660	-2.21601216037733000
4	12.62825381229430000	2.74268434100584000	0.08908525498240080	8.18232817352028000

**Table 60. Normalization parameters for  $M_R$  ANN.**

Parameter	Maximum	Minimum
$M_R^5$ (MPa)	34053.0	4800.3
$M_R^{25}$ (MPa)	15411.0	1081
$M_R^{40}$ (MPa)	6863.7	378.9
$\alpha_1$ (1/ °C <sup>2</sup> )	0.002400	-0.000194
$\alpha_2$ (1/ °C)	-0.098	-0.300
$\alpha_3$	1.430	0.490
$Sig_1$ (MPa)	2.660	-0.043
$Sig_2$	4.700	1.500
$Sig_3$	4.100	0.650
$Sig_4$	0.850	0.260

$$B_i^0 = [12.88483251257 \quad -10.23705702365 \quad -1.957618903369 \quad 3.273305236416] \quad (115)$$

### D.3 VV ANN

$$P_i = [f \quad \eta \quad VMA \quad VFA] \quad (116)$$

Where:

- f = Frequency, Hz.  
 $\eta$  = Viscosity,  $10^9$  P ( $10^8$  Pas).

**Table 61.  $W_{ik}^{-1}$  matrix elements for VV ANN.**

Element <i>k</i>	Element <i>i</i>			
	1	2	3	4
1	0.00275807935276415	9.65414347487492000	2.03545176382323000	9.60483606710040000
2	0.00699289293419363	23.57848634613580000	-14.68700301452580000	-7.85111160151172000
3	-29.85518987292190000	-0.01748605711868700	-0.05226790767927880	0.10630299509262800
4	0.00272712204182532	0.22756591526942600	-0.44128805965281300	0.51123020782505100
5	0.00885326169582901	2.81905088512526000	-16.74274657827420000	-11.51343150553350000
6	-0.00604496464330366	-3.83323067510033000	-3.76213295881730000	-4.29370215749809000
7	0.00001271343965432	178.92786633284100000	-0.00411385898011919	0.00960133688419267
8	0.01990111297026090	-1.16149781971796000	3.28168963629711000	7.53282726564379000
9	0.01005974523187870	-0.39351960943073500	-2.51237935759967000	-4.29116433585095000
10	2.20552340599479000	-0.04056518032735070	0.20605359978971700	0.15739161949478100
11	-0.02404084443474640	-6.58972054945535000	-0.71981980149770700	1.52555084062215000
12	-0.00480809655510197	-0.27885745601162500	0.20260632406742000	-0.77108867937747000
13	0.0007847111967578	28.44415144259920000	-0.87571840373706600	1.95186725224564000
14	0.00771761131363787	5.33676984624904000	-11.97622550219350000	7.71358914882133000

**Table 62.**  $B_k^1$  vector elements for VV ANN (transposed for convenience).

Element $k$	$B^1$
1	15.74835436269630000
2	12.95405722517280000
3	-32.89896917533040000
4	-1.10052248959346000
5	-10.78091133520380000
6	-6.05302142493261000
7	179.14709718593800000
8	0.65710599534106200
9	0.97891317883012100
10	4.72223785338294000
11	-6.55165918673815000
12	0.16731428319782600
13	27.93047751952220000
14	-1.37408939580495000

**Table 63.**  $W_{kj}^2$  matrix elements for VV ANN (part 1).

Element $j$	Element $k$			
	1	2	3	4
1	0.10511744512798600	0.10087889704665500	-6.08319321387257000	-6.59951922338895000
2	0.48485201906871100	-0.98061150567901500	5.28213726518926000	-0.99307488071221600
3	0.38666686767509600	0.14407696249404200	-0.64821237624430900	-0.68553604874521800
4	-0.29103025921087400	-0.12300943951262000	0.20660407620275500	0.84431006573009900
5	7.20145641626984000	151.58382852395500000	-35.04225274891410000	50.31324421340920000
6	57.80869276380200000	45.53819717827600000	34.31952056143690000	24.37102641478090000
7	0.04766296493976920	-0.00042062272941119	-1.64780015541921000	-0.14767680975504800
8	1.33157778260189000	-0.00864139577441407	-10.53694387134640000	-28.77316964591470000
9	0.95432357054777500	-1.02389021831262000	46.82499405300610000	61.27640626961720000
10	0.09476608746471290	-0.04013797559617900	15.08416115539120000	1.26248388850460000
11	0.65673641456535000	25.30163159128400000	6.86855242012598000	52.55865424871390000
12	-57.90977231272230000	57.64668837199080000	-36.95301005956680000	-51.19423424496710000
13	2.27010107107278000	-2.76393198240337000	14.26953262603660000	20.57219630346000000
14	-0.81442427169913900	-1.58075985235425000	20.32130385637230000	-21.37864285760230000

**Table 64.**  $W_{kj}^2$  matrix elements for VV ANN (part 2).

Element <i>j</i>	Element <i>k</i>			
	5	6	7	8
1	0.10958125840908900	0.17103742786951300	7.53738934561000000	0.32157150848996400
2	1.10538840213556000	-0.06005243494707140	-0.46816179656466200	-0.11362528740921000
3	-0.03668587237246070	-0.20195215673052800	0.50583875586658800	0.04117830356601680
4	0.04165310223654260	0.12412276818401500	-0.71560911337291800	-0.06643717805416860
5	-135.8256006242760000	4.39896372970834000	2.12048232621756000	1.61468697764029000
6	12.18509505034930000	4.51309256843370000	7.19546156774681000	11.77248078904480000
7	0.00470501377909039	-0.00810109614328989	-0.20468271977533900	-0.00831305598572143
8	0.14429797312686300	0.32443645525838900	-18.31175213933740000	-0.17988695146765000
9	0.48668670982841300	-1.06169701219564000	-0.47416257725070700	2.01336853261287000
10	0.02124957257916830	-0.01491154156235320	214.20333131224300000	0.05344273444888970
11	-16.55295761437330000	31.36367340855210000	0.14069168225602600	20.67506639536700000
12	105.32395565518000000	-68.59510275333000000	-0.57180295407110300	24.60816018017130000
13	3.20913352965092000	-1.46922615656989000	-0.45618908696155800	-0.74587534667358800
14	2.14653394183588000	2.86656902371875000	-1.38951291360800000	1.51498306935364000

**Table 65.**  $W_{kj}^2$  matrix elements for VV ANN (part 3).

Element <i>j</i>	Element <i>k</i>			
	9	10	11	12
1	0.67436953255572400	1.52993707048353000	-1.56378559364968000	-5.97316328323617000
2	0.83884786099458000	0.72056843262828500	0.33823343591634200	0.32995739963357400
3	0.13129904885190400	0.03393257336078320	-0.33495422276929500	1.21059369021165000
4	-0.08374413143914640	-0.14011290475212000	0.40330307484415800	-0.92068329846481200
5	-4.74183346589286000	-7.18458646900432000	-8.20175738069755000	21.46322182793860000
6	-2.22050947171933000	-3.19929780229875000	43.60123067158340000	-38.15447962643450000
7	0.04970822735474000	0.38186826752702800	0.02975701201504030	-0.07187684022207080
8	18.96102127708150000	0.34577779423701500	0.10112166202643200	-4.34637124684574000
9	136.10585968855900000	3.75489444791017000	5.73368672918881000	35.37279289616110000
10	-0.36747370936357000	1.90705035404089000	-1.42366525777415000	6.11736464999887000
11	-20.86114381473210000	4.50957253702840000	0.73758107479932900	-3.21435115847231000
12	-19.00772620196210000	44.26713771722670000	38.62379852233980000	-1.87378784809568000
13	0.17584310006536200	3.18528344468959000	0.62107582578786300	8.04752096583409000
14	2.97468553092343000	-4.21086927843771000	2.73490619946452000	-3.67293829703328000

**Table 66.**  $W_{kj}^2$  matrix elements for VV ANN (part 4).

Element <i>j</i>	Element <i>k</i>	
	<b>13</b>	<b>14</b>
1	-1.12245731810529000	0.67867713986347200
2	0.41929338131065000	-1.37665914977400000
3	0.58160889599262400	0.36777315706927400
4	-0.51666057998473900	-0.35135512626691600
5	3.27948738968729000	1.94926465685885000
6	-45.89506402313440000	70.49683570639200000
7	0.01612131389179630	-0.01152122049407600
8	3.77564707007114000	-4.91896963383303000
9	3.89920658003942000	-49.40155143998830000
10	2.24644797717875000	-0.11299018277251500
11	-9.63227261518900000	-119.1073499783990000
12	-41.84530118313840000	-35.82982088240670000
13	0.56754251531620400	-3.01209559093347000
14	2.43256581696669000	-1.47837832821775000

**Table 67.**  $B_j^2$  vector elements for VV ANN (transposed for convenience).

Element <i>j</i>	<b><math>B^2</math></b>
1	-12.23193846569030000
2	0.61294509854138200
3	-2.26121589380006000
4	1.99708243932415000
5	22.07400990717020000
6	-31.86954422722210000
7	-2.41399982513437000
8	-55.27590960198670000
9	-106.0101552356340000
10	-30.89403826224180000
11	-76.24782342311330000
12	69.28157710468700000
13	20.21945409941280000
14	6.12083493792229000

**Table 68.**  $W_j^3$  vector elements for VV ANN.

Element <i>j</i>	$W^3$
1	1.15373219918479000
2	-6.43559921490721000
3	-27.68360314597900000
4	-29.84574981371640000
5	-0.19407309170597600
6	0.11995708036519800
7	37.96893504107600000
8	34.00719477253400000
9	0.43014683810727000
10	58.47886817741680000
11	11.94908594315590000
12	-0.07969689689272150
13	1.28313108040340000
14	0.53296310828566400

**Table 69.** Normalization parameters for VV ANN.

Parameter	Maximum	Minimum
Frequency (Hz)	25	0.01
Viscosity ( $10^9$ P)	$1.99 \times 10^{-6}$	27.00
VMA (percent)	34.64	9.51
VFA (percent)	95.07	32.82
$ E^* $ (psi)	6.77	3.52

$$B^0 = -3.484481025467 \quad (117)$$

#### D.4 $|G^*|$ -BASED ANN (GV ANN)

$$P_i = \begin{bmatrix} |G^*| & VMA & VFA \end{bmatrix} \quad (118)$$

**Table 70.**  $W_{ik}^{-1}$  matrix elements for GV ANN.

Element $k$	Element $i$		
	1	2	3
1	-0.00024607061578008	0.39573112252617300	0.03137522820868100
2	0.06369415599503260	1.20396485280366000	-0.41366999743116300
3	0.12560166488947000	12.23092512080170000	-15.40428508265840000
4	144.78479285235900000	0.03602175009356860	-0.01486430375847190
5	-0.88590000706402800	-6.64620868848810000	6.76784019433308000
6	-0.24480066614146600	-175.126570586870000	110.38396928012700000
7	0.35658487276453800	-1.13633711409192000	-2.69698652853612000
8	0.05160380299493010	0.96914775793747200	-0.45058047297787600
9	-0.11763211836169300	-2.07308576925671000	0.85862809150608600
10	-0.10260986412141000	-1.89647330970902000	0.63576557888985500
11	0.83832125440623900	5.01864835388400000	-7.07830843630593000
12	-22.27016740128570000	2.82680472067850000	-1.10402495920697000

**Table 71.**  $B_k^1$  vector elements for GV ANN (transposed for convenience).

Element $k$	$B^1$
1	-13.23020275429390000
2	-1.15912963101547000
3	4.49668100338684000
4	144.90818089626700000
5	0.92374996199841500
6	187.12386013330800000
7	-0.64852041864182200
8	0.79297555520979200
9	1.27505357580263000
10	1.56260322810567000
11	-1.80964836750601000
12	-24.23180989095970000

**Table 72.**  $W_{kj}^2$  matrix elements for GV ANN (part 1).

Element <i>j</i>	Element <i>k</i>			
	1	2	3	4
1	1.68662477353906000	0.81911931325403900	-0.03005180291517210	0.00569345005879186
2	-4.86360723468991000	105.69622449695400000	-2.47849339660309000	0.18455777935409300
3	91.15855920616590000	92.66954611901590000	-40.91260113059330000	-1.67503899696897000
4	106.61660556715000000	22.90152433894880000	229.56133863086000000	-0.21741320127254800
5	0.73120568649091500	-2.04683544732935000	0.02907899740128110	-0.00680956721358145
6	20.01334655907270000	-124.1136850495880000	-12.93483076443820000	0.16320420801843400
7	11.03261781901980000	-55.35942281688430000	-0.25840813426995300	2.36249059396197000
8	6.30522135450740000	-72.37646707852670000	-2.13173103347156000	23.41004001398310000
9	-34.10766755925970000	26.04890333595410000	0.13622620891216500	-534.4781944799400000
10	-18.68321667137760000	103.90356571837300000	-2.46159833726818000	0.18433171253622200
11	19.14302423015890000	3.59998964741180000	0.25399603119775500	-44.54673896061580000
12	-0.33713658604817700	12.87184727785630000	0.13134300289504600	6.54659549746008000

**Table 73.**  $W_{kj}^2$  matrix elements for GV ANN (part 2).

Element <i>j</i>	Element <i>k</i>			
	5	6	7	8
1	0.01859496903873790	7.79141326044631000	0.01459371336584290	-4.01406752777277000
2	30.71090633980400000	5.37671972945662000	3.18886351743859000	-2.85108340883822000
3	87.71359895456880000	-77.08967734352910000	22.84350940748950000	335.75204711704400000
4	68.74692689690920000	-45.87194063996940000	12.79313464511960000	-37.77625414085690000
5	-0.0094809359102436	-1.94014227142969000	-0.01256576806807960	4.16910051124176000
6	-37.35043967525970000	5.27365300784224000	1.31038988899583000	43.16167413535480000
7	91.10288269578740000	-29.48793850026970000	-0.04849305692638800	3.23868144074583000
8	3.53501265914675000	0.83322882269153700	1.62246929641914000	6.69105720723216000
9	-0.09814064912135180	-0.02099590067358970	-0.19796523923434900	17.65358100702660000
10	55.61599363732450000	-5.35164182127019000	3.15862176137102000	-2.82977620499617000
11	-0.30334853272738200	43.07269450273440000	-0.22059949976226000	1.05780537005262000
12	0.11377535318423100	0.11441693675638400	0.15289220845030100	-1.13970260089778000

**Table 74.**  $W_{kj}^2$  matrix elements for GV ANN (part 3).

Element <i>j</i>	Element <i>k</i>			
	<b>9</b>	<b>10</b>	<b>11</b>	<b>12</b>
1	3.47596025162077000	-3.82827454649034000	0.01169888530415500	0.12954405222771200
2	94.55869709663890000	-7.34809568152935000	10.41344790169180000	21.32866301200200000
3	205.23211172111800000	-34.98627953103440000	76.29312010940660000	-30.59094661558560000
4	64.60376447639590000	-21.68091976305070000	66.41011966659030000	-26.22110679142560000
5	0.08966925765449130	-0.90205636358616400	-0.00585495017589258	0.00011267457317091
6	12.38797404837280000	-96.26501641581090000	-37.17032464251540000	0.12957951502862800
7	-50.14112337006290000	-8.38137267965061000	40.93959435883270000	-0.32474898284932000
8	-55.82517744922910000	-57.75954730123160000	2.17269724264550000	-54.42459642341290000
9	-1.13861767294711000	6.61476050123734000	0.25450956423993600	-1.38236982388117000
10	93.41332136138760000	-9.48311646261710000	49.01504550800940000	20.79054924536240000
11	2.55740586147654000	2.61695086136455000	-0.09940520779407240	3.00291187179692000
12	4.67064477635346000	8.20560279728423000	0.10724854309492400	3.33502620583327000

**Table 75.**  $B_j^2$  vector elements for GV ANN (transposed for convenience).

Element <i>j</i>	<b><math>B^2</math></b>
1	-3.02263601315923000
2	5.97704828771739000
3	-91.56648216379910000
4	-106.5989770883490000
5	-0.36740268358330700
6	-20.04954785032860000
7	-10.42449435680280000
8	-5.32258083806398000
9	32.81032420706510000
10	17.56993360741350000
11	-20.65675932973890000
12	2.35956011260892000

**Table 76.**  $W_j^3$  vector elements for GV ANN.

<b>Element <i>j</i></b>	<b><math>W^3</math></b>
1	-134.7651195030360000
2	92.96416099463190000
3	0.07847134028534860
4	0.58725325729413100
5	-146.9138139427070000
6	-12.15444670634670000
7	34.34304769221520000
8	-63.09541362586340000
9	-76.62381419958460000
10	-93.21865080014820000
11	-29.95120632059920000
12	0.71757242259101300

**Table 77.** Normalization parameters for GV ANN.

<b>Parameter</b>	<b>Maximum</b>	<b>Minimum</b>
$ G^* $ (psi)	676,000	0.0293
VMA (percent)	22.21	9.51
VFA (percent)	95.07	32.82
$ E^* $ (psi)	6.81	3.52

$$B^0 = -8.469734576039 \quad (119)$$

## APPENDIX E: ANNACAP SOFTWARE MANUAL

### E.1 INTRODUCTION

The Artificial Neural Networks for Asphalt Concrete Dynamic Modulus Prediction (ANNACAP) program has been developed under Contract No. DTFH61-02-00139 Task Order #10 LTPP Computed Parameter Dynamic Modulus to aid in populating the LTPP database with dynamic modulus data. Technical details concerning the analysis used in this program can be found in the final report for the referenced project. The purpose of this document is to provide a manual of operation for the ANNACAP program.

The dynamic modulus,  $|E^*|$ , is a fundamental property that defines the stiffness characteristic of hot mix asphalt (HMA) mixtures as a function of loading rate and temperature. The significance of this material property is threefold. First, it is one of the primary material property inputs in the *Mechanistic-Empirical Pavement Design Guide* (MEPDG) and software developed by NCHRP Project 1-37A. The MEPDG uses mastercurves and time-temperature shift factors in its internal computations. The mastercurve is constructed using a hierarchical structure of inputs ranging from laboratory tests on HMA mixtures and binders to estimates based on properties of the HMA mixtures. Second, the  $|E^*|$  is one of the primary HMA properties measured in the Superpave<sup>TM</sup> simple performance test protocol that complements the volumetric mix design. Third,  $|E^*|$  is one of the fundamental linear viscoelastic (LVE) material properties that can be used in advanced HMA and pavement models that are based on viscoelasticity.

In spite of the demonstrated significance of  $|E^*|$ , it is not included in the current LTPP materials tables because the database structure was established long before  $|E^*|$  was identified as the main HMA property in the MEPDG. It is not practical to perform MEPDG level 1 laboratory  $|E^*|$  tests on material samples from LTPP test sections at this time due to a lack of materials, budget limitations, and the absence of a suitable test method applicable to field samples obtained from relatively thin pavement structures. However, the LTPP database does contain other data that can be used to estimate the  $|E^*|$  mastercurve and associated shift factors, estimate the  $|E^*|$  at specific load durations and temperatures, or develop inputs to the models contained in MEPDG.

### E.2 DISCLAIMER

This software is provided “as is,” and any express or implied warranties, including but not limited to the implied warranties of merchantability and fitness for a particular purpose, are disclaimed. In no event shall the authors be liable for any direct, indirect, incidental, special, exemplary, or consequential damages (including, but not limited to, procurement of substitute goods or services; loss of use, data, or profits; or business interruption) however caused and in any way theory of liability, whether in contract, strict liability, or tort (including negligence or otherwise) arising in any way out of the use of this software, even if advised of the possibility of such damage.

### E.3 INSTALLATION INSTRUCTIONS

1. Insert ANNACAP Installation CD into the CD ROM or download zipped installer file from Web site. *Note: If downloading the file, remember the location where you have unzipped the files.*
2. If the CD does not autorun, press the Windows **Start** button.
3. Click on **Run**.
4. Change the directory to the location of the installer file (either the CD ROM drive or the unzipped file locations).
5. Select the **Setup** program.
6. Press **OK**.
7. Follow the onscreen instructions.
8. ANNACAP and all necessary support files will be installed.
9. A shortcut will be placed in the start menu under the *Programs → ANNACAP* path. To place a shortcut onto the desktop, users must manually perform the operation.

### E.4 USING ANNACAP

#### E.4.1 Program Main Screen

The main ANNACAP screen is shown in figure 205. This screen appears when ANNACAP is launched. All analysis is menu-driven, and the menu schematic is shown in figure 206. To perform modulus predictions, users must provide the necessary inputs by following the *File → Input* path (described in detail below). Users must also provide a directory for output to be written by following the *File → Output Directory* path. Once both have been properly input, users may perform data analysis by following the *File → Run Analysis* path. Users may access this document by following the *Help → Manual* path or find basic program information by choosing the *Help → About* path.

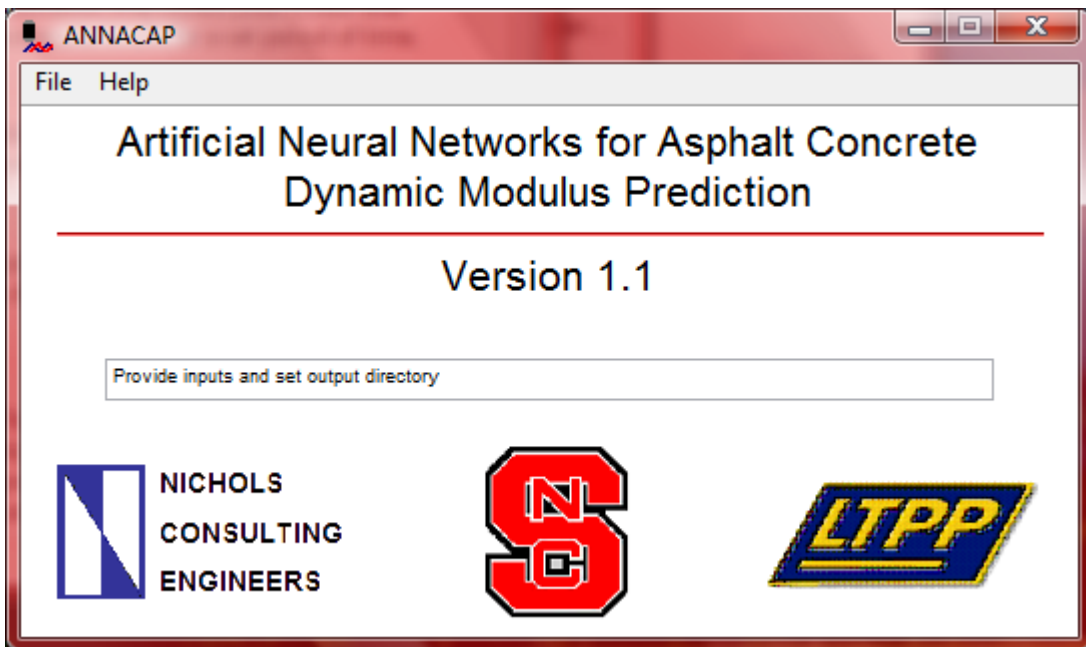


**Figure 205.** Screenshot. ANNACAP main screen.

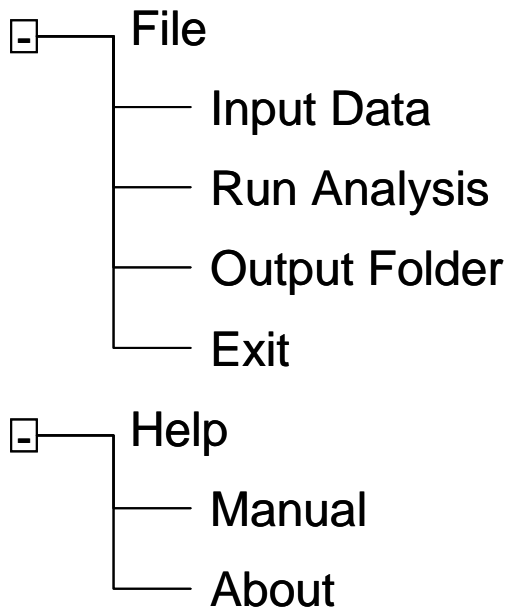


**Figure 206.** Illustration. ANNACAP menu diagram.

#### E.4.2 Input Data

Selecting the *File* → *Input* path will automatically launch the input utility. The initial screen shot is shown in figure 207. Users have four modes to choose from: (1)  $M_R$ -based ANN, (2)  $|G^*|$ -based ANN, (3) viscosity-based ANN, and (4) batch mode. The screen is divided into two regions referred to as the left side and right side and separated by bordered regions. On the left side are areas for inputting basic information for the nonbatch mode runs, choosing the mode to use, and choosing the input parameter complexity to use. On the right side are inputs specific to

the chosen analysis mode. Necessary inputs will appear on both the left and right sides of the screen as users make selections. After selecting all of the appropriate factors and entering all necessary inputs, pressing “Done” on the menu bar will return users to the main ANNACAP screen. Note that all modes will produce  $|E^*|$  predictions at 14, 40, 70, 100, and 130 °F (-10, 4.4, 21.1, 37.8, 54.4 °C) and 25, 10, 5, 1, 0.5, and 0.1 Hz.

The screenshot shows the 'Input' window titled 'Input Parameters'. On the left, under 'Layer ID', there are fields for State Code, Project ID, Project Layer, Construction Date (with a 'Choose' button), and Aging Level (set to 'Unaged'). Under 'Model', there is a dropdown menu set to 'Mr Based ANN'. On the right, there is a table titled 'Mr Measured on Mixture' with columns for Temperature (Degrees Celsius) and Resilient Modulus (GPa). The table contains three rows: 5 Degrees Celsius, 25 Degrees Celsius, and 40 Degrees Celsius.

Mr Measured on Mixture	Resilient Modulus (GPa)
5 Degrees Celsius	
25 Degrees Celsius	
40 Degrees Celsius	

**Figure 207. Screenshot. ANNACAP input screen.**

#### E.4.3 Layer ID

Under the Layer ID section, users should enter the following items:

- State code.
- Project ID.
- Project layer.
- Construction date.
- Aging level (only RTFO aging is available for certain models).
- Test date (only if “Other” aging level is chosen).

The naming convention for these items is the same as that followed in the LTPP database. Users may choose to enter the dates directly into the appropriate boxes and, if they do so, the format should be *Day-Abbreviated Month-Year* (i.e., 20-Mar-1985). Users wishing to use the calendar utility should press the **Choose** button beside the date box and navigate to the appropriate date. When the appropriate date is chosen, users must press the **OK** button.

#### E.4.4 $M_R$ -Based ANN

Selecting  $M_R$ -based ANN from the model drop-down menu will allow users to develop  $|E^*|$  predictions based on  $M_R$  inputs. On the right side of the screen, users must enter  $M_R$  values in gigapascals at three specific temperatures (41, 77, and 104 °F (5, 25, and 40 °C)) into the provided table. The appropriate input ranges for these values are as follows:

- 41° F (5 °C) = 4,938,970.10 to 696,224.65 psi (34.053 to 4.8003 GPa).
- 77 °F (25 °C) = 2,235,176.58 to 156,785.79 psi (15.411 to 1.0810 GPa).
- 104 °F (40 °C) = 995,495.52 to 54,954.80 psi (6.8637 to 0.3789 GPa).

Inputting values outside this range will cause ANNACAP to display a warning indicating that input values exceed the calibration range, but predictions will still be made. Users should also select the aging condition for the measured  $M_R$  values.

#### E.4.5 $|G^*|$ -Based ANN

Selecting  $|G^*|$ -based ANN from the model drop-down menu will allow users to develop  $|E^*|$  predictions based on  $|G^*|$  inputs. There are three different levels of input complexity: level 1, level 2, and level 3. For each level, users should input the percentage of voids in mineral aggregate (VMA) and percentage of voids filled with asphalt (VFA) in addition to  $|G^*|$  values. The appropriate ranges for these input variables are shown beside the input controls. For all input levels, ANNACAP will use the CAM model to generate a mastercurve of the data. Users may choose to force the CAM model to fit the data with a certain glassy modulus value by choosing **Input** from the **Find  $G_g$  by** drop-down menu. If **Input** is chosen, the default value is 145,037.74 psi (1 GPa), but users may change it to any desired value. If users choose **Fitting** from the **Find  $G_g$  by** drop-down menu, then the glassy modulus is treated as any other optimization parameter. If no data are available at extremely low temperatures (below 32 °F (0 °C)), users are recommended to choose **Input** and select a value between 145,037.74 and 1,450,377.38 psi (1 and 10 GPa). If for some reason a fitting error occurs with the provided input, the program will display a fitting error dialog and not allow users to predict  $|E^*|$ . If the calculated  $|G^*|$  is greater than 675,875.86 psi ( $4.66 \times 10^9$  Pa) or less than 0.029 psi (202 Pa), a warning dialog will appear, but  $|E^*|$  predictions will be performed.

##### E.4.5.1 Level 1

For level 1, users have access to complete  $|G^*|$  values at multiple temperatures and frequencies. These values should be entered directly into the table that appears on the right side of the screen. Users may choose to create this data file in another application and load it into the table by using

the **Load** button. The file should be a tab delimited text file with the same column format as the input table. The file should have column labels.

#### **E.4.5.2 Level 2**

For level 2, users have access to  $|G^*|$  values and possibly BBR stiffness values at multiple temperatures (at least two above 114.8 °F (46 °C) and two below 114.8 °F (46 °C)) but at the fixed frequency of 10 rad/s and load time of 60 s. All of the measured moduli values should be at a consistent aging level. The  $|G^*|$  values are entered in units of kilopascals, whereas the  $S(t)$  values are entered in units of megapascals following convention. The temperature is always entered in degrees Celsius. Users should enter the values into the tables on the right side of the screen.

#### **E.4.5.3 Level 3**

For level 3, users have access to  $|G^*|$  values and possibly BBR stiffness values at multiple temperatures (at least two above 114.8 °F (46 °C) and two below 114.8 °F (46 °C)) at a fixed frequency of 10 rad/s and load time of 60 s. The aging conditions are a mixture of RTFO and PAV. The units are the same as those used in level 2 input. In addition to entering these values, users should choose the high temperature Superpave<sup>TM</sup> PG for the binder from the **High Temp PG** drop-down menu. If this information is not known or cannot be determined, users may select **Unknown** from the drop-down menu. In Level 3 analysis, only the RTFO-aging conditions may be predicted.

### **E.4.6 Viscosity-Based ANN**

Selecting **Viscosity-based ANN** from the model drop-down menu will allow users to develop  $|E^*|$  predictions based on viscosity inputs. There are three different levels of input complexity: level 1, level 2, and level 3. For each level, users should input the VMA and VFA. The appropriate ranges for these input variables are shown beside the input controls. If the calculated viscosity is less than 199,000 cP (199 Pas), a warning dialog will appear, but  $|E^*|$  predictions will be performed.

#### **E.4.6.1 Level 1**

In level 1, users enter A and VTS values directly into the right side of the screen.

#### **E.4.6.2 Level 2**

In level 2, users choose the types of viscosity measures available by selecting or deselecting the radio buttons on the left side of the screen. The available measures include: R&BT temperature, penetration, absolute viscosity, and kinematic viscosity. Selecting or deselecting these measures will make appropriate input tables or controls appear on the right side of the screen. Following standard convention, the R&BT temperature is given in degrees Fahrenheit, the penetration is given by the PEN number, the absolute viscosity is input in poise, and the kinematic viscosity is input in centistokes. If users select kinematic viscosity, then they must also enter the binder-specific gravity in the  $G_b$  control. By default, ANNACAP inputs 1.03 for  $G_b$ . Users must input at least two measures of viscosity so that A and VTS can be computed.

#### **E.4.6.3 Level 3**

In level 3, users choose the binder grade. Typical values compiled during the NCHRP 1-37A project are available, and the binder grades can be either Superpave™ -based, viscosity-based (AC system only), or penetration-based. The binder grade-to-viscosity relationship is summarized in table 78.

**Table 78. Relationship between binder purchase specification grade and A and VTS parameters.**

Asphalt Binder Grade	A	VTS	Asphalt Binder Grade	A	VTS
PG 46-34	11.5040	-3.9010	PG 70-28	9.7150	-3.2170
PG 46-40	10.1010	-3.3930	PG 70-34	8.9650	-2.9480
PG 46-46	8.7550	-2.9050	PG 70-40	8.1290	-2.6480
PG 52-10	13.3860	-4.5700	PG 76-10	10.0590	-3.3310
PG 52-16	13.3050	-4.5410	PG 76-16	10.0150	-3.3150
PG 52-22	12.7550	-4.3420	PG 76-22	9.7150	-3.2080
PG 52-28	11.8400	-4.0120	PG 76-28	9.2000	-3.0240
PG 52-34	10.7070	-3.6020	PG 76-34	8.5320	-2.7850
PG 52-40	9.4960	-3.1640	PG 82-10	9.5140	-3.1280
PG 52-46	8.3100	-2.7360	PG 82-16	9.4750	-3.1140
PG 58-10	12.3160	-4.1720	PG 82-22	9.2090	-3.0190
PG 58-16	12.2480	-4.1470	PG 82-28	8.7500	-2.8560
PG 58-22	11.7870	-3.9810	PG 82-34	8.1510	-2.6420
PG 58-28	11.0100	-3.7010	AC-2.5	11.5167	-3.8900
PG 58-34	10.0350	-3.3500	AC-5	11.2614	-3.7914
PG 58-40	8.9760	-2.9680	AC-10	11.0134	-3.6954
PG 64-10	11.4320	-3.8420	AC-20	10.7709	-3.6017
PG 64-16	11.3750	-3.8220	AC-3	10.6316	-3.5480
PG 64-22	10.9800	-3.6800	AC-40	10.5338	-3.5104
PG 64-28	10.3120	-3.4400	PEN 40-50	10.5254	-3.5047
PG 64-34	9.4610	-3.1340	PEN 60-70	10.6508	-3.5537
PG 64-40	8.5240	-2.7980	PEN 85-100	11.8232	-3.6210
PG 70-10	10.6900	-3.5660	PEN 120-150	11.0897	-3.7252
PG 70-16	10.6410	-3.5480	PEN 200-300	11.8107	-4.0068
PG 70-22	10.2990	-3.4260	—	—	—

— Indicates that no additional relationships exist.

#### **E.5 BATCH MODE**

In batch mode, users enter four different files for the four different aging levels: (1) unaged or original binder data file, (2) RTFO-aged binder file, (3) PAV-aged binder file, and (4) field-aged binder file. Each file must be a tab delimited text file in order for ANNACAP to read the file. The file should have a header. Even if no data are available for some aging conditions, a file

name must be entered into the directory path on the right side. The formatting for the original-, RTFO-, and PAV-aged conditions, collectively referred to as the lab-aged files, is different than the formatting for the field-aged binder file. The formats for the two files are presented in table 79 and table 80. Users may also view the format by selecting either the **Format for Lab-Aged File** or **Format for Field-Aged File** buttons.

**Table 79. File format for lab-aged files.**

<b>Item</b>	<b>Description</b>
STATE_CODE	Code representing State or province
PROJECT_ID	Project ID code
PROJECT_LAYER	Project layer code as established in TST_LO5B
CONSTRUCTION_DATE	Date layer was constructed
SAMPLE_TYPE	1—original binder, 2—RTFO/TFO binder, 3—PAV binder
SAMPLE_DATE	Date of sampling
TEST_DATE	Date of testing
GSTAR_1	Binder $ G^* $ at temperature 1 (kPa)
GSTAR_PHASE_ANGLE_1	Phase angle at temperature 1 (degree)
GSTAR_TEMP_1	$ G^* $ temperature 1 ( $^{\circ}$ C)
GSTAR_2	Binder $ G^* $ at temperature 2 (kPa)
GSTAR_PHASE_ANGLE_2	Phase angle at temperature 2 (degree)
GSTAR_TEMP_2	$ G^* $ temperature 2 ( $^{\circ}$ C)
GSTAR_3	Binder $ G^* $ at temperature 3 (kPa)
GSTAR_PHASE_ANGLE_3	Phase angle at temperature 3 (degree)
GSTAR_TEMP_3	$ G^* $ temperature 3 ( $^{\circ}$ C).
GSTAR_4	Binder $ G^* $ at temperature 4 (kPa)
GSTAR_PHASE_ANGLE_4	Phase angle at temperature 4 (degree)
GSTAR_TEMP_4	$ G^* $ temperature 4 ( $^{\circ}$ C)
GSTAR_5	Binder $ G^* $ at temperature 5 (kPa)
GSTAR_PHASE_ANGLE_5	Phase angle at temperature 5 (degree)
GSTAR_TEMP_5	$ G^* $ temperature 5 ( $^{\circ}$ C)
GSTAR_6	Binder $ G^* $ at temperature 6 (kPa)
GSTAR_PHASE_ANGLE_6	Phase angle at temperature 6 (degree)
GSTAR_TEMP_6	$ G^* $ temperature 6 ( $^{\circ}$ C)
GSTAR_SOURCE	LTPP module from which $ G^* $ was extracted (i.e., TST)
RING BALL	Ring/ball temperature in Fahrenheit
RING BALL SOURCE	LTPP module from which TR&B was extracted (i.e., TST)
PENETRATION_39.2F	Penetration at 39.2 $^{\circ}$ F (PEN)
PENETRATION_39.2F_SOURCE	LTPP module from which PEN at 39.2 $^{\circ}$ F was extracted (i.e., TST)
PENETRATION_77F	Penetration at 77 $^{\circ}$ F (PEN)
PENETRATION_77F_SOURCE	LTPP module from which PEN at 77 $^{\circ}$ F was extracted (i.e., TST)
PENETRATION_115F	Penetration at 115 $^{\circ}$ F (PEN)
PENETRATION_115F_SOURCE	LTPP module from which PEN at 115 $^{\circ}$ F was extracted (i.e., TST)
ABSOLUTE_VISCOSITY	Absolute viscosity at 140 $^{\circ}$ F (poise)
ABSOLUTE_VISCOSITY_SOURCE	LTPP module from which absolute viscosity was extracted (i.e., TST)

KINEMATIC_VISCOSITY	Kinematic viscosity at 275 °F (centistokes)
KINEMATIC_VISCOSITY_SOURCE	LTPP module from which kinematic viscosity was extracted (i.e., TST)
VMA	Voids in mineral aggregate as percent total volume
VMA_SOURCE	LTPP module from which VMA was extracted (i.e., TST)
VFA	Voids filled with asphalt as percent VMA
VFA_SOURCE	LTPP module from which VFA was extracted (i.e., TST)
AIR_VOIDS	Air voids as percent total volume
AIR_VOIDS_SOURCE	LTPP module from which air voids was extracted (i.e., TST)
GMB	Bulk-specific gravity of the mix.
GMB_SOURCE	LTPP module from which $G_{mb}$ was extracted (i.e., TST)
GMM	Maximum specific gravity of the mix
GMM_SOURCE	LTPP module from which $G_{mm}$ was extracted (i.e., TST)
EFFECTIVE_AC	Effective asphalt content as percentage of total mix volume
EFFECTIVE_AC_SOURCE	LTPP module from which the effective volume of the binder ( $V_{be}$ ) was extracted (i.e., TST)
MR_5	Resilient modulus at 5 °C (GPa)
MR_25	Resilient modulus at 25 °C (GPa)
MR_40	Resilient modulus at 40 °C (GPa)
MR_SOURCE	LTPP module from which $M_R$ was extracted (i.e., TST)
BINDER_GRADE	Purchase specification grade of binder (RTFO aging only)

°C = (°F-32)/1.8

1 P = 10 Pas

1 psi = 6.86 kPa

**Table 80. File format for field-aged files.**

<b>Item</b>	<b>Description</b>
STATE_CODE	Code representing State or province.
PROJECT_ID	Project ID code.
PROJECT_LAYER	Project layer code as established in TST_LO5B.
CONSTRUCTION_DATE	Date layer was constructed.
SAMPLE_TYPE	Four-field-aged binder.
GSTAR_SAMPLE_DATE	Date of sampling for $ G^* $ .
GSTAR_1	Binder $ G^* $ at temperature 1 (kPa).
GSTAR_PHASE_ANGLE_1	Phase angle at temperature 1 (degree).
GSTAR_TEMP_1	$ G^* $ temperature 1 (°C).
GSTAR_2	Binder $ G^* $ at temperature 2 (kPa).
GSTAR_PHASE_ANGLE_2	Phase angle at temperature 2 (degree).
GSTAR_TEMP_2	$ G^* $ temperature 2 (°C).
GSTAR_3	Binder $ G^* $ at temperature 3 (kPa).
GSTAR_PHASE_ANGLE_3	Phase angle at temperature 3 (degree).
GSTAR_TEMP_3	$ G^* $ temperature 3 (°C).
GSTAR_4	Binder $ G^* $ at temperature 4 (kPa).
GSTAR_PHASE_ANGLE_4	Phase angle at temperature 4 (degree).
GSTAR_TEMP_4	$ G^* $ temperature 4 (°C).
GSTAR_5	Binder $ G^* $ at temperature 5 (kPa).
GSTAR_PHASE_ANGLE_5	Phase angle at temperature 5 (degree).
GSTAR_TEMP_5	$ G^* $ temperature 5 (°C).
GSTAR_6	Binder $ G^* $ at temperature 6 (kPa).
GSTAR_PHASE_ANGLE_6	Phase angle at temperature 6 (degree).
GSTAR_TEMP_6	$ G^* $ temperature 6 (°C).
GSTAR_SOURCE	LTPP module from which $ G^* $ was extracted (i.e., TST).
BINDER_SAMPLE_DATE	Date of sampling for viscosity.
RING BALL	Ring/ball temperature in Fahrenheit.
RING_BALL_SOURCE	LTPP module from which TR&B was extracted (i.e., TST).
PENETRATION_39.2F	Penetration at 39.2 °F (PEN).
PENETRATION_39.2F_SOURCE	LTPP module from which PEN at 39.2 °F was extracted (i.e., TST).
PENETRATION_77F	Penetration at 77 °F (PEN).
PENETRATION_77F_SOURCE	LTPP module from which PEN at 77 °F was extracted (i.e., TST).
PENETRATION_115F	Penetration at 115 °F (PEN).
PENETRATION_115F_SOURCE	LTPP module from which PEN at 115 °F was extracted (i.e., TST).
ABSOLUTE_VISCOSITY	Absolute viscosity at 140 °F (poises).

ABSOLUTE_VISCOSITY_SOURCE	LTPP module from which absolute viscosity was extracted (i.e., TST).
KINEMATIC_VISCOSITY	Kinematic viscosity at 275 °F (centistokes).
KINEMATIC_VISCOSITY_SOURCE	LTPP module from which kinematic viscosity was extracted (i.e., TST).
VMA	Voids in mineral aggregate as percent total volume.
VMA_SOURCE	LTPP module from which VMA was extracted (i.e., TST).
VFA	Voids filled with asphalt as percent VMA.
VFA_SOURCE	LTPP module from which VFA was extracted (i.e., TST).
AIR_VOID_SAMPLE_DATE	Date of sampling for air voids.
AIR_VOIDS	Air voids as percent total volume.
AIR_VOIDS_SOURCE	LTPP module from which air voids was extracted (i.e., TST).
GMB	Bulk specific gravity of the mix.
GMB_SOURCE	LTPP module from which $G_{mb}$ was extracted (i.e., TST).
GMM	Maximum specific gravity of the mix.
GMM_SOURCE	LTPP module from which $G_{mm}$ was extracted (i.e., TST).
EFFECTIVE_AC	Effective asphalt content as percent of total mix volume.
EFFECTIVE_AC_SOURCE	LTPP module from which $V_{be}$ was extracted (i.e., TST).
MR_SAMPLE_DATE	Date of sampling for $M_R$ .
MR_5	Resilient modulus at 5 °C (GPa).
MR_25	Resilient modulus at 25 °C (GPa).
MR_40	Resilient modulus at 40 °C (GPa).
MR_SOURCE	LTPP module from which $M_R$ was extracted (i.e., TST).

°C = (°F-32)/1.8

1 psi = 6.86 kPa

## E.6 OUTPUT DIRECTORY

Following the *File → Output Directory* path will launch the output directory dialog, as seen in figure 208. If no output directory is chosen or if users would like to change the current output directory, they should press the browse folder button to the right of the directory path (circled in black in figure 208). When this button is pressed, the folder selection dialog will appear (see figure 209). Users should then navigate to the desired output folder and select the **Current Folder** button (circled in black in figure 209). When selected, users return to the output directory dialog screen. To keep the chosen directory, users should press **OK** to return to the main screen. If users do not choose to keep the directory, press **Cancel**.



**Figure 208. Screenshot. Output directory dialog.**

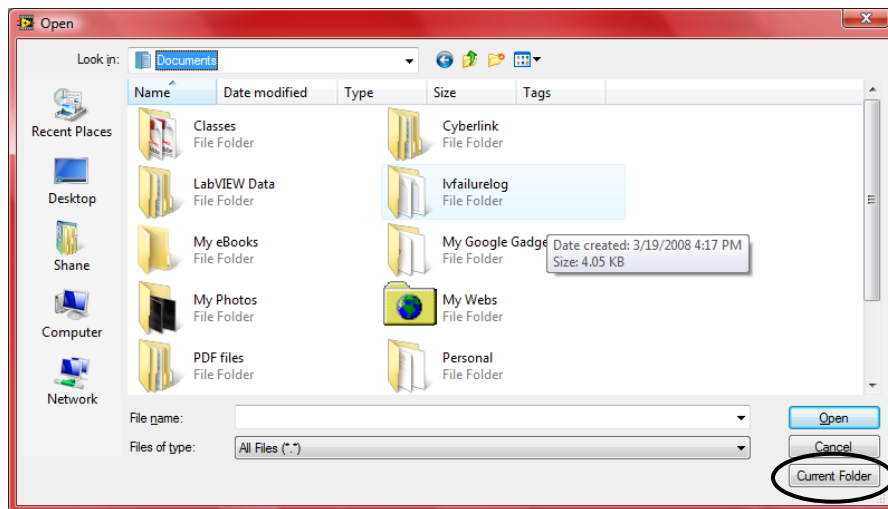


**Figure 209. Screenshot. Choosing output directory.**

## E.7 RUN ANALYSIS

To perform the dynamic modulus calculation, users should choose the *File → Run Analysis* path. The run analysis feature will become active only after ANNACAP has received valid input values. If an output directory has not been selected, an error message will appear, and the analysis will not be performed. Users must select a valid output directory and follow the *File → Run Analysis* path.

If users have chosen to follow either the  $M_R$ -based ANN,  $|G^*|$ -based ANN, or viscosity-based ANN, a single output file with the quantities shown in table 81 will be generated and located in the output directory. The file name for this file will be *Project\_ID-Project\_Layer-Aging Code-Model Type-Predicted Modulus.out*. If users have chosen to follow the batch mode analysis technique, two different files will be generated: (1) a summary file with one row per layer and (2) a detailed output data file including 30 rows per layer (one row for each temperature and frequency combination). The summary analysis file for the batch mode will be formatted as shown in table 82. The file name for this file will be *Models\_Summary\_Batch\_Mode.out*. The format for the main output file will be similar to that of the individual layer analysis and is shown in table 83. This file will be titled *Predicted\_Modulus\_Batch\_Mode.out*. Both the summary and detailed output files will be located in the user-selected output directory. When

running batch mode, users must rename the previous runs that are in the output directory because ANNACAP will overwrite existing file names without any warning to the user.

**Table 81. Output data format for single ANNACAP use.**

Item	Description
STATE_CODE	Code representing State or province as input by user
PROJECT_ID	Project ID code as input by user
PROJECT_LAYER	Project layer code as input by user
CONSTRUCTION_DATE	Date layer was constructed as input by user
SAMPLE_TYPE	1-original binder, 2-RTFO/TFO binder, 3-PAV binder, and 4-field binder
PREDICTIVE_MODEL	$M_R$ ANN, VV- ANN, GV-  $G^*$   ANN
TEMPERATURE	Temperature of modulus prediction (°F)
FREQUENCY	Frequency of modulus prediction (Hz)
$E^*$  _PREDICTION	Predicted dynamic modulus (psi)
VMA	Voids in mineral aggregate as percent total volume
VFA	Voids filled with asphalt as percent VMA
VISCOSITY	Viscosity input ( $10^9$ P) only for viscosity ANN model
A	Viscosity model intercept A (only for viscosity ANN model)
VTS	Viscosity model slope (only for viscosity ANN model)
MR_5C	Resilient modulus at 5 °C (only for $M_R$ model) (MPa)
MR_25C	Resilient modulus at 25 °C (only for $M_R$ model) (MPa)
MR_40C	Resilient modulus at 40 °C (only for $M_R$ model) (MPa)
$G^*$	Binder shear modulus (psi) only for   $G^*$   ANN model
WLF_COEFFICIENT_1	WLF shifting function coefficient $C_1$ (only for level 1 input   $G^*$   ANN model)
WLF_COEFFICIENT_2	WLF shifting function coefficient $C_2$ (only for level 1 input   $G^*$   ANN model)
CAM_COEFFICIENT_1	CAM fitting coefficient $G_g$ (only for   $G^*$   ANN model) (Pa)
CAM_COEFFICIENT_2	CAM fitting coefficient $\omega_c$ (only for   $G^*$   ANN model) (Pa)
CAM_COEFFICIENT_3	CAM fitting coefficient $k$ (only for   $G^*$   ANN model) (Pa)
CAM_COEFFICIENT_4	CAM fitting coefficient “me” (only for   $G^*$   ANN model) (Pa)
SIGMOIDAL_COEFFICIENT_1	Sigmoidal fitting function coefficient $\delta$ (psi)
SIGMOIDAL_COEFFICIENT_2	Sigmoidal fitting function coefficient $\alpha$
SIGMOIDAL_COEFFICIENT_3	Sigmoidal fitting function coefficient $\beta$
SIGMOIDAL_COEFFICIENT_4	Sigmoidal fitting function coefficient $\gamma$
SHIFT_FACTOR_COEFFICIENT_1	Shift factor fitting function coefficient $\alpha_1$ (°C)
SHIFT_FACTOR_COEFFICIENT_2	Shift factor fitting function coefficient $\alpha_2$ (°C)
SHIFT_FACTOR_COEFFICIENT_3	Shift factor fitting function coefficient $\alpha_3$ (°C)
SAMPLE_DATE	Date that binder was sampled (only for field-aged binder)
SAMPLE_AGE	Age of test sample relative to construction (days) (only for field-aged binder)

°C = (°F-32)/1.8

1 psi = 6.86 kPa

**Table 82. Summary file format from batch mode in ANNACAP.**

<b>Item</b>	<b>Description</b>
STATE_CODE	Code representing State or province as input by user
PROJECT_ID	Project ID code as input by user
PROJECT_LAYER	Project layer code as input by user
CONSTRUCTION_DATE	Date layer was constructed as input by user
SAMPLE_TYPE	1-original binder, 2-RTFO/TFO binder, 3-PAV binder, and 4-field binder
AVAILABLE_MODELS	Listing of models that can be used in modulus prediction with the available input data
VIOLATED_MODELS	Listing of available models for which the input data violates the calibration range
CHOSEN_MODEL	$M_R$ -resilient modulus ANN, VV-viscosity ANN, GV- $ G^*$ ANN, GV-PAR- $ G^*$ ANN with inconsistent aging conditions, VV-grade, viscosity ANN with viscosity coming from binder grade, *-V, *ANN model with inputs violating the input range

**Table 83. Output data format for batch mode ANNACAP use.**

<b>Item</b>	<b>Description</b>
SECTION_ID	Unique ID combining State code, project ID and layer, sample type, and model name
STATE_CODE	Code representing State or province as input by user
PROJECT_ID	Project ID code as input by user
PROJECT_LAYER	Project layer code as input by user
CONSTRUCTION_DATE	Date layer was constructed as input by user
SAMPLE_TYPE	1-original binder, 2-RTFO/TFO binder, 3-PAV binder, and 4-field binder
PREDICTIVE_MODEL	$M_R$ -resilient modulus ANN, VV-viscosity ANN, GV- $ G^*$ ANN, GV-PAR- $ G^*$ ANN with inconsistent aging conditions, VV-grade, viscosity ANN with viscosity coming from binder grade, *-V, *ANN model with inputs violating the input range
TEMPERATURE	Temperature of modulus prediction (°F)
FREQUENCY	Frequency of modulus prediction (Hz)
$ E^*$ _PREDICTION	Predicted dynamic modulus (psi).
VMA	Voids in mineral aggregate as percent total volume (blank for MR ANN)
VFA	Voids filled with asphalt as percent VMA (only for viscosity and $ G^*$ ANN)
VISCOSITY	Viscosity input ( $10^9$ P) (only for viscosity ANN model)
A	Viscosity model intercept A (only for viscosity ANN model)
VTS	Viscosity model slope (only for viscosity ANN model)
MR_5C	Resilient modulus at 5 °C (only for $M_R$ model) (MPa)
MR_25C	Resilient modulus at 25 °C (only for $M_R$ model) (MPa)
MR_40C	Resilient modulus at 40 °C (only for $M_R$ model) (MPa)
$ G^*$	Binder shear modulus (psi) only for $ G^*$ ANN model
WLF_COEFFICIENT_1	WLF shifting function coefficient $C_1$ (not used in batch mode)

WLF_COEFFICIENT_2	WLF shifting function Coefficient C <sub>2</sub> (Not used in batch mode)
CAM_COEFFICIENT_1	CAM fitting coefficient G <sub>g</sub> (only for  G*  ANN model) (Pa)
CAM_COEFFICIENT_2	CAM fitting coefficient $\omega_c$ (only for  G*  ANN model) (Pa)
CAM_COEFFICIENT_3	CAM fitting coefficient k (only for  G*  ANN model) (Pa)
CAM_COEFFICIENT_4	CAM fitting coefficient m <sub>e</sub> (only for  G*  ANN model) (Pa)
SIGMOIDAL_COEFFICIENT_1	Sigmoidal fitting function coefficient $\delta$ (psi)
SIGMOIDAL_COEFFICIENT_2	Sigmoidal fitting function coefficient $\alpha$
SIGMOIDAL_COEFFICIENT_3	Sigmoidal fitting function coefficient $\beta$
SIGMOIDAL_COEFFICIENT_4	Sigmoidal fitting function coefficient $\gamma$
SHIFT_FACTOR_COEFFICIENT_1	Shift factor fitting function coefficient $\alpha_1$ (°C)
SHIFT_FACTOR_COEFFICIENT_2	Shift factor fitting function coefficient $\alpha_2$ (°C)
SHIFT_FACTOR_COEFFICIENT_3	Shift factor fitting function coefficient $\alpha_3$ (°C)
QUALITY_CONTROL_#1	A—the output data passed QC #1; F—the input data did not pass QC #1
QUALITY_CONTROL_#2	A—the output data passed QC check 2; F—the input data did not pass QC #2
QUALITY_CONTROL_#3	A—the output data passed QC check 3 or QC #3 did not apply; F—the input data did not pass QC #3
QUALITY_CONTROL_#4	A—the output data passed QC #4 or QC #4 did not apply; F—the input data did not pass QC #4
QUALITY_CONTROL_#5	A—the output data passed QC #5; F—the input data did not pass QC #5
QUALITY_CONTROL_#6	A—the output data passed QC #6 or QC #6 did not apply; F—the input data did not pass QC #6
QUALITY_CONTROL_#7	A—the output data passed QC #7 or QC #7 did not apply; F—the input data did not pass QC #7
AVAILABLE_MODELS	Listing of models that can be used in modulus prediction with the available input data
VIOLATED_MODELS	Listing of available models for which the input data violates the calibration range
CHOSEN_MODEL	Listing of model chosen for predicting the modulus
SAMPLE_DATE	Date that binder was sampled (only for field-aged binder)
SAMPLE_AGE	Age of test sample relative to construction (days) (only for field-aged binder, blank means either SAMPLE_DATE or CONSTRUCTION_DATE were not given)
INDIVIDUAL_DATA_GRADE	NCSU grade for modulus prediction; “A”—the predicted modulus is acceptable; “C”—the predicted modulus is questionable; and “F”—the predicted modulus may have severe problems
MASTERCURVE_GRADE	NCSU grade for mastercurve prediction; “A”—the predicted curve is acceptable; “C”—the predicted curve is questionable; and “F”—the predicted curve may have severe problems

°C = (°F-32)/1.8

1 psi = 6.86 kPa

## E.8 FORM OF SUPPLEMENTARY FUNCTIONS

### E.8.1 CAM Model Function

$$|G^*| = \frac{G_g}{\left(1 + \left(\frac{\omega_c}{\omega_R}\right)^k\right)^{m_e/k}} \quad (120)$$

Where:

$\omega_R$  = Reduced angular frequency.  
 $G_g$ ,  $\omega_c$ ,  $k$ , and  $m_e$  = Fitting coefficients.

$$\omega_R = \omega^* a_T \quad (121)$$

Where:

$\omega$  = Physical angular frequency of load.  
 $a_T$  = Time-temperature shift factor.

## E.9 TIME-TEMPERATURE SHIFT FACTOR FUNCTION FOR $|G^*|$

### E.9.1 Level 1 (WLF Function)

$$\log a_T = \frac{C_1(T - T_R)}{C_2 + T - T_R} \quad (122)$$

Where:

$T$  = Test temperature of interest.  
 $T_R$  = Reference temperature (chosen as 59 °F (15 °C) for ANNACAP).  
 $C_1$  and  $C_2$  = WLF fitting coefficients.

### E.9.2 Levels 2 and 3

For the GV ANN models not using level 1 input, the shift factor is given by the following:

$$\log a_T = \begin{cases} \frac{E_a}{2.303 * R} \left( \frac{1}{273 + T} - \frac{1}{273} \right) + \frac{C_1 - T_R}{C_2 - T_R} & T \leq 0 \\ \frac{C_1(T - T_R)}{C_2 + T - T_R} & T > 0 \end{cases} \quad (123)$$

Where:

$$\begin{aligned} R &= 8.314 \times 10^{-3} \text{ kJ}\cdot\text{K}^{-1}\cdot\text{mol}^{-1}. \\ E_a &= 189.879 \text{ kJ/mol.} \\ C_1 &= -13.227. \\ C_2 &= 90.349. \end{aligned}$$

## E.10 SIGMOIDAL FUNCTION

$$\log|E^*| = \delta + \frac{\alpha}{1 + e^{\beta + \gamma * \log(t_R)}} \quad (124)$$

Where:

- $t_R$  = The inverse of reduced frequency of loading, which is defined in the same way as reduced angular frequency in equation 121 but with frequency in hertz instead of radians per second.
- $\delta$ ,  $\alpha$ ,  $\beta$ , and  $\gamma$  = Fitting coefficients.

## E.11 TIME-TEMPERATURE SHIFT FACTOR FUNCTION FOR $|E^*|$

$$\log a_T = \alpha_1 T^2 + \alpha_2 T + \alpha_3 \quad (125)$$

Where:

- $a_T$  = Mixture time-temperature shift factor.
- $T$  = Temperature of interest.
- $\alpha_1$ ,  $\alpha_2$ , and  $\alpha_3$  = Fitting coefficients.

## REFERENCES

1. National Cooperative Highway Research Program. (2004). *Mechanistic-Empirical Pavement Design Guide*, Transportation Research Board, Washington, DC. Obtained from: <http://onlinepubs.trb.org/onlinepubs/archive/mepdg/home.htm>. Site last accessed August 8, 2011.
2. Advanced Research Associates. (2004). *2002 Design Guide: Design of New and Rehabilitated Pavement Structures*, NCHRP 1-37A Project, National Cooperative Highway Research Program, National Research Council, Washington, DC.
3. Witczak, M.W., et al. (2002). *Simple Performance Test for Superpave Mix Design*, NCHRP Report 465, Transportation Research Board, Washington, DC.
4. Bonaquist, R., Christensen, D., and Stump, W. (2003). *Simple Performance Tester for Superpave Mix Design: First Article Development and Evaluation*, NCHRP Report 513, Transportation Research Board, Washington, DC.
5. Bari, J. (2005). *Development of a New Revised Version of the Witczak E\* Predictive Models for Hot Mix Asphalt Mixtures*, Ph.D. Dissertation, Arizona State University, Phoenix, AZ.
6. Christensen, Jr., D.W., Pellinen, T.K., and Bonaquist, R.F. (2003). "Hirsch Model for Estimating the Modulus of Asphalt Concrete," *Journal of the Association of Asphalt Paving Technologists*, 72, 97–121.
7. Al-Khateeb, G., Shenoy, A., Gibson, N., and Harman T. (2006). *A New Simplistic Model for Dynamic Modulus Predictions of Asphalt Paving Mixtures*, Association of Asphalt Paving Technologists Annual Meeting, Paper Preprint CD, Savannah, GA.
8. AASTHO TP-62. (2010). *American Association of State Highway and Transportation Officials (AASHTO) Standard Specifications for Transportation Materials and Methods of Sampling and Testing*, 30th Ed., Washington, DC.
9. Witczak, M.W., et al. (2002). *Simple Performance Test for Superpave Mix Design*, NCHRP Report 465, Transportation Research Board, Washington, DC.
10. Elkins, G.E., et al. (2003). *Long-Term Pavement Performance Information Management System: Pavement Performance Database User Reference Guide*, Report No. FHWA-RD-03-088, Federal Highway Administration, McLean, VA.
11. Andrei, D., Witczak, M.W., and Mirza, M.W. (1999). *Development of a Revised Predictive Model for the Dynamic (Complex) Modulus of Asphalt Mixtures*, Inter Team Technical Report prepared for the NCHRP 1-37A Project, Department of Civil Engineering, University of Maryland, College Park, MD.
12. Dongré, R., Myers, L., D'Angelo, J., Paugh, C., and Gudimetla, J. (2005). "Field Evaluation of Witczak and Hirsch Models for Predicting Dynamic Modulus of Hot-Mix Asphalt," *Journal of the Association of Asphalt Paving Technologists*, 74, 381–442.

13. LaCroix, A., Mosavi Khandan, A.A., and Kim, Y.R. (2007). "Predicting the Resilient Modulus of Asphalt Concrete from the Dynamic Modulus," *Transportation Research Record 2001*, Transportation Research Board, Washington, DC.
14. Kim, R.Y., et al. (2009). *Development of a Multiaxial Viscoelastoplastic Continuum Damage Model for Asphalt Mixtures*, FHWA DTFH61-05-RA-00108, Federal Highway Administration, Washington, DC.
15. TPF-5(019). *Full-Scale Accelerated Performance Testing for Superpave and Structural Validation*, Contract DTF61-02C-00025, Federal Highway Administration, Washington, DC. Obtained from: <http://www.pooledfund.org/projectdetails.asp?id=11&status=6>. Site last accessed May 20, 2011.
16. Christensen, D. (2006). *Requirements for Voids in Mineral Aggregate for Superpave Mixtures*, NCHRP 09-25, National Cooperative Highway Research Program, Transportation Research Board, Washington, DC.
17. Christensen, D. (2006). *Air Void Requirements for Superpave Mix Design*, NCHRP 09-31, National Cooperative Highway Research Program, Transportation Research Board, Washington, DC.
18. AASHTO M226-80. (2008). "Standard Specification for Viscosity Graded Asphalt Cement," *Standard Specifications for Transportation Materials and Methods of Sampling and Testing*, 26th Ed., American Association of State Highway and Transportation Officials, Washington, DC.
19. AASHTO R30-02. (2006). "Standard Specification for Mixture Conditioning of Hot Mix Asphalt (HMA)," *Standard Specifications for Transportation Materials and Methods of Sampling and Testing*, 26th Ed., American Association of State Highway and Transportation Officials, Washington, DC.
20. FHWA. (2010). *Long Term Pavement Performance Standard Data Release 24*, DVD, Version 2010.01, Federal Highway Administration, McLean, VA.
21. Kim, Y.R. (2001). "Assessing Pavement Layer Condition using Deflection Data," *NCHRP Research Results Digest*, Vol. 254, National Cooperative Highway Research Program, National Research Council, Washington, DC.
22. Meier, R.W. (1995). *Backcalculation of Flexible pavement Moduli from Falling Weight Deflectometer Data Using Artificial Neural Networks*, Final Report, Army Engineering Waterways Experiment Station, Vicksburg, MS.
23. Cylan, H., Gopalakrishnan, K., and Guclu, A. (2007). *Nonlinear Pavement Analysis Using Artificial Neural Network Based Stress-Dependent Models*, 86th Annual Meeting of the Transportation Research Board, Washington, DC.

24. Attoh-Okine, N.O. (1994) *Predicting Roughness Progression in Flexible Pavements using Artificial Neural Networks*, 1, 55–62, Proceedings of the Third International Conference Managing Pavements, San Antonio, TX.
25. Kim, Y. and Kim, Y.R. (1998). “Prediction of Layer Moduli from FWD and Surface Wave Measurements Using Artificial Neural Network,” *Transportation Research Record* 1639, 53–61, Transportation Research Board, Washington, DC.
26. Schwartz, C.W. (2005). *Evaluation of the Witczak Dynamic Modulus Prediction Model*, Proceedings of the 84th Annual Meeting of the Transportation Research Board, Washington, DC.
27. AASHTO. (1993). *Guide for Design of Pavement Structures*, American Association of State Highway and Transportation Officials, Washington, DC.
28. ASTM D4123-82. (1995). *Standard Test Method for Indirect Tension Test for Resilient Modulus of Bituminous Mixtures*, American Society for Testing and Materials, West Conshohocken, PA.
29. Barksdale, R.D. and Alba, J. (1997). *Laboratory Determination of Resilient Modulus for Flexible Pavement Design: Final Report*, NCHRP Web Doc 14 (Project NCHRP 1-28), National Cooperative Highway Research Program, Washington DC.
30. LAW PCS. (2001). *Protocol P-07: Test Method for Determining the Creep Compliance, Resilient Modulus and Strength of Asphalt Materials Using the Indirect Tensile Test Device*, Version 1.1, Law Engineering and Environmental Services, Inc., Beltsville, MD.
31. Witczak, M.W. (2004). *Laboratory Determination of Resilient Modulus for Flexible Pavement Design*, NCHRP Project 1-28A, National Cooperative Highway Research Program, Washington, DC.
32. Zhang, W., Drescher, A., and Newcomb, D.E. (1997). “Viscoelastic Analysis of Diametrical Compression of Asphalt Concrete,” *Journal of Engineering Mechanics*, 123, 596–603.
33. AASHTO TP31-96. (1996). “Standard Test Method for Determining the Resilient Modulus of Bituminous Mixtures by Indirect Tension,” *Standard Specifications for Transportation Materials and Methods of Sampling and Testing*, 16th Ed., American Association of State Highway and Transportation Officials, Washington, DC.
34. Roque, R. and Buttlar, W.G. (1992). “The Development of a Measurement and Analysis System to Accurately Determine Asphalt Concrete Properties Using the Indirect Tensile Mode,” *Journal of the Association of Asphalt Paving Technologists*, 60, 304–332.
35. Hondros, G. (1959). “Evaluation of Poisson’s Ratio and the Modulus of Materials of a Low Tensile Resistance by the Brazilian (Indirect Tensile) Test with Particular Reference to Concrete,” *Australian Journal of Applied Science*, 10(3), 243–268.

36. Park, S.W. and Schapery, R.A. (1999). "Methods of Interconversion between Linear Viscoelastic Material Functions. Part I—A Numerical Method Based on Prony Series," *International Journal of Solids and Structures*, 36, 1653–1675.
37. Kim, Y.R., Seo, Y., King, M., and Momen, M.. (2004). "Dynamic Modulus Testing of Asphalt Concrete in Indirect Tension Mode," *Transportation Research Record* 1891, 163–173, Transportation Research Board, Washington, DC.
38. Fairhurst, C.E., Kim, Y.R., and Khosla, N.P. (1990). *Resilient Modulus Testing of Asphalt Specimens in Accordance with ASTM D 4123-82*, Proceedings of the RILEM Fourth International Symposium, Budapest, Hungry.
39. Mirza, M.W., Graul, R.A., Groeger, J.L., and Lopez, A. (1997). "Theoretical Evaluation of Poisson's Ratio and Elastic Modulus Using Indirect Tensile Test with Emphasis on Bituminous Mixtures," *Transportation Research Record* 1590, 34–44, Transportation Research Board, Washington, DC.
40. Vinson, T.S. (1989). *Fundamentals of Resilient Modulus Testing*, Proceedings of the Workshop on Resilient Modulus Testing, Oregon State University, Corvallis, OR.
41. Underwood, B.S., Kim, Y.R. and Guddati, M.N. (2006). "Characterization and Performance Prediction of ALF Mixtures Using a Viscoelastoplastic Continuum Damage Model," *Asphalt Paving Technology*, 75, 577–636.
42. Christensen, Jr., D.W. and Bonaquist, R.F. (2008). *Hirsch Model for Estimating the Modulus of Asphalt Concrete. Draft Standard Practice*, American Association of State Highway and Transportation Officials, Washington, DC.
43. ASTM D 2493-01. (2009). *Standard Test Method for Indirect Tension Test for Resilient Modulus of Bituminous Mixture*, ASTM International, West Conshohocken, PA.
44. Mirza, M.W. and Witczak, M.W. (1995). "Development of a Global Aging System for Short and Long Term Aging of Asphalt Cements," *Journal of the Association of Asphalt Paving Technologists*, 64, 393–418.
45. AASHTO T53-08. (2008). "Standard Method of Test for Determining the Resilient Modulus of Bituminous Mixtures by Indirect Tension," *Standard Specifications for Transportation Materials and Methods of Sampling and Testing*, 28th Ed., American Association of State Highway and Transportation Officials, Washington, DC.
46. AASHTO T49-07. (2008). "Standard Method of Test for Penetration of Bituminous Materials," *Standard Specifications for Transportation Materials and Methods of Sampling and Testing*, 28th Ed., American Association of State Highway and Transportation Officials, Washington, DC.
47. AASHTO T202-03. (2010). "Standard Method of Test for Viscosity of Asphalts by Vacuum Capillary Viscometer," *Standard Specifications for Transportation Materials and Methods of*

*Sampling and Testing*, 28th Ed., American Association of State Highway and Transportation Officials, Washington, DC.

48. AASHTO T201-03. (2010). “Standard Method of Test for Kinematic Viscosity of Asphalts (Bitumens),” *Standard Specifications for Transportation Materials and Methods of Sampling and Testing*, 28th Ed., American Association of State Highway and Transportation Officials, Washington, DC.
49. Kim, Y.R., Guddati, M., Feng, Z., Zhang, P., and Subramanian, V. (2005). *A Micromechanics-Based Methodology for the Study of Cracking in Asphalt Concrete*, Final Report to Texas A&M Research Foundation, Bryan, TX.
50. Bonaquist, R. (2008). *NCHRP Report 614: Refining the Simple Performance Tester for Use in Routine Practice*, Project NCHRP 9-29, National Cooperative Highway Research Program, Washington, DC.
51. Advanced Asphalt Technologies, LLC. (2004). *Western Research Institute Test Sections, Kansas US 77, Asphalt Concrete Mixture Performance Testing and Analysis*, Western Research Institute, Laramie, WY.
52. Advanced Asphalt Technologies, LLC. (2004). *Western Research Institute Test Sections, Interstate 15, Clark County, Nevada, Asphalt Concrete Mixture Performance Testing and Analysis*, Western Research Institute, Laramie, WY.





